Three-dimensional Simulations of the Ozone Layer and Atmospheric Dynamics of Earth-like Habitable Planets

Inauguraldissertation
der Philosophisch-naturwissenschaftlichen Fakultät
der Universität Bern

vorgelegt von

Elisavet Proedrou

von Griechenland

Leiter der Arbeit: PD Dr. Klemens Hocke
Institut für Angewandte Physik

Three-dimensional Simulations of the Ozone Layer and Atmospheric Dynamics of Earth-like Habitable Planets

Inauguraldissertation
der Philosophisch-naturwissenschaftlichen Fakultät
der Universität Bern

vorgelegt von

Elisavet Proedrou

von Griechenland

Leiter der Arbeit:	PD Dr. Klemens Hocke Institut für Angewandte Physik

Von der Philosophisch-naturwissenschaftlichen Fakultät angenommen.

Der Dekan:

Bern, den 18.03.2016 Prof. Dr. Gilberto Colangelo

Copyright Notice

Contents

1 Abstract

This thesis investigates how the atmospheric circulation and ozone distribution of a planet with the size, the mass, the continental distribution and topography, the oceans, and the atmospheric composition and circulation of the present day Earth (Earth-like planet) is altered by local and global radiative forcing changes using three-dimensional simulations. These simulations are generated using the coupled 3D chemistry-climate model CESM1(WACCM), which incorporates the entire atmosphere up to an altitude of 140 km, as well as parametrizations for the full atmospheric chemistry, photochemistry, cloud microphysics and small-scale gravity wave flux. These features allow for a realistic simulation of the composition and dynamics of the Earth's atmosphere.

The investigation is composed of three studies. In the first study, the effects in the lower tropospheric dynamics generated by a local radiative forcing change on the present day Earth are investigated. The forcing change is implemented by changing the local soil colour and therefore the local albedo. In order to isolate the generated perturbation from the background waves, a small-scale perturbation analysis is performed for the first 5 days of the simulation. The soil colour change generates an upwards propagating convective perturbation, which induces a radially propagating circular wave at an altitude of 2 km. This wave has a mean wave velocity of $\langle v \rangle = 200 \pm 50$ m/s, a mean horizontal wavelength $\langle \lambda \rangle = 3000 \pm 500$ km and a mean wave period $\langle p \rangle = 4 \pm 1$ h. In addition to this wave, a secondary wave is also generated over the tropical Amazon convection zone when the primary wave collides with it. The secondary wave has a mean wave velocity $\langle v \rangle = 220 \pm 40$ m/s, a mean horizontal wavelength $\langle \lambda \rangle = 2600 \pm 600$ km and a mean wave period $\langle p \rangle = 3 \pm 1$ h.

The second study expands the scope of the first study by investigating how a global radiative forcing change affects the atmospheric circulation and ozone distribution of an Earth-like planet orbiting a Sun-like star. In this study, the forcing change is implemented by tidally locking the planet. The simulations reveal that, when the full photochemistry and atmospheric dynamics are included, the planet's middle atmosphere adjusts to the new conditions within a relatively short time (roughly 80 days from the start of the simulation) and its atmospheric circulation and ozone distribution are altered.

The Brewer-Dobson circulation is replaced by a day side upwelling and a night side downwelling. The total ozone content of the tidally locked planet is reduced by 19.3% compared to the Earth due to radiation and transport changes. Specifically, the total ozone content mean is reduced by 23.21% on the day side and by 15.52% on the night side. The middle stratospheric ozone accumulates on the day side of the planet resulting in a day-night variation of 40%. In comparison, the Earth's day-night variation is only 2%. The lower stratospheric ozone is mainly influenced by the

altered circulation and is characterised by enhanced night side zone and depleted day side regions. The planet's mesospheric ozone is similar to the Earth's mesospheric ozone distribution, with decreased ozone on the day side and enhanced ozone on the night side. For a distant observer, the planet's total ozone content will vary up to 23% during its revolution around its parent star.

Finally, the third study is an extension of the second study. It investigates, in more detail, the 3D atmospheric circulation of a tidally locked planet. An intercomparison with the fast rotating Earth is performed and the effects of the sea surface temperature (SST) on the middle atmosphere of the tidally locked planet are simulated and analysed. For this study, two extreme SSTs are used: a present day Earth SST and a tidally locked aquaplanet SST. The simulation shows that the SST has a limited influence on the middle atmosphere. The warmer present day Earth SST generated, on average, a lower tropospheric heating of 3.7 K, an upper tropospheric cooling of 4 K, a lower stratospheric heating of 3.8 K, a lower mesospheric cooling of 1.13 K and an upper mesospheric heating of 4.3 K. The lower stratospheric heating is possibly generated by the increased infrared radiation flux from the warmer present day Earth SST surface, as the lower stratospheric ozone will absorb the increased infrared radiation at 9.6 μm. The SST change has no significant influence on the primary ozone layer, while the warmer SST leads to a strong increase of the secondary ozone layer. The tropospheric and stratospheric results are in agreement with past studies of the influence of SST variability on the Earth's troposphere and stratosphere. The lower mesospheric cooling is consistent with increased mesospheric wave-breaking due to the warmer present day Earth SST. Both simulations are characterised by an upwelling on the day side and downwelling on the night side, while the stratospheric and mesospheric circulation is only weakly influenced by the underlying SST. Generally, the reduced Coriolis force of the tidally locked planet leads to enhanced meridional mixing and consequently to a relatively isothermal temperature distribution of the middle atmosphere. The occurrence of large-scale vortices and variable jet streams depends, to some extent, on the SST distribution.

2 Introduction

A change in the radiative balance of an Earth-like planet is expected to alter its atmospheric dynamics and composition. The subject has not been extensively investigated so far and this thesis aims to fill this gap. Initially, the effect of a small local perturbation of the radiative balance is investigated in order to study the coupling processes between the Earth's surface and the atmosphere, by changing the regional surface colour. Then, the investigation is expanded to the effects of a global radiative forcing change by changing the planet's incident stellar radiation flux distribution. This is achieved by tidally locking the planet and altering its sea-surface temperature to fit the tidally locked energy distribution. The study focuses on the planet's middle atmosphere, as such studies have not been performed in the past. Ideas from the first and second studies are then combined in the third study, where the radiative balance of the tidally locked Earth-like planet presented in the second study is altered by changing its sea-surface temperature. One aim of the study is to investigate how strongly the SST affects the planet's middle atmosphere.

Earth receives most of its energy from the Sun, whose spectrum can be seen in Figure 2.1. The incident solar radiation flux at the top of the atmosphere is indicated with the solid line, while the observed spectrum at sea level is indicated by the grey area. At the bottom of the figure (Salby, 2012b), the ultraviolet (UV), visible and infrared parts of the spectrum are indicated by the purple, the yellow and the red regions, respectively.

The incident solar radiation flux at the top of the atmosphere, integrated over the wavelength, is given by the solar constant $\mathrm{S_o} = 1372$ W/m^2. The global average of the solar irradiance F_{inc} ($F_{inc} = S_o/4 = 343$ W/m^2) is equal to the quotient of the incoming solar power ($\pi R^2 S_o$) and the Earth's surface area ($4\pi R^2$). The Earth's radiative balance can be seen in Figure 2.2. Approximately 31 % of the $\mathrm{F_{inc}}$ (106 W/m^2) is reflected back towards space: 21 W/m^2 by the air, 69 W/m^2 by the clouds and 16 W/m^2 by the surface. Of the remaining energy, 68 W/m^2 are absorbed by the atmosphere: 48 W/m^2 by atmospheric H_2O, O_3 and aerosols, and 20 W/m^2 by the clouds (Salby, 2012b). Radiation with wavelengths smaller than 200 nm is absorbed by mesospheric O_2 molecules above 80 km altitude, while radiation with wavelengths between 200 nm and 300 nm is absorbed by stratospheric ozone molecules between 25 km and 50 km altitudes (Saha, 2008). This mechanism is responsible for the cut-off visible at 300 nm in Figure 2.1. The remaining 169 W/m^2, which comprise nearly 49 % of the incoming shortwave energy, reach the ground and are absorbed by the Earth's surface (Salby, 2012b).

The energy absorbed by the atmosphere is re-emitted in the form of longwave radiation. In total, 327 W/m^2 are emitted by the atmosphere towards the surface (120 W/m^2 by the clouds and 248 W/m^2 by H_2O, O_3, and aerosols). The surface absorbs the incident shortwave and longwave radiation and re-emits it in the form of longwave

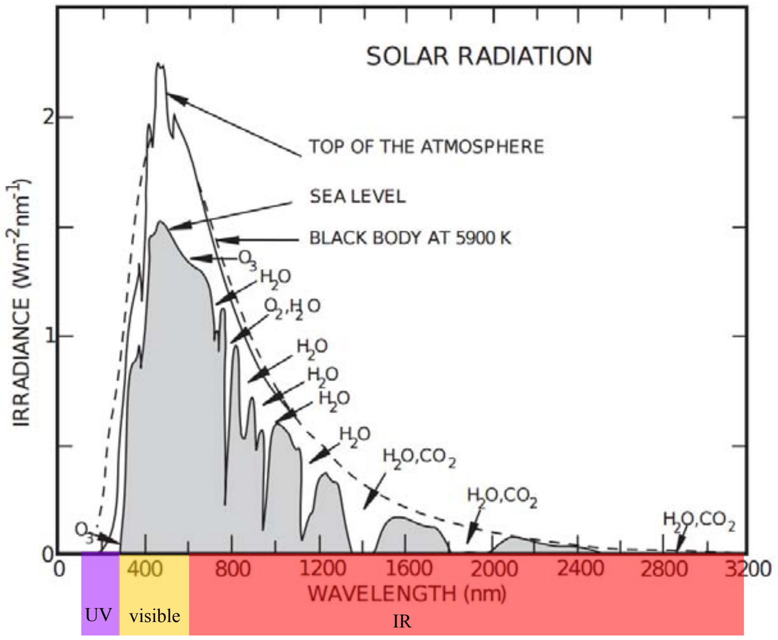

Figure 2.1: The Solar Spectrum. Solid line: Incident radiation at the top of the atmosphere. Grey area: The observed spectrum on the Earth's surface. Purple area: ultraviolet spectrum (UV). Yellow area: visible radiation spectrum. Red area: infrared spectrum. (Adapted from Salby (2012b))

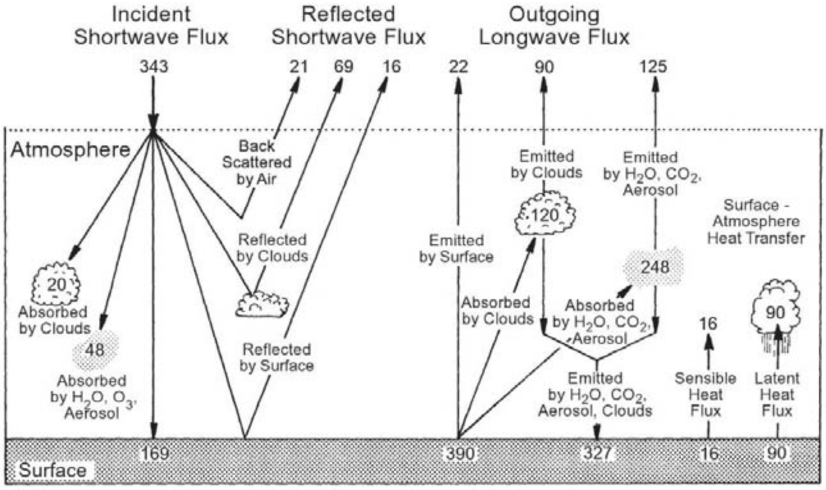

Figure 2.2: Earth radiative budget (From Salby (2012b))

radiation. A total of 390 W/m^2 are emitted upwards. Of this energy, 368 W/m^2 are re-absorbed by the atmosphere and 22 W/m^2 are released into space. The surface net radiative forcing of the surface is given by the sum of the incident shortwave and longwave absorption minus the outgoing longwave emission (169 W/m^2 + 237 W/m^2 - 390 W/m^2 = 106 W/m^2) (Salby, 2012b). Since the radiative forcing of the surface is positive, the surface is radiatively heated. Then, the heat is released in the form of sensible heat (16 W/m^2) and latent heat (90 W/m^2) flux. The planet's radiative equilibrium is maintained through the processes described in the above paragraphs.

A planet's radiative balance can be altered by several factors such as the solar energy intensity, the reflectivity of clouds or gases, the absorption by greenhouse gases, the absorption of shortwave radiation by the planet's surface, and the absorption and emission of longwave radiation by the planet's surface. This change in the planet's radiative balance is called radiative forcing. The most important factors influencing the Earth's radiative balance are the shortwave solar energy intensity, the reflectivity of clouds or gases, and the nature of the planet's surface. The atmospheric effect of a regional soil color change has only been investigated to a small extent by 2-3 studies. Manzini et al. (2006) investigated the effects of the interannual sea surface temperatures (SSTs) variations on the Northern Hemispheric winter polar stratospheric circulation with the ECHAM5 model. The model was forced with SSTs observed during the 1980 to 1999 period. The study determined that the winter ENSO phenomenon generates an enhanced planetary wave disturbance which increases the polar stratospheric air by a few degrees in late winter and early spring resulting in a weakening of the polar vortex. Cohen (2011) investigated how the Siberian snow cover variability, which also changes the Siberian surface albedo, influences the weather in remote regions several months later. They determined that increased snow cover and, therefore, increased upwelling shortwave radiation leads to the emergence of a stratospheric warming and a January tropospheric negative winter Arctic Oscillation response.

The surface albedo is defined as the ratio between the incident radiation reflected by a surface and the radiation incident on the surface. The Earth's surface albedo varies widely depending on the nature and composition of the land (Saha, 2008). A list of typical values of surface albedo can be seen in Table 2.1. As expected, the lighter the surface's colour is, the higher the surface's albedo (Saha, 2008).

Table 2.1: Typical surface albedo. The values were taken from Saha (2008) and Encyclopedia of Earth (2013)

Surface Type	Albedo
Fresh Snow	0.8
Coniferous Forest	0.05-0.15
Light coloured Sand	0.15
Dark Coloured Sand	0.25

A deepening of the surface colour results in increased absorption of the incident shortwave radiation by the surface and leads to the heating of the surface itself and the air located directly above it. For the radiative equilibrium to be maintained, the majority of the absorbed radiation must be re-emitted through the sensible and the latent heat, as well as the longwave radiation flux (Petty, 2006). This mechanism leads to the generation of atmospheric gravity waves.

The generation, propagation and dissipation of atmospheric waves were studied by Nicholls and Pielke (2000) and Gardner and Schunk (2010) using idealised model simulations. Nicholls and Pielke (2000) investigated the atmospheric waves induced by a tropical thunderstorm using an idealised 3D, fully compressible atmospheric model and concluded that it generated thermal compression and atmospheric gravity waves. Gardner and Schunk (2010) studied the effect of a large scale atmospheric perturbation using a high-resolution global thermosphere-ionosphere model. They concluded that such a perturbation would lead to the generation of multiple Traveling Atmospheric Disturbances which travel coincidently from the northern and southern auroral zones towards the Equator and into the conjugate hemisphere.

According to Seitz (2013), the influence of regional albedo changes on the Earth's radiation energy balance and, by extent, on the atmosphere and climate system have not been adequately researched either through observations or simulations. Past studies have focused on the long-term climate change effects (Walland and Simmonds (1996), Held and Suarez (1974), Kirschbaum et al. (2011a), Betts (2000)) and how they can be utilised to combat global warming through geoengineering projects (Ridgwell et al., 2007). Furthermore, to my knowledge, the generation of atmospheric gravity waves by a regional soil colour change has not yet been modelled. The gravity wave research was mainly focused on orographically and convectively induced atmospheric gravity waves and jet stream waves (Alexander et al., 2010).

Currently, large renewable energy projects with large areas of solar panels in the desert (e.g., DESERTEC (The DESERTEC Foundation, 2015)) have been proposed as possible solutions to the expected increased energy needs of the future. Such programs would significantly alter the surface albedo of the area chosen for the project. Many geoengineering ideas which involve the surface albedo change of big tracks of the Earth's surface have also been proposed to combat global warming. Therefore, these projects make imperative the increase of our understanding of the effects of a regional albedo change on the atmosphere.

The planet's radiative balance can also be altered as a result of changes in the planet's shortwave radiation distribution, affecting the planet's ozone distribution and atmospheric circulation. This change would occur if the planet became tidally locked to its parent star, with one hemisphere permanently facing the star. Such planets have been often detected orbiting in the habitable zones of M dwarf stars. An analysis of the Kepler mission data indicated that there could be as many as 40 billion terrestrial exoplanets in the Milky Way, orbiting the habitable zones of G and M stars. Of those, only 9 have so far been positively identified and currently nothing is known about their circulation patterns. Of course, a planet orbiting a G star at a distance of 1 AU, such as the Earth, can only be tidally locked by incidence (e.g Venus). However, simulating a tidally locked Earth at 1 AU permits the intercomparison of its atmospheric circulation and composition with past studies as well as the fast rotating, present day Earth.

This setup has been used in the past as an approximation for the simulation of tidally locked Earth-like planets and aquaplanets orbiting in the Habitable zones of Red dwarf stars (0.02 - 0.2 AU), also known as M stars (Tarter et al. (2007) Grenfell et al. (2014), Joshi (2003), Merlis and Schneider (2010), Yang et al. (2013), Segura et al. (2005), Edson et al. (2011), Kaspi and Showman (2015) and Menou (2013)). M stars comprise 76 % of the main-sequence stars in the vicinity of the Sun. Planets revolving around M stars are easy to detect due to the high star to planet mass and radius ratio (Tarter et al., 2007). This, coupled with their high chance of habitability, makes them prime candidates for the search for habitable extraterrestrial planets. Haberle et al. (1996), Joshi et al. (1997), Joshi (2003) and Segura et al. (2005) demonstrated that planets located in the M star's habitable zone would be habitable. Segura et al. (2005) reported that the flaring activity of M stars, which is stronger than the flaring activity of the Sun, should not present a threat to the surface organisms of such tidally locked planets.

Past studies of tidally locked Earth-like exoplanet atmospheres have largely been focused on the troposphere (Merlis and Schneider (2010), Joshi et al. (1997), Showman and Polvani (2011), Carone et al. (2014), Edson et al. (2011)).

Merlis and Schneider (2010) simulated the troposphere of an Earth-like, tidally locked aquaplanet with a rotation period equal to one Earth year using an ideal gas GCM with an active hydrological cycle, a gray radiation scheme and a slab ocean lower. They concluded that no atmospheric collapse occurred on the night side and predicted the presence of an upwelling over the day side and a downwelling over the night side. The upwelling was centred on the subsolar point and the downwelling on the antisolar point. They also showed that, irrespective of rotation rate, the troposphere of a tidally locked Earth-like aquaplanet located at a distance of 1 AU from a Sun-like star would display equatorial mid-tropospheric superrotating mean zonal winds. Furthermore, the superrotation speed of a planet rotating with a period of 365 Earth days would be slower compared to the superrotation speed of a planet rotating with a period of 1 Earth day (Merlis and Schneider, 2010).

Yang et al. (2013) demonstrated that a tidally locked aquaplanet would be habitable at even twice the Earth incident solar flux as long as clouds were present in its troposphere, ensuring the planet's habitability.

As opposed to the Sun, whose spectrum peaks in the visible yellow light, the spectrum of M stars peaks in the IR (Grenfell et al., 2014). One dimensional studies by Segura et al. (2003), Segura et al. (2005), Selsis (2000), Hedelt et al. (2013), Grenfell et al. (2014) and one 3D study by Godolt et al. (2015) showed that a change in the stellar spectral energy distribution leads to different ozone radiative heating rates and different vertical stratospheric structures for the same total amount of stellar energy incident at the top of the atmosphere of a non-tidally locked Earth-like planet. This results in a much shallower stratospheric temperature increase and impacts its middle atmospheric circulation. It is possible that such a change would also affect the middle atmospheric chemistry and circulation patterns of a tidally locked Earth-like planet orbiting an M star, complicating the cause-effect attribution analysis. It would also make it exceedingly difficult to correctly attribute the observed changes to either the tidal lock or the spectral energy distribution change. Therefore, the Earth-like planet, Sun-like star setup simplifies the tidal lock cause-effect analysis. Besides, it also facilitates the comparison with older studies, where similar setups were also used.

Grenfell et al. (2014) showed that the infrared spectrum of an Earth-like exoplanet was strongly influenced by the 200–350 nm UV output of its parent star, using a 1D stationary, hydrostatic, global-mean, 0 - 70 km, atmospheric column model. The planetary ozone profile was strongest when the UV radiative flux of the parent star was ten times stronger than the UV radiative flux of an M7 star.

Godolt et al. (2015) investigated the changes in the ozone concentration, stratospheric temperature, climate and potential habitability of an Earth-like extrasolar planets orbiting an F, G and K star, respectively, using a state-of-the-art 3D Earth climate model. The planets' position was chosen such that the total amount of energy received from the parent stars would be equal to the solar constant. The atmospheric composition of both planets was identical to that of the present day Earth. The study revealed that different stellar spectral energy distributions result in different ozone heating rates and, therefore, different vertical temperature structures, in accordance with Selsis (2000), Segura et al. (2003), Segura et al. (2005), Grenfell et al. (2007), Rugheimer et al. (2013) and Rauer et al. (2011). When orbiting a cooler K star, which emits a smaller portion of its radiation in the UV part of the spectrum, the stratosphere was characterised by lower ozone heating rates and shallower stratospheric temperature increases compared to the Earth (Godolt et al., 2015). As shown above, all but two Earth-like exoplanet studies have been 1D studies (Selsis (2000), Rugheimer et al. (2013), Rauer et al. (2011), Grenfell et al. (2014)) and only one was devoted to the study of the exoplanet's stratosphere (Godolt et al., 2015). Furthermore, only one study of the troposphere of a tidally locked Earth-like exoplanet exists (Merlis and Schneider, 2010) and no study has investigated the middle atmosphere of tidally locked Earth-like exoplanets. This thesis aims to address this gap by investigating their 3D ozone distribution and middle atmospheric circulation.

It is not unreasonable to expect that changes in the planet's radiative balance could influence a planet's habitability. Two parameters determine a planet's habitability: the presence of liquid water and the presence of ozone. Whereas liquid water determines the emergence of life (Cardenas et al., 2014), ozone determines the survival of the emergent life. The ozone layer acts as a protective shield for the organisms on the surface of the planet by absorbing the majority of the solar UV radiation between 200 nm and 300 nm, principally in the Hartley and Huggins bands (Saha (2008), Wallace and Hobbs (2006)). This can be seen in Figure 2.1, where a cut-off is visible below 300 nm. On Earth, the maximum ozone concentration is found in the lower stratosphere between 18 km and 26 km altitude, while the highest ozone volume mixing ratio is found in the middle stratosphere between 30 km and 40 km altitude (Saha, 2008). Due to the absorption of UV radiation and the high ozone density, the stratospheric temperature is increased compared to the tropospheric and the mesospheric temperatures. Therefore, ozone also determines the vertical stratospheric temperature profile (Wallace and Hobbs, 2006).

In a pure oxygen atmosphere, ozone is destroyed through the exothermic two-body collision with atomic oxygen

$$(\mathrm{k_3});\ \mathrm{O} + \mathrm{O_3} \rightarrow 2\mathrm{O_2} \tag{2.1}$$

as well as through the absorption of UV radiation, which results in the photodissociation of ozone

$$(\mathrm{J_3});\ \mathrm{O_3} + \mathrm{hv} \rightarrow \mathrm{O_2} + \mathrm{O} \tag{2.2}$$

(Brasseur and Solomon, 2005). Due to the high air density and high molecular oxygen content at stratospheric altitudes, the photodissociated ozone is regenerated through the exothermic three body recombination reaction of atomic (O) and molecular oxygen ($\mathrm{O_2}$)

$$(\mathrm{k_2});\ \mathrm{O} + \mathrm{O_2} + \mathrm{M} \rightarrow \mathrm{O_3} + \mathrm{M} \tag{2.3}$$

where M is a third body that acts as a catalyst and is needed for the conservation of energy and momentum in the recombination reaction. This third body is usually an N_2 or an O_2 molecule, as they are the most abundant atmospheric components (Wallace and Hobbs, 2006). The reaction shown above is the only process by which ozone is generated in the middle atmosphere. The atomic oxygen necessary for reaction 2.3 is produced mainly by the photodissociation of O_2 by the UV radiation in the Herzberg continuum, near 242 nm:

$$(\mathrm{J_2});\ \mathrm{O_2 + hv \rightarrow O + O} \tag{2.4}$$

Furthermore, the atomic oxygen can also be produced by the photolysis of ozone in the Hartley and Huggins bands near 310 nm (reaction 2.2) (Saha, 2008).

Equations 2.1, 2.2, 2.3, 2.4 describe the Chapman cycle. This cycle describes the ozone photochemistry in a pure oxygen atmosphere (Brasseur and Solomon (2005), Wallace and Hobbs (2006)). The rate coefficients J_2, J_3, k_2, k_3 indicate the speeds of the reactions and, therefore, determine the lifetimes of the species (Brasseur and Solomon, 2005), (Salby, 2012a). The ozone loss rate k_3 increases with temperature so that the upper stratospheric ozone is anticorrelated with temperature. Although ozone is constantly converted to atomic oxygen through equation 2.4 and then back to ozone through equation 2.3, their sum, also known as the odd oxygen family (O_x), remains relatively constant in the middle atmosphere. Therefore, the use of odd oxygen, as opposed to ozone, allows us to correctly identify the true sinks and sources. In the stratosphere, $(O_x) \approx (O_3)$, so a reduction of O_x indicates the presence of an ozone sink. In the mesosphere, $(O_x) \approx (O)$, so a reduction of O_x indicates the presence of an atomic oxygen sink. In the lower stratosphere, O_x has a lifetime of the order of several weeks, while above 30 km it has a lifetime of the order of less than 1 day. For these reasons, odd oxygen is used to discuss the significant generation and destruction of ozone in this thesis.

In the stratosphere, the two major sinks of odd oxygen (and consequently, of ozone) are the NO and OH catalytic cycles. Different catalytic processes are important in different altitude ranges (Brasseur and Solomon, 2005).

$$\begin{gathered}\mathrm{NO + O_3 \rightarrow NO_2 + O_2}\\ \mathrm{NO_2 + O \rightarrow NO + O_2}\end{gathered} \tag{2.5}$$

plays an important role in the destruction of ozone in the middle stratosphere (Wallace and Hobbs, 2006), with maximum efficiency between 35 and 45 km (Brasseur and Solomon, 2005).

$$\begin{gathered}\mathrm{OH + O_3 \rightarrow HO_2 + O_2}\\ \mathrm{HO_2 + O \rightarrow OH + O_2}\end{gathered} \tag{2.6}$$

is responsible for the destruction of ozone in the middle and upper stratosphere (Brasseur and Solomon, 2005).

$$\begin{gathered}\mathrm{OH + O_3 \rightarrow HO_2 + O_2}\\ \mathrm{HO_2 + O_3 \rightarrow OH + 2O_2}\end{gathered} \tag{2.7}$$

is important below 30 km (Wallace and Hobbs, 2006) and close to the troposphere (Brasseur and Solomon, 2005). In the same altitude range

$$\begin{aligned} \mathrm{OH} + \mathrm{O} &\rightarrow \mathrm{H} + \mathrm{O_2} \\ \mathrm{H} + \mathrm{O_2} + \mathrm{M} &\rightarrow \mathrm{HO_2} + \mathrm{M} \\ \mathrm{HO_2} + \mathrm{O_3} &\rightarrow \mathrm{OH} + 2\mathrm{O_2} \end{aligned} \tag{2.8}$$

and

$$\begin{aligned} \mathrm{OH} + \mathrm{O} &\rightarrow \mathrm{H} + \mathrm{O_2} \\ \mathrm{H} + \mathrm{O_3} &\rightarrow \mathrm{OH} + \mathrm{O_2} \end{aligned} \tag{2.9}$$

are also responsible for the destruction of odd oxygen (Brasseur and Solomon, 2005).

In the mesosphere, the major sinks of odd oxygen are OH catalytic cycles. One is equation 2.9 shown above and the other is

$$\begin{aligned} \mathrm{OH} + \mathrm{O} &\rightarrow \mathrm{H} + \mathrm{O_2} \\ \mathrm{H} + \mathrm{O_2} + \mathrm{M} &\rightarrow \mathrm{HO_2} + \mathrm{M} \\ \mathrm{HO_2} + \mathrm{O} &\rightarrow \mathrm{OH} + \mathrm{O_2} \end{aligned} \tag{2.10}$$

They lead to the rapid loss of odd oxygen (Brasseur and Solomon, 2005).

All catalytic ozone depletion cycles require sunlight. As a result, on Earth, ozone depletion stops during the night time. In the Earth's mesosphere, this results in enhanced night-time ozone. On a tidally locked Earth-like exoplanet, the night side of the planet never receives sunlight. Therefore, no ozone depletion should occur.

The stratospheric ozone maximum is found over the tropics, due to the higher incident UV radiation, compared to the extra-tropics. However, the maximal total ozone content in both the Northern and the Southern hemisphere appear at mid and polar latitudes due to the Brewer-Dobson circulation.

As can be seen in Figure 2.3, the tropospheric air is uplifted over the tropics and enters the tropic stratosphere where the odd oxygen-rich air is generated. This air is then transported polewards and downwards towards the middle and polar latitudes and deposited back into the extra-tropical troposphere by the Brewer-Dobson circulation (Andrews (2010), Müller (2012), Brasseur and Solomon (2005), Wallace and Hobbs (2006)).

The influence of the underlying sea-surface temperature (SST) on the middle atmosphere has also been investigated to only a limited extent on Earth and not at all on exoplanets. On Earth, most studies focused on the effects of the underlying SST on the troposphere rather than the middle atmosphere. A few studies have been performed with a focus on the lower stratosphere; however, none exist for the upper stratosphere and mesosphere.

Braesicke and Pyle (2004) investigated the dynamics and ozone sensitivity to different SSTs using the Met Office Unified Model. They performed a set of 20 year simulations, each with a different prescribed SST and the same simplified ozone chemistry. Their results showed that the occurrence of extreme events in the northern hemisphere winter stratosphere were strongly correlated with the underlying SSTs.

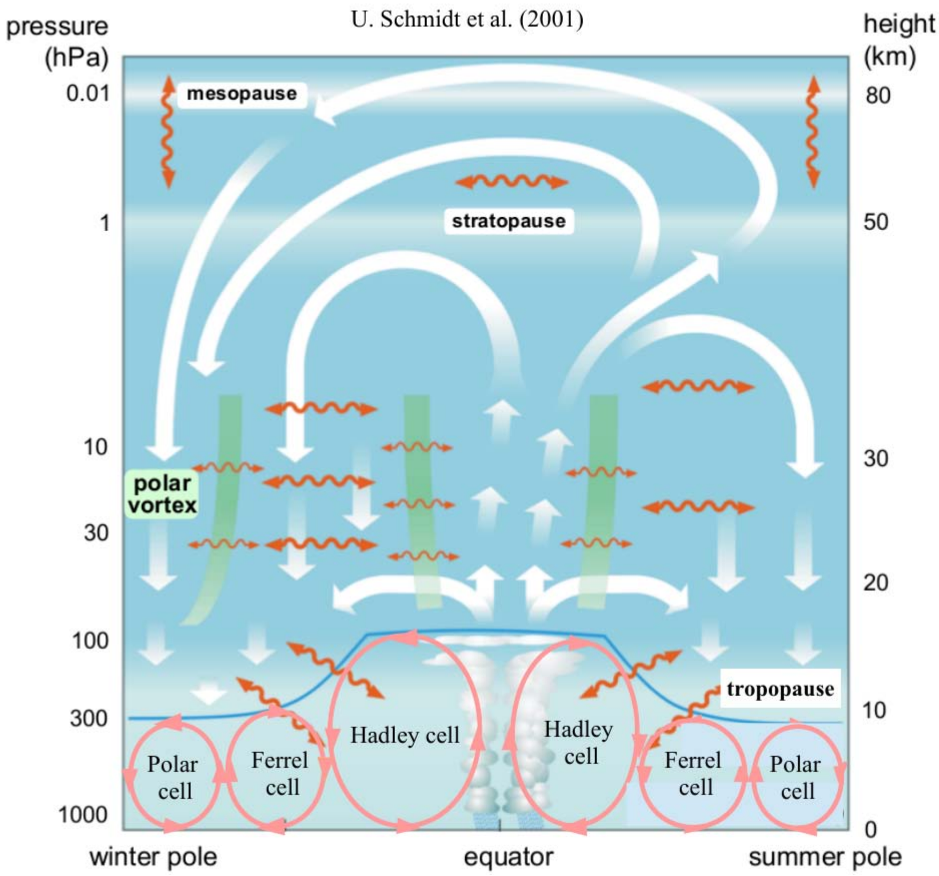

Figure 2.3: The Brewer Dobson circulation. The Brewer-Dobson circulation on Earth. The Hadley, Ferrel and Polar cells are visible in the figure for both hemispheres. The thick white arrows indicate the transformed eulerian mean mass streamfunction. The wavy orange arrows indicate two-way mixing processes. The thick green lines indicate the presence of stratospheric transport and mixing barriers. (Adapted from Bönisch et al. (2011))

Rosenlof and George (2008) discovered an anticorrelation between the lower stratospheric temperature trends over the western Tropical Pacific Ocean and the underlying SST variations, using data from the NOAA/CIRES Climate Diagnostics Center. They suggested the existence of a fairly direct influence between the SST and the lower tropical stratosphere and that the anticorrelation appears as a result of increased deep tropospheric convection generated by the SST warming.

Deckert and Dameris (2008) investigated the change in the strength of the tropical upwelling using two simulations with the same boundary conditions and concentrations of ozone-depleting substances, but different SSTs and greenhouse gas concentrations. They reported the presence of amplified deep convection over warmer tropical SSTs, accompanied by a lower stratospheric cooling.

Chen et al. (2010) investigated the tropospheric winds and stratospheric Brewer-Dobson circulation sensitivities to SST warmings using an Earth aquaplanet general circulation model. However, their study aimed to investigate how the Earth's large-scale atmospheric circulation would be affected by a warming ocean as a result of global warming rather than study an actual Earth-like exoplanet. Their results indicated that the location and sign of the SST perturbations gradient was strongly correlated with the changes in the tropospheric jet and the Hadley cell. They also reported that low latitude warming resulted in increased Brewer-Dobson circulation while high latitude warming resulted in decreased Brewer-Dobson circulation when the warming extended to the subtropics.

The aim of this thesis is to study the effects of radiative forcing changes on Earth-like planets by performing 3D simulations with the publicly available 3D, high resolution, chemistry-climate model CESM1(WACCM). The model is designed specifically for the research of the middle atmosphere, where photochemistry and nonlinear wave-mean flow interactions play the most important role. The objective of this work is to answer the following three open research questions:
Research question 1. What effect does a regional soil color change have on the Earth's tropospheric dynamics?
Research question 2. What is the 3D global middle atmospheric ozone distribution and circulation of a tidally locked Earth-like planet?
Research question 3. How does the sea-surface temperature affect the middle atmosphere of tidally locked Earth-like exoplanets?

These three questions are investigated and answered in the three publications presented in this thesis. These questions deal with different effects of the radiative forcing on atmospheric dynamics, composition and circulation which have not been sufficient addressed in the literature. First, the CESM1(WACCM) model is briefly described in Chapter 3, since it plays an essential role in all three publications. In the following chapters, the answers to each of the research questions are presented, along with the research strategy and the results.

The first research question is answered in Chapter 4 by simulating the effects of the darkening of a small area in Eastern Sahara, using the CESM1(WACCM). The outgoing atmospheric wave generated over the region of soil colour change is analysed and discussed in detail.

The second research question is answered in Chapter 5. The large scale radiative forcing change is introduced by tidally locking the planet. CESM1(WACCM) was modified to simulate a tidally locked Earth-like exoplanet orbiting around a Sun-like star at a distance of 1 AU. The global 3D distribution of the middle atmospheric ozone of the tidally locked planet is then compared to those of the present day Earth.

The third research question is answered in Chapter 6. Using the simulation setup presented in Chapter 5, two tidally locked Earth-like exoplanets with different sea-surface temperature distributions orbiting identical Sun-like stars are simulated using CESM1(WACCM). The middle atmospheric circulations and vertical ozone distributions are analysed and compared. The degree of SSTs influence on the middle atmospheric circulation, the temperature vertical profile and the ozone vertical distribution is analysed and discussed.

In Chapter 7, the results are summarised and an outlook for future research projects is presented.

3 Model

The Community Earth System Model 1 (CESM1) was used to perform the simulations presented in this thesis. It is a publicly available, coupled, 3D, high resolution, chemistry-climate Earth model, mainly developed by US researchers and supported by the National Science Foundation (NSF). An overview of its general characteristics and applications was presented by Hurrell et al. (2013). The model can realistically simulate the Earth's atmosphere, land and oceans utilizing fully coupled geophysical models and a coupler (CPL) (Figure 3.1).

CESM is composed of five geophysical models: the atmosphere (ATM), land (LND), ocean (OCN), sea-ice (ICE) and land-ice (GLC) model. The models can be set to be fully prognostic (active), data, dead or stub. Active components are fully prognostic, with their output altered depending on the input data and its interactions with the rest of the geophysical models. They provide state-of-the-art climate prediction and are computationally intensive. Data components are used for testing, spin-up and model parametrization. They cycle input data retrieved through observations and long-term CESM simulations performed by the National Center for Atmospheric Research (NCAR). They can also substitute one or more of the computationally intensive active components in “stand-alone" simulations, where the presence of one or more of the prognostic components is not necessary, in order to reduce the computational load. The term “stand-alone simulations" refers to partly coupled simulations where one or more geophysical models are data or stub. Stub components are used to satisfy the interface requirements when the presence of a component is not necessary for the model configuration. The dead components are used only during system testing, during which the dead ATM, LND, OCN, ICE and GLC components must all be run together. Dead components must never be combined with active or data components. Both, the stub and the dead components, do not produce scientifically valid output data (Vertenstein et al., 2012).

For this thesis, the perpetual year 2000 geophysical model set (a.k.a component set) (F_2000_WACCM) is used. The component set is composed of a present day (calendar year 2000) active atmosphere (WACCM) and land (CLM) models, a data ocean (docn) and data sea-ice (cice) models, and a stub land ice (sglc) model. The WACCM, CLM, docn and cice component initialization datasets are provided by previously performed long-term NCAR CESM simulations (Neale et al., 2012).

3.1 The Atmosphere geophysical model

The atmosphere geophysical model used is the Whole Atmosphere Community Climate Model (WACCM) version 5 (Neale et al., 2012). It has been used for the simulation of circulation, thermal tides, gravity waves, wave-mean flow interaction, and

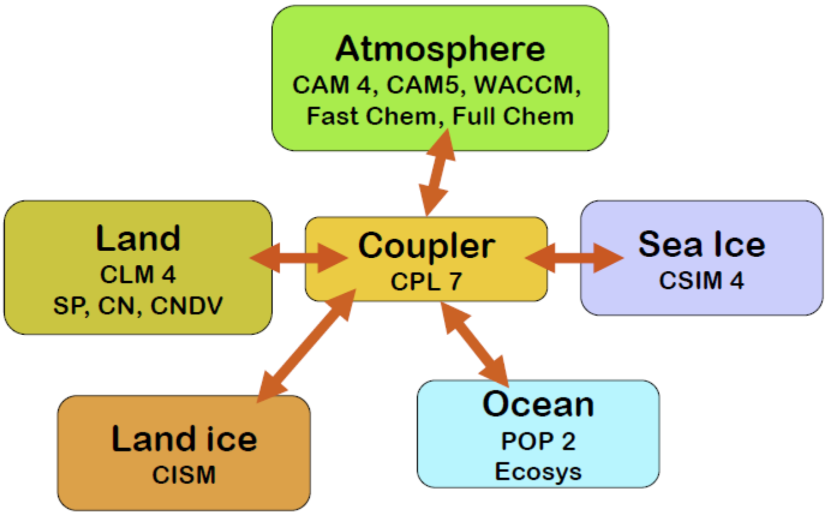

Figure 3.1: CESM coupled modeling framework. Figure taken from "The Community Earth System Model (CESM)" by David Lawrence.

atmospheric composition changes (e.g., ozone hole, greenhouse effect) in the lower, middle and upper atmosphere (Pedatella et al. (2014), Pedatella and Liu (2013), Lu et al. (2012), Tan et al. (2012a), Tan et al. (2012c), Tan et al. (2012b), Davis et al. (2013), Smith et al. (2012)). It uses a Finite-Volume (FV) dynamical core with a fully compressible horizontal discretization and a quasi-Lagrangian vertical discretization.

The model has 66 vertical output levels from the ground up to $5 \cdot 10^{-6}$ hPa. The top of the model is located at $\sim$ 150 km. The vertical resolution is 1.1 km in the troposphere, 1.1–1.4 km in the lower stratosphere, 1.75 km at the stratopause and 3.5 km above 65 km. The model has fully compressible horizontal and a quasi-Lagrangian vertical discretization (Neale et al., 2012). The vertical acceleration term of the momentum equation is not included. The vertical coordinate is terrain following below 100 hPa and purely isobaric above.

The horizontal resolution used in this study is 4°x5° (latitude x longitude). The input and output datasets have 72 longitude grid points, 46 latitude grid points and 66 altitude grid points. For any model, the smallest horizontal resolvable area is twice the grid size (Holton and Hakim, 2013). Therefore, the selected model setup can resolve changes with a horizontal dimension of $d_{horizontal} > 1000$ km and a vertical dimension of $d_{vertical} > 2.2$ km (Neale et al., 2012). The prognostic variables are updated sequentially, first by the FV dynamics and then by the FV physics implementation. The model is set to output hourly snapshot values for each parameter. The coupler timestep is set to $\Delta t = 30$ minutes, while the dynamical equations time step is $\Delta\tau = \Delta t/8$ (Neale et al., 2012). CESM1(WACCM) has full atmospheric chemistry, with 57 chemical species (Neale et al., 2012). The model's main physical processes are:

- the conversion to and from dry and wet mixing ratios for trace constituents
- the moist turbulence scheme
- the shallow and the deep convection scheme

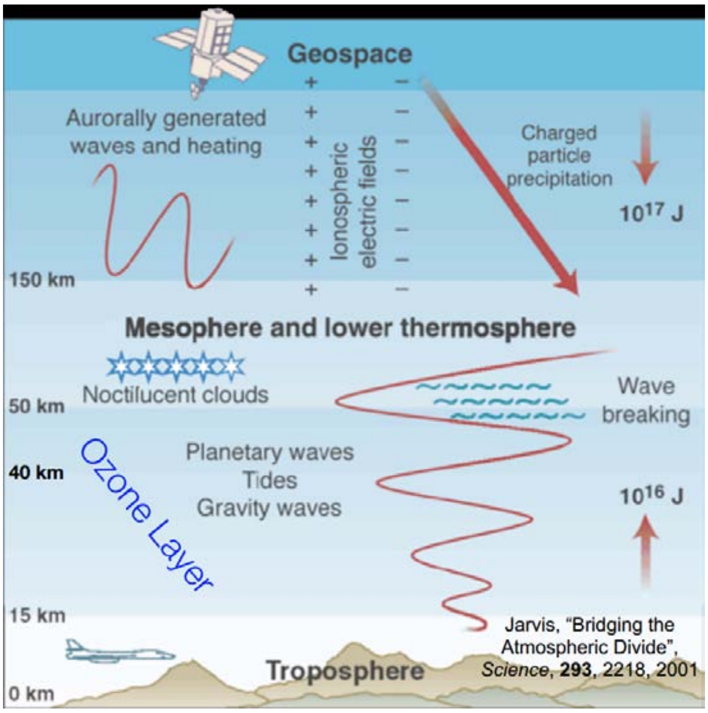

Jarvis, "Bridging the Atmospheric Divide", *Science*, **293**, 2218, 2001

Figure 3.2: Atmospheric geophysical model. The figure from Jarvis (2001) was slightly modified by Michael Mills in his presentation "WACCM: The High Top Model" by Michael Mills.

- the evaporation of convective precipitation
- the cloud microphysics and macrophysics
- the aerosols
- the condensed phase optics
- the radiative transfer
- the surface exchange formulations
- the dry adiabatic adjustment
- the prognostic greenhouse gases

(Neale et al., 2012). The gase-phase chemistry is coupled to the Modal Aerosol Model (Neale et al., 2012).

The model uses the realistic synthesized solar spectrum generated using the Kurucz method (Kurucz, 1994). The total irradiance at the top of the model is TSI = 1368.22 W/m^2. The model distinguishes between the direct and scattered radiation in both the shortwave and the longwave spectrum (Neale et al., 2012). As a result, all parameters which are affected by radiation are also divided into direct and scattered terms.

The incident shortwave and longwave flux values are determined by means of the daily values of the solar radio flux (F10.7), which are provided by the National Oceanic and Atmospheric Administration's Space Environment Center (2015) (NOAA).

In the shortwave spectrum (0.2 µm to 12.2 µm), the radiative transfer is calculated over 14 bands. In the longwave spectrum (3.1 μm to 1000.0 µm), the radiative transfer is calculated over 16 bands, which includes the spectral interval below 3.1 μm infrared contribution. The spectral interval between the soft x-rays and extreme ultraviolet irradiances (0.05 nm to Lyman-α (121.6 nm), as well as between the Lyman-α (121.6 nm) and the 100 μm radiation, is included for altitudes above 65 km (Neale et al., 2012). The modelled sources of absorption and scattering in the shortwave are H_2O, O_3, CO_2, O_2, CH_4, N_2, clouds, aerosols, and Rayleigh scattering. In the longwave spectrum, the model calculates the molecular, cloud and aerosol absorption and emission. The longwave modelled sources of absorption are H_2O, CO_2, O_3, N_2O, CH_4, O_2, N_2, $CFC-11$ and $CFC-12$. Currently the longwave scattering effects are not included in the model calculations. For negative elevation angles, the shortwave electromagnetic radiation is not calculated (Neale et al., 2012).

The photochemical equilibrium is calculated for 36 photochemical species: O_2, O_3, N_2O, NO, NO_2, N_2O_5, HNO_3, NO_3, HO_2NO_2, CH_3OOH, CH_2O, H_2O, H_2O_2, Cl_2, ClO, OClO, Cl_2O_2, HOCl, HCl, $ClONO_2$, BrCl, BrO, HOBr, $BrONO_2$, CH_3Cl, CCl_4, CH_3CCl_3, CFC11, CFC12, CFC113, HCFC22, CH_3Br, CF_3Br, CF_2ClBr, CO_2, CH_4. The model uses the O_x, NO_x, HO_x, ClO_x, and BrO_x chemical families, excluding CH_4 and its degradation products as tracers. The reaction rate equation of ozone is:

$$\begin{aligned}\frac{d(O_3)}{dt} + J_{O_3}(O_3) + k_3(O)(O_3) + a_2(H)(O_3) + a_6(OH)(O_3) +\\ a_{6b}(HO_2)(O_3) + b_4(NO)(O_3) + b_9(NO_2)(O_3) + d_2(Cl)(O_3) +\\ e_2(Br)(O_3) = k_2(M)(O_2)(O)\end{aligned} \tag{3.1}$$

It is used to calculate the photochemical and chemical interactions responsible for changing the atmospheric ozone concentration. The model includes a polar stratospheric cloud parameterization scheme. When the cosine of the solar zenith angle is larger than zero at stratospheric altitudes and the stratospheric temperature drops below 195 K, the polar stratospheric cloud parameterization scheme is activated.

3.2 The Surface geophysical model

The surface geophysical model used is the Community Land Model (CLM) (Oleson et al., 2010). It has parametrisations for the atmosphere-surface coupling, the surface colour variability, the surface albedo calculation, the absorption, reflection and transmittance of solar radiation, the absorption and emission of longwave radiation, the sensible and latent heat fluxes (ground and canopy), and the heat transfer in soil and snow. The surface albedo values at each grid cell were provided by the Moderate-resolution Imaging Spectroradiometer (MODIS), which orbits the Earth on board the Terra and Aqua satellites, at local solar noon time and, therefore, varies with the landscape (Oleson et al., 2010). The surface albedo is area-averaged for each atmospheric column. The upward longwave radiation is given by the difference

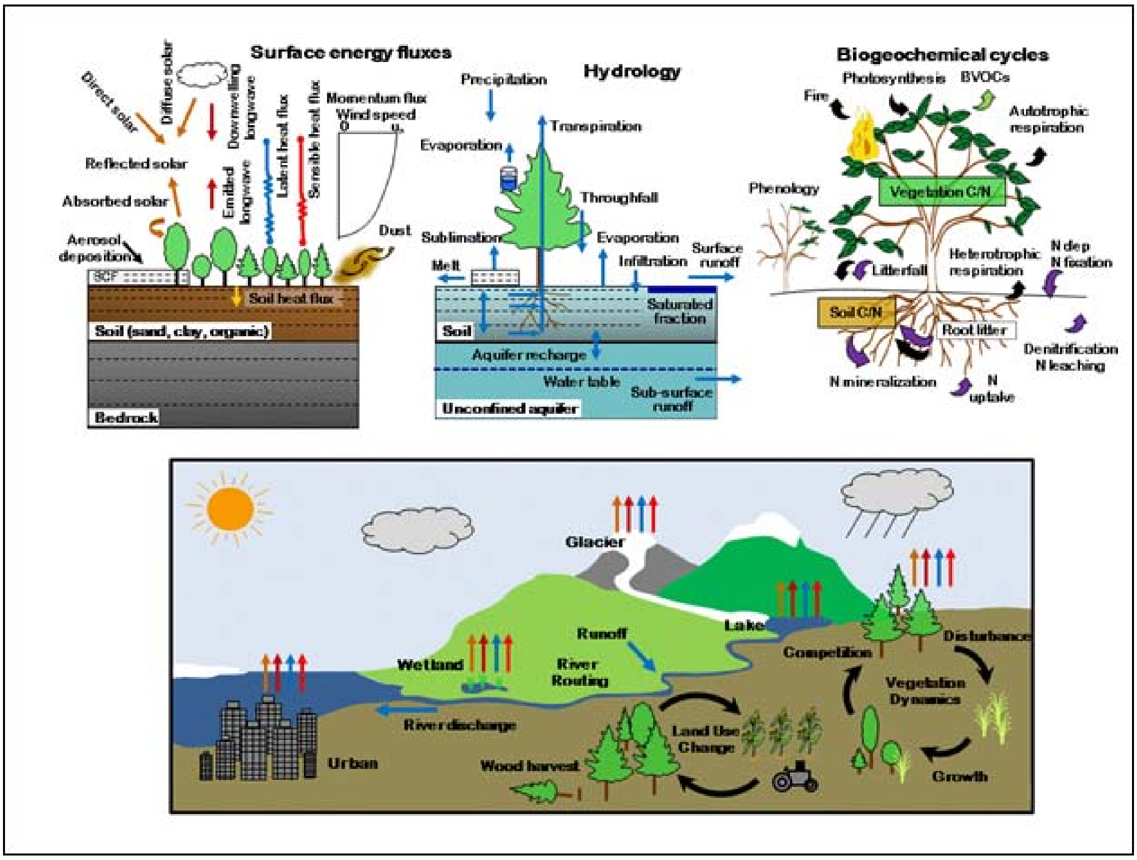

Figure 3.3: Community Land Model. Figure taken from CESM CLM website: www.cesm.ucar.edu/models/clm/

between the incident and absorbed fluxes, while the atmospheric radiation balance is calculated using the momentum, sensible heat flux, latent heat flux, land surface albedos and upward longwave radiation (which incorporates the surface emissivity). The surface parameter fluxes provided by the land model (LND) provide the surface fluxes of momentum, sensible and latent heat. They serve as the lower flux boundary conditions for the turbulent mixing, the planetary boundary layer parameterization, the vertical diffusion and the gravity wave drag. Since F_2000_WACCM uses active land and stub land-ice geophysical models, the land fluxes will be prognostic.

3.3 The Ocean geophysical model

The F_200_WACCM component set uses a prescribed data model ocean, which does not run prognostically, but rather reads in the Sea Surface Temperature (SST) and Sea Ice Concentration (SIC) datasets and then sends them to the coupler. The SST and SIC dataset is a merged surface boundary forcing dataset that provides the SST and SIC boundary data. This dataset was initially developed for uncoupled simulations with the Community Atmosphere Model (CAM) atmospheric component and is generated through the merging of the monthly mean Hadley Centre sea ice and SST dataset version 1.1 (HadISST1) and the OI SST analysis technique (OI.u2) dataset. HadISST1 is a combination of monthly, gridded, bias adjusted globally complete SST and SIC fields. The OI.u2 dataset is a combined quality-controlled ship and buoy observations, and satellite-derived SST dataset. The ocean and sea-ice surface parameter fluxes provide the surface momentum, sensible and latent heat. Since F_2000_WACCM uses data ocean, and also sea-ice, geophysical models, the ocean and sea-ice fluxes will be prognostic.

4 A traveling atmospheric wave generated by a regional soil colour change on the present day Earth

4.1 Research strategy

The Earth's radiative balance is maintained through a complex interaction between the energy received from the Sun, the energy reflected, absorbed and re-emitted by the atmosphere, and the energy absorbed and re-emitted by the surface. As stated in the Introduction, the Earth receives $S_o = 1372$ W/m^2 from the Sun, with a global average of $F_{inc} = S_o/4 = 343$ W/m^2. Of that energy, 31 % is reflected back into space, 20 % is absorbed by the atmosphere and 49 % by the surface. The surface and the atmosphere re-emit part of the absorbed energy in the form of longwave radiation. The surface re-emitted longwave radiation is emitted towards the atmosphere, while the atmosphere re-emitted longwave radiation is emitted both towards the surface and towards space, as shown in Figure 4.1.

The surface is radiatively heated, as its net radiative forcing indicates, which is given by the sum of the incident shortwave and longwave absorption minus the outgoing longwave emission. The heat is then released in the atmosphere in the form of sensible and latent heat flux as well as longwave radiation, as shown in Figure 4.1. This mechanism permits the radiative equilibrium to be maintained.

The Earth's surface albedo plays an important role in the planet's radiative equilibrium, as it determines the fraction of shortwave solar radiation absorbed by the surface and the amount of longwave radiation, sensible and latent heat emitted by it. In the visible part of the spectrum, the surface albedo is determined by the surface's colour. Therefore, the surface colour plays a central role in the Earth's radiative balance.

A region's surface albedo varies with the altitude, latitude, longitude, climate and its proximity to large water bodies. Light coloured surfaces, such as ice, sand or light coloured rocks, have a high albedo. They reflect more and absorb less shortwave radiation. Consequently, they emit less longwave radiation and release less sensible and latent heat back into the atmosphere. Dark coloured surfaces, such as deep oceans, dark forests or dark coloured rocks like basalts and granites, have a lower albedo and ,therefore, reflect less and absorb more shortwave radiation. As a result, the surface temperature is increased and the surface emits more longwave radiation and releases more sensible and latent heat back into the atmosphere (Saha, 2008).

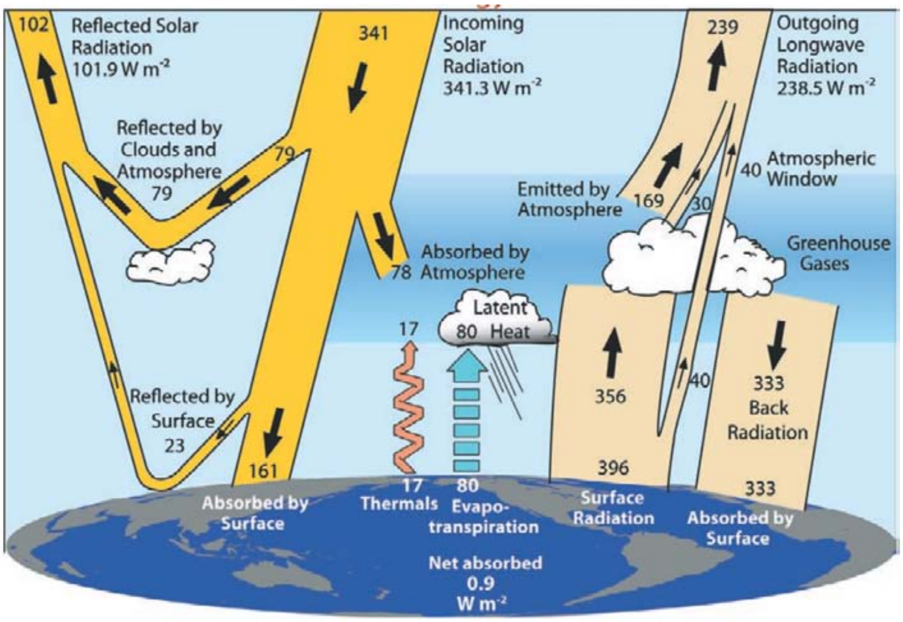

Figure 4.1: Global annual mean of the Earth's energy budget for the March 2000 - May 2004 period. The width of the arrows is proportional to the strength of the energy flow. (Trenberth et al., 2009)

Humans have changed the Earth's surface albedo since prehistoric times. With the advent of geoengineering and numerous projects intended to combat climate change, even larger changes are expected. Unfortunately, the impact of albedo variability on the atmospheric dynamics is currently largely unknown (Seitz, 2013). Past albedo change studies focused either on its effects on long-term climate change (Walland and Simmonds, 1996), (Held and Suarez, 1974), (Kirschbaum et al., 2011b), (Betts, 2000) or on climate change combating geoengineering projects (Ridgwell et al., 2007). One study attributed changes in the polar vortex to increased sudden snow fall in Eurasia (Cohen, 2011). Another investigated the relation between sea surface temperatures variations and a weakening of the polar vortex (Manzini et al., 2006).

Hegyi et al. (2014) investigated the initial transient response of the boreal winter Northern Hemisphere stratospheric polar vortex to localised sea-surface warming events. To that end, they conducted 20 perpetual winter simulations using the CESM1(WACCM). They reported a weakening of the polar vortex due to changes in the eddy-driven mean meridional circulation and the presence of negative anomalies in the eddy momentum flux convergence. They further showed that the initial state and subsequent internal variation of the extratropical atmosphere is as important as the type of SST forcing in determining the response of the stratospheric polar vortex. Furthermore, the interactions between the internal variability of the vortex and the SST-driven wave anomalies determine the nature of the response of the polar vortex to the forcing.

Our study investigates the effects of a regional surface colour change on the tropospheric dynamics using CESM1(WACCM) and whether a cause-effect study can be performed under the relatively realistic atmospheric conditions provided by the model. CESM1(WACCM) is a realistic model that includes full 3D photochemistry, atmospheric transport processes and surface-atmosphere interactions. The inclusion of these interactions enables the study of atmospheric perturbations generated by land-atmosphere interactions like the soil colour change presented here. It also results in a computationally intensive model that provides output data reminiscent of observations. This makes the attribution of climate forcing and the recognition of the relevant climate processes challenging and requires advanced methods of data analysis and interpretation (Alexander et al. (2010), Walland and Simmonds (1996), Kirschbaum et al. (2011b)), making it a fundamental problem of complex system analysis. One way to overcome this problem is to perform a small perturbation analysis over a short-time interval of the order of a few days. This method allows us to isolate the forcing generated perturbations from the background waves and study the radiative and dynamical processes of land-atmosphere interactions.

The simulation setup of the study is fairly simple. The surface colour of a 10° × 8° (3×3 model pixels) Eastern Saharan region, is darkened. The region is located at 10°-20° longitude and 18°-26° latitude. The change can be safely implemented, because the surface colour change involves the alteration of only one model parameter. The simplicity of the setup facilitates the interpretation of the results.

The soil colour of the selected region is altered from sand coloured to dark forest green by changing the soil colour index parameter. The parameter is the measure of the darkness of the surface colour. A lower soil colour index indicates a lighter colour (white snow = 0), while a higher soil colour index indicates a darker colour (deep forest green = 20).

Apart from the soil colour change simulation (which will be referred to as the perturbed run henceforth), a control run is also performed, in which the model is allowed to run with no alterations. The soil colour maps for the control and perturbed run can be seen in Figure 4.2, along with the difference between the two setups. An abrupt colour change between the darkened region and its vicinity would result in a discontinuity in the soil colour map and generate artefacts in the simulation. To avoid this, we change the soil colour gradually by deepening the surface colour by 50 % on the edge and by 100 % on the center of the region. Both simulations are run for 5 model days, starting at 0:00 UT on 01.01.2000 and ending at 23:00 UT on 05.01.2000.

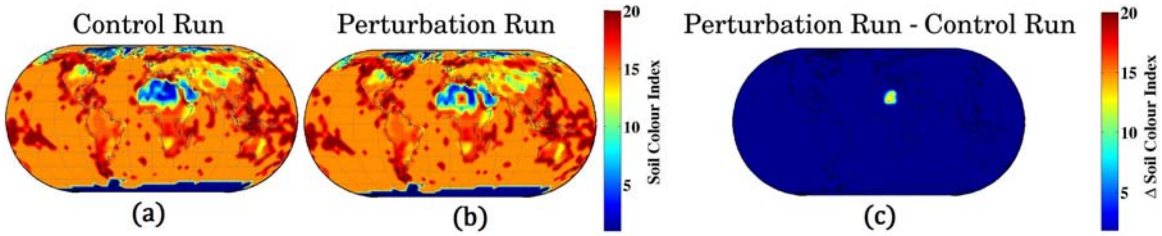

Figure 4.2: Soil colour setup. (a) Control run soil colour index, (b) Perturbed run soil colour index, (c) the difference between the perturbed and the control run soil colour indices.

To ensure the validity of our results, an ensemble simulation is also performed. The start dates of the seven simulations are the 1st, 6th, 11th, 16th, 21st, 26th and 31st of January, respectively. Each simulation is run for 5 model days, starting at 0:00 UT of the first day of the simulation and ending at 23:00 UT on the last day of the simulation.

To analyse the results a small perturbation analysis is performed on the vertical wind speed Ω. First, the control data are subtracted from the perturbed data $\Delta\Omega$. Then, the standard deviation of the $\Delta\Omega$ for the first day at 23 UT, its zonal mean and its surface area preserving global mean (σ) are calculated. Finally, to identify the significant atmospheric waves generated by the soil colour change, the $\Delta\Omega$ is divided by the σ. Variations with values $> 2\sigma$ have a significance of 95%.

In the next subsection, the effects of the soil colour change on the wind field at an altitude of 2 km are presented and discussed.

4.2 Results

The CESM1(WACCM) simulation described in Section 4.1 allows us to study the effects of a regional surface colour change on the troposphere. It results in the generation of an outwards propagating perturbation. At 2 km altitude, this perturbation generates a buoyancy oscillation that rises and falls as the day progresses and an outwards propagating circular wave.

The process by which the perturbation is generated is as follows. At sunrise (local time ≈ 06:00 UT), the altered region starts absorbing higher amounts of the incident solar radiation, compared to its surrounding regions, due to its darker surface colour. It also reflects lower amounts of the incident solar radiation (Figure 4.3a). The change in the shortwave reflected radiation over the course of the day can be seen in Figure 4.3. As the solar zenith angle decreases, the surface absorbs an increased amount of solar radiation. This results in a decreased amount of reflected radiation as can be seen in Figures 4.3a and 4.3b.

Due to the increased absorbed solar radiation, the region's surface temperature changes with approximately an hour delay (Figure 4.4). One hour after the local sunrise, only a small region close to the eastern border of the region shows signs of increased surface temperature (Figure 4.4a). At 12:00 UT, the region's surface temperature has increased by 3 K compared to the surrounding regions (Figure 4.4b). One hour after the local sunset, the region's temperature is 1.5 K higher (Figure 4.4c). By 23:00 UT, the temperature difference is reduced by a small amount, as can be seen in Figure 4.4d.

The elevated temperature leads to increased emission of longwave radiation from the region starting approximately 1 hour after local sunrise (Figure 4.5a), increasing through the day (Figure 4.5b) and decreasing slightly after local sunset as the region's temperature decreases (Figures 4.4c, 4.5c). At 23:00 UT, the surface temperature of the soil colour altered region is still increased compared to the surrounding regions (Figure 4.4d). As a result, the longwave emission is still present, albeit with decreased intensity, seven hours after local sunset (Figure 4.5d).

The higher surface temperature results in the convective heating of the air located directly above the region and the generation of an atmospheric perturbation. According to Petty (2006), if two dry bare regions are located side by side, then the

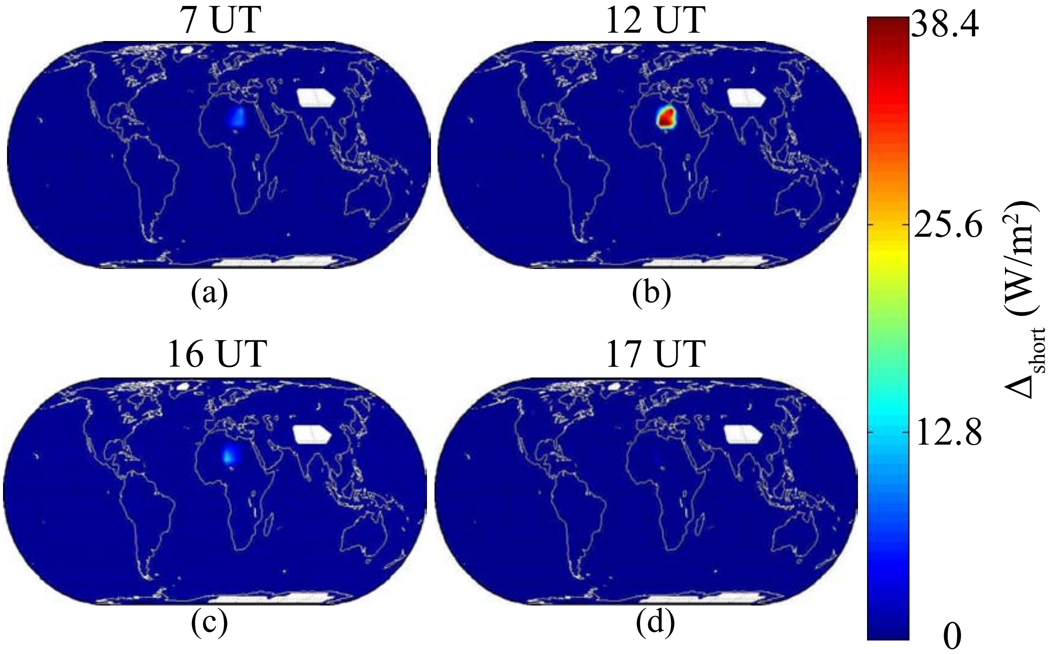

Figure 4.3: Direct reflected shortwave radiation at (a) 07:00 UT, (b) 12:00 UT, (c) 16:00 UT and (d) 17:00 UT. The figure depicts the difference in the amount of reflected solar radiation between the perturbed and control run. The change in the amount of reflected solar radiation is dependant on the radiation's angle of incidence.

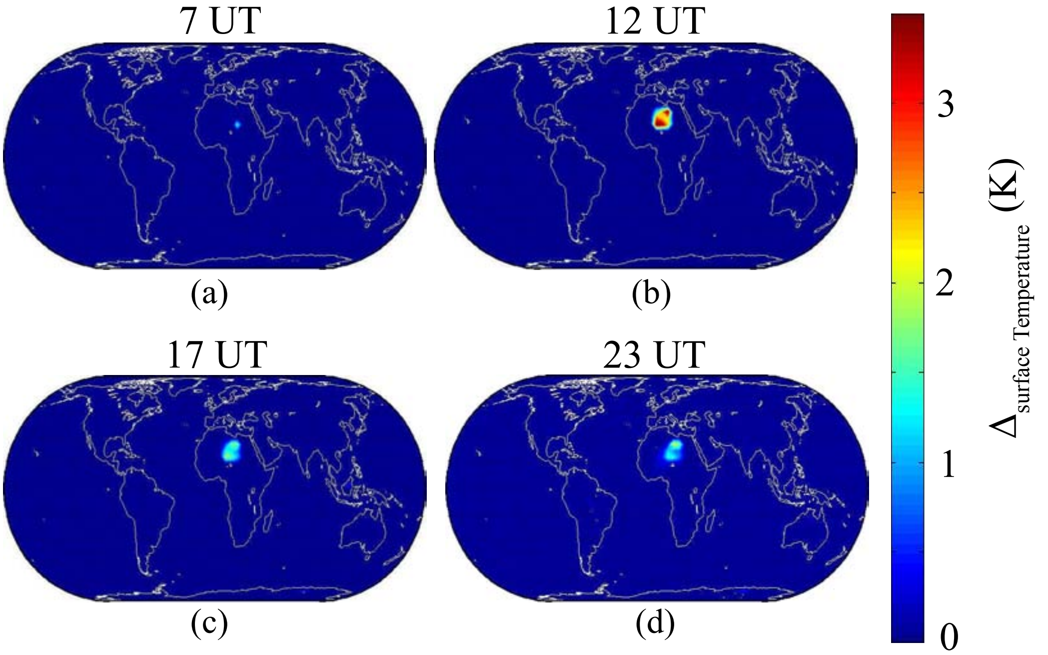

Figure 4.4: Surface temperature change at (a) 07:00 UT, (b) 12:00 UT, (c) 17:00 UT and (d) 23:00 UT. As can be seen the temperature difference between the region and the surrounding areas persists long after the local sunset (16:00 UT).

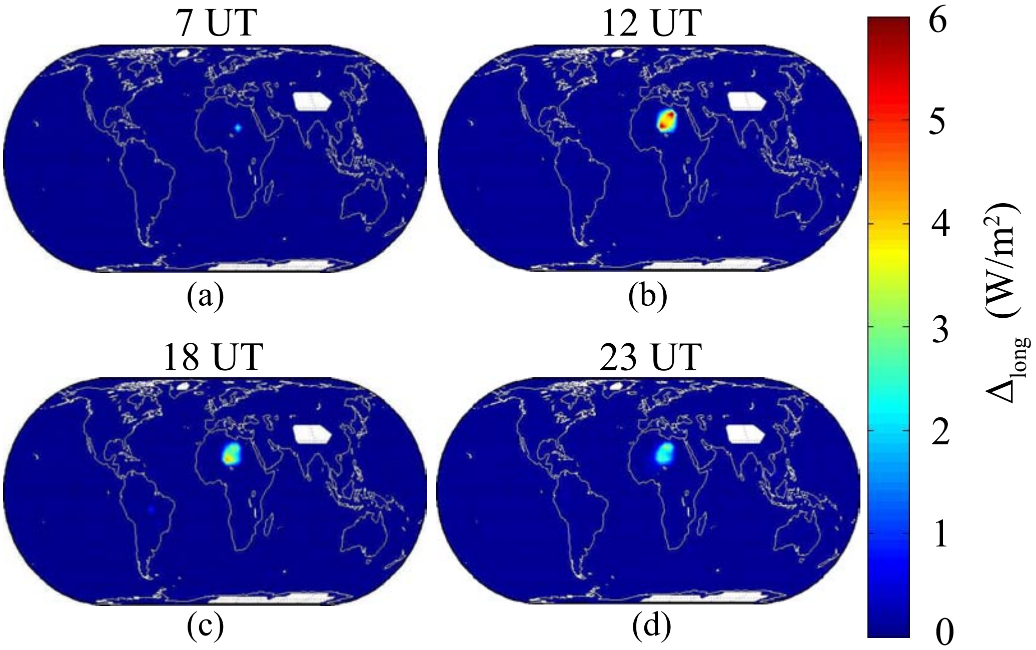

Figure 4.5: Emitted longwave radiation at (a) 07:00 UT, (b) 12:00 UT, (c) 18:00 UT and (d) 23:00 UT. The region's increased temperature results in increased longwave radiation, which persists long after local sunset (16:00 UT).

surface temperature of the darker region will increase faster compared to that of the lighter region. The temperature gradient between the two regions will result in convective air motions, as the warmer air is lifted and replaced by cooler air, flowing horizontally from the lighter region. Air located above the lighter region sinks to replace the horizontally moved air.

The perturbation in our simulation, which can be seen in Figure 4.6, is generated through the same mechanism and is convective in nature. It shares similarities with the core of a supercell, otherwise known as a rotating thunderstorm, as can be seen in Figures 4.6a - 4.6d. The air located over the Sahara region is characterised by an updraft and a downdraft, both of which are rotating clockwise around the centre of the region. Therefore, our results indicate that, in agreement with Petty (2006), the perturbation is convective in nature at tropospheric altitudes, as can be seen in Figure 4.6.

The surface colour change results in the generation of a primary perturbation, which first appears over the region at 09:00 UT (four hours after sunrise) (Figure 4.6). Figures 4.6a - 4.6d show a nearly circular wave ring moving outwards from the region. Its amplitude increases over time $A > 5\sigma$, and gives us a 5σ confidence level ($\sigma = 2 \cdot 10^{-4}$ Pa/s). Its mean wave velocity is $\langle v \rangle = 200 \pm 50$ m/s, its mean horizontal wavelength is $\langle \lambda \rangle = 3000 \pm 500$ km and its mean wave period is $\langle p \rangle = 4 \pm 1$ h. The uncertainties reflect the azimuthal variations of the wave parameters generated by changes in the background wind flow, topography, convective activity, Coriolis force and other factors which modulate the radial propagation of the wave rings.

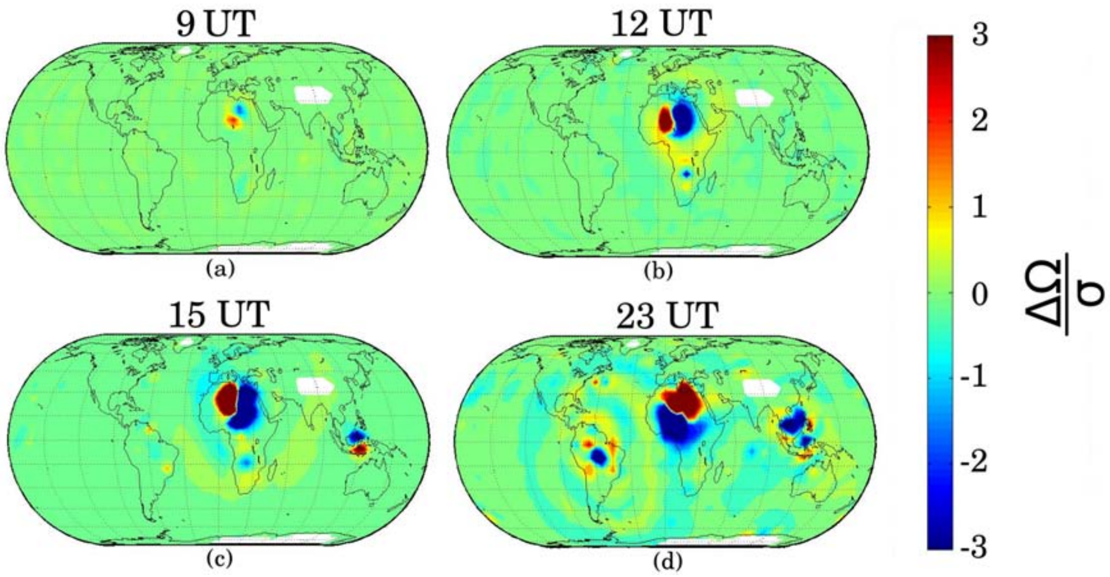

Figure 4.6: Evolution of the primary wave above the Sahara desert during the first day The difference between the vertical wind at 2 km altitude of the perturbed run minus the control run is shown at (a) 9:00 UT, (b) 12:00 UT, (c) 15:00 UT, (d) 23:00 UT. Shades of blue indicate upward motion of the air, while shades of red indicate downward motion.

Weisman and Rotunno (2000) performed a series of idealised supercell storm simulations using the Klemp and Wilhelmson (1978) numerical cloud model. The storms were generated by an ellipsoidal bubble of warm air. The bubble had a horizontal radius of 10 km and vertical radius of 1400 m with a maximum temperature perturbation of 1 K at the center of the bubble and decreasing to zero at its edges. The effects of the Coriolis parameter were ignored. Their simulation generated a convective rotational updraft 40 minutes after the start of the simulation.

Morrison and Milbrandt (2011) performed idealised 3D supercell simulations using the compressible, non-hydrostatic, 3D mesoscale Advanced Research Weather Research and Forecasting model (ARW-WRF). The surface fluxes were set to zero and the radiative transfer was neglected. They generated a supercell using a thermal perturbation at 1.5 km altitude. Their simulation also generated a convective rotational updraft.

The air motion generated in our simulation develops naturally and evolves self consistently, unlike Weisman and Rotunno (2000) and Morrison and Milbrandt (2011), who set the initial thermal condition by means of an artificial thermal air perturbation set and tuned the wind field.

The horizontal speed of the primary wave generated in our study is similar to those of Nicholls and Pielke (2000) and Gardner and Schunk (2010). Nicholls & Pielke simulated the horizontally outwards propagating circular wave from a thunderstorm region. They concluded that the generated waves were n1 and n2 wave mode Lamb waves moving with the speed of sound. The n1 mode resulted in a subsidence warming, while the n2 mode resulted in an uplift (Nicholls and Pielke, 2000), in accordance with our own results (Figure 4.6a). Our primary wave looks like an atmospheric gravity wave, as its speed is well below the speed of sound (similar to the waves simulated by Nicholls & Pielke). Waves with horizontal propagation speeds close to the speed of sound and long wavelengths, like the ones generated by the surface colour change, were classified as large-scale atmospheric gravity waves by Gardner and Schunk (2010) and Vadas and Liu (2013).

As the primary perturbation propagates outwards, it reaches the Amazon convection zone at 16:00 UT (Figure 4.7a), seven hours after its generation over the Eastern Sahara (Figure 4.6a). As the wave front comes in contact with the tropical convection zone, it scatters and generates a secondary wave, clearly visible (Figures 4.7a - 4.7b) as outgoing, periodically oscillating, concentric wave rings from the center of the tropical convection zone (10° S, 55° W).

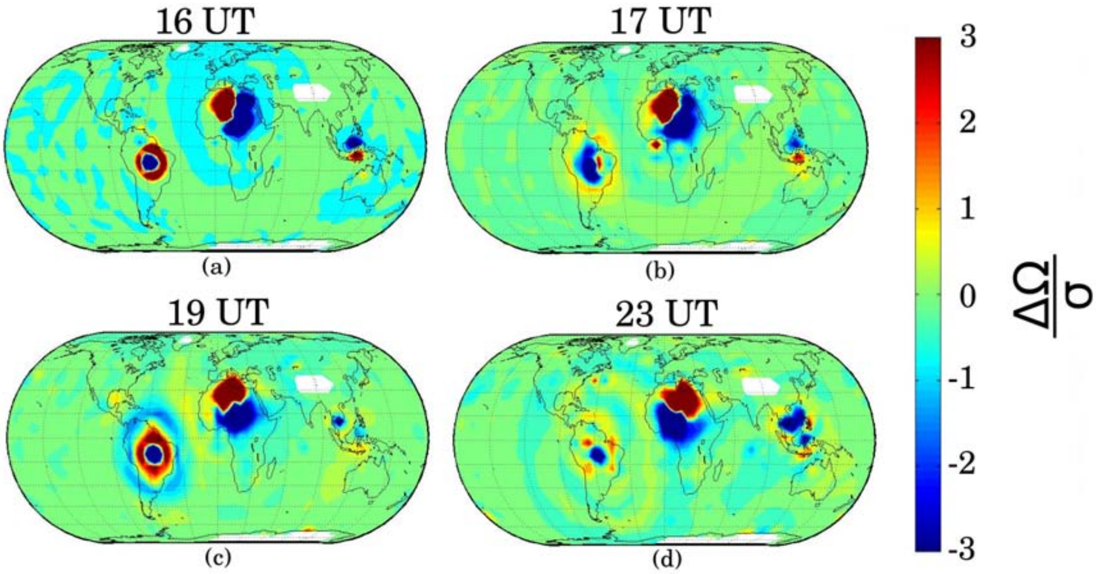

Figure 4.7: Evolution of the secondary wave above Brazil during the first day The difference between the vertical wind at 2 km altitude of the perturbed run minus the control run is shown at (a) 16:00 UT, (b) 17:00 UT, (c) 19:00 UT, (d) 23:00 UT. Shades of blue indicate upward motion of the air, while shades of red indicate downward motion.

Three hours later, at 19:00 UT, the next primary wave front reaches the tropical convection zone, scattering and amplifying the secondary perturbation (Figure 4.7c). The scattering leads to a change in the vertical air motion located over the convection zone. The upwards moving air condenses moist air and leads to the release of latent heat, which further amplifies the secondary perturbation. The strong amplitude of the secondary wave points to such a non-linear amplification process (Figures 4.7a-4.7c).

The secondary wave has a mean wave velocity of $\langle v \rangle = 220 \pm 40$ m/s, which is $\sim 70\%$ of the speed of sound for this altitude. Its mean horizontal wavelength is $\langle \lambda \rangle = 3000 \pm 500$ km and its mean wave period is $\langle p \rangle = 3 \pm 1$ h. Convectively generated primary and secondary gravity waves with characteristics similar to those of our own simulation were simulated by Vadas and Liu (2009). Vasiliy (2005) also reported the generation of secondary oceanic waves through interaction between the underlying oceanic topography. Their generation mechanism was reminiscent of the interaction of our wave and the tropical convection zone.

The primary and secondary waves are present in both the ensemble average and in each individual run, though a seasonal variation in the azimuthal wave speeds is visible. This seasonal variation can be attributed to the seasonal variation of the mean flow and the thermal structure of the lower troposphere.

The perturbation extends to the stratosphere and mesosphere as can be seen in Figure 4.8. The stratospheric perturbation is radiative in nature, generated through the absorption of the outgoing infrared radiation produced by the hot underlying surface. This is made evident by its strength compared to the surface perturbation and by the very short time interval between the surface and the stratospheric perturbation, which makes it unlikely for the perturbation to be convective in nature. The mesospheric perturbation is probably connected to global teleconnections based on wave-mean flow interactions.

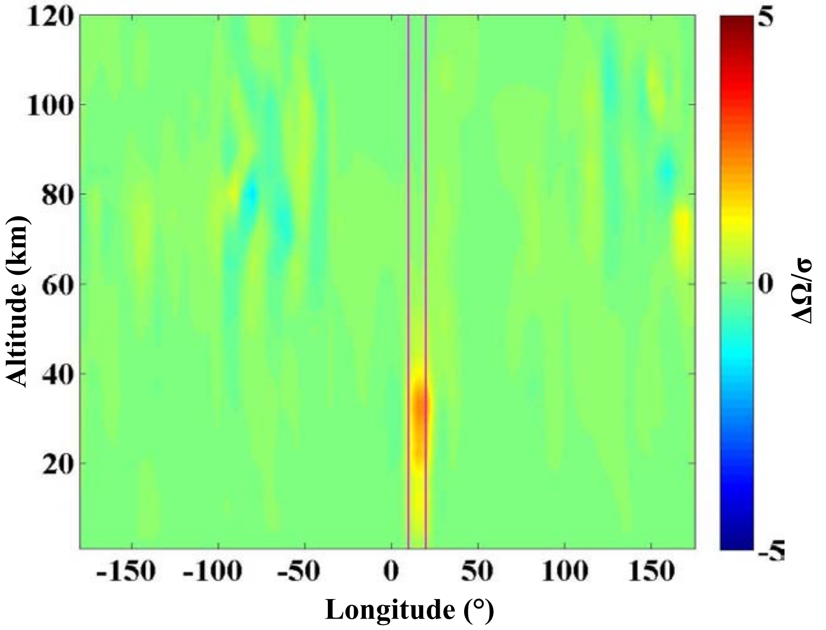

Figure 4.8: Longitude-altitude cross section at 09:00 UT on the first day of the simulation. It is centred on the 1st meridian. Shades of blue indicate upward air motion, while shades of red indicate downward motion.

Five days after the initialisation of the simulation, the circular patterns are no longer visible. Instead, enhanced fluctuations are present at seemingly random locations all over the globe as well as over Sahara and the convective zones of Brazil and Indonesia, as can be seen in Figure 4.9.

The global mean standard deviation σ increases linearly from $\sigma = 2 \cdot 10^{-4}$ on the first day to $\sigma = 27 \cdot 10^{-4}$ on the fifth day, as can be seen in Figure 4.10.

This linear increase indicates that the perturbed run diverges from the control run as the length of the simulations increases. As a result, the attribution of cause and effect, and the isolation of the soil colour-induced atmospheric perturbation becomes

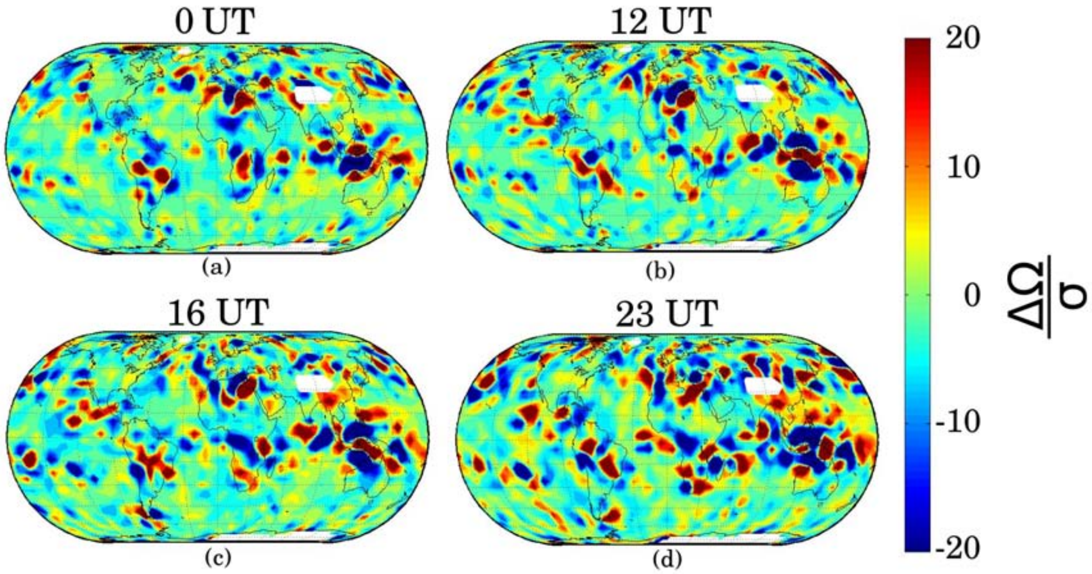

Figure 4.9: Evolution of the secondary wave above Brazil during the fifth day The difference between the vertical wind at 2 km altitude of the perturbed run minus the control run is shown at (a) 00:00 UT, (b) 12:00 UT, (c) 16:00 UT, (d) 23:00 UT. Shades of blue indicate upward motion of the air, while shades of red indicate downward motion.

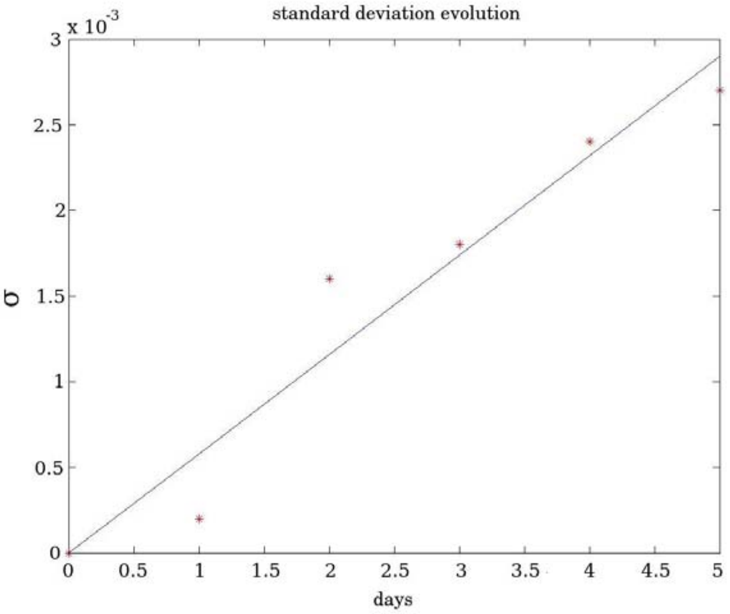

Figure 4.10: Temporal evolution of σ Evolution of the global mean standard deviation σ from the first to the fifth day

increasingly difficult. Therefore, the small perturbation analysis can be used only for the first two days of the simulations, when the perturbation waves can be clearly separated from the random background atmospheric waves.

Our study demonstrated the potential of wave propagation studies with 3D realistic climate models, which contain all the interactions between generated waves and the atmospheric jets, circulation cells, solar tides, planetary waves, random gravity waves, orography and tropical convection zones. This provided the advantage that the generation and propagation of the waves generated by the colour darkened region can be studied under realistic atmospheric conditions. This resulted in the appearance of the secondary wave over Brazil. Such an effect would not have appeared in a 1D or 2D idealised model.

It was demonstrated that it is possible to perform cause-effect, small-scale perturbation analysis in 3D models for the first few days of the simulation, as long as the amplitude of the generated perturbation remains small. The coupling of the reported primary and secondary waves indicates that the small perturbation analysis could be used for the study of similar couplings between migrating and non-migrating tides. This analysis permits the detailed study of the propagation of the generated waves in the troposphere and beyond. It also enhances our understanding of the possible effects geoengineering projects can have on the tropospheric dynamics.

5 Characterizing the three-dimensional ozone distribution of a tidally locked Earth-like planet

5.1 Research strategy

As mentioned in the Introduction, a change in the planet's rotation rate will alter the spatio-temporal distribution of the incoming stellar radiation flux and change the magnitude of the Coriolis force. These effects will in turn modify its sea and land surface temperatures, its ozone distribution and its circulation. Read (2011) described how fundamental parameters such as planetary size, planetary rotation rate and atmospheric thermal stratification play a central role in the circulation of terrestrial planets. He emphasized that the influence of other factors such as tidal locking and luminosity of the parent star must also be investigated. A planet with the size, the mass, the continental distribution and topography, the oceans, and the atmospheric composition and circulation of the present day Earth (Earth-like planet) would experience such changes if it became tidally-locked to its parent Sun-like star. Here, we mainly investigate the characteristics of the 3D ozone distribution of a tidally-locked Earth-like planet. Until now, there are only two other 3D simulation studies about the middle atmosphere of exoplanets (Yang et al. (2014), Godolt et al. (2015)).

An Earth-like habitable planet orbiting a G star at a distance of 1 AU has a lower probability of becoming tidally locked. However, retrograde planetary spin can still occur, e.g., in our own Solar System (Venus). The simulation setup used in our study has been used in past simulations to approximate tidally locked Earth-like planets and aquaplanets orbiting M stars stars by (Tarter et al., 2007), (Grenfell et al., 2014),(Joshi, 2003), (Merlis and Schneider, 2010), (Yang et al., 2013), (Segura et al., 2005), (Edson et al., 2011), (Kaspi and Showman, 2015) and (Menou, 2013). Haberle et al. (1996), Joshi et al. (1997), Joshi (2003), Segura et al. (2005) and Segura et al. (2010) demonstrated that such planets would be habitable.

The differences in the spectral energy distribution of M and G stars would result in different ozone radiative heating rates and different vertical thermal structures for the same total amount of stellar energy incident at the top of the atmosphere. This will lead to stratospheric temperature increases and will impact the planet's middle atmospheric circulation (Selsis (2000), Segura et al. (2003), Segura et al. (2005), Grenfell et al. (2007), Rugheimer et al. (2013), Rauer et al. (2011) and Godolt et al. (2015)). Therefore, one can reasonably expect that the middle atmospheric chemistry of a tidally locked Earth-like planet will be altered. Since the aim of this study is to investigate the effects of the tidal lock on the planet's ozone distribution, such an effect would complicate the cause-effect attribution analysis and make it exceedingly difficult to correctly ascribe the observed changes to either the tidal lock or the spectral energy distribution change. Therefore, the Earth-like planet - Sun-like star setup simplifies the tidal lock cause-effect analysis and facilitates its comparison with older studies, where similar setups were also used (Merlis and Schneider (2010), Grenfell et al. (2014), Joshi (2003), Yang et al. (2013), Segura et al. (2005), Joshi (2003), Edson et al. (2011), Kaspi and Showman (2015), Menou (2013)). These studies were focused mainly on the troposphere (Merlis and Schneider (2010), Joshi et al. (1997), Showman and Polvani (2011), Carone et al. (2014), Edson et al. (2011)).

The habitability of a tidally locked Earth-like planet orbiting a Sun-like star was investigated by Merlis and Schneider (2010), Yang et al. (2013), and Grenfell et al. (2014). Merlis and Schneider (2010) found that the tidal lock would generate an upwelling over the day side and a downwelling over the night side in the planet's troposphere.

Our study is characterised by a more complicated setup compared to the study presented in Chapter 4. The shortwave solar radiation distribution is altered by reducing the planet's rotation rate to 1/365th of the Earth's rotation rate. Two 90 day simulations are performed: one for the present day Earth (PDE), whose rotation rate is $\Omega_{\mathrm{PDE}} = 1\left(\frac{\text{rotation}}{\text{days}}\right)$; and one for a tidally locked Earth-like exoplanet, whose rotation is $\Omega_{\mathrm{TLE}} = \frac{1}{365}\left(\frac{\text{rotation}}{\text{days}}\right)$. On the tidally locked Earth (TLE), the subsolar point is permanently located over the same geographical region rather than moving on the globe as is the case in the PDE. The planet-star distance, the eccentricity and the stellar irradiance S_o at the top of the model are the same for both simulations. The PDE has the obliquity of the present day Earth, while the TLE has an obliquity of 0°. In order to simplify our analysis, both simulations are launched on the day of the spring equinox (21.03.2000). To achieve the tidal lock, the following model parameters are changed:

- the number of seconds in a siderial day is altered from 86164 seconds/day to $3.15 \cdot 10^{7}$ seconds/day
- the planet's rotation velocity is set to $2.31 \cdot 10^{-12}$ rad/s
- the planet's new rotation rate is 1° every 87600 seconds (the Earth rotation rate is 1° every 240 seconds)
- the position of the subsolar point is set to (0.17° N, -178.17° E) for the duration of the simulation. The simulation is initialised using model data from the year 2000 Spring Equinox, at 00:00 UT.
- the Sea Surface Temperature (SST) is changed to resemble the SST of the tidally locked Earth-like aquaplanet reported by Merlis and Schneider (2010)

- The solar zenith angle (SZA) is set to a constant value by means of the PDE Julian date.

By setting the Julian date to a constant value, the periodic 24-hour variation of SZA is stopped at all grid points of the TLE. The SZA is the central parameter used for the assessment of the incoming solar radiation in the CESM model world. The above changes result in a perpetual equinox simulation. The shortwave solar radiation flux at the top of the model for the TLE simulation is shown in Figure 5.1. The solar point is depicted by a white dot on both sides of the figure, while the anti-solar point is depicted by a magenta point in the centre of the figure.

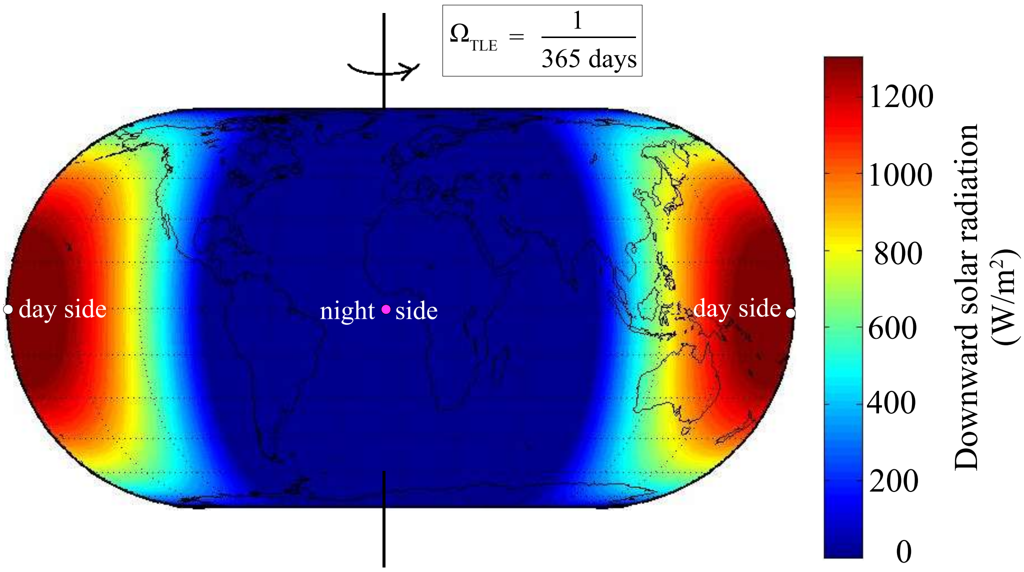

Figure 5.1: TLE Incident shortwave radiation at the top of the model Shades of red indicate high incoming solar radiation and define the day side of the planet, while shades of blue indicate low incoming solar radiation. The dark blue visible in the center of the plot indicates a lack of incoming solar radiation and defines the night side of the planet. The subsolar point is indicated with a white point on both sides of the figure. It is centred approximately at (0°, 180°) over the Pacific Ocean. The antisolar point is indicated with a magenta point in the centre of the figure and is centred approximately at (0°,0°).

The model is forced with an SST that resembles the SST reported by Merlis and Schneider (2010) to ensure the energetic self-consistency of the model. They performed a long-term simulation of an Earth-like tidally locked aquaplanet, orbiting a Sun-like star, at a distance of 1 AU. The altered SST can be seen in Figure 5.2. The CESM1(WACCM) requires the presence of an active land model. Therefore, the general topography and continents of the Earth are maintained. The atmospheric and surface initialization data are identical for both the PDE and the TLE runs and both simulations start with same PDE 3D ozone and wind fields.

The total ozone content ($TOC = \int_5^{110}[\mathrm{O_3}]\mathrm{dz}$), vertical wind Ω, the zonal and meridional wind (U, V) and the atmospheric temperature T are calculated between 5 and 110 km altitude to avoid the data gaps generated by the presence of several high

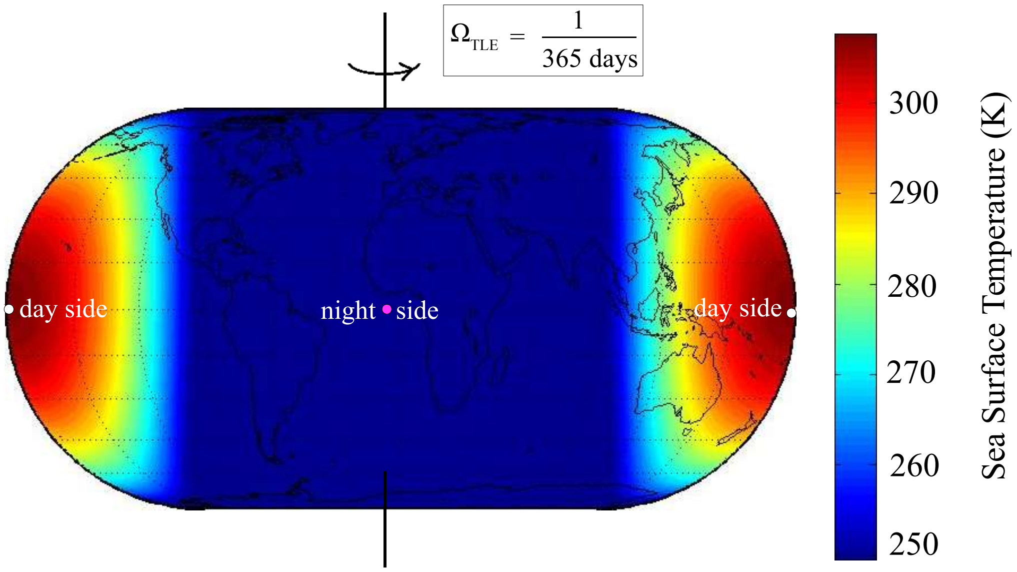

Figure 5.2: TLE Sea Surface Temperature setup. Shades of red indicate high temperatures and define the day side of the planet. Shades of blue indicate low temperature and define the night side of the planet. The subsolar point is indicated with a white point on either side of the figure. The antisolar point is indicated with a magenta point in the center of the figure.

mountains and mountain ranges (e.g Himalayas, Kilimanjaro) and the air density data gaps above 110 km altitude. The partial ozone content (POC) is calculated for the altitude ranges of 5 to 28 km, 30 to 45 km and 55 to 100 km altitude.

In the next subsection, the effects of the tidal lock on the total ozone content (TOC), the vertical wind Ω, the zonal wind U, the horizontal wind HW and the atmospheric temperature T for the present day Earth (PDE) and the tidally locked Earth (TLE) are presented and discussed. First, the latitude-longitude ozone concentration cross sections of the TLE are discussed and compared to the PDE. Then, the TLE lower and middle stratospheric and mesospheric $POCs$ and TOC are described and compared with the PDE $POCs$ and $TOCs$. Next, the global means of the TOC and $POCs$ are determined by calculating their zonal means as a function of latitude and weighted them with the surface area of the latitude belts (surface area preserving mean). Afterwards, the change in % of TOC and POC between the PDE and TLE is calculated.

$$\Delta TOC_{\%} = \frac{TOC_{TLE} - TOC_{PDE}}{TOC_{PDE}} * 100 \tag{5.1}$$

$$\Delta POC_{\%} = \frac{POC_{TLE} - POC_{PDE}}{POC_{PDE}} * 100 \tag{5.2}$$

$$\Delta TOC_{DU} = TOC_{TLE} - TOC_{PDE} \tag{5.3}$$

$$\Delta POC_{DU} = POC_{TLE} - POC_{PDE} \tag{5.4}$$

Lastly, the hemisphere means (HM) of the PDE and TLE ($TOC_{HM(PDE)}$, $TOC_{HM(TLE)}$) as well as their differences ($\Delta TOC_{HM(PLE,TLE)}$, $\Delta TOC_{HM(TLE,TLE)}$, $\Delta TOC_{HM(PDE,PDE)}$)

are calculated.

$$\Delta TOC_{HM(PLE,TLE)} = \frac{TOC_{HM(PDE)} - TOC_{HM(TLE)}}{TOC_{HM(TLE)}} \tag{5.5}$$

$$\Delta TOC_{HM(TLE,TLE)} = \frac{TOC_{HM(TLE(0^\circ))} - TOC_{HM(TLE(\phi))}}{TOC_{HM(TLE(\phi))}} \tag{5.6}$$

$$\Delta TOC_{HM(PDE,PDE)} = \frac{TOC_{HM(PDE(0^\circ))} - TOC_{HM(PDE(\phi))}}{TOC_{HM(PDE(\phi))}} \tag{5.7}$$

The TOC hemisphere mean is defined as the TOC mean of one side of the planet, which spans between 180° in longitude and 180° in latitude. The $\Delta TOC_{(PLE,TLE)}$ is defined as the difference between the TLE and the PDE hemisphere means, while the $\Delta TOC_{(TLE,TLE)}$ is defined as the difference between the TLE hemisphere centred around the 0° meridian and the hemisphere centred around the ϕ meridian. Finally, the $\Delta TOC_{(PDE,PDE)}$ is given by the difference between the PDE hemisphere centred around the 0° meridian and the hemisphere centred around the ϕ meridian.

5.2 Results

The CESM1(WACCM) simulation described in Section 5.1 allows us to study how the radiative forcing and Coriolis force changes, which appear as a result of the tidal lock, affect an Earth-like planet.

Our study reveals that the middle atmosphere adjusts to the new radiative and dynamical conditions in the surprisingly short time of 80 days. The adjustment times of the TLE total ozone content (TOC_{TLE}), the global mean stratospheric horizontal wind (HW_{TLE}), the global mean stratospheric vertical wind (Ω_{TLE}) and the global mean stratospheric temperature (T_{TLE}) for the 30 - 40 km altitude range can be seen in Figure 5.3. The temporal evolution of the PDE TOC_{PDE}, HW_{PDE}, Ω_{PDE} and T_{PDE} are also shown for comparison. The e-folding times of the TOC_{TLE}, HW_{TLE}, Ω_{TLE} and T_{TLE} are 30, 20, 15 and 40 days, respectively and can be seen, along with their PDE equivalents and standard deviations (σ), in Table 5.1. Therefore, the adjustment times TOC_{TLE}, HW_{TLE}, Ω_{TLE} and T_{TLE} are 60, 40, 30, 26 and 80 days, respectively. A comparison between the TLE and PDE σ reveals that the PDE has higher standard deviations (σ_{PDE}) compared to the TLE standard deviations (σ_{TLE}).

Table 5.1: Comparison of TOC and POC e-folding times, steady-state mean values and their standard deviations obtained for the PDE and TLE simulation on day 90.

	PDE	σ_{PDE}	TLE	σ_{TLE}
TOC (DU)	280.1	1.44	248.7	1.00
$HW_{30-45km}$ (m/s)	21.19	5.21	14.21	1.00
$\Omega_{30-45km}$ (Pa/s)	$-8.6 \cdot 10^{-7}$	$9.6 \cdot 10^{-7}$	$-1.7 \cdot 10^{-7}$	$1.3 \cdot 10^{-7}$
$T_{30-45km}$ (K)	239.9	0.85	238.4	0.43

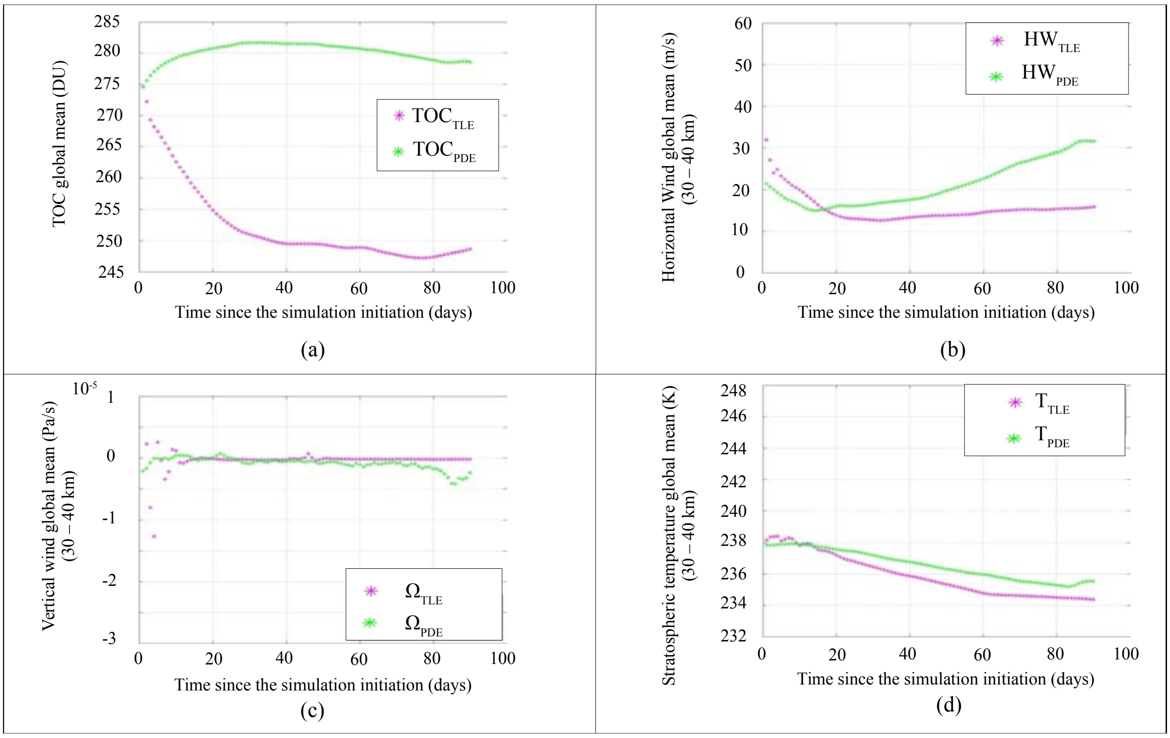

Figure 5.3: TLE temporal evolution of the TLE and PDE atmosphere (a) the TOC, (b) the HW, (c) the Ω, (d) the T, respectively. The TLE TOC, HW, and T are exponentially decaying to their steady-state value with an e-folding time of 30, 20 and 40 days, respectively. The TLE Ω is exponentially increasing to its steady-state value with an e-folding time of 15 days.

The tidal lock affects the TLE's vertical thermal structure only to a limited extent. It actually has a very similar vertical structure to the PDE with a troposphere, stratosphere and mesosphere located in the same approximate locations. However, the distribution of the atmospheric gases, temperature and atmospheric circulation is very different in each one of the two planets.

The tidal lock results in the breakdown of the Brewer Dobson circulation (Figure 2.3) and is replaced by a very different atmospheric circulation (Figures 5.4, 5.5 and 5.6). The vertical circulation is replaced by an upwelling centred on the day side and a downwelling centred on the night side, which extends from the surface to the mesosphere (Figure 5.4).

The day side upwelling is generated by the upwards movement of the radiatively heated air, due to the constant solar radiation flux it receives. The night side upwelling, on the other hand, is generated by the downward movement of the radiatively cooled night side air, which receives no solar radiation. A similar vertical circulation was predicted by Merlis and Schneider (2010) for the troposphere of a tidally locked aquaplanet with a similar size, mass, atmospheric chemistry and circulation to the present day Earth. The reported upwelling was attributed to radiative heating and the downwelling to radiative cooling of the atmosphere.

Figure 5.5 shows the PDE and TLE zonal mean zonal wind. The PDE zonal mean zonal wind is characterised by eastward winds in the Northern hemisphere and

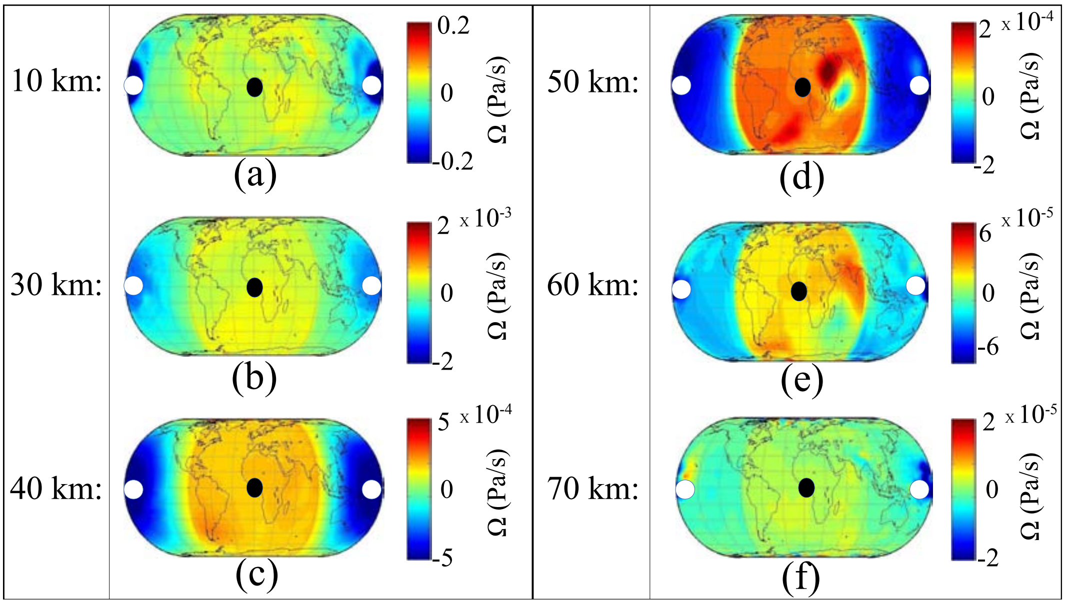

Figure 5.4: Longitude-Latitude Vertical wind circulation in the TLE (a) Vertical wind at 10 km, (b) Vertical wind at 30 km, (c) Vertical wind at 40 km, (d) Vertical wind at 50 km, (e) Vertical wind at 60 km, (f) Vertical wind at 70 km. Warm colours (positive values) indicate a downwelling wind. Cold colours (negative values) indicate an upwelling wind. Each figure is centred on the antisolar point which is indicated with a black dot. The subsolar point is indicated with a white dot on either side of each figure.

westward winds in the Southern hemisphere in the altitude range of approximately 20 - 80 km (Figure 5.5). The TLE zonal mean zonal wind, on the other hand, is characterised by alternating bands of eastward or westward wind spanning both hemispheres.

Figure 5.6 shows the TLE horizontal wind at 24 km, 36 km and 60 km altitude. It showcases the differences in the horizontal circulations at different altitudes, especially between stratospheric and mesospheric altitudes. As can be seen in Figure 5.6, at lower and middle stratospheric altitudes, jet streams form at tropical latitudes.

Unlike the PDE (Figure 5.7), the TLE horizontal wind is unidirectional. At 20 - 35 km altitude, the jet stream is eastward, while the jet stream is westward at 35 - 40 km altitude. The strong natural variability of the lower stratospheric wind field leads to considerable periodic changes ($\approx$ 15 days) in the distribution patterns of lower stratospheric ozone (16 - 28 km). Therefore, the middle atmospheric wind system of the TLE shows a high degree of spatio-temporal variability, with the direction and location of the TLE jet stream completely changing over height intervals of 10 km. In comparison, the PDE circulation is largely eastward in the Northern hemisphere and westward in the Southern hemisphere, with no vortices present.

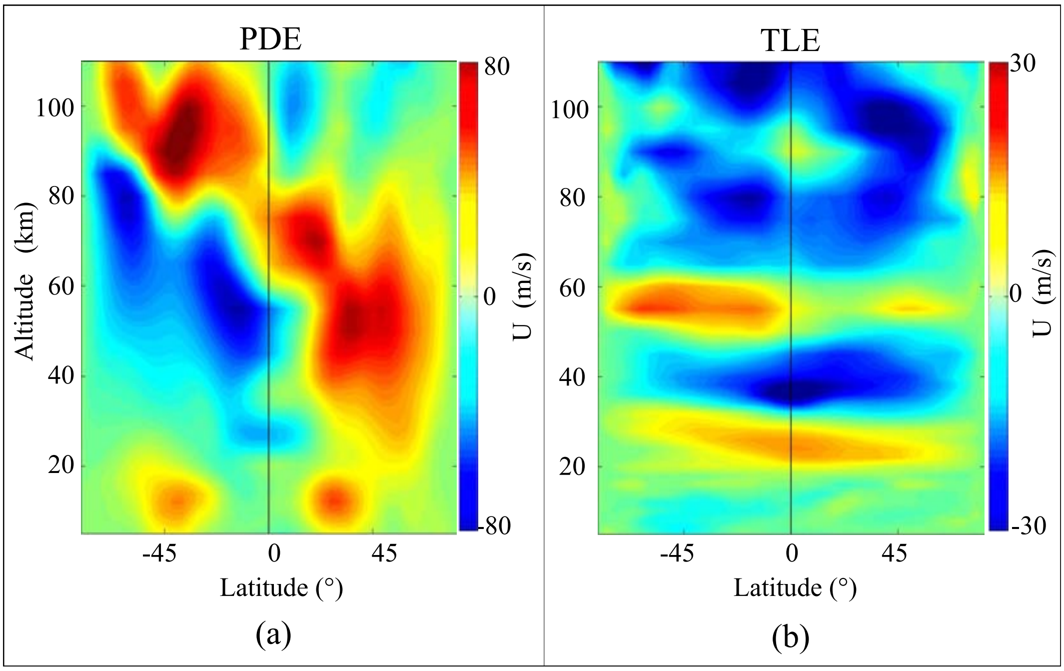

Figure 5.5: PDE and TLE zonal mean zonal wind latitude-altitude cross-sections (a) PDE zonal mean zonal wind, (b) TLE zonal mean zonal wind. Warm colours indicate movement from the west to the east, while cold colours indicate movement from the east to the west.

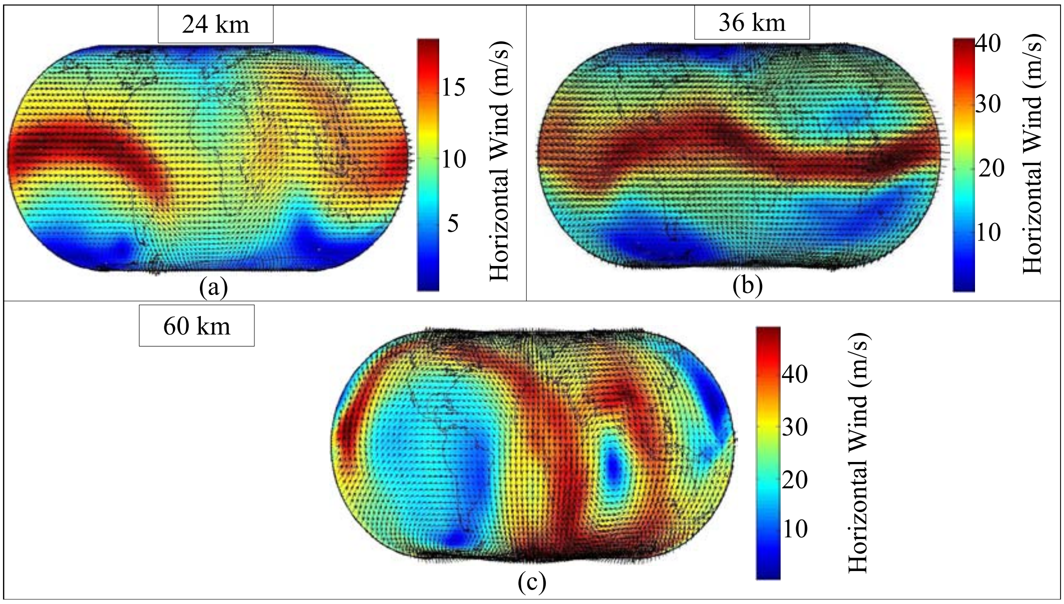

Figure 5.6: TLE Horizontal circulation at select altitudes (a) Horizontal wind at 24 km, (b) Horizontal wind at 36 km, (c) Horizontal wind at 60 km. The black arrows indicate the wind vector while the color shading shows the wind speed.

The altered solar radiation distribution results in changes in the TLE ozone distribution, as can be seen in Figure 5.8. The figure depicts the TLE and PDE O_3VMR distribution along the 180th and the 1st meridian.

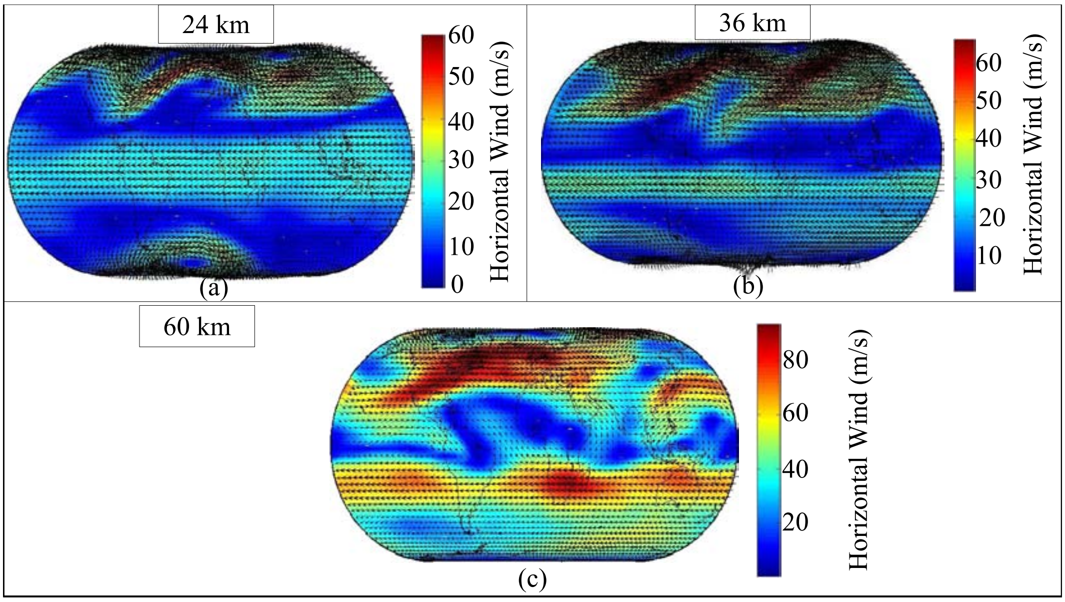

Figure 5.7: PDE Horizontal circulation at select altitudes (a) Horizontal wind at 24 km, (b) Horizontal wind at 36 km, (c) Horizontal wind at 60 km. The black arrows indicate the wind vectors while the color shading shows the wind speed.

Compared to the PDE, the TLE primary ozone layer (located between 30 and 40 km altitude) is enhanced on the day side (Figures 5.8b, 5.8d), due to the day side constant solar radiation, and depleted on the night side (Figures 5.8a, 5.8c), due to the lack of solar radiation. The TLE day-night side variation is $\sim 40\%$, which is one order of magnitude larger than the PDE day-night variation ($< 2\ \%$).

The TLE does not posses a tertiary night-time ozone layer, as can be seen in Figure 5.8c. The chemical and dynamical processes responsible for its disappearance are currently unknown, but the phenomenon could be related to the slowdown of the transport of air from the day to the night side. On the PDE, the day side to night side transport of air is fast in comparison, due to the planet's fast rotation.

As can be seen in Figures 5.8a, 5.8c, a secondary ozone layer, present only during the night time, occurs in both the PDE and the TLE. A comparison between the two figures reveals that the TLE secondary ozone layer is enhanced, compared to the PDE. This phenomenon is the result of the transport of atomic oxygen rich air from the day to the night side through both the horizontal and the vertical circulation, where it recombines to form ozone. This transport of air from the day side to the night side in the 55 - 100 km altitude region through the horizontal circulation and the vertical circulation can be seen in Figures 5.5 and 5.6, respectively. The physical process responsible for the altitude increase of the TLE secondary ozone layer to 90 - 110 km altitude (from 80 - 100 km in the PDE) is currently an open question.

At mesospheric altitudes, the photochemistry plays a dominant role in both planets. At these altitudes, ozone is photodissociated constantly towards O by the UV radiation during daytime (equation 2.2) and has a very short lifetime (~ 1 minute) as a result. During night time, the generated O_2 and O recombine to form ozone (equation 2.3). Due to the stationary subsolar point, which results in permanent night on the

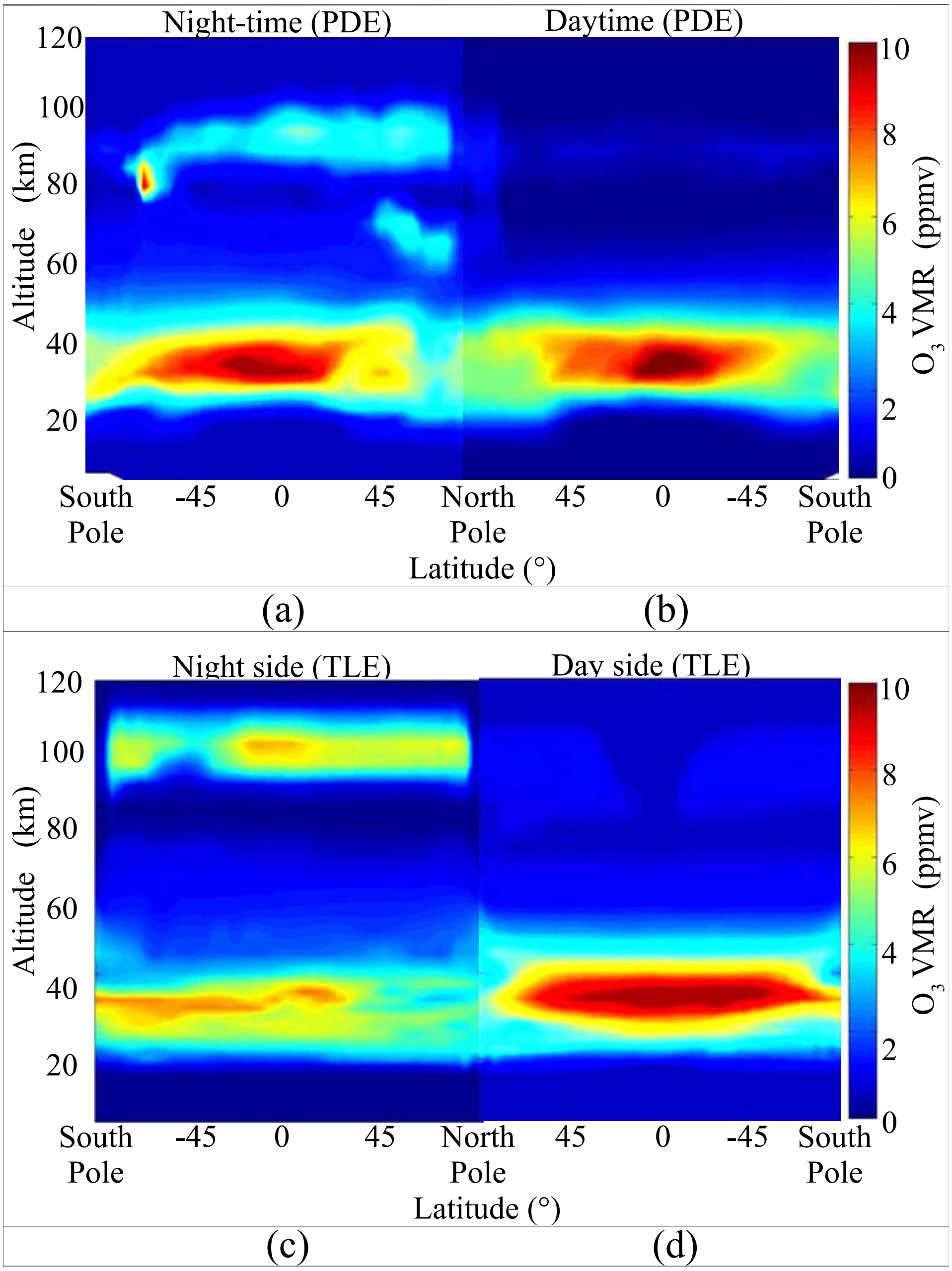

Figure 5.8: Height-latitude cross section of the O_3VMR along the meridian through the subsolar point and the antisolar point for the PDE and TLE (a) Vertical cross section of the PDE night-time hemisphere. (b) Vertical cross section of the PDE daytime hemisphere. (c) Vertical cross section of the TLE night side hemisphere. (d) Vertical cross section of the TLE day side hemisphere.

night side of the planet, the TLE night side mesospheric ozone concentration increases by $\sim$ 17.9 % compared to the PDE (Figures 5.9e, 5.9a). On the day side, the ozone remains depleted and relatively unchanged compared to the PDE (Figures 5.9e, 5.9a).

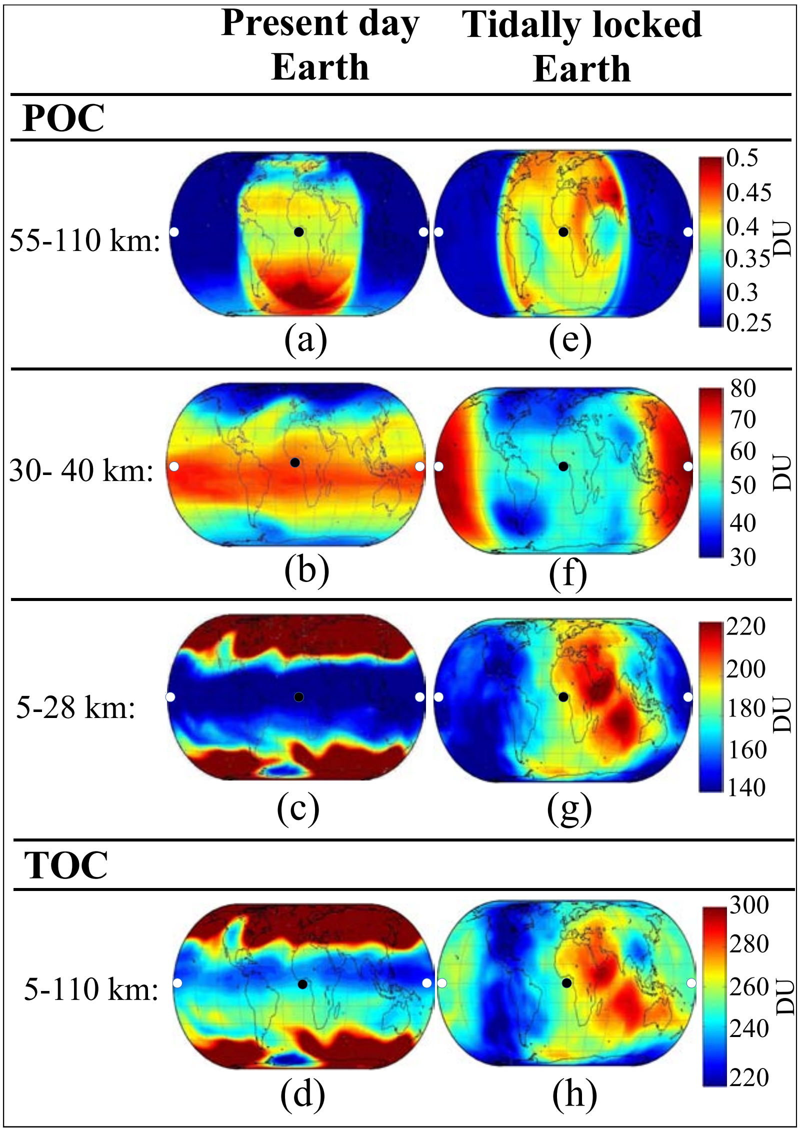

Figure 5.9: Comparative *TOC* **and** *POC* **maps for the PDE and the TLE** (a) $POC_{PDE(55-110)}$, (b) $POC_{PDE(30-45)}$, (c) $POC_{PDE(5-28)}$, (d) TOC_{PDE} at 00:00 UT on the day of the spring equinox, respectively. (e) $POC_{TLE(55-110)}$, (f) $POC_{TLE(30-45)}$, (g) $POC_{TLE(5-28)}$, (h) TOC_{TLE} on the 90th day of the TLE simulation, respectively. All figures are centred on the antisolar point which is indicated with a black dot. The subsolar point is indicated with a white dot on either side of each figure.

The middle stratosphere extends in the 30 - 40 km altitude region, where the primary ozone layer is located in both the PDE and the TLE. At these altitudes, the photochemistry plays a dominant role in both the PDE and the TLE. In the PDE, the ozone molecules are photodissociated towards atomic and molecular oxygen by the UV radiation during the day (equation 2.2). Then, due to the higher air and molecular oxygen density, they immediately recombine to form ozone (equation 2.3) (Figure 5.9b). In the TLE, the ozone generation follows a similar process. Odd oxygen is only generated on the day side. Due to the higher stratospheric air density (compared to the mesosphere), the generated atomic oxygen is immediately converted to ozone. (Figure 5.9f).

On the night side, the lack of shortwave radiation flux and the reduced mixing rates between the day and the night side lead to a visibly depleted night side *POC* and a high day-night side variation (Figure 5.9f). The mixing rates are reduced due to the day to night side transport velocities reduction in the TLE compared to the PDE ($v_{PDE} = 25$ m/s, $v_{TLE} = 13$ m/s). Due to the horizontal atmospheric circulation, the TLE has a much smaller temperature gradient compared to the PDE (Figure 5.10). The depletion is further enhanced by the large scale meridional mixing, generated as a result of the decreased TLE Coriolis force.

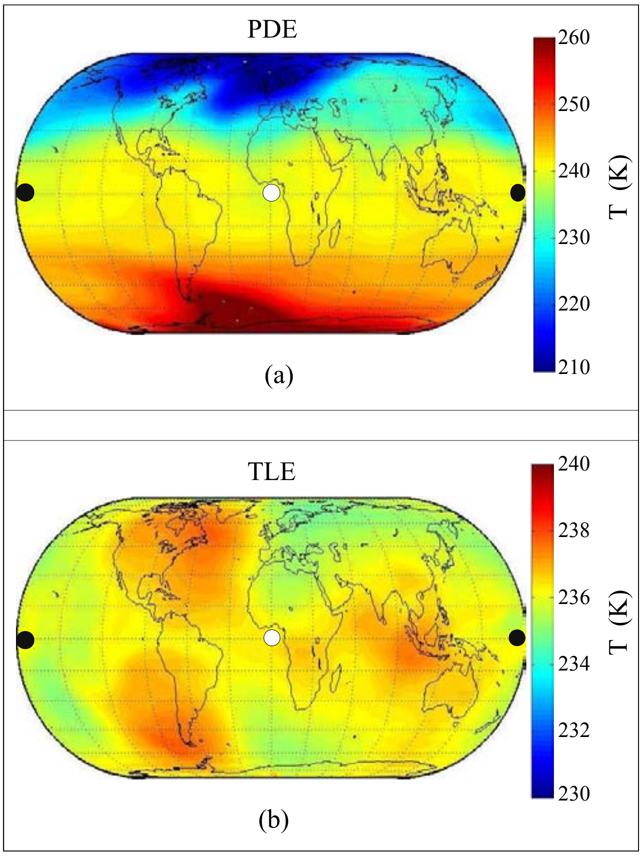

Figure 5.10: Comparative view of the PDE and TLE atmospheric temperatures at 36 km altitude (a) T_{PDE}, (b) T_{TLE}. The antisolar point is indicated with a white point in the center of the figure. The subsolar point is indicated with a black point on either sides of the figure. The middle stratospheric TLE temperature is clearly decreased compared to the PDE.

The mean night side $POC_{TLE(30-40)} = 45$ DU, while the mean day side $POC_{TLE(30-40)} = 58$ DU. Therefore, the day - night side middle stratospheric ozone variation is approximately 29% with respect to the night side, one order of magnitude larger than the PDE middle stratospheric diurnal variation ($< 5\%$).

The TLE and PDE tropospheric (5 - 14 km) *POC* is lower by two orders of magnitude compared to the lower stratospheric *TOC* (14 - 28 km) and, therefore, does not contribute considerably to the tropospheric and lower stratospheric *POC*

($POC_{(5-28)}$) presented here. The TLE and PDE $POC_{(5-28)}$ (($\mathrm{POC}_{\mathrm{TLE}(5-28)}$) and ($POC_{PDE(5-28)}$)) can be seen in Figure 5.9. At these altitudes, the lifetime of odd oxygen (and therefore ozone) is several months long due to the attenuation of the UV radiation flux at higher altitudes. Consequently, the ozone distribution is influenced mainly by the lower stratospheric dynamics. In the TLE, the lower stratospheric ozone, which was concentrated in extra-tropical latitudes at the start of the simulation, is transported through the horizontal and vertical circulation to the night side of the planet where it accumulates, generating the pronounced high POC levels.

As can be seen in Figure 5.9g, the $POC_{TLE(5-28)}$ is depleted on the day side and enhanced on the night side. The lack of stratified structure visible in the $POC_{TLE(5-28)}$ is generated by the large scale mixing that takes place, as a result of the small value of the Coriolis force. The mean night side is $POC_{TLE(5-28)} = 181$ DU, while the mean day side is $POC_{TLE(5-28)} = 158$ DU (Figure 5.9g). Therefore, the lower TLE stratospheric day-night side variation is ~ 13 % with respect to the day side. The $POC_{PDE(5-28)}$ diurnal variation is ~ 0.1 %. Therefore, the $POC_{TLE(5-28)}$ is two orders of magnitude higher compared to the $POC_{PDE(5-28)}$.

The main characteristics of the TLE total ozone content (TOC_{TLE}) are formed in the lower and middle stratosphere, as a comparison between Figures 5.9e, 5.9g and 5.9h reveals. The TOC_{TLE} day side features are generated by the enhanced middle stratospheric POC (Figure 5.9f) and the depleted day side lower stratospheric POC (Figure 5.9g) and are, therefore, produced by a combination of photochemistry and dynamics. The depleted region located over the American continent originates partly in the lower and partly in the middle stratosphere. The enhanced TOC_{TLE} night side features, on the other hand, originate in the lower stratosphere (Figure 5.9e). As can be seen in Figure 5.9h, the TOC_{TLE} is characterised by enhanced O_3 columns on the day and night side and a well mixed meridional TOC distribution. Therefore, it presents a very different picture compared to the PDE total ozone content TOC_{PDE}, which can be seen in Figure 5.9d.

The TOC_{PDE} and TOC_{TLE} global means ($TOC_{PDE(GM)}$ and $TOC_{TLE(GM)}$, respectively) are presented in Table 5.2. The day and night side TOC_{PDE} and TOC_{TLE} hemisphere means ($TOC_{PDE(HM)}$ and $TOC_{TLE(HM)}$, respectively) are presented in Table 5.3. The $TOC_{TLE(GM)}$ is reduced by 19.3 % compared to the $TOC_{PDE(GM)}$. Therefore, the TOC_{TLE} is depleted compared to the equivalent PDE, but not to the extent that would render the planet uninhabitable. The day side TOC_{TLE} is depleted compared to the daytime TOC_{PDE}, as can be seen in Figure 5.9, though it still remains within the limits of habitability.

Compared to the PDE, the $POC_{TLE(5-28)}$ global mean ($POC_{TLE(5-28)(GM)}$) is reduced by 27.7%, while the $POC_{TLE(30-45)}$ global mean ($POC_{TLE(30-40)(GM)}$) is increased by 0.8%. The $POC_{TLE(5-28)(GM)}$ reduction can be attributed to the changed dynamics, which play a dominant role at these altitudes. The increased $POC_{TLE(30-45)(GM)}$, on the other hand, can be attributed equally to the influence of dynamics and photochemistry. The $POC_{TLE(55-110)}$ global mean ($POC_{TLE(55-110)(GM)}$) is increased by 7.2% compared to the PDE and can be attributed to the effects of photochemistry and transport of atomic oxygen. This increase has no major impact on the TOC_{TLE} due to the small $POC_{TLE(55-110)}$ value (< 1 DU). As the majority of the TOC_{TLE}

Table 5.2: Comparison of the PDE and TLE *TOC* and *POC* global means. The Δ (%) and Δ (DU) are defined by equations (5.1), (5.2), and (5.3), (5.4), respectively

	PDE (DU)	TLE (DU)	Δ (%)	Δ (DU)
TOC_{GM}	291.14	244.05	19.3	47.09
$POC_{(5-28)GM}$	216.35	169.42	27.7	46.93
$POC_{(30-45)GM}$	46.45	46.84	-0.8	-0.39
$POC_{(55-110)GM}$	0.31	0.34	-7.2	-0.03

Table 5.3: Comparison of the PDE and TLE, *TOC* and *POC* day side and night side means, respectively.

	PDE Day side Mean (DU)	PDE Night side Mean (DU)	TLE Day side Mean (DU)	TLE Night side Mean (DU)
TOC_{GM}	295	287	240	249
$POC_{(5-28)GM}$	220	213	158	181
$POC_{(30-45)GM}$	52	51	58	45
$POC_{(55-110)GM}$	0.23	0.40	0.28	0.40

is located at stratospheric altitudes, the reduction of the TOC_{TLE} can be attributed equally on the changed dynamics and photochemistry.

As the planet orbits it parent star, only one side will be visible to the observers and the side will change with time, as can be seen in Figure 5.11.

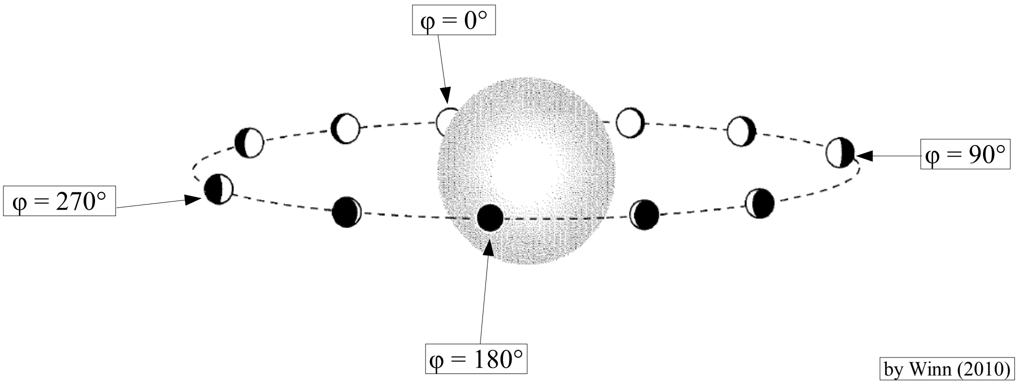

Figure 5.11: Phases of an exoplanet as seen by an observer The phases $\varphi = 0°$, $\varphi = 90°$, $\varphi = 180°$, $\varphi = 270°$ have been marked. In phase $\varphi = 0°$ only the planet's day side is visible. In phases $\varphi = 90°$and $\varphi = 270°$ half of the day side and half of the night side are visible. In phase $\varphi = 180°$ only the night side is visible.

Consequently, four hemisphere phases ($\varphi = 0°$, $\varphi = 90°$, $\varphi = 180°$, $\varphi = 270°$) of the TOC_{TLE} (Figures 5.12e - 5.12h) are presented and compared with the equivalent TOC_{PDE} phases (Figures 5.12a - 5.12d). Their values are radially integrated from the surface to the top of the atmosphere, where the phases φ follow the marked phases in Figure 5.11.

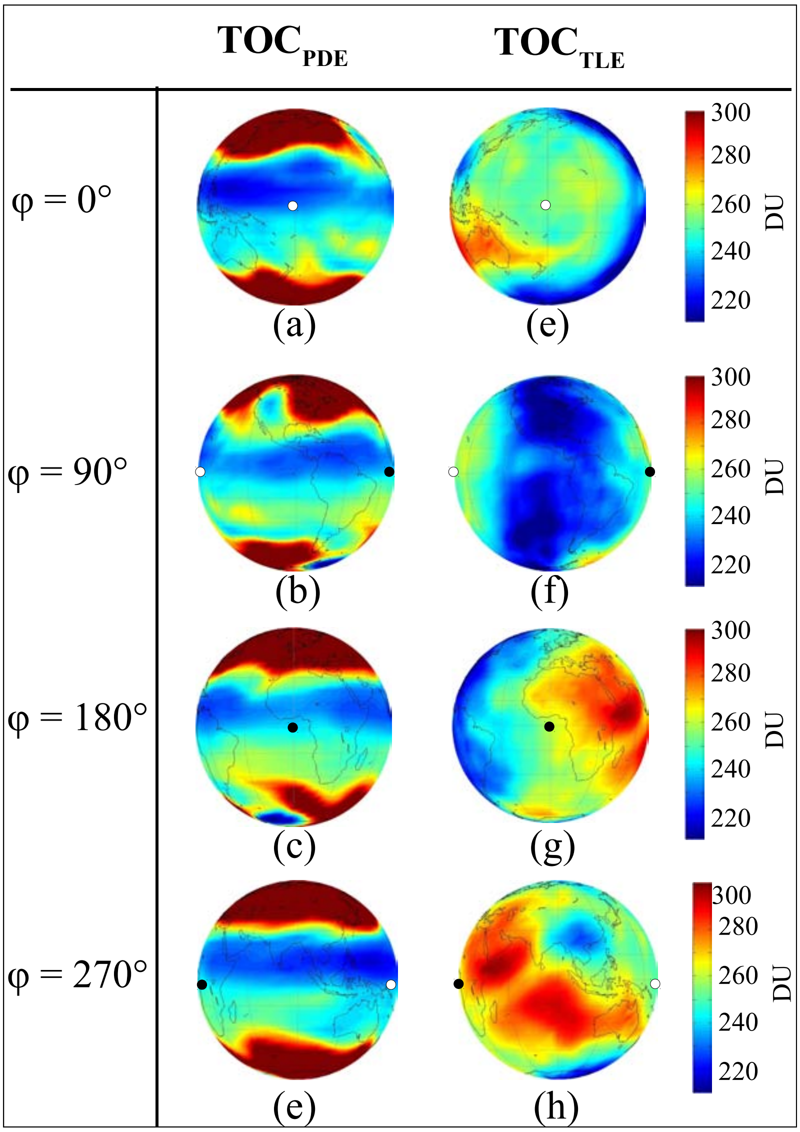

Figure 5.12: Comparative view of four different phases of the TOC_{PDE} **and** TOC_{TLE} (a) $\varphi = 0°$ of TOC_{PDE}, (b) $\varphi = 90°$ of TOC_{PDE}, (c) $\varphi = 180°$ of TOC_{PDE}, (d) $\varphi = 270°$ of TOC_{PDE}. (e) $\varphi = 0°$ of TOC_{TLE}, (f) $\varphi = 90°$ of TOC_{TLE}, (g) $\varphi = 180°$ of TOC_{TLE}, (h) $\varphi = 270°$ of TOC_{TLE}. The antisolar point is indicated with a white point. The subsolar point is indicated with a black point.

As can be seen in Figures 5.12a - 5.12d, the PDE_{TOC} displays high TOC values at extra-tropical latitudes and low TOC values at tropical latitudes. As a result, a distant observer would be unable to differentiate them, as the difference between the phases is relatively small. In the case of the TLE, on the other hand, the depletion or enhancement (depending on the observed phase) would be evident, as can be seen in Figures 5.12e - 5.12h.

In Table 5.4, the TLE and PDE differences between the TOC hemisphere mean in phase ϕ with respect to the TOC hemisphere mean in phase 0° ($\Delta TOC_{(TLE,TLE)}$ and $\Delta TOC_{(PDE,PDE)}$, respectively) are shown.

Table 5.4: Comparison of the TLE and PDE differences between the TOC hemisphere mean in phase ϕ with respect to the TOC hemisphere mean in phase 0° . The values were derived using equations 5.5, 5.6 and 5.7.

Phase φ	$\Delta TOC_{HM(PDE,TLE)}$ (DU)	$\Delta TOC_{HM(PDE,TLE)}$ (%)	$\Delta TOC_{HM(TLE,TLE)}$ (%)	$\Delta TOC_{HM(PDE,PDE)}$ (%)
0°	-56	23	0	0
90°	-51	22	2.2	3.5
180°	-39	16	-3.8	2.7
270°	-13	12	-8.1	1.4

The $TOC_{TLE(90°)}$ is depleted compared to the $TOC_{TLE(270°)}$ and is characterised by low O_3 columns, with the depleted region coinciding with the TLE dusk region (Figure 5.12f). The $TOC_{TLE(180°)}$ (Figure 5.12g) is enhanced compared to the $TOC_{TLE(0°)}$ (Figure 5.12e). High O_3 concentrations are present between the antisolar point and subsolar point. Low concentrations are present towards the North-West part of the hemisphere. The TOC_{PDE} hemisphere mean ($TOC_{HM(PDE)}$) and TOC_{TLE} hemisphere mean ($TOC_{HM(TLE)}$) values can be seen in Table 5.5. A comparison shows that the TOC_{TLE} is depleted compared to the TOC_{PDE} regardless of the hemisphere observed.

Table 5.5: Comparison of $TOC_{HM(PDE)}$ and $TOC_{HM(TLE)}$ for different phases of the planet

Phase φ	TOC_{PDE} (DU)	TOC_{TLE} (DU)
0°	295	239
90°	285	234
180°	287	249
270°	291	260

Therefore, the TOC_{TLE} distribution will change depending on the observed phase. The TOC_{TLE} phases decrease by a maximum of 23% compared to the TOC_{PDE}. The difference between the four TLE phases is ±5.15 %. A planet's spectral ozone signature is derived from the planet's TOC. It also depends on the planet's temperature structure and distribution, its vertical ozone profile, the line of sight towards the observer and other factors. Therefore, 23% ± 5.15% is the uppermost limit for the differences between the PDE and TLE spectral signatures.

Selsis (2000), Segura et al. (2003), Segura et al. (2005), Rugheimer et al. (2013), Rauer et al. (2011) and Grenfell et al. (2007) predicted that the observed spectra of exoplanets orbiting F, G, K and M stars would possess a visible ozone spectral signature, using 1D models. The strength of the signature would vary depending on the star's UV radiation emission as well as the planet's molecular oxygen content. Selsis (2000) determined that an Earth-like planet orbiting a K2 star would have a visible spectral signature, while an Earth-like planet orbiting an F9 star would not have a distinguishable ozone spectral signature. Segura et al. (2003) determined that the ozone 9.6 μm spectral line would be visible if the planet's O_2 concentration was at least 10^{-3} PAL. Segura et al. (2005) found that the ozone 9.6 μm spectral line of an Earth-like planet orbiting an M star would be similar to that of the present day Earth's. Grenfell et al. (2007) showed that the ozone concentration of an Earth-like planet orbiting a G2V, a F2V, and a K2V star, respectively would increase as the planet moves further away from the parent star. Rugheimer et al. (2013) determined that an increase in either the parent star's UV radiation or its temperature would result in increased O_3 concentrations and stronger O_3 spectral features. Rauer et al. (2011) predicted planets orbiting quiet M0 to M3 dwarfs would have stronger ozone emission spectra compared to the emission spectrum of the present day Earth, while planets orbiting very cool and quiet M4 to M7 stars would have weaker ozone emission spectral.

Our study indicates that a tidally locked Earth-like planet will have a visible ozone signature and the tidal lock will result in a 19.3 % decrease of the total ozone content global mean compared to the present day Earth. Furthermore, the total ozone content will vary $\pm$ 5.15% depending on which phase of the planet is visible.

The observational measurement errors of exoplanets currently range between 10 - 30% (Burrows, 2014). Therefore, the spectral change calculated in this study will not be critical for current exoplanet observations. However, when bigger telescopes are built and improved observational and data analysis techniques are developed, the differences in the TOC of a tidally locked Earth-like exoplanets will be detectable.

Therefore, we conclude that the middle atmosphere of a tidally-locked Earth-like exoplanet can be simulated using the realistic, high-resolution, 3D chemistry-climate model (CESM1(WACCM)) and that the planet's middle atmosphere achieves a steady state within 80 days.

The study reveals that the 3D ozone distribution of a tidally locked Earth-like planet orbiting a Sun-like star greatly differs from that of the present day Earth due to the reduced Coriolis force, the break down of the Brewer-Dobson circulation and the stationary nature of the subsolar point. The breakdown of the Brewer-Dobson circulation results in the generation of an upwelling centred over the day side and a downwelling centred over the night side, extending from the surface to the mesosphere. Furthermore, the horizontal middle atmospheric circulation is greatly altered, especially in the mesosphere.

As a result of the changes in photochemistry and dynamics, the day side primary ozone layer is enhanced, while the night side primary ozone layer is depleted compared to its PDE equivalent. The night side secondary ozone layer is enhanced for the TLE compared to the PDE, while the day side remains relatively unchanged. The tertiary ozone layer disappears. The global mean TOC_{TLE} is reduced by 19.3 % compared to the TOC_{PDE} and the $TOC_{HM(TLE)}$ is reduced by a maximum of 23 % compared to its PDE equivalent. Furthermore, the $TOC_{HM(TLE)}$ will vary be $\pm$ 5.15% depending on which phase of the planet is visible to the observer. Since our current observations have ≈ 30 % error margin, it is not possible to detect the differences between the PDE and the TLE with our current technology. Therefore, the observations will not be affected.

Finally, it is important to emphasise that this is the first study investigating the effects of the tidal lock on a tidally locked Earth-like planet using a realistic, high-resolution, 3D chemistry-climate model.

6 The middle atmospheric circulation of a tidally locked Earth-like planet and the role of the sea surface temperature

6.1 Research strategy

This study is an extension of the paper presented in Chapter 5 and aims to investigate the influence of the sea-surface temperature (SST) on the circulation and ozone distribution of a tidally-locked Earth-like planet orbiting a Sun-like star. The subject is of great interest, as it will determine the level of SST accuracy needed in future simulations of observed exoplanets.

On Earth, the influence of the sea-surface temperature on the tropospheric and lower stratospheric temperature and dynamics has been investigated by several researchers.

Braesicke and Pyle (2004) used the Met Office Unified Model with simple stratospheric chemistry to investigate the dynamics and ozone sensitivity to different SSTs. They performed a set of multi-annual simulations, each lasting 20 years. Each simulation had a different prescribed SST and the same simplified ozone chemistry. They reported that the appearance of extreme events in the northern hemisphere winter stratosphere had a stronger correlation with the underlying SSTs than with changes in the ozone.

Rosenlof and George (2008) investigated the long-term tropical lower stratospheric temperature trends over the western Tropical Pacific Ocean, in relation to variations in the SST, using data from the NOAA/CIRES Climate Diagnostics Center. They reported the discovery of an anticorrelation between stratospheric temperature anomalies and SST anomalies and proposed that a fairly direct influence between the underlying ocean and the lower tropical stratosphere exists. Furthermore, they speculated that the anticorrelation appears due to the increased deep tropospheric convection generated by an SST warming.

The presence of a lower stratospheric cooling as a result of higher tropical SSTs was reported by Deckert and Dameris (2008). They investigated the change in the strength of the tropical upwelling in two different simulations. Both simulations had the same concentrations of ozone-depleting substances but different SSTs and greenhouse gas concentrations. Deckert and Dameris (2008) reported the presence of amplified deep convection due to higher SSTs. The generated waves reached the low-latitude upper troposphere and lower stratosphere, bringing ozone-poor tropospheric air into the lower stratosphere, lowering the ozone concentration as a result.

Hegyi et al. (2014) investigated the initial transient response of the boreal winter stratospheric polar vortex to localised sea-surface warming events. To that end, they conducted 20 perpetual winter simulations using the CESM1(WACCM). They reported a weakening of the polar vortex due to changes in the eddy-driven mean meridional circulation and the presence of negative anomalies in the eddy momentum flux convergence. They further showed that the initial state and subsequent internal variation of the extratropical atmosphere is as important as the type of SST forcing in determining the response of the stratospheric polar vortex. Furthermore, the interactions between the internal variability of the vortex and the SST-driven wave anomalies determine the nature of the response of the polar vortex to the forcing.

For non-Earth planets, on the other hand, only one such study has been performed by Chen et al. (2010). They studied the tropospheric winds and stratospheric Brewer-Dobson circulation sensitivities to SST warmings using an Earth aquaplanet general circulation model. However, the study aimed to investigate the relationship between a warming ocean due to global warming and a change in the Earth's large-scale atmospheric circulation rather than an actual exoplanet. They investigated the relationship between the zonal mean tropospheric and lower stratospheric circulation, and different SST warming patterns. They reported that the location and sign of the SST perturbations gradient strongly affects the tropospheric jet and the Hadley cell. The Brewer-Dobson circulation increased when low latitude warming was present. For high latitude warmings, the Brewer-Dobson circulation decreased when the warming extended to the subtropics.

To our knowledge, no study investigating the correlation between the SST and the middle stratosphere and mesosphere exists for either the Earth or exoplanets. The sensitivity of the mesospheric conditions to SST variations is also important for the observations of other spectral signatures, like atomic oxygen and hydroxyl, whose spectral signatures will be affected by altered temperatures and/or circulation patterns.

In this study, the effects of two extreme SST cases on the middle atmospheric circulation and ozone distribution of a tidally locked Earth-like planet (TLE) are investigated. Two 90-day simulations are performed using two different SSTs. The SST of the first simulations is similar to that of the present day Earth, which is characterised by temperatures of 290 - 300 K in the tropics and 270 - 280 K in the polar regions. On account of the overall warm SST, the simulation using it will be henceforth called Warm TLE (WTLE). We emphasize that this SST distribution is correct only for the fast rotating Earth and is used only in an attempt to force an extreme SST. The SST of the second simulations is similar to the SST reported by Merlis and Schneider (2010), who used an ideal gas GCM with an active hydrological cycle, a gray radiation scheme and a slab ocean lower boundary condition to simulate a tidally locked aquaplanet with the size, mass and atmospheric composition of the present day Earth and a rotation period equal to one Earth year. The SST generated by their study was characterised by a uniform night side SST temperatures of ≈ 250 K and a monotonically and isotropically increasing day side SST which reaches a maximum ≈ 300 K in the regions surrounding the subsolar point. On account of the overall cooler SST, the simulation using it will henceforth be called Cold TLE (CTLE). Both SSTs can be seen in Figure 6.1.

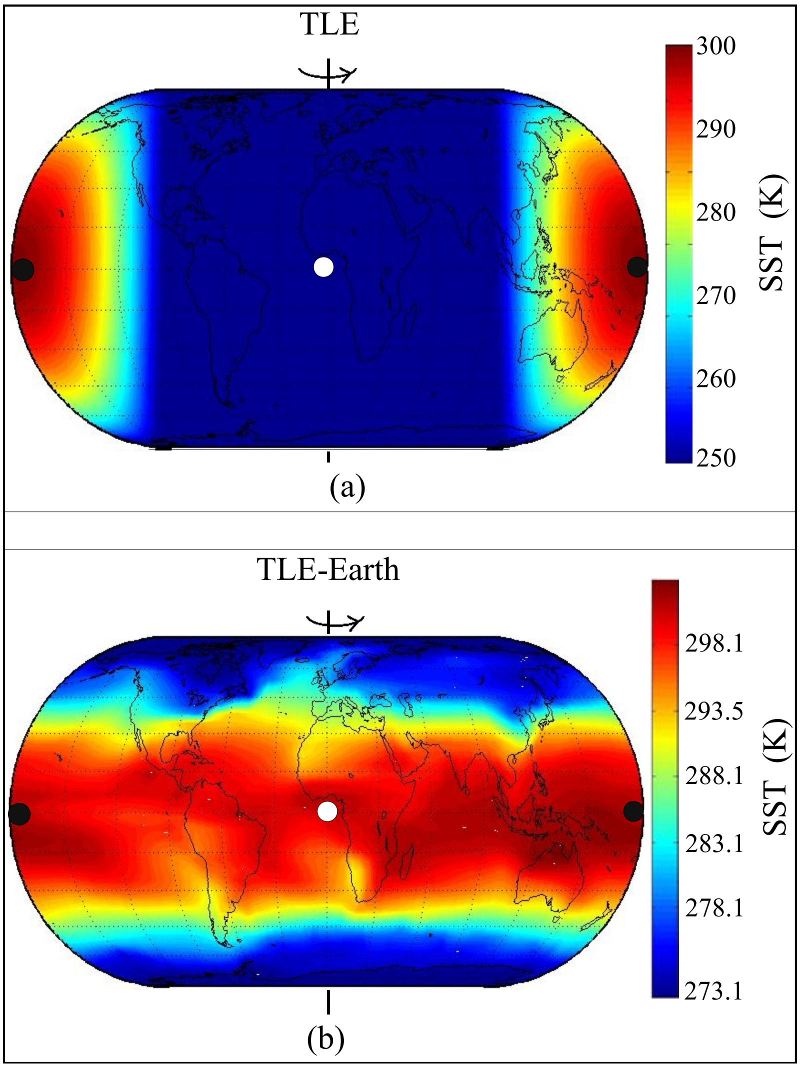

Figure 6.1: CTLE and WTLE Sea Surface Temperature setups. (a) CTLE: Shades of red indicate high temperatures and define the day side of the planet. Shades of blue indicate low temperature and define the night side of the planet (b) WTLE: Shades of red indicate high temperatures. Shades of blue indicate low temperature. The subsolar point is indicated with a white point on either side of the figure. The antisolar point is indicated with a magenta point in the center of the figure for both simulations.

Both simulations have the same planet-star distance, eccentricity, stellar irradiance at the top of the model, rotation rate and subsolar point location. Specifically, the planet-star distance is set to 1 AU, the eccentricity to $0 < e < 1$ and the stellar irradiance at the top of the model to $1366.96 < \mathrm{S_o} < 1368.60$. The rotation rate is set to $1/365^{\mathrm{th}}$ of the Earth's rotation rate. The subsolar point is permanently located over the Pacific ocean at (0.17° N, -178.17° E), which is the position of the Earth's subsolar point at 00:00 UT on the day of the Spring Equinox (21.03.2000).

To achieve the tidal lock the following model parameters are changed:

- the number of seconds in a siderial day is altered from 86164 seconds/day to $3.15 \cdot 10^7$ seconds/day
- the planet's rotational velocity is set to $2.31 \cdot 10^{-12}$ rad/s
- the planet's new rotation rate is 1° every 87600 seconds (the Earth rotation rate is 1° every 240 seconds)
- the position of the subsolar point is set to the subsolar point at 00:00 UT on the Spring Equinox (0.17° N, -178.17° E) for the duration of the simulation
- the Sea Surface Temperature (SST) is changed to resemble the SST reported by Merlis and Schneider (2010)
- The solar zenith angle (SZA) is set to a constant value by means of the present day Earth (PDE) Julian date.

The SZA is the main parameter used for the assessment of the incoming solar radiation in the CESM model world. Setting the Julian date to a constant value stops the periodic 24-hour variation of the SZA at all grid points. Through the implemented changes, a perpetual equinox is achieved. The shortwave solar radiation flux at the top of the model for the WTLE and CTLE simulations is shown in Figure 6.2. The solar point is depicted by a white dot on either side of the figure, while the anti-solar point is depicted by a magenta point in the centre of the figure.

The CESM1(WACCM) requires the presence of an active land model. Therefore, the general topography and continents of the Earth are maintained. The atmospheric and surface initialization data are identical for both the CTLE and the WTLE runs and both simulations start with same 3D ozone and wind field.

The ozone volume mixing ratio (O_3 VMR), total ozone content ($TOC = \int_5^{110}[\mathrm{O_3}]\mathrm{dz}$), vertical wind Ω, the zonal and meridional wind (U, V), the horizontal wind (HW) and the atmospheric temperature (T) are calculated between 5 km and 110 km altitude to avoid the data gaps generated by the presence of several high mountains and mountain ranges (e.g Himalayas, Kilimanjaro) and the air density data gaps above 110 km altitude.

In the next subsection, the middle atmospheric circulation (Ω, U, HW), temperature (T) and ozone distribution (TOC, O_3 VMR) of the two simulations are presented and the degree by which they are influenced by the two extreme SSTs is discussed. First, the atmospheric adjustment time of the two tidally locked Earths (TLEs) is discussed and compared to that of the present day Earth. Then, their atmospheric circulation is presented. Next, the T global average is presented and discussed. Lastly, their latitude-longitude O_3VMR cross section is presented. The TOC, O_3VMR, HW and T global means are determined by calculating their zonal means as a function of latitude and then weighting them with the surface area of the latitude belts (surface area preserving mean). The change in % between the CTLE and WTLE parameters is calculated using the following equation:

$$\Delta = \frac{parameter_{CTLE} - parameter_{WTLE}}{parameter_{WTLE}} * 100 \tag{6.1}$$

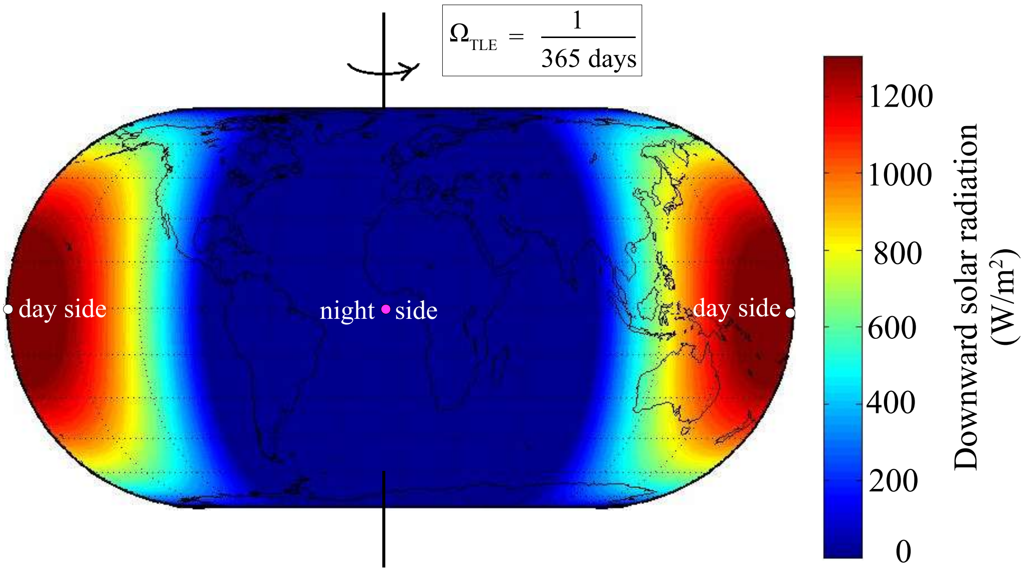

Figure 6.2: Incident shortwave radiation at the top of the model for both the CTLE and the WTLE Shades of red indicate high incoming solar radiation and define the day side of the planet. Shades of blue indicate low incoming solar radiation. The dark blue visible in the center of the plot indicates a lack of incoming solar radiation and defines the night side of the planet. The subsolar point is indicated with a white point on either side of the figure. It is centred approximately at (0°, 180°) over the Pacific Ocean. The antisolar point is indicated with a magenta point in the center of the figure and is centred approximately at (0°,0°).

The term *parameter* is used to refer to any of the TOC, O_3 VMR,U, HW and T.

The day and night side means (DSM and NSM, respectively) change is calculated using the following equations:

$$\Delta parameter_{DSM(CTLE,WTLE)} = \frac{parameter_{DSM(CTLE)} - parameter_{DSM(WTLE)}}{parameter_{DSM(WTLE)}} \tag{6.2}$$

$$\Delta parameter_{NSM(CTLE,WTLE)} = \frac{parameter_{NSM(CTLE)} - parameter_{NSM(WTLE)}}{parameter_{NSM(WTLE)}} \tag{6.3}$$

6.2 Results

The CESM1(WACCM) simulation described in Section 6.1 allows us to perform a sensitivity study and determine the influence of the SST on the middle atmospheric circulation and ozone distribution of a tidally locked planet.

The study reveals that the CTLE and WTLE middle atmosphere adjusts to the new radiative and dynamical conditions within 80 days. The adjustment times of the CTLE and WTLE total ozone column (TOC), global mean stratospheric horizontal wind (HW), global mean stratospheric vertical wind (Ω) and global mean stratospheric temperature (T) for the 30 - 40 km altitude range are shown in Figure 6.3. The temporal evolutions of the PDE TOC, HW, Ω and T are also shown for comparison.

As can be seen in Figures 6.3a, 6.3b and 6.3c, the CTLE and the WTLE TOC, HW and Ω adjustment times and values are not significantly altered by the SST change. The % change in their adjustment times can be seen in Table 6.1. The CTLE and WTLE T is visible in Figure 6.3d. Their adjustment times are also similar despite their altered slope. However, the CTLE values are decreased compared to the WTLE. This difference is also visible in the CTLE and WTLE T global average which will be presented later.

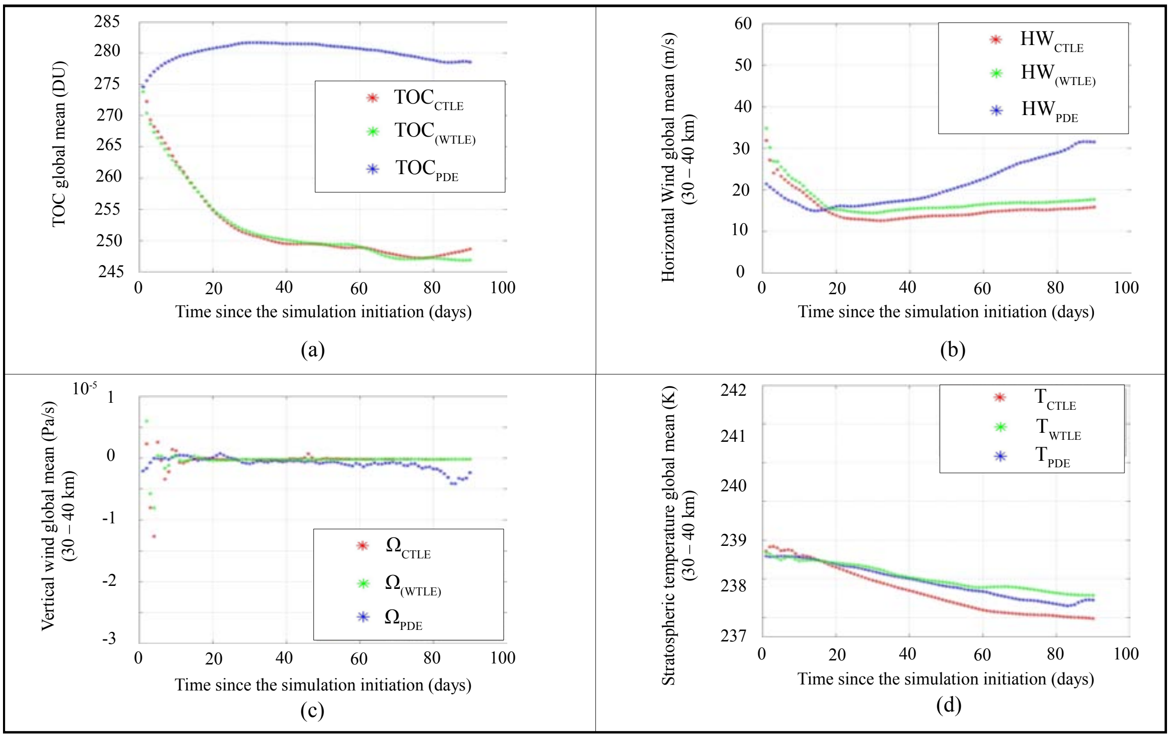

Figure 6.3: CTLE, WTLE and PDE atmospheric temporal evolution (a) the TOC, (b) the HW, (c) the Ω and (d) the T, respectively. The CTLE and WTLE TOC, HW, and T are exponentially decaying to their steady-state value with an e-folding time of 30, 20 and 40 days, respectively. The CTLE and WTLE vertical winds are exponentially increasing to their steady-state value with an e-folding time of 15 days.

The CTLE and WTLE e-folding times of the TOC, HW, Ω and T are, respectively, 30, 20, 15 and 40 days, and can be seen, along with their PDE equivalents and standard deviations (σ), in Table 6.1. Therefore, their adjustment times are 60, 40, 30 and 80 days, respectively. A comparison between the CTLE, the WTLE and the PDE σ reveals that the PDE has higher standard deviations (σ_{PDE}) compared to the CTLE and WTLE standard deviations (σ_{CTLE} and σ_{WTLE}), as can be seen in Table 6.1.

Table 6.1: Comparison of the PDE, CTLE and WTLE TOC, HW, Ω and T e-folding times, steady-state mean values and their standard deviations on day 90.

	PDE	σ_{PDE}	CTLE	σ_{CTLE}	WTLE	σ_{WTLE}
TOC (DU)	280.1	1.44	248.7	1.00	248.64	1.42
HW (m/s)	21.19	5.21	14.21	1.00	16.10	2.22
Ω (Pa/s)	$-8.6 \cdot 10^{-7}$	$9.6 \cdot 10^{-7}$	$-1.7 \cdot 10^{-7}$	$1.3 \cdot 10^{-7}$	$-2.0 \cdot 10^{-7}$	$-9.7 \cdot 10^{-8}$
T_{strat} (K)	239.9	0.85	238.4	0.43	239.6	0.27

The tidal lock results in a breakdown of the Brewer-Dobson circulation (Figure 2.3) in both the CTLE and the WTLE and is replaced by a different atmospheric circulation (Figures 6.4, 6.5, 6.6, 6.7), though the atmospheric structure is still comprised of a troposphere, a stratosphere and a mesosphere. The description of the atmospheric circulation of the two simulations is presented below.

We begin with the vertical wind. The CTLE and WTLE vertical wind is shown in Figures 6.4 and 6.5, respectively.

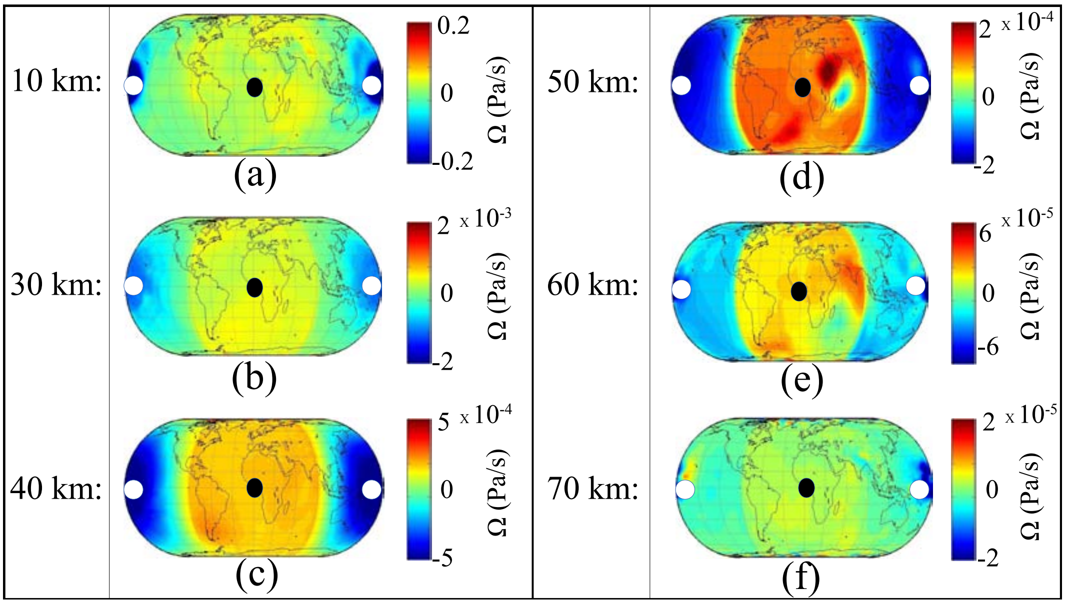

Figure 6.4: CTLE Longitude-Latitude Vertical wind circulation (a) Vertical wind at 10 km, (b) Vertical wind at 30 km, (c) Vertical wind at 40 km, (d) Vertical wind at 50 km, (e) Vertical wind at 60 km, (f) Vertical wind at 70 km. Warm colours (positive values) indicate a downwelling wind. Cold colours (negative values) indicate an upwelling wind. Each figure is centred on the antisolar point which is indicated with a black dot. The subsolar point is indicated with a white dot on either side of each figure.

A comparison between the two figures reveals that both simulations are characterised by an upwelling over the day side and a downwelling over the night side. In both simulations, the day side upwelling is generated by the upwards movement of air, which is radiatively heated by the constant shortwave radiation flux it receives.

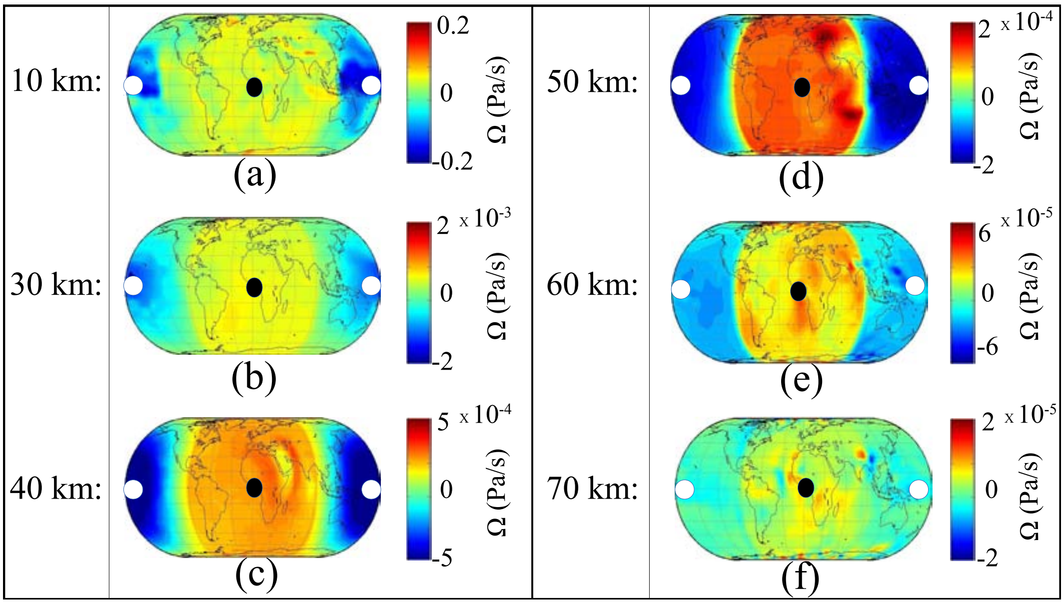

Figure 6.5: WTLE Longitude-Latitude Vertical wind circulation (a) Vertical wind at 10 km, (b) Vertical wind at 30 km, (c) Vertical wind at 40 km, (d) Vertical wind at 50 km, (e) Vertical wind at 60 km, (f) Vertical wind at 70 km. Warm colours (positive values) indicate a downwelling wind. Cold colours (negative values) indicate an upwelling wind. Each figure is centred on the antisolar point which is indicated with a black dot. The subsolar point is indicated with a white dot on either side of each figure.

The night side air, on the other hand, is radiatively cooled as a result of receiving no solar radiation and, therefore, sinks towards the surface of the planet. This result is in agreement with the results of Merlis and Schneider (2010), who reported the presence of a tropospheric dayside upwelling and night side downwelling in their tidally locked Earth-like 3D aquaplanet simulation. Our simulations show that this upwelling and downwelling behaviour also occurs in the stratospheres and mesospheres of tidally locked planets, whose heating and cooling processes differ from those of the troposphere and surface.

A comparison between Figures 6.4 and 6.5 reveals that the vertical winds of the two simulations are characterised by different small-scale variability at lower tropospheric and mesospheric altitudes as a result of the presence of vortices and jets of different magnitudes and locations. Furthermore, WTLE is characterised by a greater small-scale variability than the CTLE. We can, therefore, conclude that the SST change has only a limited effect on the vertical wind.

The CTLE and WTLE horizontal wind at 24 km, 36 km and 60 altitude can be seen in Figures 6.6 and 6.7, respectively. The lower stratospheric CTLE horizontal wind at 24 km can be seen in Figure 6.6a, while the lower stratospheric WTLE horizontal wind at 24 km can be seen in Figure 6.7a. In both simulations, the horizontal wind is characterised by the formation of a global eastward zonal jet stream.

The CTLE and WTLE stratospheric horizontal wind at 36 km is shown in Figures 6.6b and 6.7b. In both simulations, the horizontal wind is characterised by the

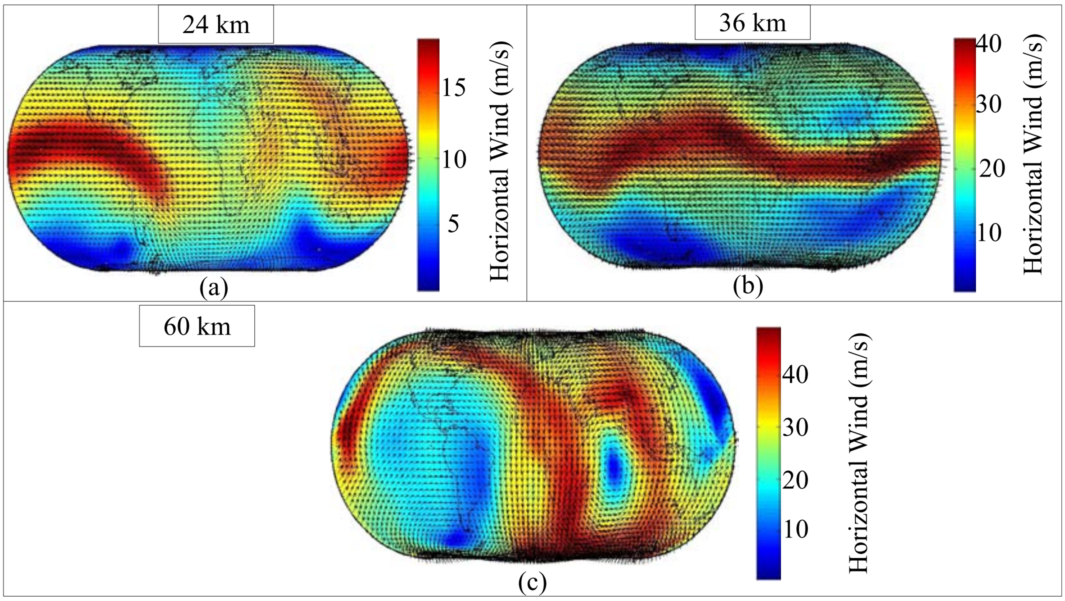

Figure 6.6: CTLE Horizontal circulation at select altitudes (a) Horizontal wind at 24 km, (b) Horizontal wind at 36 km, (c) Horizontal wind at 60 km. The black arrows indicate the wind vector while the color shading shows the wind speed.

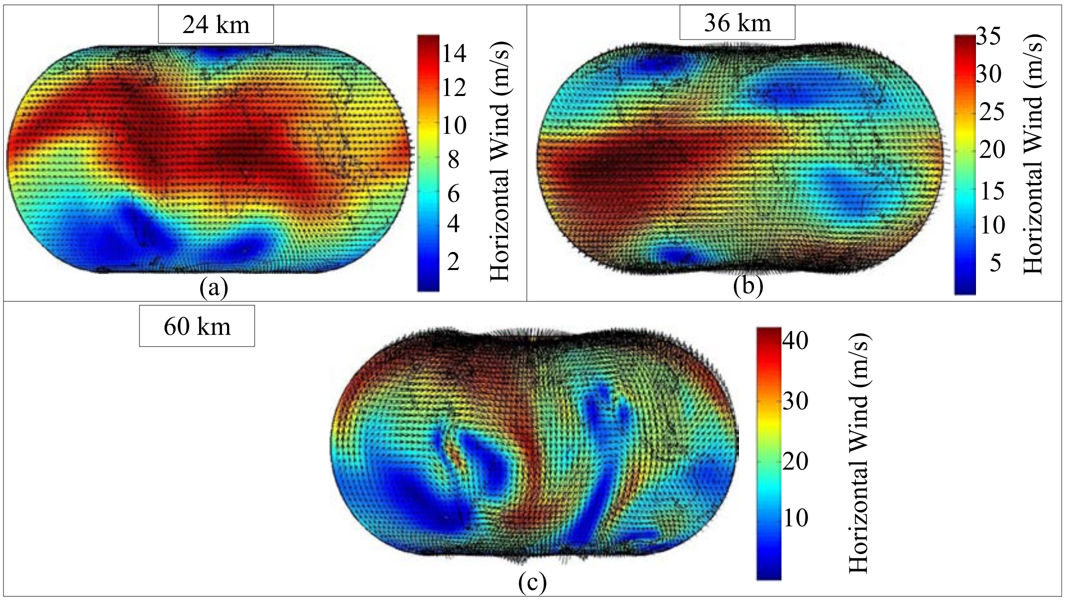

Figure 6.7: WTLE Horizontal circulation at select altitudes (a) Horizontal wind at 24 km, (b) Horizontal wind at 36 km, (c) Horizontal wind at 60 km. The black arrows indicate the wind vector while the color shading shows the wind speed.

presence of a westward global zonal jet stream with an accompanying vortex located at polar latitudes. The vortex can be seen on the left hand side of the Southern and Northern Hemispheres in Figures 6.6b and 6.7b. The blue coloured regions on the right hand side of the Southern and Northern hemispheres, on the other hand, are regions of low *HW* speeds. Similar to the 24 km circulation, the WTLE *HW* is slightly weaker and characterised by a wider jet stream compared to the CTLE *HW*.

The picture changes at mesospheric altitudes. At 60 km, the zonal jet stream is replaced by large-scale vortices in both the CTLE and the WTLE, whose locations differ. This phenomenon may be explained through the mesospheric wave-breaking mechanism. According to Nappo (2013), gravity waves are generated by tropospheric convection followed by the release of latent heat. The gravity waves then propagate upwards and break in the mesosphere, depositing their energy and decelerating the wind flow. Due to the different SST heat distributions, the convectively induced gravity waves are generated at different locations and have different energy budgets. As a result, their mesospheric wave breaking results in different energy distributions across the globe and, therefore, into the different *HW* wind circulations. Gravity waves are also generated through interaction between the planet's surface orography and the lower tropospheric wind field. When the lower tropospheric winds encounter a hill, mountain or mountain range, they are forced upwards. This vertical displacement of the stably stratified flow results in the generation of gravity waves, which transport energy and mean-flow momentum towards the middle and upper atmosphere where it is deposited Nappo (2013). While the two simulations have the same orography, their lower tropospheric horizontal wind distributions differ by 1.4 m/s on average. This results in a different terrain-generated gravity wave distribution and, therefore, a different energy deposition and wind deceleration pattern in the mesosphere, where the wave-breaking occurs. Therefore, the reported changes in the mesospheric horizontal wind are consistent with the mesospheric wave-breaking of convectively and orographically generated gravity waves.

The mesospheric circulation is more sensitive to the underlying SST compared to the stratospheric circulation, as is made evident by the regional differences in the vertical and horizontal wind maps. The discrepancy between the stratospheric and mesospheric circulation can be explained by the fact that the stratospheric dynamics are mainly driven by the insolation of stratospheric ozone.

The temperature structure of the CTLE and WTLE atmospheres is shown in Figure 6.8a. As mentioned above, both simulations possess a troposphere, a stratosphere and a mesosphere. As can be seen in Figure 6.8, the WTLE's lower troposphere ($z<3$ km) is characterised by warmer temperatures compared to the CTLE equivalent by a factor of 3.7 K on average. This temperature difference is generated by the increased upwelling longwave radiation, sensible heat and latent heat, by the warmer underlying WTLE SST.

In the region (between 10 km and 16 km), the WTLE temperature is cooler by 4 K on average compared to the CTLE, as can be seen in the purple highlighted region of Figure 6.8b. The cooling is adiabatic in nature and generated by the increased upwelling due to the warmer WTLE SST. This result is in agreement with the studies performed by Rosenlof and George (2008), Braesicke and Pyle (2004), Deckert and Dameris (2008), who reported the generation of a upper tropospheric cooling by an SST warming.

At stratospheric altitudes, between 18 km and 30 km, ozone absorbs the increased upwelling longwave radiation emitted from the warm WTLE SST and radiatively heats the WTLE stratosphere by 3.8 K on average. The WTLE stratospheric warming

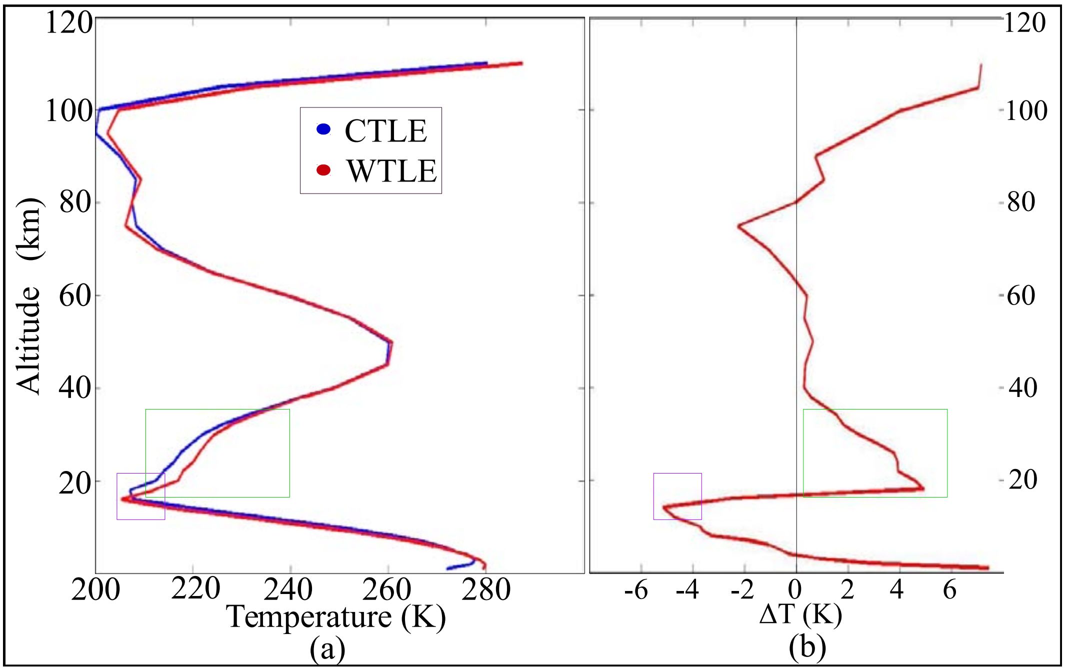

Figure 6.8: CTLE and WTLE temperature global average on day 90 The CTLE temperature is depicted using the blue colour line. The WTLE is depicted using the red colour line. The altitude range is 0 - 120 km.

can be seen in the green highlighted region of Figure 6.8b. This is in agreement with expectations of radiative coupling between the surface infrared emission and the lower stratosphere.

This effect can also be seen in Figures 6.9 and 6.11. Figure 6.9 shows the scatter plot between the ΔT at 1 km (ΔT_{1km}) and the ΔT at 24 km altitude (ΔT_{24km}). Figure 6.11 shows the degree of correlation between the ΔSST and ΔT_{24km}. $\Delta T_{altitude}$ and ΔSST are calculated using equations 6.4 and 6.5.

$$\Delta T_{altitude} = T_{WTLE} - T_{CTLE} \tag{6.4}$$

gives the difference between the WTLE and the CTLE temperatures at a given altitude and geographic location, while

$$\Delta SST = SST_{WTLE} - SST_{CTLE} \tag{6.5}$$

gives the difference between the WTLE SST and the CTLE SST at a given geographic location.

As can be seen in Figure 6.9, a linear correlation exists between the ΔSST and ΔT_{24km}, which suggests that SST changes have a direct radiative effect on the lower stratospheric temperature. Using the least squares method, we determine that the relationship between the ΔT_{1km} and the ΔT_{24km} is given by

$$\Delta T_{24km}(\Delta SST) = (0.006 \pm 0.0009)\Delta SST + 3.78 \pm 0.027 \tag{6.6}$$

Therefore, a 30 K change of the SST corresponds to a 0.18 K change of the lower stratospheric temperature. The inclination of the regression line is rather small.

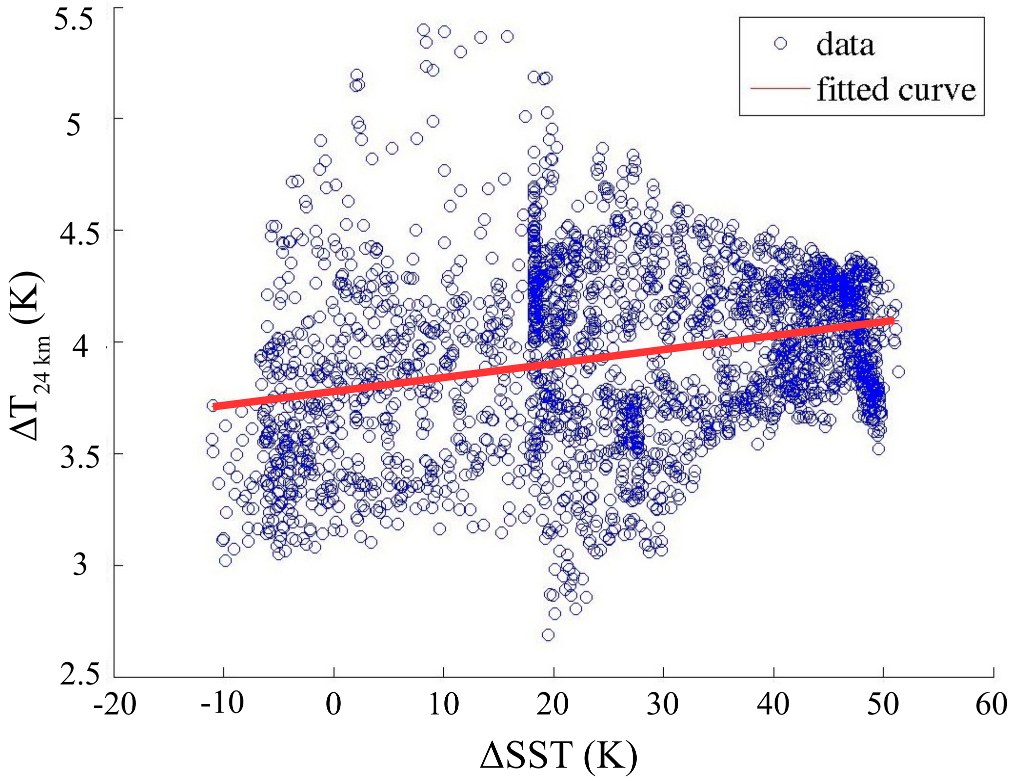

Figure 6.9: Scatter plot of ΔSST and ΔT_{24km} The plot shows the correlation between the surface ΔSST and the ΔT at 24 km altitude, together with a linear regression to the data.

This may be due to the strong mixing and quasi-isothermal behaviour of the lower stratosphere of tidally locked Earth-like planets.

A linear correlation also exists between the ΔSST and ΔT_{1km}, as can be seen in Figure 6.10. The figure suggests that SST changes have a direct radiative effect on the lower tropospheric temperature. Using the least square method, we determine that the correlation between the ΔSST and the ΔT_{1km} is given by

$$\Delta T_{24km}(\Delta SST) = (0.028 \pm 0.014)\Delta SST + 0.9 \pm 0.43 \tag{6.7}$$

Therefore, a 30 K change of the SST corresponds to a 8.6 K of the lower stratospheric temperature, which is 48 times the change generated at 24 km altitude.

A linear correlation also exists between the ΔT_{1km} and ΔT_{24km}. This indicates that the SST variation generates the temperature changes in both the lower troposphere and lower stratosphere. Using the least square method, we determine that correlation between the ΔT_{1km} and the ΔT_{24km} is given by

$$\Delta T_{24km}(\Delta T_{1km}) = (0.01 \pm 0.0019)\Delta T_{1km} + 3.8 \pm 0.022 \tag{6.8}$$

Therefore, a 30 K change of the lower tropospheric temperature corresponds to a 0.3 K of the lower stratospheric temperature.

The above results indicate that the increased thermal radiation emitted by the WTLE's surface as well as its upwelling sensible and latent heat are absorbed by its

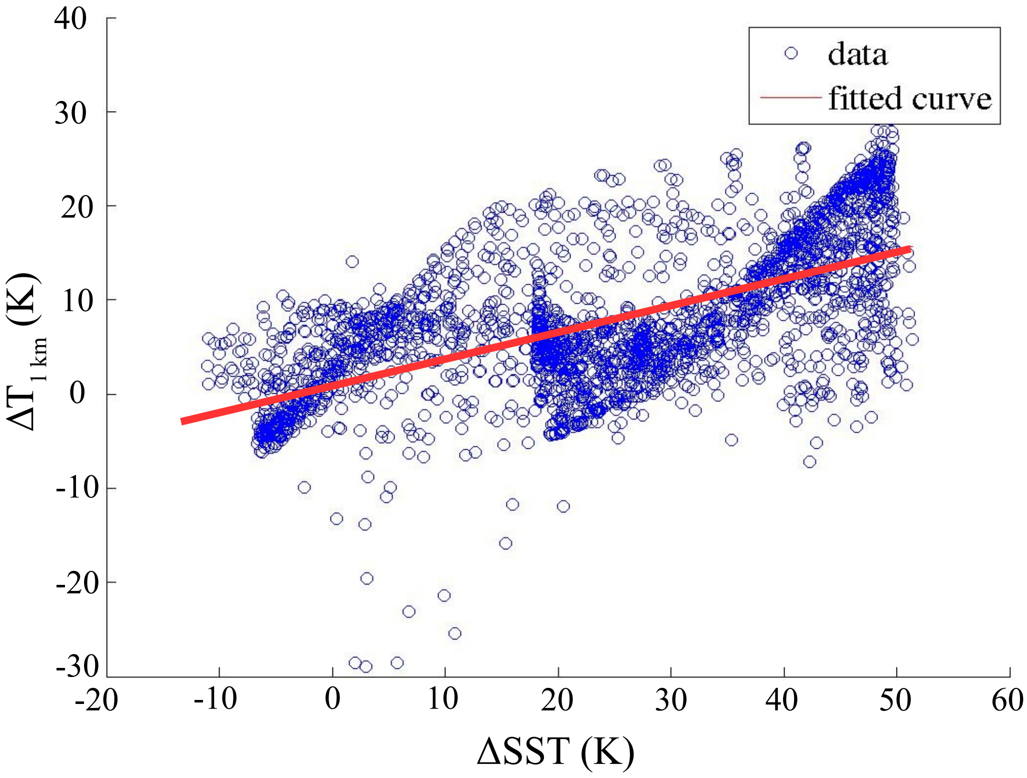

Figure 6.10: Scatter plot of ΔSST and ΔT_{1km} The plot shows the correlation between the surface ΔSST and the ΔT at 1 km altitude, together with a linear regression to the data.

lower tropospheric greenhouse gases increasing its temperature by 8.6 K for every 30 K SST change. The longwave radiation not absorbed by the lower troposphere reaches the lower stratosphere and is absorbed by the ozone 9.6 μm absorption band, a band expected to be present in the spectra of exoplanets able to maintain ozone layers. This leads to an increase in the stratospheric temperature of 0.1 K for every 30 K SST change. Therefore, a stronger absorption line could be expected for warmer SSTs.

In the lower mesosphere, on the other hand (70 km - 80 km), the WTLE temperature is lower by 1.13 K on average compared to the CTLE. The temperature difference can be explained through the mesospheric wave-breaking mechanism. The warm WTLE SST generates a higher number of gravity waves, which carry more energy compared to the CTLE as a result of the increased WTLE SST temperature. The wave momentum deposition occurring during the mesospheric wave breaking, leads to increased mesospheric upwelling and consequent adiabatic cooling.

In the upper mesosphere (90 km - 110 km), the WTLE temperature is higher by 4.3 K on average. Different gravity wave fluxes from below may induce this temperature difference by circulation changes, but the details of the underlying processes remain an open question.

Therefore, the biggest SST generated effect is present in the upper mesosphere rather than in the troposphere or stratosphere. Furthermore, the degree of the global

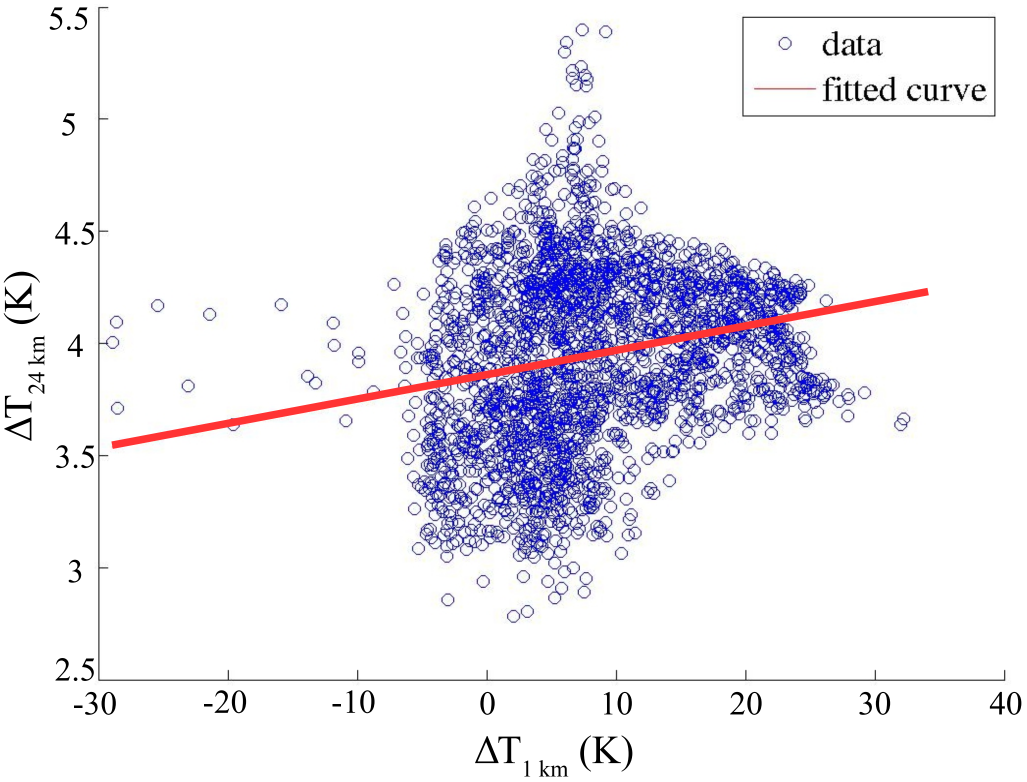

Figure 6.11: Scatter plot of ΔT_{1km} and ΔT_{24km} The plot shows the correlation between the ΔT at 1 km altitude and the ΔT at 24 km altitude, together with a linear regression to the data.

average temperature change in the middle atmosphere is much smaller than expected, both of which are unexpected results. Another interesting result is that increased SST leads to enhanced temperatures in the lower stratosphere of a tidally locked Earth-like exoplanet. Our analysis indicates that this lower stratospheric heating could be due to the enhanced upwelling of infrared radiation from the warm SST.

Next, we analyse the ozone distribution of the two simulations. The CTLE and WTLE day side and night side ozone volume mixing ratio O_3 VMR distribution can be seen in Figure 6.12. It depicts the cross section of the CTLE and WTLE O_3VMR distribution along the 1st and the 180th meridian, respectively.

A comparison between Figures 6.12b and 6.12d reveals that the SST change does not significantly affect the primary ozone layer (30 - 40 km altitude). The WTLE day side $O_3\text{VMR}_{(30-40)}$ decreases by 1.8% compared to the CTLE, while the night side $O_3\text{VMR}_{(30-40)}$ decreases by 1.27% due to the increased middle atmospheric temperature, visible in Figure 6.8.

The night time secondary ozone layer, located in both cases in the 85 - 110 km altitude range, is significantly affected. The WTLE $O_3\text{VMR}_{(85-110)}$ is enhanced by 40.5% compared to the CTLE. The mesospheric circulation changes, generated by the different upwelling gravity wave fluxes, could be responsible for the changes in the secondary ozone layer, but the details of the underlying processes remain an open question. We can, therefore, conclude that the use of an inaccurate SST in a tidally

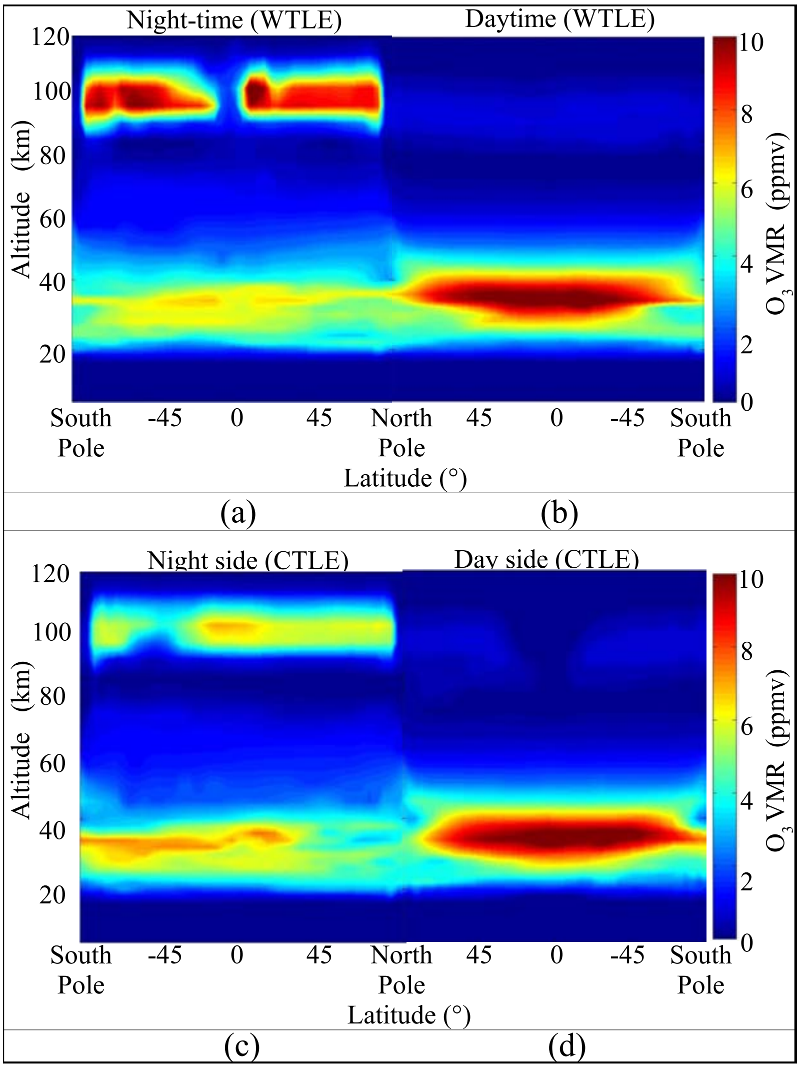

Figure 6.12: WTLE and CTLE Height-latitude cross section of O_3VMR along the meridian through the subsolar point and the antisolar point (a) Vertical cross section of the WTLE night-time hemisphere. (b) Vertical cross section of the WTLE daytime hemisphere. (c) Vertical cross section of the CTLE night side hemisphere. (d) Vertical cross section of the CTLE day side hemisphere.

locked Earth-like exoplanet may significantly affect the secondary ozone layer, while the primary ozone layer remains almost unaffected.

The gap visible over the WTLE equator at mesospheric altitudes in Figure 6.12a is a result of the local upwelling of ozone poor air from lower altitudes. This upwelling is localised in the regions close to the Atlas mountains and is possibly generated by upwelling gravity waves.

The sensitivity of a tidally locked Earth-like exoplanet atmosphere to its underlying SST was studied by simulating the atmospheric circulation, temperature and ozone distribution changes generated by the use of two extreme SSTs. One Earth-like SST and one tidally locked Earth-like aquaplanet SST were used.

Our results show that the lower tropospheric temperature global average is increased on average by 3.7 K in the WTLE compared to the CTLE due to the warmer WTLE SST. Due to the WTLE tropospheric warming, the hot air ascends and cools adiabatically, generating a cooling between 10 km and 16 km altitude, of the order of 4 K on average, compared to the CTLE. This result is in agreement with past studies of the effects of SST warmings on the Earth's upper troposphere. A stratospheric heating of 3.8 K on average, between 18 km and 30 km, is present in the WTLE compared to the CTLE, generated by the absorption of the upwelling longwave radiation by ozone through the 9.6 μm line. The enhanced, upwelling longwave radiation is generated by the warmer WTLE SST. The warmer WTLE SST also generates a lower mesospheric cooling of the order of 1.13 K on average due to increased wave generation and subsequent wave-breaking in the mesosphere. Lastly, an upper mesospheric warming of the order of 4.3 K on average is present in the WTLE compared to the CTLE. Its generation mechanism is currently an open question and under investigation.

The vertical and horizontal winds remain relatively insensitive to the underlying SST, but their small-scale structure is affected due to the presence of different horizontal circulations. The largest changes appear at mesospheric altitudes, possibly due to differences in the upwelling gravity wave flux. The dependence of atmospheric tides and planetary waves on the SST distributions could also play a role in the altered circulation.

The primary ozone layer is also not significantly affected by the SST change. The WTLE day side primary ozone layer decreases by 1.8%, while the night time primary ozone layer decreased by 1.27%. The WTLE secondary ozone layer, on the other hand, increased by 40.5%. The generation mechanism is currently an open question and under investigation.

7 Conclusions and Outlook

The aim of this thesis was to investigate how changes in the local and global radiative forcing of an Earth-like planet affected its atmospheric dynamics and ozone distribution using the realistic 3D coupled chemistry-climate model CESM1(WACCM). The model features photochemistry, wave-mean flow interactions and other processes from the surface to the thermosphere. Therefore, the atmospheric jets, circulation cells, solar tides, planetary waves, gravity waves, orography and tropical convection zones were all included in the simulations and allowed us to study the effects of the radiative forcing change under realistic conditions.

In the first study, the local radiative forcing change was implemented by changing the surface colour of a small area of the Eastern Sahara on the present day Earth. The surface colour change increased the absorbed downwelling shortwave radiation and, consequently, its surface temperature. The increased upwelling of sensible and latent heat, as well as longwave radiation, generated an upwards propagating convective perturbation over the region. The generated perturbation, in turn, induced an outwards propagating large-scale gravity wave at 2 km altitude. The wave had an amplitude $A > 5\sigma$, $\langle \lambda \rangle = 3000 \pm 500$ km, $\langle v \rangle = 200 \pm 50$ m/s and $\langle p \rangle = 4 \pm 1$ h. Seven hours after the start of the simulation, the wave reached the Amazon tropical convection zone and generated a secondary perturbation and an outgoing concentric, large-scale gravity wave. The latent heat released by the moist air of the convection zone could explain the strong amplitude of the secondary wave whose amplitude is equal to that of the primary wave. The secondary wave was characterised by $\langle \lambda \rangle = 2600 \pm 600$ km, $\langle v \rangle = 220 \pm 40$ m/s $\langle p \rangle = 3 \pm 1$ h.

The soil colour-induced temperature perturbation of the Eastern Sahara extended from the lower troposphere into the stratosphere and mesosphere. In the stratosphere, the initial generated perturbation was radiative in nature, while the mesospheric perturbation was probably related to upward atmospheric wave flux and circulation changes (teleconnections). In order to isolate the generated waves from the background waves, a small perturbation analysis was used. The method worked very well for the first day of the simulation. By the fifth day, however, the wave patterns were no longer visible. Instead, enhanced fluctuations were present at seemingly random locations all over the globe due to the divergence of the simulation from the control run, making the attribution of cause and effect difficult. Therefore, the small perturbation analysis can be used successfully only for the first two days of the simulations but has a high potential for the study of gravity wave generation, propagation and dissipation.

Our results indicated that the perturbation propagatesd outwards into the stratosphere and mesosphere. Therefore, further research should be devoted into analysing and interpreting how it effects the middle atmosphere and the wave modes of the upward propagating disturbances. Moreover, the small perturbation analysis we developed is a promising technique that can be used for the detailed study of the direct effect of the soil colour-induced long wave radiation perturbation on the stratosphere. The perturbation over the Amazon tropical convection zone was visible not only in the vertical wind field, but also in the atmospheric pressure and temperature fields. Therefore, it would be of interest to investigate how this generated perturbation will affect the rainfall and cloud formation in the region and, thereby, the underlying climate. For that, a higher resolution simulation will be needed, as the 4°x5° grid is too coarse.

In order to investigate the broader effects of a global rather than a local radiative forcing change, the global downwelling stellar radiation distribution was altered in the second study by tidally locking the planet. The radiative forcing was further altered by changing the prescribed sea-surface temperature to that of a tidally locked aquaplanet. Our study demonstrated that CESM1(WACCM) is suited for simulations of Earth-like exoplanets. The tidally locked Earth-like (TLE) planet's middle atmosphere adjusted to the new radiative forcing condition within approximately 80 days from the start of the simulation. The tidal lock altered both the atmospheric circulation and the ozone distribution of the planet and the Brewer-Dobson circulation was replaced by an upwelling on the day side and a downwelling on the night side. Furthermore, the reduction of the Coriolis force, as a result of the decreased rotation rate due to the tidal lock, contributed to the altered horizontal wind, with larger changes present in the mesosphere compared to the stratosphere.

The TLE ozone distribution was radically changed and the total ozone content was reduced by $\sim$ 19.3 % compared to the Earth (PDE). The TLE day and night side total ozone content means were reduced by 23.21 % and 15.52 %, respectively, compared to the PDE. The TLE middle stratospheric ozone accumulated on the day side of the planet leading to a day-night variation of 40 %. For comparison, the PDE's day-night variation is 2%. The TLE lower stratospheric ozone was mainly influenced by the altered circulation and characterised by enhanced night-side and depleted day-side regions. Its mesospheric ozone was similar to the PDE's mesospheric ozone distribution, with decreased ozone on the day side and enhanced ozone on the night side. For a distant observer of the planet, its was determined that the TLE's total ozone content would vary up to ± 5.15% during its revolution around its parent star. Since our current instruments and data analysis techniques have an error margin 1.5 times higher than the TOC change, observations of tidally locked planets should not be affected by the TOC change.

The study could be extended in the future by exchanging the solar spectrum with that of an M or K star, while maintaining an orbital distance that would maintain the top of the model solar irradiance at $S_0 = 1368.22$ W/m^2. This would simulate a tidally locked exoplanet orbiting an M or K star, around which a planet is more likely to become tidally locked. After such a study has been performed, a change of the incoming stellar radiation at the top of the atmosphere could also be included. This would allow the simulation of planets orbiting at varied distances from the parent star. A future study could also investigate the physical processes responsible for the disappearance of the tertiary ozone layer.

The last part of this thesis was devoted to investigating the effects of a different form of radiative forcing, namely a change in the planet's underlying sea-surface temperature (SST), which could impact the thermal structure, circulation and composition of the lower and middle atmosphere of a tidally locked Earth-like exoplanet. To that end, we simulated the atmospheric circulation and ozone distribution of a tidally locked Earth-like exoplanet, using two different underlying SSTs. The first SST was the tidally locked aquaplanet SST acquired from Merlis and Schneider (2010) and was characterised by a hot subsolar ocean and a frozen antisolar ocean surface. This simulation was named Cold TLE (CTLE). In order to force a big change, the second SST was the well-observed SST of the fast rotating present day Earth (PDE), which lacks a frozen night side ocean and was therefore named Warm TLE (WTLE). The investigation revealed that, even though the difference between the WTLE and CTLE SSTs was of the order of 23.7 K, its effects on the middle atmosphere were rather limited.

Surprisingly, it was the mesosphere, specially, its upper layers, which were more strongly affected rather than the stratosphere, as would be expected by its closer proximity to the planet's surface. Therefore, it was important to determine whether the middle atmosphere was primary altered through radiative or dynamical processes as a result of the altered SST. Our results showed that the SST had a limited influence on the middle atmosphere. The warmer present day Earth SST resulted in a mean lower tropospheric heating of 3.7 K, a mean upper tropospheric cooling of 4 K, a mean lower stratospheric heating of 3.8 K, a mean lower mesospheric cooling of 1.13 K and a mean upper mesospheric heating of 4.3 K. The lower stratospheric heating could be explained by the absorption of the increased infrared radiation flux from the warmer Earth surface, as the lower stratospheric ozone will absorb the infrared radiation at 9.6 μm. The upper tropospheric cooling and lower stratospheric heating were in agreement with past studies on the influence of the SST variability on the Earth's troposphere and stratosphere. The cooling of the WTLE middle mesosphere compared to the TLE middle mesosphere could be attributed to dynamical forcing, as a result of the increased WTLE gravity wave generation. The generation mechanism of the upper mesospheric WTLE warming, compared to the CTLE, is currently an open question.

The primary ozone layer, where the majority of the ozone is located, was also not significantly affected by the SST change, with a 1.8% decrease on the WTLE day side and a 1.27% decrease on the WTLE night side compared to the CTLE. The decrease was a result of the higher WTLE middle stratospheric temperature. The secondary WTLE ozone layer was significantly affected, increasing by 40.5%, compared to the CTLE.

Generally, the selection of the SST distribution induced middle atmospheric temperature changes of less than 8 K. It also altered the surface winds, generating upward propagating orographic and convective waves, which in turn influenced the middle atmospheric dynamics. This resulted in changes in the small-scale variability by altering the positions of vortices and jet streams.

A future study would aim to explain the physical processes responsible for the upper mesospheric temperature increase and subsequent increase of the secondary ozone layer at these altitudes.

Bibliography

Alexander, M. J., Geller, M., McLandress, C., Polavarapu, S., Preusse, P., Sassi, F., Sato, K., Eckermann, S., Ern, M., Hertzog, A., Kawatani, Y., Pulido, M., Shaw, T. A., Sigmond, M., Vincent, R., and Watanabe, S. (2010). Recent developments in gravity-wave effects in climate models and the global distribution of gravity-wave momentum flux from observations and models. *Quarterly Journal of the Royal Meteorological Society*, 136:1103–1124.

Andrews, David, G. (2010). *An Introduction to Atmospheric Physics, Second Edition*. Cambridge Univesity Press, The Edinburgh Building, Cambridge CB2 8RU, UK.

Betts, R. A. (2000). Offset of the potential carbon sink from boreal forestation by decreases in surface albedo. *Nature*, 408:187–190.

Bönisch, H., Engel, A., Birner, T., Hoor, P., Tarasick, D. W., and Ray, E. A. (2011). On the structural changes in the Brewer-Dobson circulation after 2000. *Atmospheric Chemistry & Physics*, 11:3937–3948.

Braesicke, P. and Pyle, J. A. (2004). Sensitivity of dynamics and ozone to different representations of ssts in the unified model. *Q. J. R. Meteorol. Soc*, 130:2033–2045.

Brasseur, P. G. and Solomon, S. (2005). *Aeronomy of the Middle Atmosphere, Chemistry and Physics of the Stratosphere and Mesosphere, Chemistry and Physics of the Stratosphere and Mesosphere, Third revised and enlarged Edition*. Springer, P.O. Box 17, 3300 AA Dordrecht, The Netherlands, 3rd edition.

Burrows, A. S. (2014). Spectra as windows into exoplanet atmospheres. *Proceedings of the National Academy of Sciences of the United States of America PNAS*, 111:12601–12609.

Cardenas, R., Perez, N., Martinez-Frias, J., and Martin, O. (2014). On the Habitability of Aquaplanets. *Challenges*, 5(2):284.

Carone, L., Keppens, R., and Decin, L. (2014). Connecting the dots: A versatile model for the atmospheres of tidally locked Super-Earths. *Monthly Notices of the Royal Astronomical Society*, 445(000):1–17. doi:10.1093/mnras/stu1793.

Chen, G., Plumb, R. A., and Lu, J. (2010). Sensitivities of zonal mean atmospheric circulation to sst warming in an aquaplanet model. *GEOPHYSICAL RESEARCH LETTERS*, 37:L12701.

Cohen, J. (2011). Eurasian Snow Cover Variability and Links with Stratosphere-Troposphere Coupling and Their Potential Use in Seasonal to Decadal Climate

Predictions. *US National Oceanic and Atmospheric Administration Climate Test Bed Joint Seminar Series NCEP, Camp Springs, Maryland.*

Davis, R. N., Du, J., Smith, A. K., Ward, W. E., and Mitchell, N. J. (2013). The diurnal and semidiurnal tides over Ascension Island (^{o} S, 14^o W) and their interaction with the stratospheric quasi-biennial oscillation: studies with meteor radar, eCMAM and WACCM. *Atmospheric Chemistry and Physics*, 13(18):9543–9564.

Deckert, R. and Dameris, M. (2008). Higher tropical ssts strengthen the tropical upwelling via deep convection. *GEOPHYSICAL RESEARCH LETTERS*, 35:L10813.

Edson, A., Lee, S., Bannon, P., Kasting, J. F., and Pollard, D. (2011). Atmospheric circulations of terrestrial planets orbiting low-mass stars. *Icarus*, 212:1–13.

Encyclopedia of Earth (2013). Albedo. `http://www.eoearth.org/view/article/149954/`.

Gardner, L. C. and Schunk, R. W. (2010). Generation of traveling atmospheric disturbances during pulsating geomagnetic storms. *Journal of Geophysical Research: Space Physics*, 115:2156–2202.

Godolt, M., Grenfell, J. L., Hamann-Reinus, A., Kitzmann, D., Kunze, M., Langematz, U., von Paris, P., Patzer, A. B. C., Rauer, H., and Stracke, B. (2015). 3D climate modeling of Earth-like extrasolar planets orbiting different types of host stars. *Planetary and Space Science*, 111:62–76.

Grenfell, J. L., Gebauer, S., Paris, P. v., Godolt, M., and Rauer, H. (2014). Sensitivity of biosignatures on Earth-like planets orbiting in the habitable zone of cool M-dwarf Stars to varying stellar UV radiation and surface biomass emissions. *Planetary and Space Science*, 98:66–76.

Grenfell, J. L., Stracke, B., von Paris, P., Patzer, B., Titz, R., Segura, A., and Rauer, H. (2007). The response of atmospheric chemistry on earthlike planets around F, G and K Stars to small variations in orbital distance. *Planetary and Space Science*, 55:661–671.

Haberle, R., McKay, C., Tyler, D., Reynolds, R., and Doyle, L. (1996). Can synchronously rotating planets support an atmosphere? In Laurance R. Doyle, editor, *Circumstellar Habitable Zones, Proceedings of The First International Conference, Menlo Park, CA*, page 29. Travis House Publications.

Hedelt, P., von Paris, P., Godolt, M., Gebauer, S., Grenfell, J. L., Rauer, H., Schreier, F., Selsis, F., and Trautmann, T. (2013). Spectral features of Earth-like planets and their detectability at different orbital distances around F, G, and K-type stars. *Astronomy & Astrophysics*, 553.

Hegyi, B. M., Deng, Y., Black, R. X., and Zhou, R. (2014). Initial transient response of the winter polar stratospheric vortex to idealized equatorial pacific sea surface temperature anomalies in the ncar waccm. *Journal of climate*, 27:2699–2713.

Held, I. M. and Suarez, M. J. (1974). Simple albedo feedback models of the icecaps. *Tellus*, 26:613–629.

Holton, J. R. and Hakim, G. J. (2013). *An Introduction to Dynamic Meteorology.* Academic Press, 225 Wyman Street, Waltham, MA 02451, USA.

Hurrell, J. W., Holland, M. M., Gent, P. R., Ghan, S., Kay, J. E., Kushner, P. J., Lamarque, J.-F., Large, W. G., Lawrence, D., Lindsay, K., Lipscomb, W. H., Long, M. C., Mahowald, N., Marsh, D. R., Neale, R. B., Rasch, P., Vavrus, S., Vertenstein, M., Bader, D., Collins, W. D., Hack, J. J., Kiehl, J., and Marshall, S. (2013). The community earth system model: A framework for collaborative research. *American Meteorological Society*, 94:1339–1360.

Jarvis, M. J. (2001). Bridging the atmospheric divide. *Science*, 293(5538):2218–2219.

Joshi, M. (2003). Climate Model Studies of Synchronously Rotating Planets. *Astrobiology)*, 3(2):415–427.

Joshi, M. M., Haberle, R. M., and Reynolds, R. T. (1997). Simulations of the atmospheres of synchronously rotating terrestrial planets orbiting M dwarfs Conditions for atmospheric collapse and the implications for habitability. *Icarus*, 129:450–465.

Kaspi, Y. and Showman, A. P. (2015). Atmospheric Dynamics of Terrestrial Exoplanets over a Wide Range of Orbital and Atmospheric Parameters. *Astrophysical Journal*, 804:60.

Kirschbaum, M. U. F., Whitehead, D., Dean, S. M., Beets, P. N., Shepherd, J. D., and Ausseil, A.-G. E. (2011a). Implications of albedo changes following afforestation on the benefits of forests as carbon sinks. *Biogeosciences*, 8:3687–3696.

Kirschbaum, M. U. F., Whitehead, D., Dean, S. M., Beets, P. N., Shepherd, J. D., and Ausseil, A.-G. E. (2011b). Implications of albedo changes following afforestation on the benefits of forests as carbon sinks. *Biogeosciences*, 8:3687–3696.

Klemp, J. B. and Wilhelmson, R. B. (1978). The simulation of three-dimensional convective storm dynamics. *Journal of the Atmospheric Sciences*, 35:1070–1096.

Kurucz, R. L. (1994). Synthetic Infrared Spectra. In Rabin, D. M., Jefferies, J. T., and Lindsey, C., editors, *Infrared Solar Physics*, volume 154 of *IAU Symposium*, page 523.

Lu, X., Liu, H.-L., Liu, A. Z., Yue, J., McInerney, J. M., and Li, Z. (2012). Momentum budget of the migrating diurnal tide in the Whole Atmosphere Community Climate Model at vernal equinox. *Journal of Geophysical Research: Atmospheres*, 17. doi:http://dx.doi.org/10.1002/2013JA019421.

Manzini, E., Giorgetta, M. A., Esch, M., Kornblueh, L., and Roeckner, E. (2006). The influence of sea surface temperatures on the northern winter stratosphere: Ensemble simulations with the maecham5 model. *Journal of Climate*, 19(16):3863 – 3881. doi:10.1175/JCLI3826.1.

Menou, K. (2013). Water-trapped Worlds. *Astrophysical Journal*, 774:51.

Merlis, T. M. and Schneider, T. (2010). Atmospheric dynamics of Earth-like tidally locked aquaplanets. *Journal of Advances in Modeling Earth Systems*, 2:13.

Morrison, H. and Milbrandt, J. (2011). Comparison of two-moment bulk microphysics schemes in idealized supercell thunderstorm simulations. *Monthly Weather Review*, 139(4):1103. doi:10.1175/2010MWR3433.1.

Müller, R. (2012). *Stratospheric Ozone Depletion and Climate Change*. The Royal Society of Chemistry, Thomas Graham House, Science Park, Milton Road, Cambridge CB4 0WF, UK.

Nappo, C. J. (2013). *An introduction to atmospheric gravity waves*. Academic Press.

National Oceanic and Atmospheric Administration's Space Environment Center (2015). National Oceanic and Atmospheric Administration's Space Environment Center. `wikipedia:http://www.swpc.noaa.gov/`.

Neale, R. B., Gettelman, A., Park, S., Chen, C., Lauritzen, P. H., Williamson, D. K., Conley, A., Kinnison, D., Marsh, D., Smith, A., Vitt, F., Garcia, R., Lamarque, J. F., Mills, M., Tilmes, S., Morrison, H., Cameron-Smith, W., Collins, W. D., Iacono, M. T., Easter, R. C., Liu, X., Ghan, S. J., Rasch, P. J., and Taylor, M. A. (2012). Description of the NCAR Community Atmosphere Model (CAM 5.0). *CESM database*. http://www.cesm.ucar.edu/models/cesm1.0/cam/docs/description/cam5_desc.pdf.

Nicholls, M. E. and Pielke, R. A. (2000). Thermally Induced Compression Waves and Gravity Waves Generated by Convective Storms. *Journal of the Atmospheric Sciences*, 57:3251–3271.

Oleson, K. W., Lawrence, D. M., Bonan, G. B., Flanner, M. G., Kluzek, E., Lawrence, P. J., Levis, S., Swenson, S. C., Thornton, P. E., Dai, A., Decker, M., Dickinson, R., Feddema, J., Heald, C. L., Hoffman, F., Lamarque, J., Mahowald, N., Niu, G., Qian, T., Randerson, J., Tunning, S., Sakaguchi, K., Slater, A., Stockli, R., Wang, A., Yang, Z., Zeng, X., and Zeng, X. (2010). Technical Description of version 4.0 of the Community Land Model (CLM). doi:10.5065/D6FB50WZ, http://nldr.library.ucar.edu/repository/assets/technotes/TECH-NOTE-000-000-000-848.pdf.

Pedatella, N. M., Fuller Rowell, T., Wang, H., Jin, H., Miyoshi, Y., Fujiwara, H., Shinagawa, H., Liu, H.-L., Sassi, F., Schmidt, H., Matthias, V., and Goncharenko, L. (2014). The neutral dynamics during the 2009 sudden stratosphere warming simulated by different whole atmosphere models. *Journal of Geophysical Research: Space Physics*. doi:http://dx.doi.org/10.1002/2013JA019421.

Pedatella, N. M. and Liu, H.-L. (2013). Influence of the El Niño Southern Oscillation on the middle and upper atmosphere. *Journal of Geophysical Research: Space Physics*, 118:2744–2755. doi:http://dx.doi.org/10.1002/2013JA019421.

Petty, G. W. (2006). *A First Course in Atmospheric Radiation.* Sundog Publishing, Sundog Publishing, Madison, Wisconsin, USA.

Rauer, H., Gebauer, S., Paris, P. v., Cabrera, J., Godolt, M., Grenfell, J. L., Belu, A., Selsis, F., Hedelt, P., and Schreier, F. (2011). Potential Biosignatures in Super-Earth Atmospheres I. Spectral appearance of super-Earths around M dwarfs. *Astronomy & Astrophysics*, 529:A8.

Read, P. (2011). Dynamics and circulation regimes of terrestrial planets. *Planetary and Space Science*, 59(10):900 – 914.

Ridgwell, A., Singarayer, J. S., Hetherington, A. M., and Valdes, P. J. (2007). Tackling Regional Climate Change By Leaf Albedo Bio-geoengineering. *Current Biology*, 19:146–150.

Ridgwell, A., Singarayer, J. S., Hetherington, A. M., and Valdes, P. J. (2007). Tackling Regional Climate Change By Leaf Albedo Bio-geoengineering. *Current Biology*, 19:146–150.

Rosenlof, K. H. and George, C. R. (2008). Trends in the temperature and water vapor content of the tropical lower stratosphere: Sea surface connection. *JOURNAL OF GEOPHYSICAL RESEARCH*, 113:D06107.

Rugheimer, S., Kaltenegger, L., Zsom, A., Segura, A., and Sasselov, D. (2013). Spectral Fingerprints of Earth-like Planets Around FGK Stars. *Astrobiology*, 13:251–269.

Saha, K. (2008). *The Earth's Atmosphere: Its Physics and Dynamics.* Springer, 4008 Beechwood Road, University Park, MD 20782, USA.

Salby, Murry, L. (2012a). *Physics of the Atmosphere and Climate.* Cambridge University Press, New York, NY 10013-2473, USA, 32 Avenue of Americas, N, 2nd edition.

Salby, M. L. (2012b). *Physics of the atmosphere and climate.* Cambridge University Press, Cambridge University Press, 32 Avenue of the America, New York, NY 10013-2473, USA.

Segura, A., Kasting, J., Meadows, V., Cohen, M., Scalo, J., Crisp, D., Butler, R., and Tinetti, G. (2005). Biosignatures from Earth-like planets around M-dwarfs. *Astrobiology*, 5:706–725.

Segura, A., Krelove, K., Kasting, J. F., Sommerlatt, D., Meadows, V., Crisp, D., Cohen, M., and Mlawer, E. (2003). Ozone Concentrations and Ultraviolet Fluxes on Earth-Like Planets Around Other Stars. *Astrobiology*, 3:689–708.

Segura, A., Walkowicz, L. M., Meadows, V., Kasting, J., and Hawley, S. (2010). The Effect of a Strong Stellar Flare on the Atmospheric Chemistry of an Earth-like Planet Orbiting an M Dwarf. *Astrobiology*, 10:751–776.

Seitz, R. (2013). Knowing the uknowns. *Earth's Future*. doi:10.1002/2013EF000151.

Selsis, F. (2000). Review: Physics of Planets I: Darwin and the Atmospheres of Terrestrial Planets. In Schü"rmann, B., editor, *Darwin and Astronomy : the Infrared Space Interferometer*, volume 451 of *ESA Special Publication*, page 133.

Showman, A. P. and Polvani, L. M. (2011). Equatorial Superrotation on Tidally Locked Exoplanets. *The Astrophysical Journal*, 738:71. doi:10.1088/0004-637X/738/1/71.

Smith, K. L., Polvani, L. M., and Marsh, D. R. (2012). Mitigation of 21st century Antarctic sea ice loss by stratospheric ozone recovery. *Geophysical Research Letters*, 39(20).

Tan, B., Chu, X., Liu, H.-L., , Yamashita, C., and Russell, J. M. (2012a). Atmospheric semidiurnal lunar tide climatology simulated by the whole atmosphere community climate model. *Journal of Geophysical Research*, 117:1–11. doi:10.1029/2012JA017792.

Tan, B., Chu, X., Liu, H.-L., , Yamashita, C., and Russell, J. M. (2012b). Parameterization of the inertial gravity waves and generation of the quasi-biennial oscillation. *Journal of Geophysical Research: Atmospheres*, 117. doi:10.1029/2011JD016778.

Tan, B., Chu, X., Liu, H.-L., , Yamashita, C., and Russell, J. M. (2012c). Zonal-mean global teleconnection from 15 to 110 km derived from SABER and waccm. *Journal of Geophysical Research: Atmospheres*, 117:1–11. doi:10.1029/2011JD016750.

Tarter, J. C., Backus, P. R., Mancinelli, R. L., Aurnou, J. M., Backman, D. E., Basri, G. S., Boss, A. P., Clarke, A., Deming, D., Doyle, L. R., Feigelson, E. D., Freund, F., Grinspoon, D. H., Haberle, R. M., Hauck, S. A. I., Heath, M. J., Henry, T. J., Hollingsworth, J. L., Joshi, M. M., Kilston, S., Liu, M. C., Meikle, E., Reid, I. N., Rothschild, L. J., Scalo, J., Segura, A., Tang, C. M., Tiedje, J. M., Turnbull, M. C., Walkowicz, L. M., Weber, A. L., and Young, R. E. (2007). A Reappraisal of the Habitability of Planets Around M Dwarf Stars. *Astrobiology*, 7:30–65.

The DESERTEC Foundation (2015). DESERTEC. `http://www.desertec.org/concept/`.

Trenberth, K. E., Fasullo, J. T., and Kiehl, J. (2009). Earth's global energy budget. *American Meteorological Society*, pages 311–324.

Vadas, S. L. and Liu, H.-L. (2009). Generation of large-scale gravity waves and neutral winds in the thermosphere from the dissipation of convectively generated gravity waves. *Journal of Geophysical Research*, 114.

Vadas, S. L. and Liu, H.-L. (2013). Numerical modelling of the large-scale neutral and plasma responses to the body forces created by the dissipation of gravity waves from 6 h of deep convection in Brazil. *Journal of Geophysical Research: Space Physics*, 118:2593–2617. http://www.cora.nwra.com/ṽasha/VadasLiu_JGR_2013.pdf.

Vasiliy, V. (2005). Generation of secondary internal waves by the interaction of an internal solitary wave with an underwater bank. *Journal of Geophysical Research*, 110. doi:10.1029/2004JC002467.

Vertenstein, M., Craig, T., Middleton, A., Feddema, D., and Fisher, C. (2012). CESM1.0.4 User's Guide. *CESM online database.* available from: http://www.cesm.ucar.edu/models/cesm1.0/cesm/cesm_doc_1_0_4/book1.html.

Wallace, John, M. and Hobbs, Peter, V. (2006). *Atmospheric Science an Introductory survey.* Academic Press, 525 B St # 1800, San Diego, CA 92101, 2nd edition.

Walland, D. J. and Simmonds, I. (1996). Modelled atmospheric response to changes in Northern Hemisphere snow cover. *Climate Dynamics*, 13:25–34.

Walland, D. J. and Simmonds, I. (1996). Modelled atmospheric response to changes in Northern Hemisphere snow cover. *Climate Dynamics*, 13:25–34.

Weisman, M. L. and Rotunno, R. (2000). The use of vertical wind shear versus helicity in interpreting supercell dynamics. *Journal of the Atmospheric Sciences*, 1452 - 1472(57):9. doi:10.1175/1520-0469(2000)057<1452:TUOVWS>2.0.CO;2.

Yang, J., Boué, G., Fabrycky, D. C., and Abbot, D. S. (2014). Strong Dependence of the Inner Edge of the Habitable Zone on Planetary Rotation Rate. *The Astrophysical Journal Letters*, 787:L2.

Yang, J., Cowan, N. B., and Abbot, D. S. (2013). Stabilizing cloud feedback dramatically expands the habitable zone of tidally locked planets. *The Astrophysical Journal Letters*, 771:L45.

Acknowledgement

I would like to express my gratitude to PD Dr. Klemens Hocke for the supervision, help, invaluable insights, patience, trust and support that he provided me with during my PhD. I would also like to thank Professor Niklaus Kämpfer for the supervision and financial support that he provided as head of the Microwave Physics division of the Institute of Applied Physics, as well as Professor Peter Wurz and Dr. Helmut Lammer, for supervising my PhD. Furthermore, I feel much obliged to Professor Dr. Peter Read for kindly agreeing to referee this thesis.

This PhD would not have been possible without the PhD fellowship that the Center for Space and Habitability of the University of Bern provided.

To the CESM model community modellers and staff, I would like to express my thanks for the invaluable information and advice they provided.

My sincere thanks to Dominik Scheiben, Ansgar Schanz and Martin Lainer for the technical support they provided and Yvette Eggenschwiler and Beatrice Thut for their kindness and ever present willingness to help when problems arose.

I am forever grateful to my mother Varela Danai and my aunt Eleni Varela for their guidance and moral, emotional and financial support that they provided me with during all my life. I would have never made it this far without you.

My most heartfelt thanks to my best friends, Fotini Bogiatzi, Thomas Xavianidis and Fotini Seidiropoulou for believing in me and being there for me when I needed them.

Lastly, I would like to express my deepest and most heartfelt appreciation for my fiancé Kaven Henry Yau Wong, for aiding me in proofreading this thesis. I am eternally grateful for your unconditional love, understanding, support and patience all this time.

Appendix: peer-reviewed/submitted articles

7.1 First article

The study was published in *Geoscience letters* in August 2013.

Reference:

Proedrou and Hocke: A traveling atmospheric disturbance generated by a soil colour change in a high-resolution climate model experiment. Geoscience Letters 2014 1:13. doi:10.1186/s40562-014-0013-9

Proedrou and Hocke *Geoscience Letters* 2014, **1**:13
http://www.geoscienceletters.com/content/1/1/13

Geoscience Letters
a SpringerOpen Journal

RESEARCH LETTER Open Access

A traveling atmospheric disturbance generated by a soil colour change in a high-resolution climate model experiment

Elisavet Proedrou[1,2*†] and Klemens Hocke[1,2,3†]

Abstract

The climate model CESM-WACCM is used to study the way a soil colour change of the eastern region of the Sahara affects the dynamics of the troposphere. The soil colour is darkened for 5 days. The difference between the perturbed model run and the control model run is used to isolate the soil colour change-induced atmospheric perturbation from random atmospheric waves which are stronger by an order of magnitude or more. The perturbation generates a circular wave radially propagating away from the Sahara on the first day of the simulation. After nine hours, the wave front reaches the convection zone in Brazil where a secondary wave is generated and can be clearly seen until 23:00 UT. The mean wave velocities of the traveling atmospheric disturbances are $\langle v \rangle = 200 \pm 50$ m/s for the primary wave and $\langle v \rangle = 220 \pm 40$ m/s for the secondary wave. The mean horizontal wavelengths are $\langle \lambda \rangle = 3000 \pm 500$ km for the primary wave and $\langle \lambda \rangle = 2600 \pm 600$ km for the secondary wave. The mean wave periods are $\langle p \rangle = 4 \pm 1$ h for the primary wave and $\langle p \rangle = 3 \pm 1$ h for the secondary wave. Since the perturbed model run diverges from the control run with the passage of time, the attribution of cause and effect becomes difficult after a few days. Analysis of the simulation data of the first day leads to a deeper understanding of global teleconnections, radiative transfer and wave-coupling processes between the surface and the atmospheric layers.

Keywords: Small perturbation analysis; Traveling atmospheric disturbance; Secondary wave generation; Land-atmosphere interaction; Surface albedo; Lower troposphere; High-resolution climate model

Background

In our study we investigate whether a high-resolution global climate model can be used to study the generation, propagation and dissipation of atmospheric waves induced by a soil colour change. We are especially interested to know if a cause-effect study can be performed under realistic atmospheric conditions. The attribution of cause and effects is a fundamental problem of complex systems.

At present two types of numerical models are available for studying the climate processes. The idealized models and the realistic models [1]. Idealized models allow us to conduct detailed studies and hence increase our understanding of simplified or isolated processes. Due to their simplicity these models neglect the role of more complex interactions and hence do not provide a holistic view of the climate system. Realistic models on the other hand, consider almost all processes of the climate system and provide high-resolution climate data, which are rather close to the observations. As a result realistic model data are almost as difficult to understand as the observations. Therefore the recognition of the relevant climate processes, the attribution of climate forcing and their effect on the climate requires advanced methods of data analysis and interpretation (e.g [2-4]).

The generation, propagation and dissipation of atmospheric waves are often studied by means of idealized model simulations. Nicholls & Pielke [5] conducted such a study using an idealised three-dimensional, fully compressible atmospheric model. Their goal was

---

*Correspondence: elisavet.proedrou@iap.unibe.ch
†Equal contributors
[1] Institute of Applied Physics, University of Bern, Sidlerstrasse 5, Bern, Switzerland
[2] Center for Space and Habitability, University of Bern, Bern, Switzerland
Full list of author information is available at the end of the article

to investigate the properties of the atmospheric waves induced by a tropical thunderstorm. Their study showed that the thunderstorm generated not only atmospheric gravity waves, but also thermal compression waves. Gardner & Schunk [6] used a high-resolution global thermosphere-ionosphere model to examine the effect a large scale perturbation (in this case a pulsating geomagnetic storm) has on the atmosphere. They concluded that this type of storm generates multiple Traveling Atmospheric Disturbances (TADs) coincidently travelling from the northern and southern auroral zone towards the equator and into the conjugate hemisphere.

Atmospheric disturbances are also induced by albedo changes, which can be due to changes in the type of the vegetation, the soil colour, the formation of clouds and other causes. Surface albedo itself can include snow cover, surface water and vegetation change too. Only in the case of a desert like the Sahara, surface albedo might be mainly governed by the soil color. Seitz [7] gives a brief survey about the influences of albedo changes on the Earth's radiation energy balance. According to Seitz [7], the effects of regional albedo changes on the climate system are still not well observed, simulated and understood. Past regional albedo change studies have focused on the effects on long-term climate change [3,4,8,9] and how it can be utilized in geoengineering projects to combat global warming [10]. To our knowledge, there is only one study, which attributed a sudden snow cover in Eurasia to a polar vortex change [3].

Our study is the first to extract and discuss the tropospheric waves induced by a regional soil colour change using a realistic high-resolution 3-D climate model. In the simulation, we change the soil colour of a desert region since this change can be safely implemented in the complex climate model which we use. Furthermore, this simple scenario will allow a clear interpretation of the simulation results.

In the present study, we concentrate on the effects the soil colour change has on the lower troposphere. The generated atmospheric perturbation has a small amplitude so that a small-scale perturbation analysis can be applied to the first 1-2 days of the model simulation. This allows us to study the global propagation of the TADs through the lower troposphere in detail.

Model description

The Community Earth System Model (CESM) version 1.04 was used to perform our simulation. It is composed of a coupler (CPL) and five fully coupled geophysical models: atmosphere (ATM), land (LND), ocean (OCN), sea-ice (ICE), land-ice (GLC). The models can be set as fully prognostic, data, or stub and are "state-of-the-art climate prediction and analysis tools" [11] when set in prognostic mode.

The ATM in our simulation is the Whole Atmosphere Community Climate Model (WACCM) version 5 [12]. WACCM is often used for the simulation of circulation, thermal tides, gravity waves, wave-mean flow interaction, and atmospheric composition changes in the middle atmosphere [13-20].

It has a fully compressible horizontal discretization, and a quasi-Lagrangian vertical discretization approximation, which ignores the acceleration term in the vertical component of the momentum equation. This approximation is good for scales greater than 10 km [12]. It has 66 vertical levels from the ground up to $5 \cdot 10^{-6}$ hPa (2.5 – 149 km). The vertical coordinate is purely isobaric above 100 hPa, but is terrain following below that level. The model top is $\sim$ 150 km. The vertical resolution is 1.1 km in the troposphere, 1.1-1.4 km in the lower stratosphere, 1.75 km at the stratopause and 3.5 km above 65 km. The horizontal resolution of our simulation is 4° × 5° (latitude × longitude), with 72 longitude and 46 latitude grid points. The coupler timestep is $\Delta t = 30$ minutes while the time step for the dynamics equations is $\Delta\tau = \Delta t/8$ [12].

The smallest wavelength that our model experiment can resolve by the finite differencing (that is used by default in WACCM) is twice that of the grid size [21]. Therefore the resolvable waves in the equatorial troposphere have a horizontal wavelength of $\lambda_{horizontal} > 1000$ km, a vertical wavelength of $\lambda_{vertical} > 2.2$ km, a period of $p_{horizontal} > 2$ h and a wave velocity of $v < \Delta x/\Delta\tau = \Delta x/(\Delta t/8) = 500/(1800/8) \approx 2200$ m/s. Thus the simulation can adequately resolve large scale waves [21].

The land model provides the surface albedo, area-averaged for each atmospheric column, and the upward longwave surface flux, which incorporates the surface emissivity, for input into the radiation scheme. The surface fluxes of momentum, sensible heat, and latent heat serve as the lower flux boundary conditions for the planetary boundary layer parameterization, the vertical diffusion and the gravity wave drag. The atmospheric radiation is calculated using the momentum, sensible heat flux, latent heat flux, land surface albedos and upward longwave radiation. The upward longwave radiation is calculated by taking the difference between the incident and absorbed fluxes. The incident flux values are determined by means of the daily values of the solar radio flux (F10.7) which are provided by the National Oceanic and Atmospheric Administration's (NOAA) Space Environment Center [22].

The land model used was the Community Land Model (CLM), which has atmosphere-surface coupling, surface colour variability, surface albedo calculation, absorption, reflection, and transmittance of solar radiation, absorption and emission of longwave radiation, sensible heat (ground and canopy) latent heat fluxes and heat transfer in soil and snow [23]. The surface albedo calculation depends on whether the top surface is a vegetated canopy or bare ground.

In the case of bare ground the surface albedo calculation requires only the soil colour, which varies with the colour class (soil colour index). The term bare ground refers to any surface that is not covered by vegetation and can therefore be a glacier, a lake, a wetland, snow covered soil or bare soil. In the case of our simulation the only parameter that affects the surface albedo of the perturbed east Saharan area is the soil colour, which is determined by the value of the soil colour index of the area.

The CLM soil colour indices are prescribed so that they reproduce the observed Moderate-resolution Imaging Spectroradiometer (MODIS) local solar noon surface albedo values at the CLM grid cell [23]. MODIS is a set of spectroradiometers in orbit on board the Terra and Aqua satellites. They provide measurements of large scale global dynamics (e.g changes in the cloud cover, radiation budget, processes on the oceans, the land and lower atmosphere). They capture data in 36 spectral bands (0.4 μm - 14.4 μm) at varying spatial resolutions and image the entire Earth every 1 - 2 days [24].

Methods

Simulation setup

In the simulation setup we used the perpetual year 2000 component set (F_2000_WACCM) [11]. A component set is the assemble of a particular mix of geophysical models along with geophysical model-specific configurations and namelist settings. In this case it is a set of two fully prognostic, present day, coupled atmosphere and land geophysical models (WACCM,CLM), a prescribed data ocean geophysical model (docn), a prescribed sea-ice (CICE) geophysical model and no land-ice geophysical model ([11]). With it, we conduct two simulations. In the first one, from now on referred to as control run, all the input parameter fields remain unchanged. In the second one, from now on referred to as perturbed run, the colour of a small region of the east Sahara, that spans 3 × 3 pixels (longitude: 10°-20°, latitude: 18°-26°), is darkened from beige (bright sand) to very dark green (the colour of the darkest forests). To avoid a discontinuity in the soil colour map, the soil colour change is gradually performed with a small change of 50% at the edge of the Sahara array (soil colour index = 15) and a maximal change in the center of the array (soil colour index = 20) as shown in Figure 1. The simulation spans 5 days starting at 0:00 UT on 01/01/2000 and ending at 23:00 UT on 05/01/2000.

Data analysis

The surface albedo, the surface temperature, the atmospheric pressure and the vertical wind are extracted from the output datasets for the control and the perturbed run. In the present letter, we only show the results obtained for the vertical wind at 2 km altitude. A comprehensive study of the disturbances in all parameters at all altitudes is planed as a follow-up-study. In addition we have to design advanced algorithms for the analysis of different wave modes. However the initial data analysis presented here already provides many new results.

As a first step the above parameters are interpolated to the altitude of 2 km from 0:00 UT to 23:00 UT. Then the control run is subtracted from the perturbed run at each timestep. The mean standard deviation $\sigma = 2 \cdot 10^{-4}$ Pa/s for the first day at 23:00 UT is taken as reference for the normalization of the vertical wind fluctuations. To calculate it we derive at first the zonal means of σ as a function of latitude for 23:00 UT. Then we obtain the global mean of sigma σ from the zonal means of sigma σ_z by calculation of the surface area preserving mean. For recognition of significant atmospheric waves in the global plots, we divide the vertical wind fluctuations $d\Omega$ by σ. Variations $> 2\sigma$ have a significance (confidence level) of 90%.

Results and discussion

The change in surface colour resulted in the appearance of fast propagating primary and secondary waves at 2 km altitude.

Primary perturbation

As can be seen in Figure 2a, the primary perturbation, appears over the Sahara at 9:00 UT (four hours after sunrise). The surface colour change causes a convective perturbation in the lower troposphere, a buoyancy oscillation that rises and falls as the day progresses (Figure 2). The warm colours in the figure indicate downward air

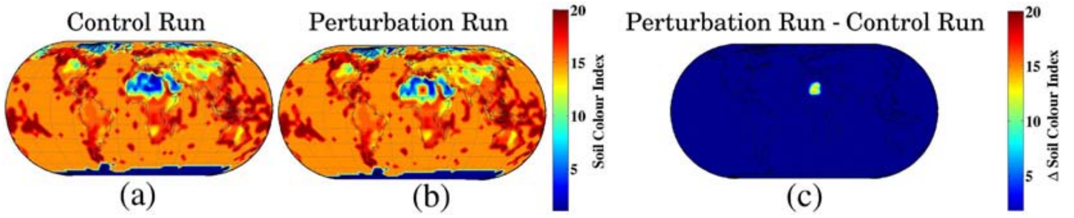

Figure 1 Simulation setup. (a) soil colour index of the control run, **(b)** soil colour index of the perturbed run, **(c)** difference between the soil colour indices of the perturbed and the control run.

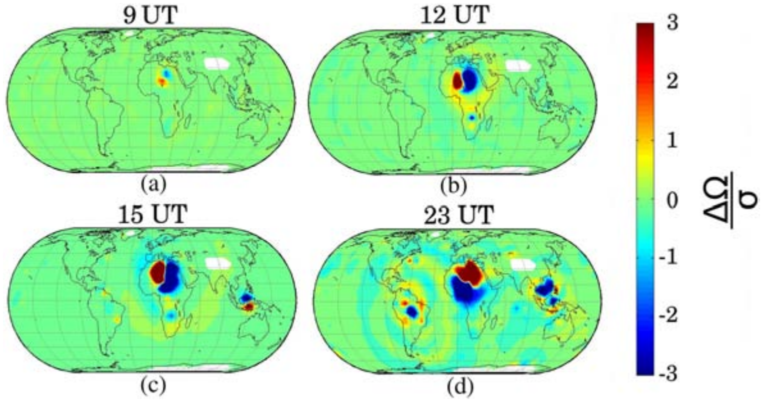

Figure 2 Evolution of the atmospheric perturbation due to the soil colour change in Eastern Sahara during day 1. The difference between the vertical wind at 2 km altitude of the perturbed run minus the control run is shown at **(a)** 9:00 UT, **(b)** 12:00 UT, **(c)** 15:00 UT, **(d)** 23:00 UT. Shades of blue indicate upward motion of the air, while shades of red indicate downward motion.

motion and the cold colours indicate upward motion since WACCM provides the vertical wind in [Pa/s].

As can be seen in Figure 2b,c,d the perturbation amplitude increases with time to a value of $A > 5\sigma$. We have therefore a 5σ confidence ($\sigma = 2 \cdot 10^{-4}$ Pa/s at this altitude).

Figure 2b shows a nearly circular wave ring outgoing from the surface colour change region in the eastern Sahara. The wave ring is also visible in Figure 2c (15:00 UT). The mean horizontal wavelength $\langle\lambda\rangle$ of the wave is calculated as follows:

i. The center of the disturbance is known for the primary wave (22° N, 15° E). In the case of the secondary wave, its center is determined by an educated guess (10° S, 55° W).
ii. The positions of the inner and outer ring of the wave (R_{inner} and R_{outer}) are visible in the global maps of the vertical wind fluctuations at 12:00 UT). Then the ring positions are manually determined, from the center towards the North, East, South and West direction. This gives us four values for the inner and four values for the outer ring.
iii. Then the mean horizontal wavelength is calculated: $\langle\lambda\rangle = <\lambda> = 2 \cdot (<R_{outer}> - <R_{inner}>)$.

The calculated values for $< R_{inner} >$ and $< R_{outer} >$ together with their standard deviations can be seen in Figure 3. The calculated mean horizontal wavelength of the primary wave is $\langle\lambda\rangle = 3000$ km.

The mean wave speed v is calculated as follows. First the mean horizontal speeds of the inner and outer radii are taken from the inclination of the above mentioned linear regression lines: $v_{inner} = dR_{inner}/dt = 240$ m/s, $v_{outer} = dR_{outer}/dt = 170$ m/s. Then the mean of the above calculated horizontal speeds is taken $\langle v\rangle = (v_{inner} + v_{outer})/2 \approx 200$ m/s. Its standard deviation is $\sigma_v = 50$ m/s.

The mean wave period is calculated taking the ratio of the mean horizontal wavelength and the mean horizontal velocity of the wave $\langle p\rangle = \langle\lambda\rangle/\langle v\rangle = 4$ h. Its uncertainty is calculated using the Gaussian error propagation law $\sigma_p = \sqrt{(\sigma_\lambda/\langle v\rangle)^2 + \left(\langle\lambda\rangle \cdot \sigma_v/\langle v\rangle^2\right)^2} = 1$ h.

The derived uncertainties mainly reflect the azimuthal variations of the wave parameters. These variations are possibly due to azimuthal changes in the background wind flow, topography, convective activity, Coriolis force and other factors which modulate the radial propagation of the wave rings.

In summary, the soil colour change induced a circular large scale wave with a wave speed close to the speed

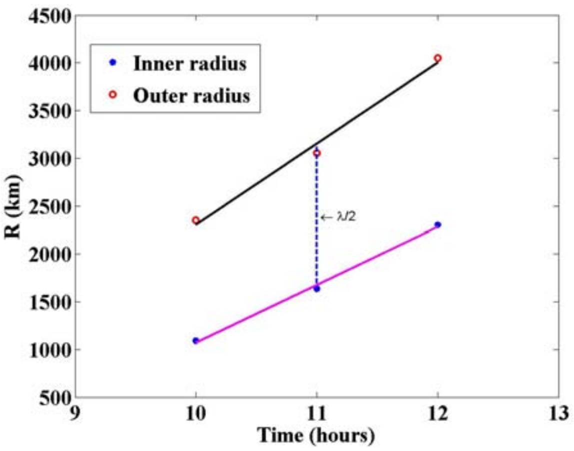

Figure 3 Evolution of the inner and outer radius of the primary wave ring. The three point pairs of the inner and outer radius are at 10:00 UT, 11:00 UT and 12:00 UT. The horizontal wavelength is two times the mean distance between the two linear regression lines.

of sound. The wave characteristics are quite similar to those in the numerical simulation of Nicholls & Pielke [5]. They interpreted the horizontally propagating circular wave outgoing from a thunderstorm region with the speed of sound as a Lamb wave mode n1 and n2. The n1 mode moved faster and resulted in deep subsidence warming, while the second mode propagated at half the speed and resulted in weak-low level uplift. The appearance of an uplift as a result of a thermally induced gravity wave is in accordance with our own results (Figure 2a). Parallel to Nicholls & Pielke, the primary wave in our simulation is mostly soliton-like which might be interpreted as a shock wave front (as done by Nicholls & Pielke). On the other hand large scale waves with speeds close to the speed of sound are often found in the thermosphere. They have periods of several hours and horizontal wavelengths of a few thousands kilometres. Gardner & Shunk [6] as well as Vadas [25] classify these large-scale waves as atmospheric gravity waves.

In the case of our simulation, the surface colour change resulted in an increase in the fraction of solar radiation absorbed by the region. This resulted in an increase in the surface temperature and therefore in an increase in the temperature of the air located directly over the perturbed region. The observed buoyancy oscillation at 2 km altitude could be a result of either convective or radiative heating. The convective heating would be consistent with the evolution of the central perturbation, as the air seems to rise over the perturbation and then fall as the day progresses, with the opposite happening to the air around it (Figure 2).

Secondary perturbations

Surprisingly, two secondary perturbations (or secondary waves) appear in Figure 4. The first appears over Indonesia at 14:00 UT. The pathway between this perturbation and the source region, in the Sahara, is unclear because the primary wavefront has not arrived in Indonesia at the time the perturbation appears.

Later the wave front of the primary wave approaches Brazil at 15:00 UT (Figure 2c) and reaches its tropical convection zone at 16:00 UT (Figure 4a).

As the wave front comes in contact with the tropical convection zone, it scatters and a secondary wave is generated. The secondary wave is clearly visible as concentric wave rings outgoing from the center of the tropical convection zone (10° S, 55° W). The vertical wind in the tropical convection zone also has a periodic oscillation which can be seen in Figure 4a. The outward propagation of the generated secondary wave can be seen in Figure 4a,b.

As can be seen in Figure 4c at 19:00 UT another wave front generated by the perturbation over the Sahara, scatters on the Brazilian tropical convection zone. Besides wave scattering based on the Huygens-Fresnel principle, we think that the latent heat release by periodic, vertical advection of moist air masses is another reason for the generation and amplification of a secondary wave over Brazil (Figure 4a,c).

The parameters of the secondary wave are estimated for the time interval between 19:00 UT and 23:00 UT. The wave parameters are derived in the same manner as for the primary wave. The point pairs of the inner and outer rings and their linear regression lines are shown in Figure 5. The estimated wave parameters are: $\langle\lambda\rangle = 2600 \pm 600$ km, $\langle v\rangle = 220 \pm 40$ m/s, $\langle p\rangle = 3 \pm 1$ h.

In summary, the soil colour change induced a secondary circular large scale wave with a wave speed ∼ 70% of the speed of sound.

The generation of secondary waves from convectively generated gravity waves was simulated by Vadas [26], with the wave characteristics being quite similar to those in our simulation. The generation of secondary oceanic waves through interaction with the topography in a manner

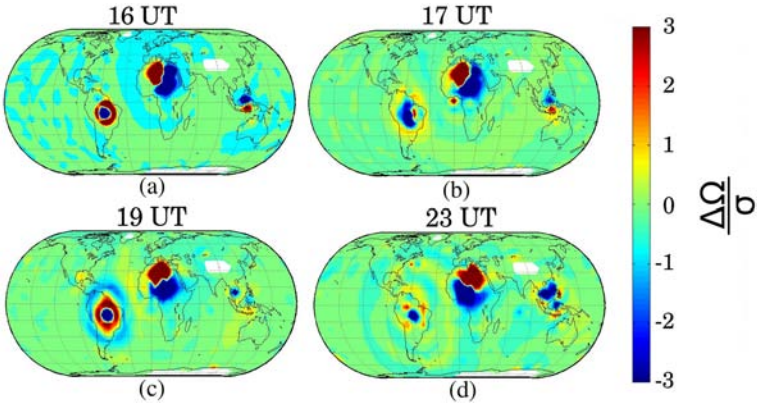

Figure 4 Evolution of the secondary wave above Brazil during day 1. The difference between the vertical wind at 2 km altitude of the perturbed run minus the control run is shown at **(a)** 16:00 UT, **(b)** 17:00 UT, **(c)** 19:00 UT, **(d)** 23:00 UT.

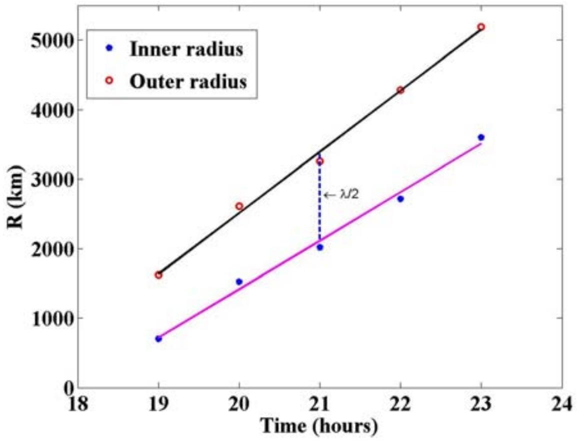

Figure 5 Evolution of the inner and outer radius of the secondary wave ring outgoing from Brazil. The five point pairs of the inner and outer radius are at 19:00 UT, 20:00 UT, 21:00 UT, 22:00 UT and 23:00 UT. The horizontal wavelength is two times the mean distance between the two linear regression lines.

similar to the interaction of our wave with the tropical convection zone, was reported by Vlasenko [27].

The scattering of the primary wave front results in a change in the vertical motion. Updrafts might produce condensation of moist air resulting in latent heat release which may further amplify the secondary wave. Indeed the strong amplitude of the secondary wave points to such an amplification process which would affect the precipitation rate and the regional climate.

An ensemble simulation was also performed, between 01.01.2000 and 01.06.2000, with a 5 day gap between each run. The main features (primary wave and excitation of secondary waves) are present in both the ensemble average and in each individual run. However the shape of the primary wave ring can differ indicating a seasonal variation in the azimuthal wave speeds, which is likely due to a seasonal variation of the mean flow and the thermal structure of the lower troposphere. For example, in June the southward propagation of the primary wave is enhanced compared to January. In March, a secondary wave is generated in the vicinity of Lake Victoria (Tanzania), where a tropical convention zone is present during that time of the year (rainy season) [28]. These examples show the potential of wave propagation studies with a realistic high-resolution climate model.

Evolution five days later

Five days after the initiation of the simulation, no circular wave patterns are visible. And while enhanced fluctuations are visible in the vicinity of the Sahara and the convective zones over Brazil and Indonesia, disturbances are also visible in a seemingly random distribution all over the globe. Furthermore the global mean standard deviation σ linearly increases over the 5 days of our simulation from $\sigma = 2 \cdot 10^{-4}$ on the first day to $\sigma = 27 \cdot 10^{-4}$ on the fifth day. This indicates that the perturbed run diverges more and more from the control run with increase of time, making the attribution of cause and effect difficult. Our small perturbation analysis is only applicable for the first two days when the perturbation waves can be clearly separated from the random atmospheric waves. The coupling of the primary and secondary waves in our study could be exemplary to a similar coupling between migrating and non-migrating tides.

Conclusions

The soil colour change of a surface area in the eastern Sahara generates a traveling atmospheric disturbance. The advantage of our high-resolution climate model experiment is that we can study, for the first time, the generation and propagation of the TAD under realistic atmospheric conditions. This means that all the interactions between the TAD and the atmospheric jets, circulation cells, solar tides, planetary waves, random gravity waves, orography and tropical convection zones are included in the simulation. We find that the interaction of the TAD with the tropical convection zones over Brazil is most obvious.

The soil colour perturbation generates a primary atmospheric wave outgoing from the source region in the Sahara. It has an amplitude of $A > 5\sigma$, a mean horizontal wavelength of $\langle\lambda\rangle = 3000 \pm 500$ km, a mean wave velocity of $\langle v\rangle = 200 \pm 50$ m/s and a mean period of $\langle p\rangle = 4 \pm 1$ h.

As the primary wave reaches Brazil, the wave front scatters at the tropical convection zone and generates secondary atmospheric outgoing waves. The latent heat release by moist air amplify the secondary wave to an amplitude of $A > 5\sigma$. The wave has a mean horizontal wavelength of $\langle\lambda\rangle = 2600 \pm 600$ km, a mean wave velocity of $\langle v\rangle = 220 \pm 40$ m/s and a mean period of $\langle p\rangle = 3 \pm 1$ h.

In the present letter we only discussed the dynamical response of the global troposphere at 2 km height to the soil colour change in Sahara. This brief analysis of the numerical experiment already gave new results on the land-atmosphere interaction, global teleconnections and wave dynamics. We expect that a future analysis of the simulation data at different altitudes will provide us with a better understanding of how regional soil colour changes affect the atmospheric layers above. For example how much energy and momentum are transported by wave coupling and radiative transfer, which wave modes are most important and which role do the soil colour changes play on the generation of non-migrating atmospheric tides.

Another topic would be the investigation of the dependences of the primary and secondary TAD parameters on the location, size and strength of the sources. Such studies are relevant for geoengineering as well as for understanding of the climate processes and wave-wave interactions.

Abbreviations

ATM: Atmospheric geophysical model; CESM: Community earth system model; CICE: Sea - ice data model; CLM: Community land model; CPL: Coupler to CESM; GLC: Land-ice geophysical model in CESM; ICE: Sea-ice geophysical model in CESM; docn: prescribed data ocean model; LND: Land geophysical model in CESM; MODIS: Moderate-resolution imaging spectroradiometer; OCN: Ocean geophysical model in CESM; TAD: Traveling atmospheric disturbance; WACCM: Whole atmosphere community climate model; NOAA: National oceanic and atmospheric administration.

Competing interests

The authors declare that they have no competing interests.

Authors' contributions

EP performed the simulations and data analysis. KH contributed to the data analysis and interpretation. Both authors read and approved the final manuscript.

Acknowledgements

We would like to thank the Center for Space and Habitability (University of Bern) for the PhD fellowship that made this study possible. We would like to thank the WACCM forum for the invaluable information it provided. We would also like to thank Dominik Scheiben and Ansgar Schanz for the computer technical support they provided. Finally we would like to thank Niklaus Kämpfer, Peter Wurz, Helmut Lammer, and Raymond Pierrehumbert for the valuable discussions and advises.

Author details

[1]Institute of Applied Physics, University of Bern, Sidlerstrasse 5, Bern, Switzerland. [2]Center for Space and Habitability, University of Bern, Bern, Switzerland. [3]Oeschger Centre for Climate Change Research, University of Bern, Bern, Switzerland.

Received: 28 February 2014 Accepted: 5 August 2014

References

1. Held IM (2005) The gap between simulation and understanding in climate modeling. Bull Am Meteorological Soc 86:1609–1614
2. Alexander MJ, Geller M, McLandress C, Polavarapu S, Preusse P, Sassi F, Sato K, Eckermann S, Ern M, Hertzog A, Kawatani Y, Pulido M, Shaw TA, Sigmond M, Vincent R, Watanabe S (2010) Recent developments in gravity-wave effects in climate models and the global distribution of gravity-wave momentum flux from observations and models. Q J R Meteorological Soc 136:1103–1124
3. Walland DJ, Simmonds I (1996) Modelled atmospheric response to changes in Northern Hemisphere snow cover. Climate Dyn 13:25–34
4. Kirschbaum MUF, Whitehead D, Dean SM, Beets PN, Shepherd JD, Ausseil A-GE (2011) Implications of albedo changes following afforestation on the benefits of forests as carbon sinks. Biogeosciences 8:3687–3696
5. Nicholls ME, Pielke RA (2000) Thermally induced compression waves and gravity waves generated by convective storms. J Atmos Sci 57:3251–3271
6. Gardner LC, Schunk RW (2010) Generation of traveling atmospheric disturbances during pulsating geomagnetic storms. J Geophys Res: Space Phys 115:2156–2202
7. Seitz R (2013) Knowing the uknowns. Earth's Future. doi:10.1002/2013EF000151
8. Held IM, Suarez MJ (1974) Simple albedo feedback models of the icecaps. Tellus 26:613–629
9. Betts RA (2000) Offset of the potential carbon sink from boreal forestation by decreases in surface albedo. Nature 408:187–190
10. Ridgwell A, Singarayer JS, Hetherington AM, Valdes PJ (2007) Tackling regional climate change by leaf Albedo bio-geoengineering. Curr Biol 19:146–150
11. Vertenstein M, Craig T, Middleton A, Feddema D, Fisher C (2012) CESM 1.0.4 user's guide. Available from: http://www.cesm.ucar.edu/models/cesm1.0/cesm/cesm_doc_1_0_4/book1.html
12. Neale RB, Gettelman A, Park S, Chen C, Lauritzen PH, Williamson DK, Conley AJ, Kinnison D, Marsh D, Smith AK, Vitt F, Garcia R, Lamarque JF, Mills M, Tilmes S, Morrison H, Cameron-Smith W, Collins WD, Iacono MT, Easter RC, Liu X, Ghan SJ, Rasch PJ, Taylor MA (2012). Description of the NCAR Community Atmosphere Model (CAM 5.0). http://www.cesm.ucar.edu/models/cesm1.0/cam/docs/description/cam5_desc.pdf
13. Pedatella NM, Fuller-Rowell T, Wang H, Jin H, Miyoshi Y, Fujiwara H, Shinagawa H, Liu H-L, Sassi F, Schmidt H, Matthias V, Goncharenko L (2014) The neutral dynamics during the 2009 sudden stratosphere warming simulated by different whole atmosphere models. J Geophys Res: Space Phys. http://dx.doi.org/10.1002/2013JA019421
14. Pedatella NM, Liu H-L (2013) Influence of the El Niño southern oscillation on the middle and upper atmosphere. J Geophys Res: Space Phys 118:2744–2755. http://dx.doi.org/10.1002/2013JA019421
15. Lu X, Liu H-L, Liu AZ, Yue J, McInerney JM, Li Z (2012) Momentum budget of the migrating diurnal tide in the whole atmosphere community climate model at vernal equinox. J Geophys Res: Atmos 17. http://dx.doi.org/10.1002/2013JA019421
16. Tan B, Chu X, Liu H-L, Yamashita C, Russell JM (2012) Atmospheric semidiurnal lunar tide climatology simulated by the whole atmosphere community climate model. J Geophys Res 117:1–11. doi:10.1029/2012JA017792
17. Tan B, Chu X, Liu H-L, Yamashita C, Russell JM (2012) Zonal-mean global teleconnection from 15 to 110 km derived from SABER and waccm. J Geophys Res: Atmos 117:1–11. doi:10.1029/2011JD016750
18. Tan B, Chu X, Liu H-L, Yamashita C, Russell JM (2012) Parameterization of the inertial gravity waves and generation of the quasi-biennial oscillation. J Geophys Res: Atmos 117. doi:10.1029/2011JD016778
19. Davis RN, Du J, Smith AK, Ward WE, Mitchell NJ (2013) The diurnal and semidiurnal tides over Ascension Island (° s, 14° w) and their interaction with the stratospheric quasi-biennial oscillation: studies with meteor radar, eCMAM and waccm. Atmos Chem Phys 13(18):9543–9564
20. Smith KL, Polvani LM, Marsh DR (2012) Mitigation of 21st century Antarctic sea ice loss by stratospheric ozone recovery. Geophys Res Lett 39(20):L20701
21. Holton JR, Hakim GJ (2013) An introduction to dynamic meteorology. Academic Press, Waltham, MA 02451, USA, p 552
22. National Oceanic and Atmospheric Administration's Space Environment Center. www.sec.noaa.gov
23. Oleson KW, Lawrence DM, Bonan GB, Flanner MG, Kluzek E, Lawrence PJ, Levis S, Swenson SC, Thornton PE, Dai A, Decker M, Dickinson R, Feddema J, Heald CL, Hoffman F, Lamarque J, Mahowald N, Niu G, Qian T, Randerson J, Tunning S, Sakaguchi K, Slater A, Stockli R, Wang A, Yang Z, Zeng X, Zeng X (2010) Technical description of version 4.0 of the community land model (CLM). NCAR/TN-478+STR. doi:10.5065/D6FB50WZ. http://nldr.library.ucar.edu/repository/assets/technotes/TECH-NOTE-000-000-000-848.pdf
24. Moderate-resolution Imaging Spectroradiometer NASA Webpage. http://modis.gsfc.nasa.gov/
25. Vadas SL, Liu H-L (2013) Numerical modelling of the large-scale neutral and plasma responses to the body forces created by the dissipation of gravity waves from 6 h of deep convection in Brazil. J Geophys Res: Space Phys 118:2593–2617. http://www.cora.nwra.com/~vasha/VadasLiu_JGR_2013.pdf
26. Vadas SL, Liu H-L (2009) Generation of large-scale gravity waves and neutral winds in the thermosphere from the dissipation of convectively generated gravity waves. J Geophys Res 114:A10310
27. Vasiliy V (2005) Generation of secondary internal waves by the interaction of an internal solitary wave with an underwater bank. J Geophys Res 110. doi:10.1029/2004JC002467
28. Kizzan M, Rodhe A, Xu C-Y, Ntale HK, Halldin S (2009) Temporal rainfall variability in the Lake Victoria Basin in East Africa during the twentieth century. Theor Appl Climatol 98:119–135. doi:10.1007/s00704-008-0093-6

doi:10.1186/s40562-014-0013-9
Cite this article as: Proedrou and Hocke: **A traveling atmospheric disturbance generated by a soil colour change in a high-resolution climate model experiment.** *Geoscience Letters* 2014 **1**:13.

7.2 Second article

The study was submitted in *Earth, Planets and Space Science* in March 2015. The reprint is the latest version of the article (submitted on 12.01.2016) and differs from the final published manuscript.

FULL PAPER

Characterizing the three-dimensional ozone distribution of a tidally locked Earth-like planet

Elisavet Proedrou[1,2*] and Klemens Hocke[1,2,3]

[*] Correspondence:
elisavet.proedrou@iap.unibe.ch
[1] Institute of Applied Physics, University of Bern Sidlerstrasse 5, CH-3012 Bern, Switzerland
Full list of author information is available at the end of the article
[†] Equal contributor

Abstract

We simulate the 3D ozone distribution of a tidally locked Earth-like exoplanet using the high-resolution, 3D chemistry-climate model CESM1(WACCM) and study how the ozone layer of a tidally locked Earth (TLE) ($\Omega_{TLE} = 1/365\, days$) differs from that of our present day Earth (PDE) ($\Omega_{PDE} = 1/1\, day$). The middle atmosphere reaches a steady state asymptotically within the first 80 days of the simulation. An upwelling, centred on the subsolar point is present on the day side, while a downwelling, centred on the antisolar point is present on the night side. In the mesosphere, we find quite similar global ozone distributions for the TLE and the PDE with decreased ozone on the day side and enhanced ozone on the night side. In the lower mesosphere, a jet stream transitions into a large-scale vortex around a low pressure system located at low latitudes of the TLE night side. In the middle stratosphere the odd oxygen concentration is approximately equal to the ozone concentration ($(O_x) \approx (O_3)$). At these altitudes the lifetime of odd oxygen is ~ 16 hours, and the transport processes significantly contribute to the global distribution of stratospheric ozone. Compared to the PDE where the strong Coriolis force acts as a mixing barrier between low and high latitudes, the transport processes of the TLE are governed by jet streams variable in zonal and meridional direction. In the middle TLE stratosphere, we find high ozone values on the day side, due to the increased atomic oxygen production on the day side where it immediately recombines with molecular oxygen to form ozone. On the night side on the other hand, the ozone is depleted. The downwelling air on the night side contributes to the decreased night side stratospheric ozone. As a result of the reduced Coriolis force the tropical and extratropical air masses are well mixed and the global temperature distribution of the TLE stratosphere has smaller horizontal gradients than the PDE. Compared to the PDE, the total ozone column global mean is reduced by ~ 19.3 %. The day side and the night side total ozone column means are reduced by 23.21 % and 15.52 %, respectively. Finally we present the TOC maps which would be seen by a remote observer for 4 phases of the TLE during its revolution around the star. The mean TOC values of the four phases of the TLE vary by up to 23%.

Keywords: exoplanet; tidally locked Earth; middle atmosphere; circulation; ozone layer; photochemistry; total ozone; daytime; day side; night side

1. Introduction

In this study we simulate and analyse the middle atmospheric ozone distribution of a tidally locked Earth-like exoplanet orbiting Sun-like star (TLE) using a realistic, high-resolution, 3D chemistry-climate model. Our main aim is to investigate the evolution of the TLE's ozone layer towards a steady state, determine its main characteristics and compare them to those of the present day Earth (PDE). This comparative study aims to increase our understanding of the role of photochemistry and transport processes in the middle atmosphere of exoplanets. We are also interested in the planet's total ozone column (TOC) and its day side-night side variation. In the case of the present day Earth, the day - night variation of the total ozone column is less than 2%.

An exoplanet's ozone layer can be observed by means of the 9.6 micrometer absorption line. The importance of the existence of an ozone layer lies in its ability to protect life on the surface of the planet from the harmful stellar UV radiation. It has been determined that for the generation of a protective ozone layer only a small amount of oxygen (0.1 of the present atmospheric levels) is sufficient enough[1].

Yang et. al (2014) [2] studied the dependence of a planet's habitability on its rotation rate using two 3D models, CAM3 and CCSM3. CAM3 was a 3D GCM standalone atmospheric circulation model, which calculated the atmospheric circulation and radiative transfer, as well as the small-scale vertical convection, clouds, and precipitation. CCSM3 was a 3D GCM coupled ocean-atmosphere model. Its ocean component calculated the ocean circulation using an ocean with uniform depth and albedo and no circulation. The CCSM3's atmospheric components were CAM3 or CAM4. They were able to simulate the marine stratus layered shallow convective, the deep convective clouds and the liquid and ice cloud condensates. CAM4 was a cloud scheme similar to CAM3 and an improved deep convection scheme. Both models were precursors of the model used in this paper. Their study focused on the troposphere of the simulated planets. They demonstrated that a slow rotating Earth-like planet (rotation speed = 1 rotation/243 days), located at a distance of 0.7 AU away from a Sun-like star would be habitable. They also determined that a Earth-like planet rotating at a rate of 1 rotation/day required half the stellar flux compared to a Earth-like planet rotating at a rate of 1 rotation/243 days to maintain an Earth like climate.

The abundance and close proximity of M stars, as well as their ease of detection due to a better mass and radius ratios of star and planet, make them prime targets for the search for terrestrial habitable exoplanets [3]. Due to the relatively small distance between an M star and its habitable planets, the planets have a high probability of becoming tidally locked.

Habitability studies performed for such tidally locked exoplanets by Haberle et al. (1996) [4], Joshi et al. (1997) [5], Joshi (2003) [6] have shown that terrestrial planets located in an M star's habitable zone (0.02 - 0.2 AU) [3] would be habitable as long as liquid water and the chemical constituents necessary for the emergence of life were present on them for a sufficiently long period of time. Furthermore, Segura et al. (2010) [7] concluded that the flares emitted by M stars should not present a threat for the surface life of an orbiting habitable planet. In our study we investigate the ozone distribution, and therefore the habitability, of a tidally locked exoplanet revolving around an M star using.

M stars have a weaker UV and visible emission, than the Sun, with the spectrum peeking in the infrared. The impact of different stellar spectral energy distributions on the ozone distribution of habitable non-tidally locked terrestrial extrasolar planets has been studied by [8], [9], [10], [11], [12], [13] and [14].

Selsis (2000) used a 1D atmospheric model to simulate the evolution of the chemical and thermal structure of the Earth if it was orbiting a F9 and K2 star. His simulations revealed that the amount of ozone increased with the increase of the UV/visible ratio. F9 stars have a higher UV/visible ratio than the Sun. K2 stars on the other hand, have a lower UV/visible ratio. The study also showed that the thickness of the ozone layer increased with the strength of the UV flux, resulting in higher amounts of ozone for the F9 planet and lower amounts for the K2 planet, compared to the Earth. Despite the decreased amounts of ozone, the K2 planet would have a visible O_3 spectral signature as a result of the temperature contrast between the surface and the atmosphere. The F9 planet would have no distinguishable ozone spectral signature, despite the planet's higher atmospheric ozone levels. [8].

Segura et al. (2003) used a 1D coupled radiative-convective photochemical model to calculate the spectra of Earth-like planets orbiting a F2V, a G2V, a K2V [9] and an M star [10], respectively. They determined that in the case of the F2V, G2V and K2V orbiting planets, the ozone 9.6 μm spectral line should be visible if the planet's O_2 concentration was at least 10^{-3} of the present Earth atmospheric levels (PAL). They also determined that at 1 PAL O_2 levels, the ozone concentration in an F2V planet, would be weaker than around a G2V or a K2V star. This result contrasts with the results produced by the [8] study. For the case of an active M star orbiting planet, Segura et al. found that an Earth-like ozone layer similar would develop, resulting in an observable O_3 9.6 μm spectral line, comparable to the Earth's [10].

Grenfell et al. (2007) used a 1D coupled radiative-convective photochemical column model to calculate the atmospheric composition changes on a planet with the Earth's atmospheric composition, when subjected to 5-10% changes of its orbital position around a solar-type G2V, F2V, and K2V star. They found that as the planets were moved outwards, the ozone increased by $\sim$ 10 %, as a result of the decreased stratospheric temperature [11].

Rugheimer et al. (2013) simulated the spectra of clear and cloudy Earth-like planets orbiting F, G and K stars, at the 1 AU equivalent distance, using a geometrical 1D model global atmosphere model. They determined that an increase in either the parent star's UV radiation or its temperature, resulted in increased O_3 concentrations and stronger O_3 spectral features. An increase in the star's temperature also resulted in increased O_3 concentrations and stronger O_3 spectral features [12].

Rauer et al. (2011) calculated the molecular molecular absorption bands of super-Earth planetary atmospheres orbiting M stars, using a plane-parallel, 1D climate model, coupled with a chemistry model. They predicted that the ozone emission spectra observed during a secondary eclipse for planets orbiting quiet M0 to M3 dwarfs would be stronger than the PDE. On the other hand, the ozone emission spectra of planets orbiting very cool and quiet M4 to M7 stars would be weaker, as a result of increases in their mid-atmospheric temperatures [13].

Grenfell et al. (2013) performed a sensitivity study of the atmosphere of an Earth-like planet, using a global-mean radiative-convective-photochemical column model. They varied the stellar class and planetary gravity of the planet and investigated how the changes affected the resulting photochemistry and climate and hence the potential observed biosignatures. Their study revealed that for an M0 star, the stratospheric ozone generation is still dominated by the Chapman cycle, but it is somewhat suppressed (89.2 %) compared to the Sun scenario (90.5 %). The ozone generation through the smog mechanism is increased (9.1 %) compared to the Sun scenario (0.8 %). The balance between the Chapman mechanism and the smog mechanism is shifted towards the smog mechanism as one moves towards cooler stars. For cool M5-M7 stars, the ozone photochemistry has shifted completely the Chapman production to smog-dominated stratospheric ozone production [15].

Godolt et al. (2015) studied the influence of F, G and K stars on the stratospheric temperature, climate and potential habitability of Earth-like extrasolar planets using a state-of-the-art 3D Earth climate model which accounts for local and dynamical processes. The planets were positioned at such orbital distances around the stars, so that the total amount of energy received from the parent stars would equal the solar constant. A fixed Earth-like atmosphere was used and no atmospheric chemistry calculations were performed. The study revealed that, similar to [8], [9], [10], [11], [12], [13] and [14], different stellar spectral energy distributions result in different ozone heating rates and therefore different vertical temperature structures. The stratosphere of planets orbiting K stars, which are cooler than our Sun and therefore emit a smaller portion of their radiation in the UV part of the spectrum, was characterised by lower ozone heating rates and shallower stratospheric temperature increases compared to the Earth [14].

The above studies demonstrated that for the same total amount of stellar energy incident on the top of the atmosphere, changes in the stellar spectral energy distribution result in ozone radiative heating rate changes. This leads to different stratospheric temperature structures in Earth-like exoplanets. For non-tidally locked, M star orbiting, planets, the reduced UV radiation emission, could result in the development of a cooler stratosphere and changes in their stratospheric ozone concentration. It is reasonable to assume that tidally locked planets would be equally affected.

The study of the ozone concentration of a tidally locked planet, would need to account for both the effects of the tidal lock and the altered stellar irradiance spectrum. This would complicate the cause effect attribution analysis making the attribution of the ozone distribution changes on either the tidal lock or the altered UV radiation exceedingly challenging. We therefore chose to not include the effects of the altered UV radiation in our study and focus only on the magnitude of the impact of tidal locking on the Earth-like planet orbiting a Sun-like star.

Past studies on the atmospheres of tidally locked Earth-like exoplanets were focused on the troposphere. Merlis and Schneider (2010) [16] used an ideal gas GCM with an active hydrological cycle, a gray radiation scheme and a slab ocean lower boundary condition to simulate the troposphere of an Earth-like, tidally locked aquaplanet with a rotation period equal to one Earth year. Their study revealed that while the subsolar point temperature in the lower troposphere is ~ 300 K, the antisolar point temperature is much smaller but it never drops below 240 K and therefore no atmospheric collapse occurs on the night side. Furthermore, they reported the presence of a strong upwelling above the subsolar point on the day side, due to radiative heating. On the night side they reported the presence of a downwelling, generated by radiative cooling, centred over the antisolar point.

Yang, Cowan and Abbot (2013) [17] showed that the presence of clouds in the troposphere of a tidally locked aquaplanet, especially over the subsolar point, can ensure habitability at almost twice the solar flux on Earth.

Grenfell et al. (2014) [18] performed a 1D simulation of an Earth-like exoplanet atmosphere using a global-mean, stationary, hydrostatic, atmospheric column model which extends from the surface up to ~ 70 km, with the starting composition, pressure and temperature of the 1976 U.S Standard Atmosphere [19]. In the simulation, the UV emission of a cool M7 star was varied and the resulting climate-photochemical response of the planetary atmosphere including numerous, catalytic processes of O_3 depletion was calculated. The study showed that the strongest O_3 emission is generated at ten times the stellar UV radiative flux of an M7 star and that an exoplanet's O_3 9.6 mum spectral line profile is strongly influenced by the 200–350 nm UV output of the parent star.

A fundamental parameter for the description and the observation of the planetary ozone layer is the total ozone column (TOC). Currently the Earth's TOC is measured by several satellite missions such as Aura/OMI [20] and Metop/GOME-2 [21] providing global maps of TOC with a horizontal resolution of 80 km x 40 km. The O_3 distribution is determined primarily by the Brewer-Dobson circulation and the photochemistry [22].

Below, we first describe the model used for our simulations and the simulation setup. Next we present the partial ozone content (POC) and TOC of the planet. Lastly we present four different phases of the planet's TOC as seen by an observer.

2. Model Description

The Community Earth System Model (CESM) version 1.04 is used to perform our simulation. It consists of five fully coupled geophysical models: atmosphere (ATM), land (LND), ocean (OCN), sea-ice (ICE), land-ice (GLC). The models can be set as fully prognostic, data or stub and are "state-of-the-art climate prediction and analysis tools" [23] when set in prognostic mode.

The surface parameter fluxes are provided by the land (LND), the ocean (OCN), the surface ice (GLC) and the sea ice (ICE) models. They provide the lower flux boundary conditions for the turbulent mixing, the planetary boundary layer parametrization, the vertical diffusion, and the gravity wave drag. In our simulation the OCN, GLC and ICE use prescribed data while the LND is an active model (Community Land Model (CLM)). CLM calculates among other parameters, the absorption, reflection and transmittance of solar radiation, the absorption and emission of longwave radiation, the surface colour variability, the surface albedo calculation, the sensible heat, the latent land surface heat fluxes, the heat transfer in soil and snow and the atmosphere-surface coupling [24].

The atmospheric model used in our simulation is the Whole Atmosphere Community Climate Model version 4 (CESM1(WACCM)) [24]. CESM1(WACCM) has been used to simulate the circulation, gravity waves and atmospheric composition changes due to chemistry and photochemistry in the lower, middle and upper atmosphere [25], [26], [27], [28], [29], [30], [31], [32]. Furthermore it is fully coupled to the land, and ocean models [23].

It has 66 vertical levels from the ground up to $5 \cdot 10^{-6}$ hPa (150 km) and is purely isobaric above 100 hPa. It has a vertical resolution of 1.1 km in the troposphere, 1.1-1.4 km in the lower stratosphere, 1.75 km at the stratopause and 3.5 km above 65 km. The coupler timestep is $\Delta t = 30$ minutes while the timestep for the dynamics equations is $\Delta\tau = \Delta t/8$ [24]. It has a composition identical to that of the present day Earth on 21.03.2000 [24].

CESM1(WACCM) has full tropospheric and stratospheric chemistry as well as mesospheric chemistry, with 57 chemistry species [24]. The gas-phase chemistry is coupled to the Modal Aerosol Model [24]. The stratospheric distributions of long-lived species are taken from previously performed CESM1(WACCM) simulations [24]. The main physical processes included in the model are:

- the conversion to and from dry and wet mixing ratios for trace constituents
- the moist turbulence
- the shallow and the deep convection
- the evaporation of convective precipitation
- the cloud microphysics and macrophysics

- the aerosol processes
- the condensed phase optics
- the radiative transfer
- the surface exchange formulations
- the dry adiabatic adjustment
- the prognostic greenhouse gases

[24].

The radiative transfer calculations in the longwave and shortwave are provided by the radiation code RRTMG ([33], [34], which is an accelerated and modified version of the correlated k-distribution model, RRTM. It efficiently calculates the irradiance and heating rate in broad spectral intervals, while retaining a high level of accuracy relative to measurements and high-resolution line-by-line models. It also distinguishes between the direct and scattered solar radiation.

The radiative transfer is calculated over 14 bands in the shortwave spectrum (0.2 μm to 12.2 μm) and 16 bands in the longwave spectrum (3.1 μm to 1000.0 μm). The 16$^{\text{th}}$ longwave band includes the infrared contribution from the spectral interval below 3.1 μm. Above 65 km the model also covers the spectrum interval between soft x-rays and extreme ultraviolet irradiances (0.05 nm to Lyman-α (121.6 nm) and the spectrum interval between the Lyman-α (121.6 nm) and 100 μm [24].

The total shortwave fluxes have an accuracy of 1-2 W/m^2 compared to the standard RRTM SW (using DISORT with 16 streams) for clear sky conditions and with aerosols and an accuracy of 6 W/m^2 in overcast sky conditions. The total longwave fluxes have an accuracy of 1.0 W/m^2 at all levels. "Longwave radiative transfer is performed over a single angle for one upward and one downward calculation" [24]. The absorption coefficients for the k-distributions for both the shortwave and the longwave radiation calculations in RRTMG are obtained from the line-by-line radiation model LBLRTM ([35], [36]).

The calculation of the photolysis coefficients is divided into the 120 nm - 200 nm and 200 nm - 750 nm regions. The total photolytic rate constants are calculated by the model by integrating the product of the wavelength dependent exo-atmospheric flux, the atmospheric transmission function, the molecular absorption cross-section and the quantum yield for each absorbing species. The exo-atmospheric flux is provided by observations and varies over the 11-year solar sunspot cycle. The transmission function is wavelength-dependent and a function of the model abundance of ozone and molecular oxygen. For wavelengths above 200 nm the molecular absorption cross-section and the quantum yield are calculated by the model, while below 200 nm, their values are pre-defined. This approach works for all species except NO and O_2 for which detailed photolysis parametrisations are included in the model. The impact of clouds on photolysis rates is parametrised but the impact of tropospheric and stratospheric aerosols on photolysis rates is not calculated [24].

The CESM model uses the Kurucz solar source function whose radiative transfer calculation is based upon solar measurements. It assumes a total solar irradiance at the top of the atmosphere of TSI = 1368.22 W/m^2. The value is then "scaled in each spectral band through the specification of a time-varying solar spectral irradiance" [24]. The model uses a combination of solar parametrizations to specify spectral irradiances over two spectral intervals (soft x-ray to Lyman-α (λ= 121.6 nm) and from Lyman-α to 100 μm). The first spectral interval fluxes are calculated using the parametrization of [37]. It accepts as input the 10.7 cm solar radio flux (f 10.7), whose daily values are obtained from the NOAA's Space Environment Center (www.sec.noaa.gov) and its 81-day average (f 10.7a). The second spectral interval fluxes are calculated using the empirical model of the wavelength-depending sunspot and facular influences ([38] and [39]) ([24]).

In the shortwave, H_2O, O_3, CO_2, O_2, CH_4, N_2, clouds, aerosols, and Rayleigh scattering are the modelled sources of absorption and scattering. In the longwave, H_2O, CO_2, O_3, N_2O, CH_4, O_2, N_2, $\mathrm{CFC}-11$ and $\mathrm{CFC}-12$ are the molecular sources of absorption. The shortwave radiation is calculated only for zenith angles larger than zero [24].

The model computes the chemical equilibrium of 36 photochemical species (O_2, O_3, N_2O, NO, NO_2, N_2O_5, HNO_3, NO_3, HO_2NO_2, CH_3OOH, CH_2O, H_2O, H_2O_2, Cl_2, ClO, OClO, Cl_2O_2, HOCl, HCl, $ClONO_2$, BrCl, BrO, HOBr, $BrONO_2$, CH_3Cl, Ccl_4, CH_3CCl_3, CFC11, CFC12, CFC113, HCFC22, CH_3Br, CF_3Br, CF_2ClBr, CO_2, CH_4). The model atmospheric tracers are O_x, NO_x, HO_x, ClO_x, and BrO_x chemical families, excluding O_2, along with CH_4 and its degradation products. The main photochemical and chemical interactions responsible for changing the atmospheric ozone concentration are described by the reaction rate of ozone $\frac{d(O_3)}{dt} + J_{O_3}(O_3) + k_3(O)(O_3)+a_2(H)(O_3)+a_6(OH)(O_3)+a_{6b}(HO_2)(O_3)+ b_4(NO)(O_3)+b_9(NO_2)(O_3)+ d_2(Cl)(O_3) + e_2(Br)(O_3) = k_2(M)(O_2)(O)$.

$\frac{d(O_3)}{dt}$ is the production rate of O_3. The J_{O_3} is the photolysis rate of ozone and its values were taken from different sources depending on its molecular absorption cross-section σ and the quantum yield (ϕ) (σ: 136.5-175 nm (Tanaka et al. (1953))), σ: 175-847 nm (Ackerman (1971)), σ: 185-350 nm (WMO (1985)), σ: 185-350 nm ϕ $<$ 280 nm (Marsh (1999)), $\phi >$ 280 nm ([40])). The $k_3, a_2, a_6, a_{6b}, b_4, b_9, d_2, e_2, k_2(M)$ are the chemical rate constants of the reactions and are taken from JPL06-2 [40].

A polar stratospheric cloud parametrization scheme is incorporated in the model. It is activated when the cosine of the solar zenith angle is larger than zero at stratospheric altitudes and the stratospheric temperature drops below 195 K [24].

The starting values of the zonal mean climatology of the local O_3 concentration, the temperature, the overhead column O_3 and other chemicals used by the model are based on satellite and in-situ Earth observations [24]. A detailed model description can be found in [24].

3. Methods

3.1. Simulation Setup

We perform two simulations, one for the present day Earth (PDE) with a rotation rate of $\Omega_{PDE} = 1 \left(\frac{\text{rotation}}{\text{days}}\right)$ and a second one for a tidally locked Earth-like exoplanet with a rotation rate of $\Omega_{TLE} = \frac{1}{365}\left(\frac{\text{rotation}}{\text{days}}\right)$. Therefore, the TLE rotation rate is $(\frac{1}{365})^{\text{th}}$ of the PDE rotation rate. The slow TLE rotation rate results in one side of TLE permanently facing the Sun-like star.

The Sun-Earth distance is 1 AU in both cases and the eccentricity is that of the present day Earth on the day of the Spring Equinox. In our simulation we use active, fully prognostic atmosphere and land geophysical models and a data ocean geophysical model. The solar irradiance at the top of the atmosphere is $S_0 = 1368.22\ \mathrm{W/m^2}$ [24]. The simulation begins on the day of the spring equinox (21.03.2000). The duration of the simulation is 90 days. Several model parameters are changed to obtain a tidally locked planet:

- obliquity
- the number of seconds in a siderial day
- the number of seconds the planet needs to rotate by 1 degree
- the cosine of the solar zenith angle (SZA)
- the position of the subsolar point
- the Sea Surface Temperature (SST)

The TLE's obliquity is set to 0 ° for the duration of the simulation. The number of seconds in a siderial day is altered from 86164 sec/day to $3.15 \cdot 10^{7}$ sec/day. As a result the earth's rotation velocity changes from $8.43 \cdot 10^{-10}$ rad/sec to $2.31 \cdot 10^{-12}$ rad/sec. The planet is set to rotate one degree every 87600 seconds (the Earth rotates one degree every 240 seconds). The SZA is set to a constant value by means of the PDE Julian date. By setting the Julian date to a constant value, the periodic 24-hour variation of SZA is stopped at all grid points of the TLE. The SZA is the central parameter for the assessment of the incoming solar radiation in the CESM model world. The position of the subsolar point is set to remain constant at (0.17° N, -178.17° E), which is the position of the subsolar point at 00:00 UT on the Spring Equinox.

The subsolar point and the distribution of the shortwave solar radiation at the top of the model for the duration of the simulation can be seen in Figure 1. Shades of red indicate high incoming solar radiation on the day side of the planet while shades of blue indicate low incoming solar radiation. The dark blue visible in the center of the figure indicates zero incoming radiation on the night side of the planet. The subsolar point is indicated with a white point on either side of Figure 1. It is centred approximately at (0°, 180°) over the Pacific Ocean. The antisolar point is indicated with a magenta point in the center of the figure and is centred approximately at (0°,0°).

The prescribed SST input dataset was altered to closely resemble the SST reported by Merlis and Schneider [16], which can be seen in Figure 2. The SST is highest at the subsolar point with a temperature $\approx$ 300 K and decreases monotonically and isotropically as one moves away from the subsolar point. The night side SST has a uniform value of 250 K.

The continents and topography of the Earth were maintained as the use of the standalone atmospheric geophysical model CESM1(WACCM) without an active land model is not supported. We emphasize that the initialization data is the same for both runs. This means that the TLE simulation run starts with the same 3D ozone and wind field as the PDE simulation run.

Although the possibility of tidal locking of an Earth-like planet within the habitable zone of a Sun-like star is low, the existence of Venus shows that a slow rotating planet can occur. As mentioned in the Introduction, Yang et. al. [2] demonstrated that very slowly rotating and tidally locked planets located at a distance of 0.7 AU from a Sun-like star, can maintain an Earth-like atmosphere despite their close distance to the parent star. Their models were designed for tropospheric simulations and lacked the full stratospheric chemistry and resolution available in CESM1(WACCM). Furthermore, several past studies of tidally locked exoplanets orbiting M stars used models with solar spectrum and atmospheric composition similar to that of the PDE [16], [6], [17], [41], [42], [43]. Our method therefore also fosters the intercomparison and interpretation of the differences with these past models. Lastly the use of the Earth's starting atmospheric composition for our simulations simplifies the intercomparison and interpretation of the differences between the PDE and TLE model runs.

3.2 Ensemble simulation

To verify the validity of our results, an ensemble simulation with 5 runs, is performed. This is the typical sensitivity setup used in atmospheric physics simulation studies. The first two runs are set 5 and 10 days before the spring equinox, respectively. One run is set on the day of the spring equinox. The last two runs are set 5 and 10 days after the spring equinox, respectively. The main features of the simulation, described in detail in the Results and Discussion section (Section 4), are present in the ensemble average and in each individual run, with the extend of the enhanced and depleted $\mathrm{TOC_{TLE}}$ regions varying slightly, in accordance with the variability of the starting conditions. The deviation from the ensemble average is of the order of ~ 1 % and can be seen in Table 1.

3.3 Data Analysis

The O_3 volume mixing ratio, the air density, the zonal, meridional and vertical wind as well as the downward shortwave flux are extracted from the output datasets of the simulation run. As a first step the above parameters are interpolated for the altitudes of 1 to 140 km with a variable step $1.7 < \text{step} < 104$ km. Then the O_3 concentration is calculated by multiplying the O_3 volume mixing ratio with the air number density $[O_3] = O_{3VMR} \cdot [air]$. It is useful to note that trace gases like ozone and atomic oxygen are usually given in volume mixing ratio (VMR).

As a next step, the POCs (partial ozone column densities) for the troposphere and lower stratosphere, middle stratosphere and mesosphere (5 to 28 km, 30 to 45 km and 55 to 100 km) are calculated by interpolating the O_3 concentration from the lower to the higher limits for each case $POC_{5-28} = \int_5^{28} [O_3]dz$, $POC_{30-45} = \int_{30}^{45} [O_3]dz$, $POC_{55-110} = \int_{55}^{110} [O_3]dz$.

Due to the presence of several high mountains and mountain ranges (e.g Himalayas, Kilimanjaro) and the presence of data gaps in the air density parameter above the altitude of 110 km, we calculate the TOC between the altitudes of 5 and 110 km ($TOC = \int_5^{110} [O_3]dz$).

As a next step, the global means of the TOC and POCs are calculated by calculating their zonal means as a function of latitude and then weighting them with the surface area of the latitude belts (surface area preserving mean). Then, the change in % of TOC and POC between the PDE and TLE is calculated.

$$\Delta TOC_{\%} = \frac{TOC_{TLE} - TOC_{PDE}}{TOC_{PDE}} * 100 \tag{1}$$

$$\Delta POC_{\%} = \frac{POC_{TLE} - POC_{PDE}}{POC_{PDE}} * 100 \tag{2}$$

$$\Delta TOC_{DU} = TOC_{TLE} - TOC_{PDE} \tag{3}$$

$$\Delta POC_{DU} = POC_{TLE} - POC_{PDE} \tag{4}$$

Lastly, we calculate the hemisphere means (HM) of PDE and TLE ($TOC_{HM(PDE)}$, $TOC_{HM(TLE)}$) as well as their differences ($\Delta TOC_{HM(PLE,TLE)}$, $\Delta TOC_{HM(TLE,TLE)}$, $\Delta TOC_{HM(PDE,PDE)}$). The TOC hemisphere mean is the TOC mean of one side of the planet which spans 180 ° in longitude and 180 ° in latitude. First calculating the hemisphere TOC zonal mean as a function of latitude and then weight it with the surface area of the hemisphere latitude belts (surface area preserving mean). $\Delta TOC_{(PLE,TLE)}$ is the difference between the hemisphere mean of the TLE and PDE. The $\Delta TOC_{(TLE,TLE)}$ is the difference between the TLE hemisphere centred around the 0° meridian and the hemisphere centred around the ϕ meridian. The $\Delta TOC_{(PDE,PDE)}$ is the difference between the PDE hemisphere centred around the 0° meridian and the hemisphere centred around the ϕ meridian.

$$\Delta TOC_{HM(PLE,TLE)} = \frac{TOC_{HM(PDE)} - TOC_{HM(TLE)}}{TOC_{HM(TLE)}} \tag{5}$$

$$\Delta TOC_{HM(TLE,TLE)} = \frac{TOC_{HM(TLE(0^\circ))} - TOC_{HM(TLE(\phi))}}{TOC_{HM(TLE(\phi))}} \tag{6}$$

$$\Delta TOC_{HM(PDE,PDE)} = \frac{TOC_{HM(PDE(0^\circ))} - TOC_{HM(PDE(\phi))}}{TOC_{HM(PDE(\phi))}} \tag{7}$$

3.4 Terminology

A tidally locked planet can be divided into the day side and the night side. The day side is the permanently illuminated hemisphere that is always facing the parent star. The position of the maximum solar flux, located at the centre of the day side is the subsolar point. The night side is the hemisphere that is never illuminated by the parent star. The position at the centre of the night side, located 180° away from the subsolar point, is the antisolar point. The border region of these two hemispheres, the terminator [3], is located 90° away from the subsolar and antisolar points and stretches from the North to the South Pole. This region can be divided into the dawn terminator region (located 90° to the West of the subsolar point) and the dusk terminator region (located 90° to the East of the subsolar point).

The VMR gives the amount of a trace gas in parts per million (ppmv), e.g. 10 ppmv means 10 ozone molecules per 1 million air molecules. The TOC is measured in Dobson units (DU). One Dobson unit "refers to a layer of gas that would be 10 μm thick under standard temperature and pressure" [44] and is equal to 2.69 10^{16} ozone molecules/cm^2, or 2.69 10^{20} ozone molecules/m^2 [44].

4. Results and Discussion

4.1 Atmospheric steady state

The TLE middle atmosphere adjusts to the new conditions within 80 days. The adjustment times of the TLE total ozone column ($\mathrm{TOC_{TLE}}$), the global mean horizontal wind ($\mathrm{HW_{TLE}}$), the global mean vertical wind ($\mathrm{VW_{TLE}}$) and the global mean stratospheric temperature ($\mathrm{T_{strat(TLE)}}$) to the new tidally locked conditions can be seen in Figure 3. The $\mathrm{HW_{TLE}}$, $\mathrm{VW_{TLE}}$ and $\mathrm{T_{strat(TLE)}}$ are calculated for the altitude region of 30 - 40 km altitude. In the figure the temporal evolution of the PDE $\mathrm{TOC_{PDE}}$, $\mathrm{HW_{PDE}}$, $\mathrm{VW_{PDE}}$ and $\mathrm{T_{strat(PDE)}}$ is also showed for comparison.

The steady atmospheric state is reached at double the e-folding time. The e-folding time is the time interval in which an exponentially decreasing quantity decreases by a factor of e. The e-folding times of the above mentioned parameters along with their steady-state mean values and their standard deviations can be seen in Table 2. A comparison between the TLE and the PDE standard deviations reveals that the PDE standard deviations are actually bigger than the TLE standard deviations.

The $\mathrm{TOC_{TLE}}$, $\mathrm{HW_{TLE}}$, $\mathrm{VW_{TLE}}$, $\mathrm{T_{strat(TLE)}}$ have an e-folding time of 30, 20, 15 and 40 days, respectively. Therefore the steady state is reached in approximately 60, 40, 30 and 80 days, respectively. A comparison between the PDE and the TLE adjustment times reveals that the TLE middle atmosphere adjusts to the new conditions within approximately 2.5 months and with global mean of total ozone maintaining a value of approximately 249 DU (Table 2).

4.2 Ozone distribution

The Earth has a primary, secondary and tertiary ozone layer, all of which can be seen in Figures 4a, 4b. They depict the ozone $\mathrm{O_3}$VMR distribution of the present day Earth at 00:00 UT, on the day of the Spring Equinox (21.03.2000) along the prime and the 180° meridian.

The primary ozone layer is located in the stratosphere between 20 and 50 km and displays a maximum in the vicinity of the tropics at an altitude of 34-36 km [22]. It is present during both the daytime and the night-time, though a small (< 2 %) diurnal variation has been detected [45]. The tropopause is characterized by altitude variations (visible in Figures 4a and 4b). It is located at higher altitudes in the tropics and lower altitudes in the poles.

The secondary ozone layer is located in the mesosphere between 80 and 100 km, with a maximum at $\sim$ 90 km. As can be seen in Figures 4a, 4b, the ozone is depleted during the daytime ($\sim$ 1 ppmv) compared to the night-time ($\sim$ 2.5 to 8 ppmv) [46], [47].

During daytime the stratospheric and mesospheric molecular oxygen is photodissociated towards atomic oxygen by the solar UV radiation ($\lambda < 242.4$ nm):

$$(J_2);\ O_2 + hv \rightarrow O + O \tag{8}$$

It then recombines with molecular oxygen, through the three body process recombination, to produce ozone.

$$(k_2);\ O + O_2 + M \rightarrow O_3 + M \tag{9}$$

M is a third body catalyst needed for the conservation of energy and momentum. In the stratosphere, the ozone generated through reaction 9 is photodissociated towards atomic oxygen by the UV radiation ($\lambda < 320$ nm) (Figure 4b).

$$(J_3);\ O_3 + hv \rightarrow O_2 + O \tag{10}$$

Due to the high air and molecular oxygen density O_2 and O rapidly recombine to form ozone through reaction 9. As a result the stratospheric diurnal variation is of the order of 2 % (Figures 4a,b).

In the mesosphere, the generated ozone is either photodissociated by UV radiation ($\lambda < 320$ nm) towards atomic oxygen through reaction 10 or converted to O_2 through a two-body collision with atomic oxygen.

$$(k_3);\ O + O_3 \rightarrow 2O_2 \tag{11}$$

During the night time, the absence of UV radiation results in the increase of the mesospheric ozone, through reaction 9 and the emergence of the secondary ozone layer (Figure 4a).

Ozone is destroyed not only through photodissociation by the incident UV radiation and interaction with O, but also through catalytic cycles with NO and OH. In the middle stratosphere [48] O_3 is destroyed by NO through

$$\begin{aligned} NO + O_3 &\rightarrow NO_2 + O_2 \\ NO_2 + O &\rightarrow NO + O_2 \end{aligned} \tag{12}$$

This catalytic cycle is most efficient between 35 and 45 km [22]. It is the most important ozone depletion cycle in the stratosphere. In the middle and upper stratosphere [22], O_3 is destroyed through

$$\begin{aligned} OH + O_3 &\rightarrow HO_2 + O_2 \\ HO_2 + O &\rightarrow OH + O_2 \end{aligned} \tag{13}$$

Below 30 km [48] and close to the troposphere [22], O_3 is destroyed through interaction with OH, by

$$\begin{aligned} OH + O_3 &\rightarrow HO_2 + O_2 \\ HO_2 + O_3 &\rightarrow OH + 2O_2 \end{aligned} \tag{14}$$

In the same altitude range

$$\begin{aligned} OH + O &\rightarrow H + O_2 \\ H + O_2 + M &\rightarrow HO_2 + M \\ HO_2 + O_3 &\rightarrow OH + 2O_2 \end{aligned} \tag{15}$$

and

$$\begin{aligned} OH + O &\rightarrow H + O_2 \\ H + O_3 &\rightarrow OH + O_2 \end{aligned} \tag{16}$$

are also responsible for the destruction of ozone [22].

In the mesosphere, ozone is destroyed primarily by OH [22].

$$\begin{aligned} OH + O &\rightarrow H + O_2 \\ H + O_3 &\rightarrow OH + O_2 \end{aligned} \tag{17}$$

The quantities of atomic oxygen and ozone fluctuate during the day as a result of the rapid cycles of photolysis and recombination. However their sum, also known as odd oxygen $\mathrm{O_x}$ remains almost constant. A reduction of ozone could indicate either the presence of a sink or an impermanent change towards atomic oxygen. A reduction of odd oxygen, on the other hand, reveals the presence of a sink a permanent sink. Consequently odd oxygen will be used to discuss the generation and destruction of ozone in this paper.

The PDE possesses a tertiary night-time ozone layer can be seen in Figure 4a in the region between 60 and 80 km in the vicinity of the North Pole. It was first detected and modelled by Marsh et al. [49] and is present only within a small region at high latitudes during the night-time.

The atmosphere of the TLE has a vertical structure similar to the PDE, with a troposphere, stratosphere and mesosphere. However the characteristics of these layers differ markedly from those of the PDE. Due to the tidal lock, the geographic locations of the daytime and night-time hemispheres are static.

Figures 4c, 4d depict the $\mathrm{O_3}$VMR distribution of the tidally locked Earth along the meridians intersecting the antisolar and subsolar points, respectively. The day side $\mathrm{O_3}$VMR of the TLE primary ozone layer (Figure 4d) is characterised by a higher $\mathrm{O_3}$VMR and a wider coverage area compared to its PDE daytime equivalent (Figure 4b). The night side of the TLE primary ozone layer on the other hand (Figure 4c), appears depleted compared to its PDE night-time equivalent (Figure 4b). Since the production of odd oxygen requires shortwave radiation, the night side displays a reduced ozone concentration compared to the day side. The TLE day-night side variation of the primary ozone layer is $\sim 40\%$, one order of magnitude larger than that of the PDE (< 2 %). The global mean altitude averaged middle atmospheric horizontal wind is 13.2 m/s in the TLE and 27.5 m/s in the PDE. The enhanced day-night side variation can be explained by this reduction in the transport velocities of ozone from the day side to the night side in the TLE stratosphere compared to the PDE stratosphere as well as the static locations of the daytime and night-time hemispheres. The primary TLE ozone layer is also characterised by altitude variations (Figures 4c, 4d), which are present in both the day and the night side, but are much less pronounced compared to the PDE (Figures 4a, 4b).

The TLE secondary ozone layer can also be seen in Figures 4c, 4d. As in the case of the rotating Earth, the secondary ozone layer is only present during night-time. The formation mechanism of the secondary ozone layer of TLE is similar to the observed night-time ozone layers present both the Earth's mesosphere and the upper atmosphere of Venus [50].

The day side TLE $\mathrm{O_3}$VMR (Figure 4d) is similar to the daytime PDE primary ozone layer (Figure 4b). The TLE night side secondary ozone layer (Figure 4c), is characterised by an enhanced $\mathrm{O_3}$VMR compared to the PDE night-time (Figures 4d, 4a, respectively). This is due to the transport of odd oxygen from the day side to the night side through both the horizontal and vertical circulation, where it recombines to form ozone. The transport of air from the day side to the night side in the 55 - 100 km altitude region through the horizontal circulation and the vertical circulation can be seen in Figures 6 and 8, respectively.

The TLE does not possess a tertiary night-time ozone layer as can be seen in Figure 4c. The chemical and dynamical processes that cause the disappearance of the TLE tertiary layer are currently an open question. It could be related to the fact that the air is not rapidly brought from the day to the night side in the case of the TLE compared to the PDE.

4.3 Atmospheric circulation

The PDE stratospheric ozone distribution is determined by the atmospheric wave driven Brewer-Dobson circulation, which is responsible for the transport of the air from the equatorial troposphere to the stratosphere. As can be seen in Figure 5, air rises from the tropical troposphere into the stratosphere. It is then transported towards the poles and descends back into the troposphere in middle and high latitudes, as a result of the conservation of mass [51], [52]. Due to the land-ocean distribution differences in the Southern and Northern Hemisphere, the Brewer-Dobson circulation differs in the two hemispheres, with a much stronger Southern winter polar vortex compared to the Northern winter polar vortex. As a result, the horizontal mixing seldom reaches the Antarctic region and is confined to lower latitudes in the Southern Hemisphere. In the Northern Hemisphere on the other hand, the horizontal mixing often reaches the North pole region [52].

In the TLE the vertical air transport is achieved through a different mechanism, as a result of the breakdown of the Brewer-Dobson circulation, which can be seen in Figures 6, 7 and 8. The middle atmospheric wind system of the TLE shows a high degree of spatio-temporal variability, with the direction and location of the TLE jet stream completely changing over height intervals of 10 km (Figure 6).

Figure 6 shows the zonal mean of the zonal wind for the PDE (Figure 6a) and the TLE (6b), from 5 to 110 km altitude. A comparison between the two figures reveals that the TLE zonal mean zonal wind is markedly different from the PDE equivalent. In the PDE the a southward air motion contributes to the geostrophic zonal wind. In the TLE on the other hand, the air motion is southward in the Northern Hemisphere and northward motion in the Southern hemisphere at tropospheric, middle stratospheric and mesospheric altitudes. It is therefore clear that there is a tendency for the formation of only one jet stream over the globe with a high wind speed in meridional or zonal direction at different altitudes. In the lower stratosphere, atmospheric transport can occur over the poles or along the equator from the day to the nightside depending on the altitude.

The meridional wind zonal mean of the TLE is smaller compared to the PDE, possibly due to smaller horizontal gradients in the temperature field of the TLE and the lack of the overturning circulation cells at the poles.

Figure 7 shows the horizontal wind at the select altitudes 24 km (Figure 7a), 36 km (Figure 7b) and 60 km (Figure 7c). As can be seen, the horizontal circulation differs greatly between different altitudes and this applies to the entire atmosphere. It also differs from the equivalent PDE circulation, which is not shown here. At lower and middle stratospheric altitudes jet streams are present, which encompass the entire globe, and whose strongest component is located in the equator. At 20 - 35 km the jet stream is eastward while at 35 - 40 km altitude the jet stream is westward, as can be seen in Figures 7a and 7b. The strong natural variability of the lower stratospheric wind field leads to considerable periodic changes ($\approx$ 15 days) in the distribution patterns of lower stratospheric ozone (16-28 km), while at the same time the global mean of total ozone is maintained. The PDE circulation at these altitudes is characterised by the presence of a westward equatorial jet stream and two eastward extra-tropical jet streams. At mesospheric altitudes, the meandering jet stream can transit into large-scale vortices as can be seen in Figure 7c). In comparison, in the PDE the circulation is largely eastward in the Northern hemisphere and westward in the Southern hemisphere, with no vortices present.

The Brewer-Dobson circulation is replaced by an upwelling on the day side of the planet and a downwelling on the night side. The upwelling is centred in the subsolar point, while the downwelling is centred on the antisolar point. Both extend from the surface to the middle mesosphere. The day side receives a constant flux of solar radiation and is radiatively heated. The upwards movement of the heated air creates the reported upwelling. The night side on the other hand, receives no solar radiation and is therefore radiatively cooled, with the cooler air sinking and creating the reported downwelling. However compared to the PDE the TLE has a much smaller temperature gradient compared to the PDE, as can be seen in Figure 9 for the altitude of 36 km.

Merlis and Schneider [16] also predicted the presence of an upwelling on the day side, centred on the subsolar point and a downwelling on the night side, centred over the antisolar point, in their simulated tidally locked aquaplanet troposphere. They also attributed the upwelling to radiative heating and the downwelling to radiative cooling.

4.4 Mesospheric Partial Ozone Column

On the Earth's mesospheric daytime hemisphere, the atomic oxygen is more abundant than ozone, so atomic oxygen can be used as a measure of odd oxygen $((\mathrm{O_x}) \approx (\mathrm{O}))$. Figure 10a depicts the PDE mesospheric POC ($\mathrm{POC_{PDE(55-110)}}$) at 00:00 UT on the day of the spring equinox. The ozone is depleted on the daytime side of the planet and enhanced on the night-time side of the planet. A sharp transition region, between the daytime and the night-time hemispheres is present. The partitioning of odd oxygen is towards atomic oxygen on the daytime and towards ozone on the night-time hemisphere, respectively. At these altitudes the lifetime of odd oxygen ranges between a few hours at 55 km, to $\sim$ 1 month at 95 km. After sunset, the atomic oxygen rapidly recombines to form ozone as can be seen in Figure 10a. The mean PDE night side POC is 0.40 DU and the mean PDE day side POC is 0.23 DU. Therefore the PDE mesospheric diurnal variation is $\sim$ 74% with respect to the daytime.

The night-time mesospheric TLE ozone is well mixed from the equator to the poles (Figure 10e). The day side ozone is visibly depleted due to the planet's tidal lock, with O_2 and O_3 constantly photodissociated towards odd oxygen. Due to its long lifetime, odd oxygen is then transported, through the horizontal circulation, as can be seen in Figure 6, from the day to the night side where it recombines to form ozone. The ozone is further enhanced by the transportation of odd oxygen-rich air to the night side through the vertical circulation by means of an upwelling centred over the subsolar point and then a downwelling centred on the antisolar point, where it recombines to form ozone. Consequently the POC appears enhanced on the night side compared to its PDE counterpart. From Figure 10e we have determined that the mean TLE night side POC is 0.40 DU and the mean TLE day side POC is 0.28 DU. Therefore the TLE mesospheric day-night side variation is $\sim$ 43 % with respect to the day side. This is a considerable decrease compared to its PDE counterpart.

4.5 Stratospheric Partial Ozone Column

The $\mathrm{O_3}$VMR is much more abundant than atomic oxygen in the Earth's stratosphere. Therefore in the stratosphere odd oxygen is used as a measure of ozone $((\mathrm{O_x}) \approx (\mathrm{O_3}))$.

4.5.1 Middle Stratospheric Partial Ozone Column

The PDE middle stratosphere ranges from 30 to 45 km and is the region with the highest stratospheric $\mathrm{O_3}$VMR. At these altitudes the ozone distribution is governed mainly by the photochemistry and to a smaller degree by the dynamics. Odd oxygen is mainly generated during the daytime through photolysis of molecular oxygen (reaction (8))and has an average lifetime of $\tau_{\mathrm{O_x}} \sim 16.5$ days. It is destroyed during the night-time through recombination with atomic oxygen (reaction (11)) and catalytic chemical reactions by NO and OH [22].

In Figure 10b, the Earth's middle stratospheric ozone is displayed. The increased solar radiation flux that the equatorial latitudes receive, leads to enhanced ozone generation. Due to its relatively long lifetime as well as the strong Coriolis force odd oxygen remains enhanced during the night-time and therefore displays a small diurnal variation ($< 5\%$) [45]. As can be seen in Figure 10b the POC has a zonal latitudinal dependence as a result of the strong Coriolis force which creates a mixing barrier. Consequently the middle stratospheric POC ($\mathrm{POC_{PDE(30-45)}}$) is enhanced in the tropics and depleted in the poles.

In Figure 10f, the TLE's middle stratospheric ozone is displayed. On the TLE the ozone is only generated on the day side and transported to the night side through the horizontal circulation. On the night side ozone is depleted through reactions with O and catalytic cycles. The global mean transport velocities between the day and the night side of the middle stratosphere (13 m/s) are smaller by 47 % compared to the mesosphere (25 m/s), so the mixing between the day and the night side occurs at a slower rate. Furthermore, the middle stratospheric global mean temperature is reduced in the TLE compared to the PDE as can be seen in Figure 9. As a consequence the ozone generation rates on the day side will be increased, resulting in a visibly enhanced POC. On the night side, a combination of the lack of shortwave radiation flux, increased destruction rates and slow transport velocities leads to a visibly depleted night side POC and a high day-night side difference. The above effects are further enhanced by the large scale meridional mixing due to the small Coriolis force. As can be seen in Figure 10f, the mean night side POC is 45 DU and the mean day side POC is 58 DU. Therefore the TLE day - night side middle stratospheric ozone variation is $\sim$ 29 % with respect to the night side, one order of magnitude larger than the PDE middle stratospheric diurnal variation.

4.5.2 Lower Stratospheric and Tropospheric Partial Ozone Column

The PDE lower stratosphere ranges from 14 to 28 km and the troposphere ranges from the surface to 14 km approximately. Figure 10c displays the PDE lower stratospheric and tropospheric POC ($\mathrm{POC_{PDE(5-28)}}$). At these altitudes the odd oxygen (and therefore ozone) has a lifetime of several months due to the attenuation of the

UV radiation flux at higher altitudes and as a result the ozone distribution is influenced mainly by the dynamics. The Brewer-Dobson circulation transports ozone-rich air from the mid-stratosphere to the polar regions where the overturning circulation cell shifts the ozone-rich air into the lower polar stratosphere [22] where it accumulates. The PDE lower stratospheric diurnal variation is ~ 0.1 %, which is in agreement with the diurnal variation observed by the SMILES experiment on the International Space Station [45]. The PDE tropospheric [O_3] is lower by an order of magnitude compared to the stratosphere and therefore does not contribute considerably to the $\mathrm{POC}_{\mathrm{PDE}(5-28)}$.

In the lower TLE stratosphere the ozone, which was concentrated in extra-tropical latitudes at the start of the simulation, was transported, through the horizontal and vertical circulation, to the night side of the planet where it accumulated, generating the high levels of ozone visible in the Southern night side. Furthermore any ozone generated on the day side of the planet is transported, through the horizontal and vertical circulation, to the night side of the planet where it accumulates due to its long lifetime. As a result, the $\mathrm{POC}_{\mathrm{TLE}(5-28)}$ appears depleted on the day side and enhanced on the night side (Figure 10g).

Due to the small value of the Coriolis force, large scale meridional mixing takes place. The mean night side POC is 181 DU and the mean day side POC is 158 DU (Figure 10g). Therefore the lower TLE stratospheric day-night side variation is ~ 13 % with respect to the day side, which is two orders of magnitude higher compared to the PDE. The TLE tropospheric [O_3] is lower by two orders of magnitude compared to the stratosphere and therefore also does not contribute considerably to the $\mathrm{POC}_{\mathrm{TLE}(5-28)}$.

4.6 Total Ozone Column

Selsis [8], Segura et al. [10], Rugheimer et al. [12], Rauer et al. [13], Grenfell et al. (2007) [11] and Kaltenegger et al. [53] predicted that exoplanets orbiting around F, G, K and M stars would produce a visible ozone spectral signature, with the strength of the signature varying depending on star's UV radiation emission as well as the planet's molecular oxygen content. A planet's spectral ozone signature is derived from the planet's TOC, though the relation is not linear, as it also depends on the planet's temperature structure and the distribution, the vertical ozone profile, the line of sight towards the observer, other atmospheric constituents and other factors.

The $\mathrm{TOC}_{\mathrm{TLE}}$ (Figure 10h) displays enhanced O_3 columns on both the day and the night side and is characterised by a well mixed meridional TOC distribution ($\mathrm{TOC}_{\mathrm{TLE}}$). A comparison between Figures 10f, 10g and Figure 10h reveals that the main characteristics of the $\mathrm{TOC}_{\mathrm{TLE}}$ are formed in the lower and middle stratosphere.

Specifically, the enhanced TLE night side TOC features originate in the lower stratosphere and are due to transportation of ozone generated on the day side to the night side (Figures 10h, 10g) through the horizontal and vertical circulation. The enhanced TLE day side TOC features are generated by the combined enhanced middle stratospheric POC (Figure 10f) and the depleted day side lower stratospheric POC (Figure 10g) and are therefore produced by a combination of photochemistry and dynamics. The depleted feature present on the left side of the globe (over the American continent) originates partly in the lower and partly in the middle stratosphere. In the lower stratosphere (Figure 10g) the depletion appears as a result of the transport of the ozone depleted air present at the start of the simulation in the tropics, to their current location through the horizontal and vertical circulation. In the middle stratosphere (Figure 10f) the depletion is the result of the lack of UV radiation on the night side of the planet combined with downwelling of ozone poor air from the mesospheric day side (Figure 10e).

The PDE and TLE TOC global means are presented in Table 3. The day and night side PDE and TLE hemisphere means are presented in Table 4. The $\mathrm{TOC_{TLE}}$ global mean is 244.05 DU, while the $\mathrm{TOC_{PDE}}$ global mean is 291.14 DU. The $\mathrm{TOC_{TLE}}$ global mean is therefore reduced by 19.3 % compared to the $\mathrm{TOC_{PDE}}$ global mean. Therefore the TLE O_3 global concentration is depleted compared to the equivalent PDE, but not the extent that would render the planet hostile for life. The day side TLE O_3 concentration is also depleted compared to the daytime PDE O_3 daytime concentration, though it still remains within the limits of habitability.

The $\mathrm{POC_{TLE(5-28)}}$ global mean is reduced by 27.7%, while the $\mathrm{POC_{TLE(30-45)}}$ global means is increased by 0.8%, respectively compared to the PDE. As mentioned before, due to the long lifetime of odd oxygen (and hence ozone) at these altitudes, the $\mathrm{POC_{TLE(5-28)}}$ reduction can be attributed to the changed dynamics, which play a dominant role at these altitudes. The increased $\mathrm{POC_{TLE(30-45)}}$ on the other hand can be attributed equally to the influence of dynamics and photochemistry, due to the shortened lifetimes of odd oxygen at these altitudes. The $\mathrm{POC_{TLE(55-110)}}$ global mean is increased by 7.2% compared to the PDE and at these altitudes can be attributed to the effects of photochemistry and transport of atomic oxygen. This increase has no major impact on the $\mathrm{TOC_{TLE}}$ due to the small $\mathrm{POC_{TLE(55-110)}}$ value (< 1 DU). As the bulk of the $\mathrm{TOC_{TLE}}$ is provided by the stratosphere, the reduction of the $\mathrm{TOC_{TLE}}$ can be attributed equally on the changed dynamics and photochemistry.

4.7 Phases of the TLE

As the planet moves around its parent star, different phases of the planet become visible to the observer (Figure 11). The figure is an alteration of a figure by Winn [54]. At any given time, only one side of the planet will be visible to the observers. It is therefore of interest to present the hemisphere TLE TOC and compare it with that of the PDE.

We present the hemispheric TOC maps of the phases $\varphi = 0°$, $\varphi = 90°$, $\varphi = 180°$ and $\varphi = 270°$ of our simulated exoplanet. In phase $\varphi = 0°$, only the planet's day side is visible. In phases $\varphi = 90°$ and $\varphi = 270°$, half of the day side and half of the night side become visible. In phase $\varphi = 180°$ only the night side is visible. Only the TOC values which are radially integrated from the surface to the top of the atmosphere are shown.

Figures 12a, 12b, 12c, 12d show these phases for the PDE. The phases are characterised by high ozone values at high latitudes. An observer at a far distance would not notice a difference in the TOC maps of the PDE.

The situation is different for the TLE. An observer would notice TOC depletion or enhancement depending on the observed hemisphere. This can be seen in Figures 12e, 12f, 12g and 12h which present the $\mathrm{TOC_{TLE}}$ of the subsolar hemisphere ($\mathrm{TOC_{TLE(0°)}}$), the dusk hemisphere ($\mathrm{TOC_{TLE(90°)}}$), the antisolar hemisphere ($\mathrm{TOC_{TLE(180°)}}$) and the dawn hemisphere ($\mathrm{TOC_{TLE(270°)}}$), respectively.

The % change $\Delta TOC_{(TLE,TLE)}$ in their hemisphere mean compared to the ($\mathrm{TOC_{TLE(0°)}}$) can be seen in Table 6. It is clear that the $\mathrm{TOC_{TLE(90°)}}$ is depleted compared to the $\mathrm{TOC}_{\mathrm{TLE}(270^\circ)}$. It is characterised by low O_3 columns, with the depleted region coinciding with the TLE dusk region (Figure 12f).

The $\mathrm{TOC}_{\mathrm{TLE}(180^\circ)}$ (Figure 12g) is enhanced compared to the $\mathrm{TOC}_{\mathrm{TLE}(0^\circ)}$ (Figure 12e) and is characterised by high O_3 concentrations between the antisolar point (depicted with a white point) and the subsolar point (depicted with a black point), and low concentrations towards the North-West part of the hemisphere.

A comparison between the $\mathrm{TOC}_{\mathrm{PDE}}$ and $\mathrm{TOC}_{\mathrm{TLE}}$ values in Table 5 reveals that the $\mathrm{TOC}_{\mathrm{TLE}}$ is depleted compared to the $\mathrm{TOC}_{\mathrm{PDE}}$ no matter which hemisphere is observed.

It is therefore clear that the $\mathrm{TOC}_{\mathrm{TLE}}$ distribution will differ depending on which side of the planet is observed. The difference of the four phases between the PDE and the TLE is on average $\Delta TOC \sim 20$ %. Depending on the temperature structure of the atmosphere, the vertical ozone profile and other factors the change in the observed spectral line can be at most 10 %. Since the measurement errors of the observed exoplanet spectra currently range between 10-30% [55], the difference will not be critical for observations at present. However as bigger telescopes and improved observing and data analysis techniques are developed, the hemispheric TOC differences of the tidally locked exoplanets might be detectable.

5. Conclusions

We discussed and compared the 3D ozone distributions of the present day Earth (PDE) and a tidally-locked Earth-like exoplanet revolving around a Sun-like star (TLE). We demonstrated that it is possible to simulate the middle atmosphere of a tidally-locked Earth-like exoplanet using the realistic, high-resolution, 3D chemistry-climate model (CESM1(WACCM)). We further demonstrated that the simulation achieves a steady state for the middle atmosphere within 80 days.

A comparison between the middle atmospheres of the PDE and TLE reveals that the TLE ozone distribution is greatly altered due to the reduced Coriolis force and the break down of the Brewer-Dobson circulation. The TLE simulation shows an upwelling centred over the day side and a downwelling centred over the night side. The primary ozone layer is enhanced on the day side and depleted on the night side compared to its PDE equivalent. The secondary ozone layer is enhanced on the night side, while the day side remains relatively unchanged and the tertiary ozone layer disappears.

We studied the TOC of four phases of the planet, with respect to a remote observer. The TOC hemisphere means are reduced by ~ 19.8 % compared to the PDE.

The observations conducted with our existing telescopes have a 30 % error margin, which is approximately 1.5 times higher than the $\approx 20\%$ TOC change. Therefore even though the TOC of the TLE greatly differs from that of the PDE, it is not possible, with our current technology, to detect the difference and the observations will therefore not be affected.

The atmospheric phenomena discussed in this paper are generated as a result of the interplay between photochemistry and dynamics, making the study of the middle atmosphere of Earth-like planets a new branch of research.

In the present paper we focused on the ozone distribution of an Earth-like tidally locked planet, only briefly mentioning the planet's atmospheric circulation. However, the variable jet streams and large-scale vortices in the middle atmosphere of the TLE are astonishing. More investigations with advanced data analysis techniques are required to describe the 3D circulation of the TLE. A 3D study of a tidally locked Earth-like planet orbiting an M dwarf star where both the different stellar spectrum and the tidal lock are included in the model is also a possible future project.

When only atmospheric chemistry is considered, as in the case of Segura et al. 2005 [10], the total ozone column of an Eartn-like planet is determined by the stellar spectrum's UV radiation. The use of a flaring M star spectrum, whose UV radiation output in the 200 nm region is comparable to the Sun's, results in no decrease and even an increase of the total ozone column. The use of a quiescent M star spectrum on the other hand, whose UV output in the 200 nm region is more than three order of magnitude lower than the Sun's, results in a decrease of the total ozone column by 40 %.

When dynamics but no photochemistry or atmospheric chemistry are considered, as in the case of the 3D Godolt et. al 2015 study [14] the stratospheric temperature of an Earth-like planet is also determined by the stellar spectrum's UV radiation. Higher UV radiation (e.g an F star spectrum) results in increased stratospheric temperatures, while lower UV radiation (e.g a K star spectrum) leads to decreased stratospheric temperatures. Had the simulations included photochemistry and atmospheric chemistry, their outcomes would possibly show a different behaviour than described above.

The ozone generation and destruction rates depend on the ambient temperature, the abundance of atomic and molecular oxygen, and the photodissociation of the ozone molecules by the stellar UV radiation. Therefore, the final total ozone column will depend on the balance reached between these three processes, whose prediction is not trivial. A combination of tidal locking and a spectrum change, will probably result in the overall decrease of the planet's total ozone column, compared to a spectrum change-only simulation.

List of abbreviations used
ATM = Atmosphere model
CESM = Community Earth System Model
CICE = Sea-Ice data model
CLM = Community Land Model
CPL = Coupler to CESM
GLC = Land-Ice geophysical model in CESM
ICE = Sea-Ice geophysical model in CESM
docn = prescribed data ocean model
LND = Land geophysical model in CESM
MODIS = Moderate-resolution Imaging Spectroradiometer
OCN = Ocean geophysical model in CESM
WACCM = Whole Atmosphere Community Climate Model
NOAA = National Oceanic and Atmospheric Administration
PDE = present day Earth
TLE = tidally locked Earth
TOC = Total ozone column
POC = Partial ozone column
$\mathrm{TOC_{PDE}}$ = TOC for the PDE
$\mathrm{TOC_{TLE}}$ = TOC for the TLE
$\mathrm{POC_{PDE}}$ = POC for the PDE
$\mathrm{POC_{TLE}}$ = POC for the TLE
$\mathrm{POC_{PDE(5-28)}} = \mathrm{POC_{(5-28)}}$ for the PDE
$\mathrm{POC_{TLE(5-28)}} = \mathrm{POC_{(5-28)}}$ for the TLE
$\mathrm{TOC_{PDE(0^\circ)}} = 0^\circ$ phase of the PDE
$\mathrm{TOC_{TLE(0^\circ)}} = 0^\circ$ phase of the TLE

Competing interests

The authors declare that they have no competing interests.

Author's contributions

EP performed the simulations, data analysis and interpretation. KH contributed to the data analysis and interpretation. Both authors read and approved the final manuscript.

Acknowledgements

We would like to thank the Center for Space and Habitability (University of Bern) for the PhD fellowship that made this study possible. We would like to thank the WACCM forum for the invaluable information it provided. We would also like to thank Ansgar Schanz and Martin Lainer for the computer technical support they provided. Finally we would like to thank Niklaus Kämpfer, Peter Wurz and Helmut Lammer for the valuable discussions and advises.

References

Author details

[1]Institute of Applied Physics, University of Bern Sidlerstrasse 5, CH-3012 Bern, Switzerland. [2]Center for Space and Habitability, University of Bern, Sidlerstrasse 5, CH-3012 Bern, Switzerland. [3]Oeschger Centre for Climate Change Research, University of Bern, Falkenplatz 16, CH-3012 Bern, Switzerland.

References

1. Kasting, J.F., Donahue, T.M.: The evolution of atmospheric ozone. journal of Geophysical Research **85**, 3255–3263 (1980). doi:10.1029/JC085iC06p03255
2. Yang, J., Boué, G., Fabrycky, D.C., Abbot, D.S.: Strong Dependence of the Inner Edge of the Habitable Zone on Planetary Rotation Rate. The Astrophysical journal Letters **787**, 2 (2014). doi:10.1088/2041-8205/787/1/L2
3. Tarter, J.C., Backus, P.R., Mancinelli, R.L., Aurnou, J.M., Backman, D.E., Basri, G.S., Boss, A.P., Clarke, A., Deming, D., Doyle, L.R., Feigelson, E.D., Freund, F., Grinspoon, D.H., Haberle, R.M., Hauck, S.A.I., Heath, M.J., Henry, T.J., Hollingsworth, J.L., Joshi, M.M., Kilston, S., Liu, M.C., Meikle, E., Reid, I.N., Rothschild, L.J., Scalo, J., Segura, A., Tang, C.M., Tiedje, J.M., Turnbull, M.C., Walkowicz, L.M., Weber, A.L., Young, R.E.: A reappraisal of the habitability of planets around m dwarf stars. Astrobiology **7**, 30–65 (2007). doi:10.1089/ast.2006.0124
4. Haberle, R.M., McKay, C.P., Tyler, D., Reynolds, R.T., Doyle, L.R.: Can synchronously rotating planets support an atmosphere? In: Doyle, L.R. (ed.) Circumstellar Habitable Zones, Proceedings of The First International Conference, Menlo Park, CA, p. 29 (1996). Travis House Publications
5. Joshi, M.M., Haberle, R.M., Reynolds, R.T.: Simulations of the atmospheres of synchronously rotating terrestrial planets orbiting m dwarfs: Conditions for atmospheric collapse and the implications for habitability. Icarus **129**, 450–465 (1997)
6. Joshi, M.: Climate model studies of synchronously rotating planets. Astrobiology **3**, 415–427 (2003). doi:10.1089/153110703769016488
7. Segura, A., Walkowicz, L.M., Meadows, V., Kasting, J., Hawley, S.: The Effect of a Strong Stellar Flare on the Atmospheric Chemistry of an Earth-like Planet Orbiting an M Dwarf. Astrobiology **10**, 751–776 (2010). doi:10.1089/ast.2009.037
8. Selsis, F.: Review: Physics of Planets I Darwin and the Atmospheres of Terrestrial Planets. In: Schü"rmann, B. (ed.) Darwin and Astronomy the Infrared Space Interferometer. ESA Special Publication, vol. 451, p. 133 (2000)
9. Segura, A., Krelove, K., Kasting, J.F., Sommerlatt, D., Meadows, V., Crisp, D., Cohen, M., Mlawer, E.: Ozone Concentrations and Ultraviolet Fluxes on Earth-Like Planets Around Other Stars. Astrobiology **3**, 689–708 (2003). doi:10.1089/15311070332273602
10. Segura, A., Kasting, J.F., Meadows, V., Cohen, M., Scalo, J., Crisp, D., Butler, R.A.H., Tinetti, G.: Biosignatures from Earth-like planets around M-dwarfs. Astrobiology **5**, 706–725 (2005). doi:10.1089/ast.2005.5.70
11. Grenfell, J.L., Stracke, B., von Paris, P., Patzer, B., Titz, R., Segura, A., Rauer, H.: The response of atmospheric chemistry on earthlike planets around F, G and K Stars to small variations in orbital distance **55**, 661–671 (2007). doi:10.1016/j.pss.2006.09.00
12. Rugheimer, S., Kaltenegger, L., Zsom, A., Segura, A., Sasselov, D.: Spectral Fingerprints of Earth-like Planets Around FGK Stars **13**, 251–269 (2013). doi:10.1089/ast.2012.088
13. Rauer, H., Gebauer, S., Paris, P.v., Cabrera, J., Godolt, M., Grenfell, J.L., Belu, A., Selsis, F., Hedelt, P., Schreier, F.: Potential Biosignatures in Super-Earth Atmospheres I. Spectral appearance of super-Earths around M dwarfs. Astronomy & Astrophysics **529**, 8 (2011). doi:10.1051/0004-6361/20101436
14. Godolt, M., Grenfell, J.L., Hamann-Reinus, A., Kitzmann, D., Kunze, M., Langematz, U., von Paris, P., Patzer, A.B.C., Rauer, H., Stracke, B.: 3D climate modeling of Earth-like extrasolar planets orbiting different types of host stars. Planetary and Space Science **111**, 62–76 (2015). doi:10.1016/j.pss.2015.03.01
15. Grenfell, J.L., Gebauer, S., Godolt, M., Palczynski, K., Rauer, H., Stock, J., von Paris, P., Lehmann, R., Selsis, F.: Potential Biosignatures in Super-Earth Atmospheres II. Photochemical Responses. Astrobiology **13**, 415–438 (2013). doi:10.1089/ast.2012.0926
16. Merlis, T.M., Schneider, T.: Atmospheric dynamics of earth-like tidally locked aquaplanets. journal of Advances in Modeling Earth Systems **2**, 13 (2010). doi:10.3894/JAMES.2010.2.13
17. Yang, J., Cowan, N.B., Abbot, D.S.: Stabilizing cloud feedback dramatically expands the habitable zone of tidally locked planets. The Astrophysical journal Letters **771**, 45 (2013). doi:10.1088/2041-8205/771/2/L45
18. Grenfell, J.L., Gebauer, S., Paris, P.v., Godolt, M., Rauer, H.: Sensitivity of biosignatures on Earth-like planets orbiting in the habitable zone of cool M-dwarf Stars to varying stellar UV radiation and surface biomass emissions. Planetary and Space Science **98**, 66–76 (2014). doi:10.1016/j.pss.2013.10.00
19. National Oceanic & Atmospheric Administration, U.s.A.F. National Aeronautics & Space Administration: U.S. Standard Atmosphere, U.S. Government Printing Office, Washington, D.C., 1976 (1976)
20. Veefkind, J.P., de Haan, J.F., Brinksma, E.J., Kroon, M., Levelt, P.F.: Total ozone from the ozone monitoring instrument (omi) using the doas technique. IEEE Geoscience and Remote Sensing Society **44**, 1239–1244 (2006). doi:10.1109/TGRS.2006.871204

21. Valks, P.J.M., de Haan, J.F., Veefkind, J.P., van Oss, R.F., Balis, D.S., pp. 129–130. University of Athens, Athens, University of Athens (2004)
22. Brasseur, P.G., Solomon, S.: Aeronomy of the Middle Atmosphere, Chemistry and Physics of the Stratosphere and Mesosphere, Chemistry and Physics of the Stratosphere and Mesosphere, Third Revised and Enlarged Edition, 3rd edn. Springer, P.O. Box 17, 3300 AA Dordrecht, The Netherlands (2005)
23. Vertenstein, M., Craig, T., Middleton, A., Feddema, D., Fisher, C.: CESM 1.0.4 User's Guide (2012). available from: http://www.cesm.ucar.edu/models/cesm1.0/cesm/cesm_doc_1_0_4/ book1.html
24. Neale, R.B., Gettelman, A., Park, S., Chen, C., Lauritzen, P.H., Williamson, D.K., Conley, A.J., Kinnison, D., Marsh, D., Smith, A.K., Vitt, F., Garcia, R., Lamarque, J.F., Mills, M., Tilmes, S., Morrison, H., Cameron-Smith, W., Collins, W.D., Iacono, M.T., Easter, R.C., Liu, X., Ghan, S.J., Rasch, P.J., Taylor, M.A.: Description of the NCAR Community Atmosphere Model (CAM 5.0) (2012). http://www.cesm.ucar.edu/models/cesm1.0/cam/docs/description/ cam5_desc.pdf
25. Pedatella, N.M., Fuller-Rowell, T., Wang, H., Jin, H., Miyoshi, Y., Fujiwara, H., Shinagawa, H., Liu, H.-L., Sassi, F., Schmidt, H., Matthias, V., Goncharenko, L.: The neutral dynamics during the 2009 sudden stratosphere warming simulated by different whole atmosphere models. journal of Geophysical Research: Space Physics **119**, 1306–1324 (2014). doi:10.1002/2013JA019421
26. Pedatella, N.M., Liu, H.-L.: Influence of the El Niño Southern Oscillation on the middle and upper atmosphere. journal of Geophysical Research: Space Physics **118**, 2744–2755 (2013). doi:10.1002/jgra.50286.
27. Lu, X., Liu, H.-L., Liu, A.Z., Yue, J., McInerney, J.M., Li, Z.: Momentum budget of the migrating diurnal tide in the Whole Atmosphere Community climate model at vernal equinox. journal of Geophysical Research: Atmospheres **17**, 07112 (2012). doi:http://dx.doi.org/10.1002/2013JA019421
28. Tan, B., Chu, X., Liu, H.-L., , Yamashita, C., Russell, J.M.: Atmospheric semidiurnal lunar tide climatology simulated by the whole atmosphere community climate model. journal of Geophysical Research **117**, 06327 (2012). doi:10.1029/2012JA017792
29. Tan, B., Chu, X., Liu, H.-L., , Yamashita, C., Russell, J.M.: Zonal-mean global teleconnection from 15 to 110 km derived from SABER and waccm. journal of Geophysical Research: Atmospheres **117**, 10106 (2012). doi:10.1029/2011JD016750
30. Tan, B., Chu, X., Liu, H.-L., , Yamashita, C., Russell, J.M.: Parameterization of the inertial gravity waves and generation of the quasi-biennial oscillation. journal of Geophysical Research: Atmospheres **117**, 06103 (2012). doi:10.1029/2011JD016778
31. Davis, R.N., Du, J., Smith, A.K., Ward, W.E., Mitchell, N.J.: The diurnal and semidiurnal tides over ascension island (^{o} s, 14^{o} w) and their interaction with the stratospheric quasi-biennial oscillation: studies with meteor radar, eCMAM and waccm. Atmospheric Chemistry and Physics **13**, 9543–9564 (2013). doi:10.5194/acp-13-9543-2013
32. Smith, K.L., Polvani, L.M., Marsh, D.R.: Mitigation of 21st century Antarctic sea ice loss by stratospheric ozone recovery. Geophysical Research Letters **39**, 20701 (2012). doi:10.1029/2012GL053325
33. Iacono, M., Delamere, J., Mlawer, M. E.and Shephard, Clough, S., Collins, W.: Radiative forcing by long-lived greenhouse gases: Calculations with the aer radiative transfer models. Journal of Geophysical Research: Atmospheres **113** (2008). doi:10.1029/2008JD009944
34. Mlawer, E., Taubman, S., Brown, P., Iacono, M., Clough, S.: Radiative transfer for inhomogeneous atmospheres: Rrtm, a validated correlated-k model for the longwave. J. Geophys. Res. **102**, 16663–16682 (1997). doi:10.1029/97JD00237
35. Clough, S., Iacono, M.: Line-by-line calculation of atmospheric fluxes and cooling rates 2. application to carbon dioxide, ozone, methane, nitrous oxide and the halocarbons. J. Geophys. Res. **100**, 16519–16535 (1995). doi:10.1029/95JD01386
36. Clough, S.A., Shephard, M.W., Mlawer, E.H., Delamere, J.S., Iacono, M.J., Cady-Pereira, K., Boukabara, S., Brown, P.D.: Atmospheric radiative transfer modeling: a summary of the aer codes. J. Quant. Spectrosc. Radiat. Transfer **91**, 233–244 (2005). doi:10.1016/j.jqsrt.2004.05.058
37. Solomon, S., Qiang, L.: Solar extreme-ultraviolet irradiance for general circulation models. J. Geophys. Res. **110**, 10306 (2005). doi:10.1029/2005JA011160
38. Lean, J.: Evolution of the sun's spectral irradiance since the maunder minimum. Geophys. Res. Lett. **27**(16), 2425–2428 (2000). doi:10.1029/2000GL000043
39. Wang, Y.-M., Lean, J.L., Sheeley, N.R.J.: Modeling the sun's magnetic field and irradiance since 1713. The Astrophysical Journal **625**(1), 522 (2005)
40. Sander, e.a. S. P.: Chemical Kinetics and Photochemical Data for Use in Atmospheric Studies. Evaluation Number 15. National Aeronautics and Space Administration, Jet Propulsion Laboratory, Pasadena, CA (2006)
41. Edson, A., Lee, S., Bannon, P., Kasting, J.F., Pollard, D.: Atmospheric circulations of terrestrial planets orbiting low-mass stars. Icarus **212**, 1–13 (2011). doi:10.1016/j.icarus.2010.11.023
42. Kaspi, Y., Showman, A.P.: Atmospheric Dynamics of Terrestrial Exoplanets over a Wide Range of Orbital and Atmospheric Parameters. Astrophysical journal **804**, 60 (2015). doi:10.1088/0004-637X/804/1/60
43. Menou, K.: Water-trapped Worlds. Astrophysical journal **774**, 51 (2013). doi:10.1088/0004-637X/774/1/51
44. Liu, X., Chance, K., Sioris, C.E., Kurosu, T.P.: Impact of using different ozone cross sections on ozone profile retrievals from global ozone monitoring experiment (gome) ultraviolet measurements. Atmospheric Chemistry and Physics **7**(13), 3571–3578 (2007). doi:10.5194/acp-7-3571-2007
45. Sakazaki, T., Fujiwara, M., Mitsuda, C., Imai, K., Manago, N., Naito, Y., Nakamura, T., Akiyoshi, H., Kinnison, D., Sano, T., Suzuki, M., Shiotani, M.: Diurnal ozone variations in the stratosphere revealed in observations from the Superconducting Submillimeter-Wave Limb-Emission Sounder (SMILES) on board the International Space Station (ISS). journal of Geophysical Research: Atmospheres **118**, 2991–3006 (2013). doi:10.1002/jgrd.50220
46. Kaufmann, M., Gusev, O.A., Grossmann, K.U., Mart'in-Torres, F.J., Marsh, D.R., Kutepov, A.A.: Satellite observations of daytime and nighttime ozone in the mesosphere and lower thermosphere. journal of Geophysical Research **108**, 4272 (2003). doi:10.1029/2002JD002800
47. Marsh, D.R., Skinner, W.R., Marshall, A.R., Hays, P.B., Ortland, D.A., Yee, J.-H.: High resolution doppler imager observations of ozone in the mesosphere and lower thermosphere. journal of Geophysical Research **107(D19)**, 4390

(2002). doi:10.1029/2001JD001505

48. Wallas, J.M., Hobbs, P.V.: Atmospheric Science an Introductory Survey, 2nd edn. Academic Press, 525 B St # 1800, San Diego, CA 92101 (2006)
49. Marsh, D., Smith, A., Brasseur, G., Kaufmann, M., Grossmann, K.: The existence of a tertiary ozone maximum in the high-latitude middle mesosphere. Geophysical Research Letters **28**, 4531–4534 (2001). doi:10.1029/2001GL013791
50. Montmessin, F., Bertaux, J.L., Lefevre, F., Marcq, E., Belyaev, D., Gerard, J.C., Korablev, O., Fedorova, A., Sarago, V., Vandaele, A.C.: A layer of ozone detected in the nightside upper atmosphere of venus. Icarus **216**, 82–85 (2011). doi:10.1016/j.icarus.2011.08.010
51. Andrews, G. David: An Introduction to Atmospheric Physics, Second Edition. Cambridge Univesity Press, The Edinburgh Building, Cambridge CB2 8RU, UK (2010)
52. Müller, R.: Stratospheric Ozone Depletion and Climate Change. The Royal Society of Chemistry, Thomas Graham House, Science Park, Milton Road, Cambridge CB4 0WF, UK (2012)
53. Kaltenegger, L., Sasselov, D., Rugheimer, S.: Water-planets in the Habitable Zone: Atmospheric Chemistry, Observable Features, and the Case of Kepler-62e and -62f. The Astrophysical journal Letters **775**, 47 (2013). doi:10.1088/2041-8205/775/2/L47
54. Winn: Exoplanets. University of Arizona Press, ??? (2010)
55. Burrows, A.S.: Spectra as windows into exoplanet atmospheres. Proceedings of the National Academy of Sciences of the United States of America PNAS **111**, 12601–12609 (2014). doi:10.1073/pnas.1304208111

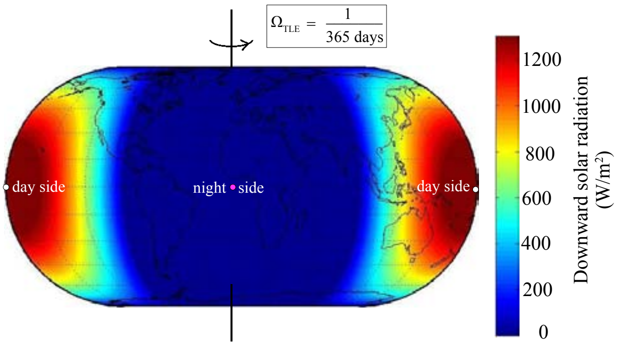

Figure 1 Simulation Setup Downward shortwave top of the model flux setup for the TLE simulation. The subsolar point is indicated with a white point and the antisolar point with a magenta point. Shades of red indicate high incoming solar radiation and define the day side of the planet. Shades of blue indicate low incoming solar radiation. The dark blue visible in the center of the plot indicates lack of incoming solar radiation and defines the night side of the planet.

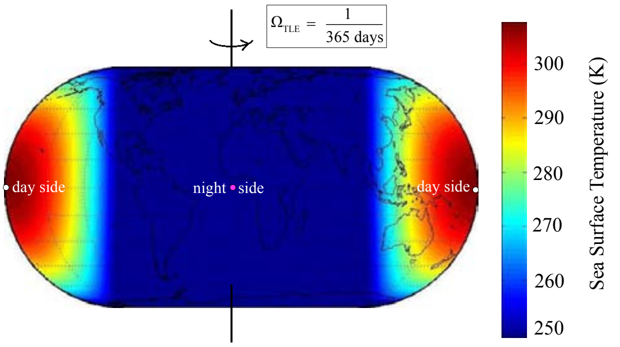

Figure 2 Sea Surface Temperature Tidally locked Earth SST. The subsolar point is indicated with a white point and the antisolar point with a magenta point. Shades of red indicate high temperatures and define the day side of the planet. Shades of blue indicate low temperature. It defines the night side of the planet. The subsolar point is indicated with a white point on either side of the figure. The antisolar point is indicated with a magenta point in the center of the figure.

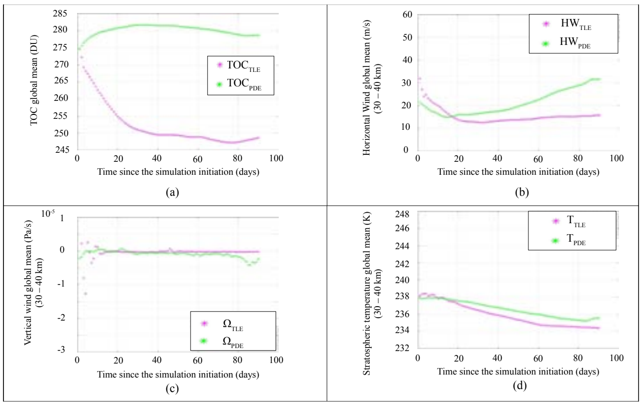

Figure 3 TLE temporal evolution of the TLE and PDE atmosphere (a) the TOC, (b) the HW, (c) the VW, (d) the $\mathrm{E_{kin}}$, (e) the $\mathrm{T_{strat}}$, respectively. The TLE TOC, HW, $\mathrm{E_{kin}}$ and $\mathrm{T_{strat}}$ are exponentially decaying to their steady-state value with an e-folding time of 30, 15, 13 and 20 days, respectively. The TLE VW is exponentially increasing to its steady-state value with an e-folding time of 15 days.

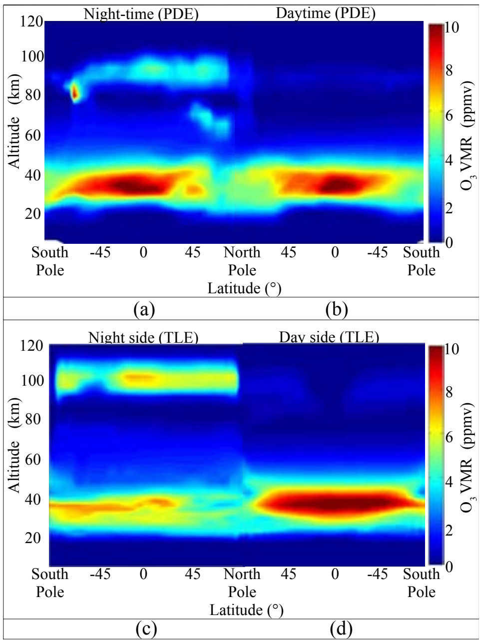

Figure 4 Height-latitude cross section of O$_3$VMR along the meridian through the subsolar point and the antisolar point for the PDE and TLE (a) Vertical cross section of the PDE night-time hemisphere. (b) Vertical cross section of the PDE daytime hemisphere. (c) Vertical cross section of the TLE night side hemisphere. (d) Vertical cross section of the TLE day side hemisphere.

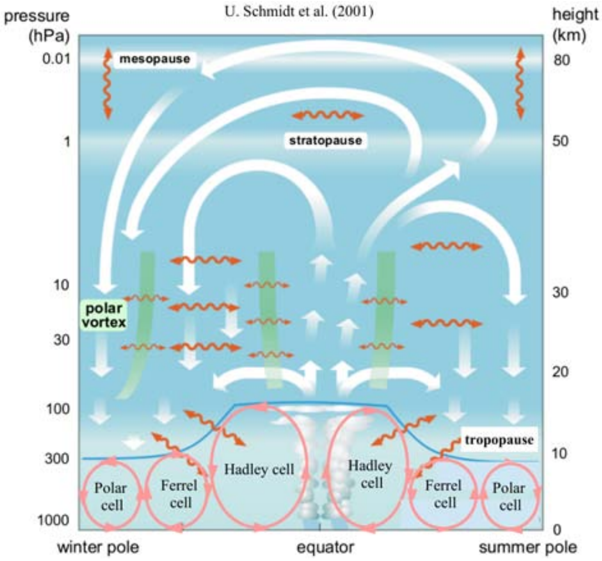

Figure 5 The Brewer-Dobson circulation in the PDE The Hadley, Ferrel and Polar cells are visible in the figure for both hemispheres (Adapted from Schmidt et al.).

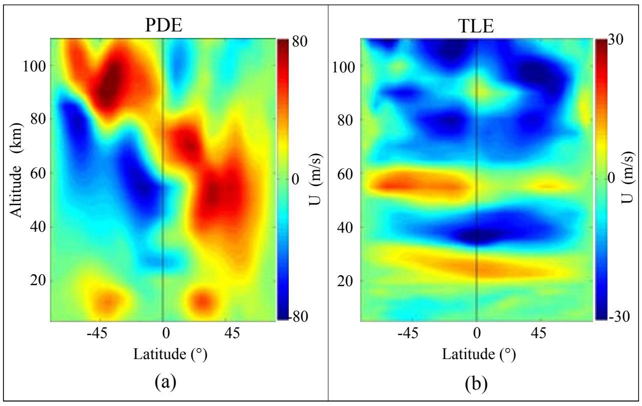

Figure 6 PDE and TLE zonal mean zonal wind latitude-altitude plots (a) PDE zonal mean zonal wind, (b) TLE zonal mean zonal wind. Warm colours indicate movement from the west to the east, while cold colours indicate movement from the east to the west.

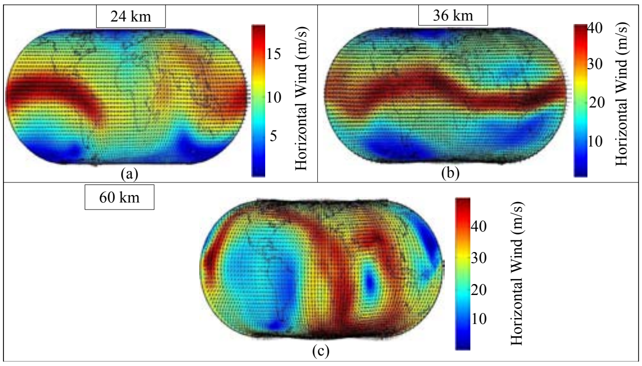

Figure 7 TLE Horizontal circulation at select altitudes (a) Horizontal wind at 24 km, (b) Horizontal wind at 36 km, (c) Horizontal wind at 60 km. The black arrows indicate the wind vector while the color shading shows the wind speed.

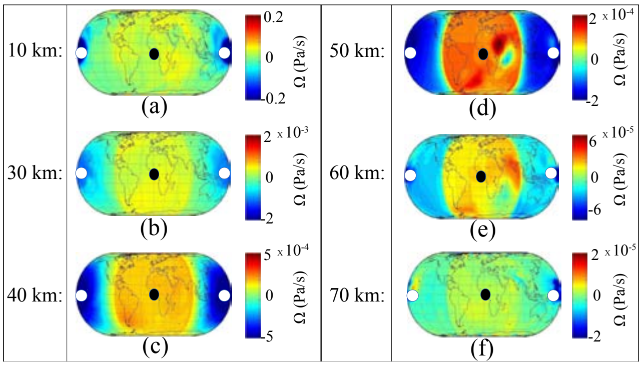

Figure 8 Longitude-Latitude Vertical wind circulation in the TLE (a) Vertical wind at 10 km, (b) Vertical wind at 30 km, (c) Vertical wind at 40 km, (d) Vertical wind at 50 km, (e) Vertical wind at 60 km, (f) Vertical wind at 70 km. Warm colours (positive values) indicate a downwelling wind. Cold colours (negative values) indicate an upwelling wind. Each figure is centred on the antisolar point which is indicated with a black dot. The subsolar point is indicated with a white dot on either side of each figure.

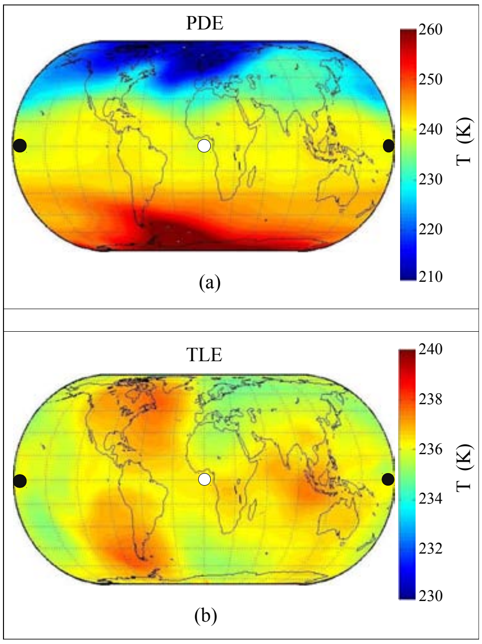

Figure 9 Comparative view of the PDE and TLE atmospheric temperatures at 36 km altitude (a) $\mathrm{T_{PDE}}$, (b) $\mathrm{T_{TLE}}$. The antisolar point is indicated with a white point. The subsolar point is indicated with a black point. The middle stratospheric TLE temperature is clearly decreased compared to the PDE.

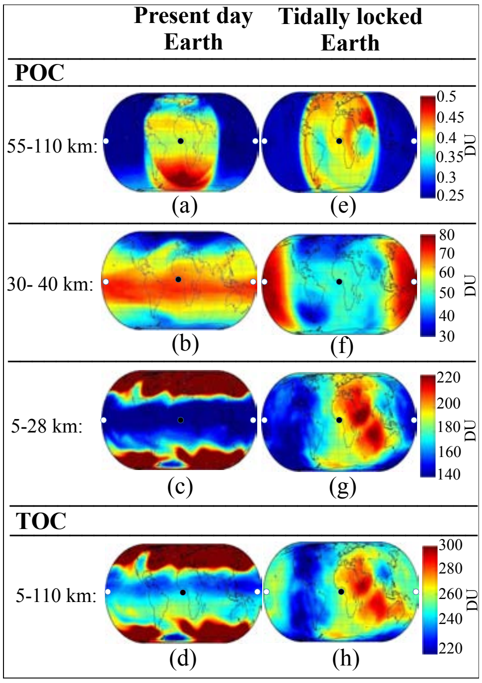

Figure 10 Comparative TOC and POC maps for the PDE and the TLE (a) $\mathrm{POC_{PDE(55-110)}}$, (b) $\mathrm{POC_{PDE(30-45)}}$, (c) $\mathrm{POC_{PDE(5-28)}}$, (d) $\mathrm{TOC_{PDE}}$ at 00:00 UT on the day of the spring equinox, respectively. (e) $\mathrm{POC_{TLE(55-110)}}$, (f) $\mathrm{POC_{TLE(30-45)}}$, (g) $\mathrm{POC_{TLE(5-28)}}$, (h) $\mathrm{TOC_{TLE}}$ on the 90^{th} day of the TLE simulation, respectively. All figures are centred on the antisolar point which is indicated with a black dot. The subsolar point is indicated with a white dot on either side of each figure.

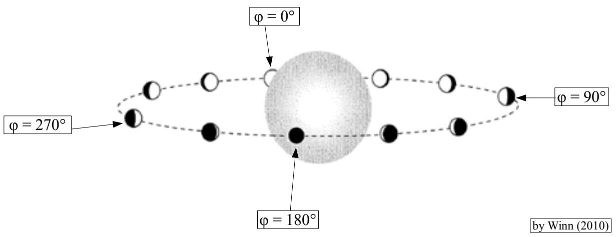

Figure 11 Phases of an exoplanet as seen by an observer The phases $\varphi = 0^\circ$, $\varphi = 90^\circ$, $\varphi = 180^\circ$, $\varphi = 270^\circ$ have been marked. In phase $\varphi = 0^\circ$ only the planet's day side is visible. In phases $\varphi = 90^\circ$and $\varphi = 270^\circ$ half of the day side and half of the night side are visible. In phase $\varphi = 180^\circ$ only the night side is visible.

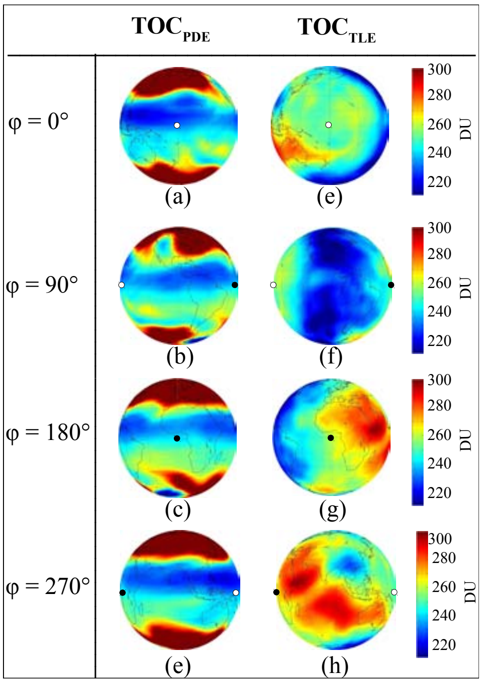

Figure 12 Comparative view of four different phases of the $\mathbf{TOC_{PDE}}$ and $\mathbf{TOC_{TLE}}$ (a) $\varphi = 0^\circ$ of $\mathrm{TOC_{PDE}}$, (b) $\varphi = 90^\circ$ of $\mathrm{TOC_{PDE}}$, (c) $\varphi = 180^\circ$ of $\mathrm{TOC_{PDE}}$, (d) $\varphi = 270^\circ$ of $\mathrm{TOC_{PDE}}$. (e) $\varphi = 0^\circ$ of $\mathrm{TOC_{TLE}}$, (f) $\varphi = 90^\circ$ of $\mathrm{TOC_{TLE}}$, (g) $\varphi = 180^\circ$ of $\mathrm{TOC_{TLE}}$, (h) $\varphi = 270^\circ$ of $\mathrm{TOC_{TLE}}$. The antisolar point is indicated with a white point. The subsolar point is indicated with a black point.

Table 1 Comparison of the deviation of the $\mathrm{TOC_{TLE}}$ Global Mean of the ensemble runs from the ensemble average

Date of the start of the simulation	$\mathrm{TOC_{GM}}$ (DU)	Deviation (DU)	Deviation (%)
11.03	245.3	-2.01	-0.93
16.03	242.4	0.88	0.37
21.03	244.1	-0.8	-0.33
26.03	243.5	-0.22	0.08
31.03	243.6	-0.35	0.12
ensemble average	243.3	0	0

Table 2 Comparison of TOC and POC e-folding times, steady-state mean values and their standard deviations obtained for the PDE and TLE simulation on day 90.

	PDE	σ_{PDE}	TLE	σ_{TLE}
TOC (DU)	280.1	1.44	248.7	1.00
HW (m/s)	21.19	5.21	14.21	1.00
Ω (Pa/s)	$-8.6 \cdot 10^{-7}$	$9.6 \cdot 10^{-7}$	$-1.7 \cdot 10^{-7}$	$1.3 \cdot 10^{-7}$
$\mathrm{T_{strat}}$ (K)	239.9	0.85	238.4	0.43

Table 3 Comparison of TOC and POC global means obtained for the PDE and TLE simulation on day 90. The $\Delta_{\%}$ are defined in equations (1) and (2), while Δ_{DU} are defined in equations (3) and (4).

	PDE (DU)	TLE (DU)	$\Delta_{\%}$ (%)	Δ_{DU} (DU)
TOC_{GM}	291.14	244.05	19.3	47.09
$POC_{(5-28)GM}$	216.35	169.42	27.7	46.93
$POC_{(30-45)GM}$	46.45	46.84	-0.8	-0.39
$POC_{(55-110)GM}$	0.31	0.34	-7.2	-0.03

Table 4 Comparison of TOC and POC day side and night side means obtained for the PDE and TLE simulation on day 90.

	PDE Day side Mean (DU)	PDE Night side Mean (DU)	TLE Day side Mean (DU)	TLE Night side Mean (DU)
$\mathrm{TOC_{GM}}$	295	287	240	249
$\mathrm{POC_{(5-28)GM}}$	220	213	158	181
$\mathrm{POC_{(30-45)GM}}$	52	51	58	45
$\mathrm{POC_{(55-110)GM}}$	0.23	0.40	0.28	0.40

Table 5 Comparison of $\mathrm{TOC_{HM(PDE)}}$ and $\mathrm{TOC_{HM(TLE)}}$ hemisphere means for different phases of the planet

Phase φ	$\mathrm{TOC_{PDE}}$ (DU)	$\mathrm{TOC_{TLE}}$ (DU)
$0°$	295	239
$90°$	285	234
$180°$	287	249
$270°$	291	260

Table 6 Comparison of difference $\mathrm{TOC_{HM(PDE)}}$ and $\mathrm{TOC_{HM(TLE)}}$ hemisphere means for different phases of the planet

Phase φ	$\Delta TOC_{HM(PDE,TLE)}$ (DU)	$\Delta TOC_{HM(PDE,TLE)}$ (%)	$\Delta TOC_{HM(TLE,TLE)}$ (%)	$\Delta TOC_{HM(PDE,PDE)}$ (%)
$0°$	-56	23	0	0
$90°$	-51	22	2.2	3.5
$180°$	-39	16	-3.8	2.7
$270°$	-13	12	-8.1	1.4

7.3 Third article

The study was submitted in *Progress in Earth and Planetary Science* in June 2015. The reprint is the latest version of the article (submitted on 22.01.2016). The article is currently under review.

RESEARCH

The middle atmospheric circulation of a tidally locked Earth-like planet and the role of the sea surface temperature

Elisavet Proedrou[1,2*], Klemens Hocke[1,2,3] and Peter Wurz[1,4]

Abstract

We investigate the influence of the sea surface temperature (SST) changes on the middle atmosphere of a tidally locked planet using the coupled 3D chemistry-climate model CESM1(WACCM). Two 90 day simulations are performed using two extreme SSTs: a present day Earth-like SST and a tidally locked aquaplanet SST. Our results show that changes in the SST have an influence on the lower stratospheric temperature and the secondary ozone layer. Both atmospheres exhibit a day side upwelling and a night side downwelling extending from the surface to the mesosphere. They are also characterised by comparable lower and middle stratospheric horizontal winds and relatively different mesospheric horizontal winds. The temperature of the warm Earth-like SST (WTLE) atmosphere is altered as a result of the SST changes, compared to the Earth-aquaplanet SST (CTLE). Specifically the WTLE lower tropospheric temperature is increased by 3.7 K on average, due to the absorption of the increased upwelling longwave radiation and the increased sensible and latent heat. The WTLE upper troposphere temperature is decreased by 4 K on average, is adiabatic in nature and is generated by the increased WTLE upwelling. The WLTE lower stratospheric temperature is increased by 3.8 K on average due to the absorption of the increased upwelling longwave radiation. The lower mesospheric temperature is decreased by 1.13 K on average due to increased mesospheric wave breaking. The upper mesospheric temperature is increased by 4.3 K and its generation mechanism is currently unknown. Furthermore, the secondary ozone layer O_3VMR is increased by 40.5%. The occurrence of large-scale vortices and variable jet streams depends, to some extent, on the SST distribution.

Keywords: exoplanet; tidally locked Earth; middle atmosphere; circulation; atmospheric dynamics; absorption lines; M star; spectral line; SST; sea surface temperature

1 Introduction

In this study, we simulate and analyse how differences in the underlying sea-surface temperature (SST) of a tidally locked Earth-like planet orbiting a Sun-like star alter its circulation and ozone distribution using a realistic, high-resolution, 3D chemistry-climate model. For the simulation two different SSTs were used. The first is a present day Earth (PDE) SST, while the second is the tidally locked aquaplanet SST generated by Merlis and Schneider (2010) [Mer10]. We compare the evolution of the ozone layer towards a steady-state and determine their atmospheric structure and circulation. The study aims to determine the level of SST accuracy needed in simulations and observations of future simulations of observed exoplanets.

The importance of the presence of an ozone layer in a planetary atmosphere in its ability to protect lifeforms from the harmful stellar UV radiation. It is ,therefore, important to determine whether very different underlying SSTs will significantly alter a planet's ozone layer is of high importance for habitability studies.

Currently, planets located in the Habitable Zones of M stars are considered prime targets for the search for terrestrial habitable exoplanets (Tarter et al. (2007)

---

[*] Correspondence: elisavet.proedrou@iap.unibe.ch
[1] Institute of Applied Physics, University of Bern Sidlerstrasse 5, Bern, Switzerland
Full list of author information is available at the end of the article
[†] Equal contributor

[Tar07]). This is due to the abundance of M-stars and a good mass and radius star-to-planet ratio. Furthermore, the detection of planets orbiting an M star is easier due to the close proximity of the habitable zone to the M star and leads to higher probability of the planet becoming tidally locked.

Haberle et al. (1996) [Hab96], Joshi et al. (1997) [Jos97] and Joshi (2003) [Jos03] showed that terrestrial planets located in an M star's habitable zone (0.02 - 0.2 AU) (Tarter et al. (2007) [Tar07]) would be habitable provided that liquid water and the chemical constituents necessary for the emergence of life existed for sufficiently long time period. The flaring activity of M stars has been cited as a danger for the habitability of such planets, however, Segura et al. (2010) [Seg10] showed that the flares should not present a threat for the surface life. In our study we investigate the ozone distribution and, therefore, one condition for the habitability of a tidally locked exoplanet revolving around an M star.

Due to being less massive than the Sun, M stars have weaker UV and visible emission and their spectrum peaks in the infrared. However, the enhanced stellar activity of M stars can result in EUV and UV emissions are stronger than those of the quiet Sun. The different stellar spectral energy distributions will impact the planet's ozone distribution and the atmospheric temperature structure. Selsis et al. (2000) [Sel00], Segura et al. (2003) [Seg03], Segura et al. (2005) [Seg05], Grenfell et al. (2007) [Gre07], Rugheimer et al. (2013) [Rug13], Rauer et al. (2011) [Rau11] and Godolt et al. (2015) [God15] investigated the impact of different stellar spectral energy distributions on the ozone distribution of habitable non-tidally locked terrestrial extrasolar planets.

Selsis (2000) [Sel00] simulated the evolution of the chemical and thermal atmospheric structure of an Earth-like planet's when placed in the orbit of a F9 and K2 star using a 1D atmospheric model. He reported that an increase in the UV/visible light ratio results in the thickening of the planetary ozone layer compared to the Earth.

Segura et al. (2003) [Seg03] calculated the spectra of Earth-like planets orbiting a F2V, a G2V and a K2V star using a 1D coupled radiative-convective photochemical model and determined that the F2V planet would have a lower ozone concentration compared to the G2V or a K2V planet. This contrasts with the results of Selsis et al. (2000) [Sel00].

Segura et al. (2005) [Seg05] calculated the spectra of Earth-like planets orbiting a M star and determined that an ozone layer similar to that of the Earth would develop.

Grenfell et al. (2007) [Gre07] calculated the atmospheric composition changes of an Earth-like planet when subjected to 5-10% changes of its orbital position around a G2V, a F2V, and a K2V star using a 1D coupled radiative-convective photochemical column model. As the planet moved outwards, the ozone increased by ~ 10 % due to the decreased stratospheric temperature.

Rugheimer et al. (2013) [Rug13] used a geometrical 1D model global atmosphere model to simulate the spectra of clear and cloudy Earth-like planets orbiting a F, a G, and a K star at the 1 AU equivalent distance. They reported that an increase in either the parent star's UV radiation or its temperature resulted in increased O_3 concentrations and stronger O_3 spectral features.

Rauer et al. (2011) [Rau11] used a plane-parallel, 1D climate model, coupled with a chemistry model to calculate the molecular absorption bands of super-Earth planetary atmospheres orbiting M stars. They reported that the ozone emission of planets orbiting quiet warm M0 - M3 dwarfs would be stronger than the Earth's. The ozone emission spectra of planets orbiting cool and quiet M4 - M7 on the other hand, stars would be weaker due to increases in the planet's mid-atmospheric temperatures.

Grenfell et al. (2013) [Gre13] used a global-mean radiative-convective-photochemical column model to perform a sensitivity study on the atmosphere of an Earth-like planet. The stellar class and planetary gravity of the planet was varied and the effects of the resulting photochemistry and climate changes investigated. According to their results, the stratospheric ozone generation of an Earth-like planet orbiting an M0 star is still dominated by the Chapman cycle but to a lesser extent compared to the Earth and the smog generation mechanism is strengthened. Moving towards cooler stars the Chapman mechanism is weakened and the smog mechanisms is strengthened. For cool M5-M7 stars, the ozone photochemistry shifted completely from the Chapman production to smog-dominated stratospheric ozone production.

Godolt et al. (2015) [God15] studied the influence of F, G and K stars on the stratospheric temperature, climate and potential habitability of Earth-like exoplanets planets using a state-of-the-art 3D Earth climate model which accounts for local and dynamical processes. They used a fixed Earth-like atmosphere with no atmospheric chemistry and positioned the planets at orbital distances that ensured, that the total amount of energy received from the parent stars would equal the solar constant. The results of the study confirmed that when the atmospheric chemistry is maintained unaltered, different stellar spectral energy distributions will result in different ozone heating rates and therefore, different vertical temperature structures, in accordance with Segura et. al (2000) [Sel00], Segura et al. (2003) [Seg03], Segura et al. (2005) [Seg05], Grenfell et al. (2007) [Gre07], Rugheimer et al. (2013) [Rug13] and Rauer et al. (2011) [Rau11]. Specifically the stratospheres of Earth-like planets orbiting stars less massive than the Sun will be characterised by lower ozone heating rates and shallower stratospheric temperature increases compared to the Earth.

The above studies demonstrated that for non-tidally locked, M star orbiting, planets the reduced UV radiation emission would result in a cooler stratosphere and changes in their stratospheric ozone concentration. It is reasonable to assume that tidally locked planets would be equally affected.

The ozone concentration of a tidally locked Earth-like planet orbiting an M star would be altered by the effects of the tidal lock and the altered stellar irradiance spectrum and make the attribution of the ozone distribution changes on either the tidal lock or the altered UV radiation exceedingly challenging. Therefore, we chose not to include the effects of the altered UV radiation in our study and focus only on the impact of the tidal locking on the Earth-like planet orbiting a Sun-like star.

Past studies of tidally locked Earth-like atmospheres limited themselves to the troposphere (Merlis and Schneider (2010) [Mer10], Yang, Cowan and Abbot (2013) [Yan13], Grenfell et al. (2014) [Gre14]).

Merlis and Schneider (2010) [Mer10] simulated the troposphere of an Earth-like, tidally locked aquaplanet with a rotation period equal to one Earth year using an ideal gas GCM with an active hydrological cycle, a gray radiation scheme and a slab ocean. They reported a maximum subsolar point surface temperature of $\sim$ 300 K and a minimum antisolar point temperature of 240 K. Since the surface temperature never dropped below 240 K, no atmospheric collapse occurred on the night side. They also reported the presence of a strong upwelling above the subsolar point on the day side and a downwelling, centred over the antisolar point, on the night side. The upwelling was generated by the increased radiative heating, while the downwelling was generated by the increased radiative cooling.

Yang, Cowan and Abbot (2013) [Yan13] demonstrated that clouds in the troposphere of a tidally locked aquaplanet, especially when located over the subsolar point, can ensure habitability at almost twice the Earth stellar flux.

Grenfell et al. (2014) [Gre14] used a global-mean, stationary, hydrostatic, atmospheric column model, extending from the surface to $\sim$ 70 km, to perform a 1D simulation of an Earth-like exoplanet atmosphere. The planet's atmosphere had the starting composition, pressure and temperature of the 1976 U.S Standard Atmosphere [Wik15]. The UV emission of a cool M7 star was varied and the resulting climate-photochemical response of the planetary atmosphere including numerous catalytic processes of O_3 depletion were calculated. Grenfell et al. (2014) [Gre14] showed that the strongest O_3 emission is generated when the stellar UV radiative flux is ten times that of an M7 star. They also reported that the exoplanet's O_3 9.6 μm spectral line profile is influenced strongly by the 200–350 nm UV output of the parent star.

The influence of the sea-surface temperature on the tropospheric and lower stratospheric temperature and dynamics has been investigated by several researchers for the present day Earth but not for exoplanets.

Braesicke and Pyle (2004) [Bra04] investigated the dynamics and ozone sensitivity to different SSTs using the Met Office Unified Model with simple stratospheric chemistry. They performed multi-annual simulations, each lasting 20 years. The simulations shared the same simplified ozone chemistry but different prescribed SSTs. According to their results, the appearance of extreme events in the winter stratosphere were more strongly correlated with the underlying SSTs rather than with changes of the ozone layer.

Rosen and Reid (2008) [Ros08] used data provided by the NOAA/CIRES Climate Diagnostics Center to investigate the long-term tropical lower stratospheric temperature trends over the western Tropical Pacific Ocean, in relation to variations in the SST. Their study revealed the presence of an anticorrelation between stratospheric temperature anomalies and SST anomalies. Rosenlof and Reid proposed the existence of a fairly direct influence between the underlying ocean and the lower tropical stratosphere and speculated that the anticorrelation is generated by the increased deep tropospheric convection generated by the SST warming.

Decker and Dameris (2008) [Dec08] reported the presence of a lower stratospheric cooling due to higher tropical SSTs. Their study investigated how the strength of the tropical upwelling is influenced by changes in the underlying SST and greenhouse gas concentrations. To that end, they performed two simulations with different SSTs and greenhouse gas concentrations. They concluded that the deep convection was amplified by the higher underlying SST and waves were generated. The waves enhanced the residual meridional circulation and the upwelling of ozone-poor tropospheric air into the lower stratosphere in the tropics.

One study by Hegy et al. (2013) [Heg14] was performed using the CESM1(WACCM) model version 1.0.2 to investigate the initial transient response of the boreal winter stratospheric polar vortex to localised SST warming events. They conducted twenty perpetual winter simulations. According to their results, the polar vortex was weakened by changes in the eddy-driven mean meridional circulation and negative anomalies appeared in the eddy momentum flux convergence. They also demonstrated that the initial state and subsequent internal variation of the extratropical atmosphere is equally important to the type of SST forcing in determining the response of the stratospheric polar vortex. Furthermore, they found that the interactions between the internal variability of the vortex and the SST-driven wave anomalies govern the nature of the polar vortex response to the forcing.

Chen et al. (2010) [Che10] used an Earth-like aquaplanet general circulation model to study the tropospheric winds and stratospheric Brewer-Dobson circulation sensitivities to SST warmings. The main aim of the study was to investigate the relationship between a warming ocean due to global warming and a change in the Earth's large-scale atmospheric circulation. The authors concluded that the location and sign of the SST perturbations gradient strongly influenced the tropospheric jet and the Hadley cell. They reported an increase in the Brewer-Dobson circulation in the presence of a low latitude warming and a decrease in the presence of a high latitude warming extending to the subtropics.

To the extent of our knowledge, the correlation between the SST and the middle atmosphere has not been investigated for a tidally locked Earth-like planet whose circulation largely differs from the Brewer-Dobson circulation of the fast rotating, present day Earth. The sensitivity of the mesospheric conditions to SST variations is crucial for the observations of the spectral signatures of mesospheric gases, who will be affected by altered temperatures and/or circulation patterns.

Below, we first describe the model used and the simulation setup. Next we present and analyse the atmospheric evolution to a steady-state, the atmospheric circulation, the atmospheric temperature structure and the ozone volume mixing ration distribution (O_3VMR).

2 Model Description

The simulation is performed using the Community Earth System Model (CESM) version 1.04 which consists of five fully coupled geophysical models: atmosphere (ATM), land (LND), ocean (OCN), sea-ice (ICE), land-ice (GLC). The models have five possible different modes: fully prognostic, data, stub and dead. The fully prognostic mode provides “state-of-the-art climate prediction and analysis tools” (Vertenstein et al. (2012) [Ver12]).

The atmospheric model used to perform our study is the Whole Atmosphere Community Climate Model version 4 (CESM1(WACCM)) (Neal et al. 2012) [Nea12]). CESM1(WACCM) has been used to simulate the circulation, gravity waves and atmospheric composition changes of the present day Earth by Pedatella et al. (2014) [Ped14], Pedatella et al. (2013) [Ped13], Lu et al. (2012) [Lu12], Tan et al. (2012a) [Tan12a], Tan et al. (2012b) [Tan12c], Tan et al. (2012c)[Tan12b], Davis et al.

(2013) [Dav13], Smith et al. (2012) [Smi12]. It is fully coupled to the land, ocean and ice models (Vertenstein et al. (2012) [Ver12]).

It has a fully compressible horizontal discretization and a quasi-Lagrangian vertical discretization approximation which is good for scales larger than 10 km (Neal et al. (2012) [Nea12]). It has 66 vertical levels starting on the surface of the planet and up to $5 \cdot 10^{-6}$ hPa (2.5 - 149 km). The model top is located at $\sim$ 150 km. The vertical coordinate is terrain following below 100 hPa and purely isobaric above 100 hPa. The vertical resolution is 1.1 km in the troposphere, 1.1–1.4 km in the lower stratosphere, 1.75 km at the stratopause and 3.5 km above 65 km (Neal et al. (2012) [Nea12]).

CESM1(WACCM) has full tropospheric, stratospheric and mesospheric chemistry, with 57 chemical species (Neal et al. (2012) [Nea12]). The gas-phase chemistry is coupled to the Modal Aerosol Model (Neal et al. (2012) [Nea12]). The stratospheric distributions of long-lived species are taken from previously performed CESM1(WACCM) simulations.

The longwave and shortwave radiative transfer calculations are provided by the radiation code RRTMG (Iacono et al. (2008) [Iac08], Mlawer et al. (1997) [Mla97]). It is capable of efficiently calculating the irradiance and heating rate in broad spectral intervals, while retaining a high level of accuracy relative to measurements and high-resolution line-by-line models. It also distinguishes between the direct and scattered solar radiation.

The shortwave radiative transfer is calculated over 14 bands (0.2 μm to 12.2 μm) while the longwave radiative transfer is calculated over 16 bands (3.1 μm to 1000.0 μm). The 16th longwave band includes the infrared contribution from the spectral interval below 3.1 μm. Above 65 km the model covers the spectrum interval between soft x-rays and extreme ultraviolet irradiances (0.05 nm to Lyman-α (121.6 nm) and the spectrum interval between the Lyman-α (121.6 nm) and 100 μm (Neale et al. (2012) [Nea12]).

The total shortwave fluxes are accurate within 1-2 W/m^2 compared to the standard RRTM SW for clear sky conditions and aerosols, and 6 W/m^2 in overcast sky conditions. The total longwave fluxes are accurate within 1.0 W/m^2 at all levels. "'The longwave radiative transfer is performed over a single angle for one upward and one downward calculation" (Neale et al. (2012) [Nea12]). The absorption coefficients for the k-distributions for both the shortwave and the longwave radiation calculations in RRTMG are obtained from the line-by-line radiation model LBLRTM (Clough and Iacono (1995) [Clo95], Clough et al. (2005) [Clo05]).

The calculation of the photolysis coefficients is divided into the 120 nm - 200 nm and 200 nm - 750 nm regions. The total photolytic rate constants are calculated by the model by integrating the product of the wavelength dependent exo-atmospheric flux, the atmospheric transmission function, the molecular absorption cross-section and the quantum yield for each absorbing species. The exo-atmospheric flux is taken from observations and varies over the 11-year solar sunspot cycle. The transmission function is wavelength-dependent and a function of the model abundance of ozone and molecular oxygen. For wavelengths above 200 nm the molecular absorption cross-section and the quantum yield are calculated by the model, while below 200 nm, their values are pre-defined. For NO and O_2 detailed photolysis parametrisations are included in the model. The impact of clouds on the photolysis rates is parametrised. The impact of tropospheric and stratospheric aerosols on photolysis rates on the other hand, is not calculated (Neale et al. (2012) [Nea12]).

The CESM model uses the Kurucz solar source function, whose radiative transfer calculation is based upon solar measurements. The model assumes a total solar irradiance at the top of the atmosphere equal to TSI = 1368.22 W/m^2. The value is then "scaled in each spectral band through the specification of a time-varying solar spectral irradiance" (Neale et al. (2012) [Nea12]). A combination of solar parametrizations is used to specify spectral irradiances over the soft x-ray to Lyman-α and the Lyman-α to 100 μm spectral interval. The first spectral interval fluxes are calculated using the parametrization of Solomon and Qiang (2005) [Sol05]. It accepts as input the 10.7 cm solar radio flux (f 10.7), whose daily values are obtained from the NOAA's Space Environment Center (www.sec.noaa.gov) and its 81-day average. The second spectral interval fluxes are calculated using the empirical model of the wavelength-depending sunspot and facular influences (Lean et al. (2000) [Lea00] and Wang et al. (2005) [Wan05]) (Neal et al. (2012) [Nea12]).

The modelled sources of radiation absorption and scattering in the shortwave electromagnetic spectrum are H_2O, O_3, CO_2, O_2, CH_4, N_2, clouds, aerosols, and Rayleigh scattering. The sources of molecular radiation absorption in the longwave electromagnetic spectrum are H_2O, CO_2, O_3, N_2O, CH_4, O_2, N_2, $CFC-11$ and $CFC-12$. The shortwave electromagnetic radiation is calculated only for zenith angles larger than zero (Neale et al. (2012) [Nea12]). The zonal mean climatology of the local O_3 concentration, the temperature, the overhead column O_3 and other chemicals is based on satellite and in-situ Earth observations (Neal et al. (2012) [Nea12]).

The model computes the chemical equilibrium of 36 photochemical species (O_2, O_3, N_2O, NO, NO_2, N_2O_5, HNO_3, NO_3, HO_2NO_2, CH_3OOH, CH_2O, H_2O, H_2O_2, Cl_2, ClO, OClO, Cl_2O_2, HOCl, HCl, $ClONO_2$, BrCl, BrO, HOBr, $BrONO_2$, CH_3Cl, Ccl_4, CH_3CCl_3, CFC11, CFC12, CFC113, HCFC22, CH_3Br, CF_3Br, CF_2ClBr, CO_2, CH_4). The model atmospheric tracers are O_x, NO_x, HO_x, ClO_x, and BrO_x chemical families, excluding O_2, along with CH_4 and its degradation products. The main photochemical and chemical interactions responsible for changing the atmospheric ozone concentration are described by the reaction rate of ozone $\frac{d(O_3)}{dt} + J_{O_3}(O_3) + k_3(O)(O_3) + a_2(H)(O_3) + a_6(OH)(O_3) + a_{6b}(HO_2)(O_3) + b_4(NO)(O_3) + b_9(NO_2)(O_3) + d_2(Cl)(O_3) + e_2(Br)(O_3) = k_2(M)(O_2)(O)$. $\frac{d(O_3)}{dt}$ is the production rate of O_3. J_{O_3} is the photolysis rate of ozone. $k_3, a_2, a_6, a_{6b}, b_4, b_9, d_2, e_2, k_2(M)$ are the chemical rate constants of the reactions and are taken from JPL06-2 (Sander et al. (2006) [San06]).

A polar stratospheric cloud parametrization scheme is incorporated in the model. It is activated when the cosine of the solar zenith angle is larger than zero at stratospheric altitudes and the stratospheric temperature drops below 195 K (Neal et al. (2012) [Nea12]).

The momentum, sensible heat flux, latent heat flux, land surface albedos and upward longwave electromagnetic radiation are used to calculate the atmospheric radiation. The upward longwave radiation is given by the difference of the incident and the absorbed fluxes. The incident flux values are in turn, determined from the daily values of the solar radio flux (F10.7) which are provided by the National Oceanic and Atmospheric Administration's (NOAA) Space Environment Center [Nat15].

The starting values of the zonal mean climatology of the local O_3 concentration, the temperature, the overhead column O_3 and other chemicals used by the model are provided by satellite and in-situ Earth observations (Neal et al. (2012) [Nea12]). A detailed model description can be found in Neal et al. (2012) [Nea12].

3 Methods

3.1 Simulation Setup

We perform two 90-day simulations with different SST distributions for a tidally locked Earth-like planet (TLE). The first first SST distribution is that of the present day Earth. It is characterised by temperatures of 290 - 300 K in the tropics and 270 - 280 K in the polar regions. Due to the overall warm SST, the simulation using this SST it will be hereafter called Warm TLE (WTLE). This SST distribution is only used to force an extreme SST and is otherwise incorrect for a tidally locked planet. The second SST distribution resembles the SST reported by Merlis and Schneider (2010) [Mer10]. It was characterised by a uniform night side SST 250 K temperature and a monotonically and isotropically increasing day side SST that reached a maximum of 300 K within a 30 degrees radius centred on the subsolar point. On account of the overall cooler SST the simulation will be called Cold TLE (CTLE). Both SSTs can be seen in Figure 1.

The tidally locked planet is located at a distance of 1 AU from the parent star, has an eccentricity of $0 < e < 1$, a stellar irradiance at the top of the model $1366.96 < S_o < 1368.60$ and a rotation rate that is $1/365^{\text{th}}$ of the Earth's rotation rate. The subsolar point is permanently located (0.17° N, -178.17° E) in the Pacific Ocean, which is the position of the Earth's subsolar point at 00:00 UT on the day of the Spring Equinox (21.03.2000).

The parameters altered to achieve the tidal lock and a perpetual equinox are:

- the number of seconds in a siderial day: altered from 86164 seconds/day to $3.15 \cdot 10^7$ seconds/day
- the planet's rotational velocity: set to $2.31 \cdot 10^{-12}$ rad/s
- the planet's new rotation rate: set to 1° every 87600 seconds (the Earth rotation rate is 1° every 240 seconds)
- the position of the subsolar point: set to (0.17° N, -178.17° E) for the duration of the simulations
- the Sea Surface Temperature (SST): changed to resemble the SST reported by Merlis and Schneider (2010)[Mer10]
- The solar zenith angle (SZA): set to a constant value by means of the present day Earth (PDE) Julian date.

The SZA is the main parameter used for the assessment of the incoming solar radiation in the CESM model. By setting the Julian date to a constant value we stop the periodic 24-hour variation of the SZA at all grid points. Figure 2 shows the shortwave solar radiation flux at the top of the model for the WTLE and CTLE simulations. The solar point is depicted by a white dot located on either side of the figure, while the anti-solar point is depicted by a magenta point located in the centre of the figure.

The CESM1(WACCM) requires the presence of an active land model and, therefore, has the general topography and continents of the Earth. The atmospheric and surface initialization data are identical for all simulations and all start with same 3D ozone and wind field.

In the next subsection we present the middle atmospheric circulation (Ω, HW), temperature (T) and ozone distribution (TOC, O_3VMR) of the two simulations and we discuss the degree by which they are influenced by the two extreme SSTs. We first discuss the atmospheric adjustment time of the two tidally locked Earths (TLEs) and compare it to the present day Earth. Then, we present and discuss their atmospheric circulation, their atmospheric temperature structure and their latitude-longitude O_3VMR cross section.

It should be noted that while the possibility of tidal locking of an Earth-like planet within the habitable zone of a Sun-like star has a low probability, the similarity of the solar spectrum and atmospheric composition to the PDE fosters the intercomparison and interpretation of the differences in the model runs. Furthermore, since several past studies of tidally locked exoplanets have used models with solar spectrum and atmospheric composition similar to that of the PDE, this setup fosters the intercomparison and interpretation of the changes with past models."

3.2 Data Analysis

The zonal wind (U), the meridional wind (V), the vertical wind (Ω), the atmospheric temperature (T), the air number density (M) and the ozone volume mixing ratio (O_3VMR) are extracted from the output datasets of the simulation run. The above parameters are then interpolated for the altitudes of 1 to 140 km. Next the zonally averaged zonal, meridional and vertical wind are calculated from 5 to 110 km. The O_3 concentration is calculated for the altitudes of 1 to 110 km by multiplying the ozone volume mixing ratio with the air number density ($[O_3] = O_{3\mathrm{VMR}} \cdot [\mathrm{air}]$). As a next step, the total ozone column density (TOC) is calculated by interpolating the O_3 concentration between the altitudes of 5 and 110 km ($\mathrm{TOC} = \int_5^{110} [O_3] \mathrm{dz}$). The altitude limits are imposed in order to avoid the data gaps generated by the presence of several high mountains and mountain ranges at low altitudes (e.g Himalayas, Kilimanjaro) and the air density data gaps above 110 km altitude. The TOC, HW, Ω and T global means are determined by calculating their zonal means as a function of latitude and then weighting them with the surface area of the latitude belts (surface area preserving mean). The change in % between the CTLE and WTLE parameters is calculated using the following equation:

$$\Delta = \frac{parameter_{CTLE} - parameter_{WTLE}}{parameter_{WTLE}} * 100 \qquad (1)$$

where the term *parameter* is used to refer to any of the TOC, Ω, HW, T and O_3VMR.

3.3 Terminology

The day side of a tidally locked planet is the permanently illuminated hemisphere that is always facing the parent star, while the night side is the hemisphere that is never illuminated by the parent star. The subsolar point is defined as the position of maximum solar flux, located at the centre of the day side and has a solar zenith angle (SZA) equal to zero (SZA = 0°). The antisolar point is defined as the centre of the night side (SZA = 180°).

4 Results and Discussion

4.1 Atmospheric steady state

According to our results, the middle atmospheres of the CTLE and WTLE adjust to the new radiative and dynamical conditions within 80 days from the start of the simulation. Figure 3 shows the adjustment times of the CTLE and WTLE total ozone column (TOC), and the global mean stratospheric horizontal wind (HW), global mean stratospheric vertical wind (Ω) and global mean stratospheric temperature (T) for the 30 - 40 km altitude range. The temporal evolutions of the PDE TOC, HW, Ω and T are also provided.

The CTLE and the WTLE TOC, HW and Ω adjustment times and values are not significantly altered by the SST change, as can be seen in Figures 3a, 3b and 3c. The % change in their adjustment times is shown in Table 1. The CTLE and WTLE T adjustment times are shown in Figure 3d. As one can see their adjustment times are comparable despite their altered slope and the CTLE values are decreased compared to the WTLE. This difference is also visible in the CTLE and WTLE T global average which will be presented in Section 4.3.

The CTLE and WTLE e-folding times of the TOC, HW, Ω and T along with their PDE equivalents and standard deviations (σ) are shown in Table 1. They are 30, 20, 15 and 40 days, respectively. Therefore, their adjustment times are 60, 40, 30 and 80 days, respectively. A comparison between the CTLE, the WTLE and the PDE σ in Table 1 reveals that the PDE has higher standard deviations (σ_{PDE}) compared to the CTLE and WTLE standard deviations (σ_{CTLE} and σ_{WTLE}).

4.2 Atmospheric circulation

The tidal lock results in a breakdown of the Brewer-Dobson circulation (Figure 4) in both the CTLE and the WTLE. As can be seen in Figures 5, 6, 7, 8 it is replaced by a very different atmospheric circulation. Despite the different atmospheric a troposphere, a stratosphere and a mesosphere is present in both simulations. Below we present a description of the atmospheric circulation of the two simulations.

4.2.1 Vertical wind

The CTLE and WTLE vertical wind are shown in Figures 5 and 6, respectively. The day side air rises as a result of being radiatively heated by the constant shortwave radiation flux it receives from the parent star. On the night side the lack of incoming radiation results in the radiatively cooling of the air which subsequently sinks towards the surface. This results in the appearance of a day side upwelling and a night side downwelling extending from the surface to the mesosphere. Merlis and Schneider (2010) [Mer10] predicted the presence of such a vertical wind setup for the troposphere of a tidally locked Earth-like aquaplanet orbiting a Sun-like star.

A comparison between Figures 5 and 6 reveals that the vertical winds of the two simulations are very similar. They are characterised by different small-scale variability showing vortices and jets of different magnitudes and locations in the CTLE and WLTE simulations. The WTLE atmosphere is characterised by a greater small-scale variability compared to the CTLE. We can, therefore, conclude that the SST change has only a limited effect on the vertical wind.

4.2.2 Horizontal wind

The CTLE and WTLE horizontal wind at stratospheric and mesospheric altitudes are shown in Figures 7 and 8. The CTLE horizontal wind at 24 km is shown in Figure 7a, while the WTLE horizontal wind at 24 km is shown in Figure 8a. A comparison between the two figures reveals that in both simulations, the horizontal wind is characterised by the presence of a global eastward zonal jet stream.

The CTLE and WTLE stratospheric horizontal wind at 36 km is shown in Figures 7b and 8b. In both simulations, a westward global zonal jet stream with an accompanying vortex located at polar latitudes is present. The vortex can be seen on the left hand side of the Southern and Northern Hemispheres in Figures 7b and 8b. The blue coloured regions on the right hand side of the Southern and Northern hemispheres, on the other hand, are regions of low HW speeds. The WTLE horizontal wind is slightly weaker and has a wider jet stream compared to the CTLE.

The situation is different at mesospheric altitudes. At 60 km altitude, the zonal jet stream is replaced by large-scale vortices in both the CTLE and the WTLE, located at different geographical locations.

The mesospheric wave-breaking mechanism may explain this phenomenon. Gravity waves are generated by tropospheric convection followed by the release of latent heat. They then propagate upwards and break when they reach the mesosphere. There they deposit their energy and, in the process, decelerate the wind flow (Nappo (2013) [Nap13]). As a result of the different SST heat distributions in the WTLE and CTLE, the convectively induced gravity waves are generated at different locations with different energy budgets. This leads to different wave-breaking patterns and different gravity wave energy dissipation rates, and gives rise to different horizontal wind circulations patterns in the two simulations.

Gravity waves are also generated through interaction between the planet's surface orography and the lower tropospheric wind field (Nappo (2013) [Nap13]). The encounter between the tropospheric wind and a hill, mountain or mountain range vertically displaces the stably stratified wind flow upwards. This leads to the generation of upwards propagating gravity waves which transport energy and mean-flow momentum towards the middle and upper atmosphere. There it is deposited through the wave-breaking mechanism (Nappo (2013) [Nap13]). In the case of the WTLE and CTLE, both simulations have the same Earth-like orography but different SSTs. As a result different sea and land breezes are generated, which lead to different lower tropospheric horizontal wind distributions (1.4 m/s in average) and therefore different terrain-generated gravity wave distributions. Consequently, the mesospheric energy deposition and wind deceleration are different for the two simulations. Therefore, the reported changes in the mesospheric horizontal wind are possibly induced by differences in the energy and momentum fluxes of the convectively and orographically generated gravity waves of the two simulations.

As can be seen in Figure 3b, the middle atmospheric horizontal wind speeds of the CTLE and the WTLE are slower compared to the PDE. They are also characterised by stronger and wider jet streams and the presence of large scale vortices at various geographical locations. The slower wind speeds could be attributed to the smaller CTLE and WTLE Coriolis force, compared to the PDE.

We can, consequently, conclude that the mesospheric circulation is more sensitive to the underlying SST compared to the stratospheric circulation, as is made evident by the regional differences in the vertical and horizontal wind maps. The discrepancy between the stratospheric and mesospheric circulation can be explained by the fact that the stratospheric dynamics are mainly driven by the insolation of stratospheric ozone.

4.3 **Atmospheric temperature structure**

Next we present the temperature structure of the CTLE and WTLE atmospheres, which can be seen in Figure 9(a). An inspection of Figures 9(a) and 9(b) shows that the WTLE's lower troposphere (z<3 km) is warmer than its CTLE equivalent by a factor of 3.7 K on average. This temperature is generated by the increased upwelling longwave radiation, sensible and latent heat from the underlying WTLE SST which is warmer by approximately 23.7 K compared to the CTLE.

In the 10 km - 15 km region, the WTLE temperature is cooler by 4 K on average compared to the CTLE, as can be seen in the purple highlighted region of Figure 9(b). The adiabatic cooling is generated by the increased upwelling of the subsolar region air, which is radiatively and convectively heated by the warm WTLE SST. This result is in agreement with the studies performed by Rosenlof and Reid (2008) [Ros08], Breasicke and Pyle (2004) [Bra04], Decher and Dameris (2008) [Dec08], who reported the generation of an upper tropospheric cooling by an SST warming.

In the lower stratosphere, between between 18 km and 30 km, the increased upwelling longwave radiation emitted from the warm WTLE SST is absorbed by ozone and radiatively heats the WTLE stratosphere, increasing its temperature by 3.8 on average. This warming is shown in the green highlighted region of Figure 9(b) and is in agreement with expectations of radiative coupling between the surface infrared emission and the lower stratosphere.

To investigate this coupling, we correlate the atmospheric temperature differences with the SST differences obtained from the two simulations. The difference values are calculated by the following equations:

$$\Delta T_{altitude} = T_{WTLE} - T_{CTLE} \tag{2}$$

gives the difference between the WTLE and the CTLE temperatures at a given altitude and geographic location, while

$$\Delta SST = SST_{WTLE} - SST_{CTLE} \tag{3}$$

gives the difference between the WTLE and the CTLE SSTs at a given geographic location.

Figure 10 shows the relationship between the ΔSST and the ΔT at 1 km altitude (ΔT_{1km}). The figure indicates that there is a linear correlation between the two quantities and that the SST changes have a direct radiative effect on the lower tropospheric temperature. Using the least squares method, we determine that the correlation between the ΔSST and the ΔT_{1km} is given by:

$$\Delta T_{24km}(\Delta SST) = (0.028 \pm 0.014)\Delta SST + 0.9 \pm 0.43 \tag{4}$$

Therefore, a 30 K change of the SST corresponds to a 8.6 K change of the lower stratospheric temperature.

Figure 11 shows the relationship between the ΔT at 1 km (ΔT_{1km}) and the ΔT at 24 km altitude (ΔT_{24km}). There is a linear correlation between the two quantities and it demonstrates that the SST variation generates the temperature changes in both the lower troposphere and lower stratosphere. Using the least square method, we determine that the relationship between the ΔT_{1km} and the ΔT_{24km} is given by:

$$\Delta T_{24km}(\Delta T_{1km}) = (0.01 \pm 0.0019)\Delta T_{1km} + 3.8 \pm 0.022 \tag{5}$$

Therefore, a 30 K change of the lower tropospheric temperature corresponds to a 0.3 K change of the lower stratospheric temperature.

Figure 12 shows the relationship between the ΔSST and ΔT_{24km}. As can be seen, a linear correlation exists between the ΔSST and ΔT_{24km}, which suggests that SST changes have a direct radiative effect on the lower stratospheric temperature. Using the least square method, we determine that the correlation between the ΔT_{1km} and the ΔT_{24km} is given by

$$\Delta T_{24km}(\Delta SST) = (0.006 \pm 0.0009)\Delta SST + 3.78 \pm 0.027 \tag{6}$$

Therefore, a 30 K change of the SST corresponds to a 0.18 K change of the lower stratospheric temperature. The inclination of the regression line is rather small. This may be due to the strong mixing and quasi-isothermal behaviour of the lower stratosphere of tidally locked Earth-like planets.

The above results suggest that the increased thermal radiation emitted by the WTLE's surface together with the upwelling sensible and latent heat are absorbed by the lower tropospheric greenhouse gases. They then increase the WTLE's temperature by 8.6 K for every 30 K SST increase. The longwave radiation not absorbed by the lower troposphere reaches the lower stratosphere. There it is absorbed by the ozone 9.6 μm absorption band, a band expected to be present in the spectra of exoplanets capable of sustaining an ozone layer. The result is a stratospheric temperature increase of 0.1 K for every 30 K SST increase. Therefore, a stronger absorption line could be expected for warmer SSTs.

The lower mesospheric temperature (70 km - 80 km) on the other hand, is cooler by 1.13 K on average compared to the CTLE. This temperature difference can be explained using the mesospheric wave-breaking mechanism mentioned above. The higher number and more energetic gravity waves generated by the warm WTLE SST, lead to higher wave momentum deposition in the lower mesosphere and, therefore, to a lower mesospheric adiabatic cooling.

The picture reverses in the upper mesosphere (90 km - 110 km), where the WTLE temperature is higher by 4.3 K on average, compared to the CTLE. This temperature difference may be induced by circulation changes generated by different gravity wave fluxes from below, but the details of the underlying processes remain an open question.

We can therefore conclude, that increased SST leads to enhanced temperatures in the lower stratosphere of a tidally locked Earth-like exoplanet. Our results indicate that this lower stratospheric heating could be due to the enhanced upwelling of infrared radiation from the warm SST. Generally, the difference between the WLTE and the CLTE simulation is smaller than we expected.

4.4 Ozone volume mixing ratio distribution

Figure 13 shows the CTLE and WTLE day side and night side ozone volume mixing ratio O_3VMR distribution. It depicts the cross section of the CTLE and WTLE O_3VMR distribution along the 1st and the 180th meridian, respectively.

A comparison between Figures 13b and 13d reveals that the primary ozone layer (30 - 40 km altitude) is not significantly affected. The increased WTLE middle atmospheric temperature (Figure 9) results in the decrease of the WTLE day side O_3VMR by 1.8% and a night side decrease of 1.27%.

On the other hand, the night time secondary ozone layer, located in both cases in the 85 - 110 km altitude range, is significantly affected. The WTLE O_3VMR is enhanced by 40.5% compared to the CTLE. It is possible that the mesospheric circulation changes, generated by the different upwelling gravity wave fluxes, are responsible for the changes in the secondary ozone layer, but the details of the underlying processes remain an open question.

We can, therefore, conclude that the use of an inaccurate SST in a tidally locked Earth-like exoplanet may significantly affect the secondary ozone layer, while the primary ozone layer remains almost unaffected.

The gap visible at mesospheric altitudes over the WTLE equator in Figure 13a appears as a result of local upwelling of ozone poor air from lower altitudes and is located in the regions close to the Atlas mountains and the Atlantic Ocean. It is possibly generated by upwelling gravity waves, not present in the CTLE.

5 Conclusions

We studied the sensitivity of a tidally locked Earth-like atmosphere to its underlying SST by simulating the atmospheric circulation, temperature and ozone distribution changes generated by two different SST distributions. The first SST distribution represented the well-observed SST of the fast rotating, present day Earth and the simulation using it was called WLTE. The second SST distribution was the SST of a tidally locked Earth-like aquaplanet. It was provided by Merlin and Schneider (2010) [Mer10] and the simulation using it was named CLTE.

Our results show that the tidal lock results in the breakdown of the Brewer-Dobson circulation, which is replaced by a dayside downwelling, centred on the subsolar point and a night side upwelling, centred on the antisolar point. The tidal lock also alters the horizontal wind at all altitudes, resulting in lower wind speeds, wider and stronger jet streams and the appearance of large scale vortices at various locations compared to the PDE, possibly due to the reduced TLE Coriolis force.

We determined that the vertical and horizontal winds are relatively insensitive to changes of the underlying SST. However, the small-scale variability is affected by the SST changes. A strong effect appears at mesospheric altitudes, possibly due to differences in the upwelling gravity wave flux. The dependence of atmospheric tides and planetary waves on the SST distributions could also play a role.

We found that the WTLE lower tropospheric temperature global average is increased, on average, by 3.7 K compared to the CTLE due to the warmer WTLE SST. The WTLE tropospheric warming causes the hot air to ascend and cool adiabatically, generating a cooling of 4 K on average in the altitude regions between 10 km and 15 km, compared to the CTLE. This result is in agreement with past studies of the effects of SST warmings on the Earth's upper troposphere. Between 18 km and 30 km, a stratospheric heating of 3.8 K on average, is present in the WTLE compared to the CTLE, generated by the absorption of the upwelling longwave radiation by ozone through the 9.6 μm line. The enhanced, upwelling longwave radiation is generated by the warmer WTLE SST.

The lower mesospheric cooling (1.13 K) on average is also generated by the warmer WTLE, due to increased wave generation and subsequent wave-breaking in the mesosphere. An upper mesospheric warming (4.3 K) is also present in the WTLE compared to the CTLE but its generation mechanism is currently an open question and under investigation.

The primary ozone layer is not significantly affected by the SST change with the WTLE day side primary ozone layer decreasing by 1.8% and the night time primary ozone layer decreasing by 1.27%. The WTLE secondary ozone layer, on the other hand, increased by 40.5%. The generation mechanism is currently an open question and under investigation.

A future study would aim to explain the physical processes responsible for the increase of the upper mesospheric temperature and strengthening of the secondary ozone layer accompanying the increase in the underlying SST.

List of abbreviations used

ATM = Atmospheric geophysical model
CESM = Community Earth System Model
CICE = Sea-Ice data model
CLM = Community Land Model
CPL = Coupler to CESM
docn = prescribed data ocean model
GLC = Land-Ice geophysical model in CESM
ICE = Sea-Ice geophysical model in CESM
LND = Land geophysical model in CESM
MODIS = Moderate-resolution Imaging Spectroradiometer
NOAA = National Oceanic and Atmospheric Administration
OCN = Ocean geophysical model in CESM
SZA = Solar Zenith Angle
TLE = Tidally Locked Earth
WTLE = Warm Tidally Locked Earth
CTLE = Cold Tidally Locked Earth
TOC = Total O_3 Content
WACCM = Whole Atmosphere Community Climate Model
HW = Horizontal Wind
Ω = Vertical Wind
$Ekin$ = Integrated atmospheric kinetic energy
T = Temperature
O_3VMR = ozone volume mixing ratio

Competing interests

The authors declare that they have no competing interests.

Author's contributions

EP performed the simulations and data analysis. KH contributed to the data analysis and interpretation. PW contributed to the revising of the paper. All authors read and approved the final manuscript.

Acknowledgements

We would like to thank the Center for Space and Habitability (University of Bern) for the PhD fellowship and the Institute of applied Sciences (University of Bern) for the funding that made this study possible. We would like to thank the WACCM forum for the invaluable information it provided. We would also like to thank Schanz Ansgar and Martin Leiner for the computer technical support they provided. Finally we would like to thank Niklaus Kämpfer, and Helmut Lammer for the valuable discussions and advises.

Author details

[1]Institute of Applied Physics, University of Bern Sidlerstrasse 5, Bern, Switzerland. [2]Center for Space and Habitability, University of Bern, Switzerland. [3]Oeschger Centre for Climate Change Research, University of Bern, Switzerland. [4]Physics Institute, University of Bern, Switzerland.

References

Bön11. Bönisch, H, Engel, A, Birner, T, Hoor, P, Tarasick, D.W, Ray, E.A (2011) On the structural changes in the brewer-dobson circulation after 2000. Atmospheric Chemistry & Physics 11, 3937–3948. doi:10.5194/acp-11-3937-2011

Bra04. Braesicke, P, Pyle, J.A (2004) Sensitivity of dynamics and ozone to different representations of ssts in the unified model. Q. J. R. Meteorol. Soc 130, 2033–2045. doi:10.1256/qj.03.183

Che10. Chen, G, Plumb, R.A, Lu, J (2010) Sensitivities of zonal mean atmospheric circulation to sst warming in an aquaplanet model. GEOPHYSICAL RESEARCH LETTERS 37, 12701. doi:10.1029/2010GL043473

Clo95. Clough, S, Iacono, M (1995) Line-by-line calculation of atmospheric fluxes and cooling rates 2. application to carbon dioxide, ozone, methane, nitrous oxide and the halocarbons. J. Geophys. Res. 100, 16519–16535. doi:10.1029/95JD01386

Clo05. Clough, S.A, Shephard, M.W, Mlawer, E.H, Delamere, J.S, Iacono, M.J, Cady-Pereira, K, Boukabara, S, Brown, P.D (2005) Atmospheric radiative transfer modeling: a summary of the aer codes. J. Quant. Spectrosc. Radiat. Transfer 91, 233–244. doi:10.1016/j.jqsrt.2004.05.058

Dav13. Davis, R.N, Du, J, Smith, A.K, Ward, W.E, Mitchell, N.J (2013) The diurnal and semidiurnal tides over Ascension Island (^{o} S, 14^o W) and their interaction with the stratospheric quasi-biennial oscillation: studies with meteor radar, eCMAM and WACCM. Atmospheric Chemistry and Physics 13(18), 9543–9564

Dec08. Deckert, R, Dameris, M (2008) Higher tropical ssts strengthen the tropical upwelling via deep convection. Geophysical Rresearch Letters 35, 10813. doi:10.1029/2008GL033719

God15. Godolt, M, Grenfell, J.L, Hamann-Reinus, A, Kitzmann, D, Kunze, M, Langematz, U, von Paris, P, Patzer, A.B.C, Rauer, H, Stracke, B (2015) 3D climate modeling of Earth-like extrasolar planets orbiting different types of host stars. Planetary and Space Science 111, 62–76. doi:10.1016/j.pss.2015.03.01

Gre07. Grenfell, J.L, Stracke, B, von Paris, P, Patzer, B, Titz, R, Segura, A, Rauer, H (2007) The response of atmospheric chemistry on earthlike planets around F, G and K Stars to small variations in orbital distance. Planetary and Space Science 55, 661–671. doi:10.1016/j.pss.2006.09.00

Gre13. Grenfell, J.L, Gebauer, S, Godolt, M, Palczynski, K, Rauer, H, Stock, J, von Paris, P, Lehmann, R, Selsis, F (2013) Potential Biosignatures in Super-Earth Atmospheres II. Photochemical Responses. Astrobiology 13, 415–438. doi:10.1089/ast.2012.0926

Gre14. Grenfell, J.L, Gebauer, S, Paris, P.v, Godolt, M, Rauer, H (2014) Sensitivity of biosignatures on Earth-like planets orbiting in the habitable zone of cool M-dwarf Stars to varying stellar UV radiation and surface biomass emissions. Planetary and Space Science 98, 66–76. doi:10.1016/j.pss.2013.10.00

Hab96. Haberle, R.M, McKay, C.P, Tyler, D, Reynolds, R.T, Doyle, L.R (1996) Can synchronously rotating planets support an atmosphere? In: Laurance R. Doyle (ed.) Circumstellar Habitable Zones, Proceedings of The First International Conference, Menlo Park, CA, p 29. Travis House Publications

Heg14. Hegyi, B.M, Deng, Y, Black, R.X, Zhou, R (2014) Initial transient response of the winter polar stratospheric vortex to idealized equatorial pacific sea surface temperature anomalies in the ncar waccm. Journal of climate 27, 2699–2713. doi:10.1175/JCLI-D-13-00289.1

Iac08. Iacono, M, Delamere, J, Mlawer, M E.and Shephard, Clough, S, Collins, W (2008) Radiative forcing by long-lived greenhouse gases: Calculations with the aer radiative transfer models. Journal of Geophysical Research: Atmospheres **113**. doi:10.1029/2008JD009944

Jos97. Joshi, M.M, Haberle, R.M, Reynolds, R.T (1997) Simulations of the atmospheres of synchronously rotating terrestrial planets orbiting M dwarfs Conditions for atmospheric collapse and the implications for habitability. Icarus 129, 450–465

Jos03. Joshi, M (2003) Climate Model Studies of Synchronously Rotating Planets. Astrobiology) 3(2), 415–427. doi:10.1089/153110703769016488

Lea00. Lean, J (2000) Evolution of the sun's spectral irradiance since the maunder minimum. Geophys. Res. Lett. 27(16), 2425–2428. doi:10.1029/2000GL000043

Lu12. Lu, X, Liu, H-L, Liu, A.Z, Yue, J, McInerney, J.M, Li, Z (2012) Momentum budget of the migrating diurnal tide in the Whole Atmosphere Community Climate Model at vernal equinox. Journal of Geophysical Research: Atmospheres **17**. doi:http://dx.doi.org/10.1002/2013JA019421

Mer10. Merlis, T.M, Schneider, T (2010) Atmospheric dynamics of Earth-like tidally locked aquaplanets. Journal of Advances in Modeling Earth Systems 2, 13. doi:10.3894/JAMES.2010.2.1

Mla97. Mlawer, E, Taubman, S, Brown, P, Iacono, M, Clough, S (1997) Radiative transfer for inhomogeneous atmospheres: Rrtm, a validated correlated-k model for the longwave. J. Geophys. Res. 102, 16663–16682. doi:10.1029/97JD00237

Nap13. Nappo, C.J (2013) An Introduction to Atmospheric Gravity Waves, Academic Press, ???

Nat15. National Oceanic and Atmospheric Administration's Space Environment Center National Oceanic and Atmospheric Administration's Space Environment Center. `wikipedia:http://www.swpc.noaa.gov/`

Nea12. Neale, R.B, Gettelman, A, Park, S, Chen, C, Lauritzen, P.H, Williamson, D.K, Conley, A.J, Kinnison, D, Marsh, D, Smith, A.K, Vitt, F, Garcia, R, Lamarque, J.F, Mills, M, Tilmes, S, Morrison, H, Cameron-Smith, W, Collins, W.D, Iacono, M.T, Easter, R.C, Liu, X, Ghan, S.J, Rasch, P.J, Taylor, M.A (2012) Description of the NCAR Community Atmosphere Model (CAM 5.0). CESM database. http://www.cesm.ucar.edu/models/cesm1.0/cam/docs/description/cam5_desc.pdf

Ped13. Pedatella, N.M, Liu, H-L (2013) Influence of the El Niño Southern Oscillation on the middle and upper atmosphere. Journal of Geophysical Research: Space Physics 118, 2744–2755. doi:http://dx.doi.org/10.1002/2013JA019421

Ped14. Pedatella, N.M, Fuller-Rowell, T, Wang, H, Jin, H, Miyoshi, Y, Fujiwara, H, Shinagawa, H, Liu, H-L, Sassi, F, Schmidt, H, Matthias, V, Goncharenko, L (2014) The neutral dynamics during the 2009 sudden stratosphere warming simulated by different whole atmosphere models. Journal of Geophysical Research: Space Physics. doi:http://dx.doi.org/10.1002/2013JA019421

Rau11. Rauer, H, Gebauer, S, Paris, P.v, Cabrera, J, Godolt, M, Grenfell, J.L, Belu, A, Selsis, F, Hedelt, P, Schreier, F (2011) Potential Biosignatures in Super-Earth Atmospheres I. Spectral appearance of super-Earths around M dwarfs. Astronomy & Astrophysics 529, 8. doi:10.1051/0004-6361/20101436

Ros08. Rosenlof, K.H, George, C.R (2008) Trends in the temperature and water vapor content of the tropical lower stratosphere: Sea surface connection. JOURNAL OF GEOPHYSICAL RESEARCH 113, 06107. doi:10.1029/2007JD009109

Rug13. Rugheimer, S, Kaltenegger, L, Zsom, A, Segura, A, Sasselov, D (2013) Spectral Fingerprints of Earth-like Planets Around FGK Stars. Astrobiology 13, 251–269. doi:10.1089/ast.2012.088

San06. Sander, e.a S. P. (2006) Chemical Kinetics and Photochemical Data for Use in Atmospheric Studies. Evaluation Number 15. National Aeronautics and Space Administration, Jet Propulsion Laboratory, Pasadena, CA

Seg03. Segura, A, Krelove, K, Kasting, J.F, Sommerlatt, D, Meadows, V, Crisp, D, Cohen, M, Mlawer, E (2003) Ozone Concentrations and Ultraviolet Fluxes on Earth-Like Planets Around Other Stars. Astrobiology 3, 689–708. doi:10.1089/153110703322736024

Seg05. Segura, A, Kasting, J.F, Meadows, V, Cohen, M, Scalo, J, Crisp, D, Butler, R.A.H, Tinetti, G (2005) Biosignatures from Earth-like planets around M-dwarfs. Astrobiology 5, 706–725. doi:10.1089/ast.2005.5.70

Seg10. Segura, A, Walkowicz, L.M, Meadows, V, Kasting, J, Hawley, S (2010) The Effect of a Strong Stellar Flare on the Atmospheric Chemistry of an Earth-like Planet Orbiting an M Dwarf. Astrobiology 10, 751–776. doi:10.1089/ast.2009.037

Sel00. Selsis, F (2000) Review: Physics of Planets I: Darwin and the Atmospheres of Terrestrial Planets. In: Schü"rmann, B. (ed.) Darwin and Astronomy : the Infrared Space Interferometer. ESA Special Publication, vol 451, p 133

Smi12. Smith, K.L, Polvani, L.M, Marsh, D.R (2012) Mitigation of 21st century Antarctic sea ice loss by stratospheric ozone recovery. Geophysical Research Letters **39**(20)

Sol05. Solomon, S, Qiang, L (2005) Solar extreme-ultraviolet irradiance for general circulation models. J. Geophys. Res. 110, 10306. doi:10.1029/2005JA011160

Tan12a. Tan, B, Chu, X, Liu, H-L, , Yamashita, C, Russell, J.M (2012) Atmospheric semidiurnal lunar tide climatology simulated by the whole atmosphere community climate model. Journal of Geophysical Research 117, 1–11. doi:10.1029/2012JA017792

Tan12b. Tan, B, Chu, X, Liu, H-L, , Yamashita, C, Russell, J.M (2012) Parameterization of the inertial gravity waves and generation of the quasi-biennial oscillation. Journal of Geophysical Research: Atmospheres **117**. doi:10.1029/2011JD016778

Tan12c. Tan, B, Chu, X, Liu, H-L, , Yamashita, C, Russell, J.M (2012) Zonal-mean global teleconnection from 15 to 110 km derived from SABER and waccm. Journal of Geophysical Research: Atmospheres 117, 1–11. doi:10.1029/2011JD016750

Tar07. Tarter, J.C, Backus, P.R, Mancinelli, R.L, Aurnou, J.M, Backman, D.E, Basri, G.S, Boss, A.P, Clarke, A, Deming, D, Doyle, L.R, Feigelson, E.D, Freund, F, Grinspoon, D.H, Haberle, R.M, Hauck, S.A.I, Heath, M.J, Henry, T.J, Hollingsworth, J.L, Joshi, M.M, Kilston, S, Liu, M.C, Meikle, E, Reid, I.N, Rothschild, L.J, Scalo, J, Segura, A, Tang, C.M, Tiedje, J.M, Turnbull, M.C, Walkowicz, L.M, Weber, A.L, Young, R.E (2007) A Reappraisal of the Habitability of Planets Around M Dwarf Stars. Astrobiology 7, 30–65. doi:10.1089/ast.2006.012

Ver12. Vertenstein, M, Craig, T, Middleton, A, Feddema, D, Fisher, C (2012) CESM 1.0.4 User's Guide. available from: http://www.cesm.ucar.edu/models/cesm1.0/cesm/cesm_doc_1_0_4/book1.html

Wan05. Wang, Y-M, Lean, J.L, Sheeley, N.R.J (2005) Modeling the sun's magnetic field and irradiance since 1713. The Astrophysical Journal 625(1), 522

Wik15. Wikipedia U.S Standard Atmosphere. `https://en.wikipedia.org/wiki/U.S._Standard_Atmosphere`

Yan13. Yang, J, Cowan, N.B, Abbot, D.S (2013) Stabilizing cloud feedback dramatically expands the habitable zone of tidally locked planets. The Astrophysical Journal Letters 771, 45. doi:10.1088/2041-8205/771/2/L4

Figures

Tables

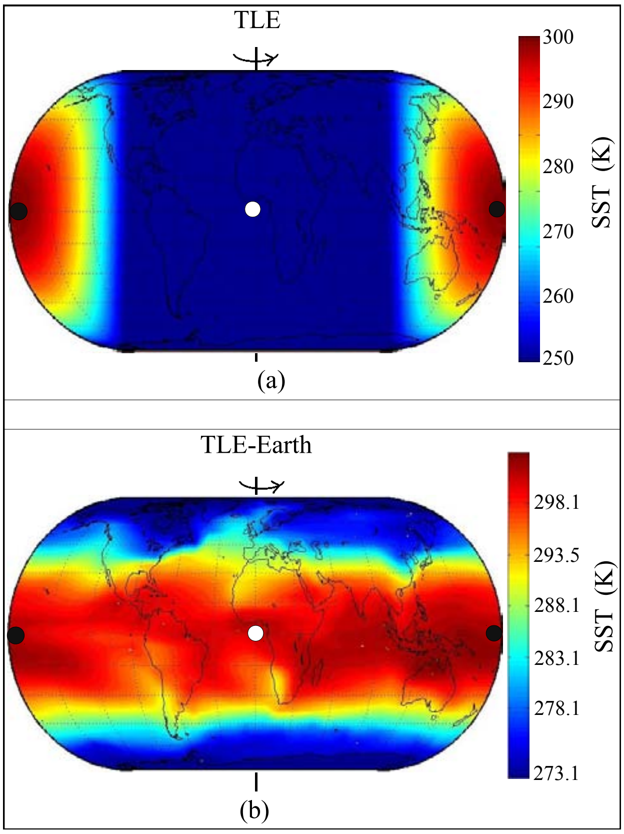

Figure 1 CTLE and WTLE Sea Surface Temperature setups. (a) CTLE: Shades of red indicate high temperatures and define the day side of the planet. Shades of blue indicate low temperature and define the night side of the planet (b) WTLE: Shades of red indicate high temperatures. Shades of blue indicate low temperature. The subsolar point is indicated with a white point on either side of the figure. The antisolar point is indicated with a magenta point in the center of the figure for both simulations.

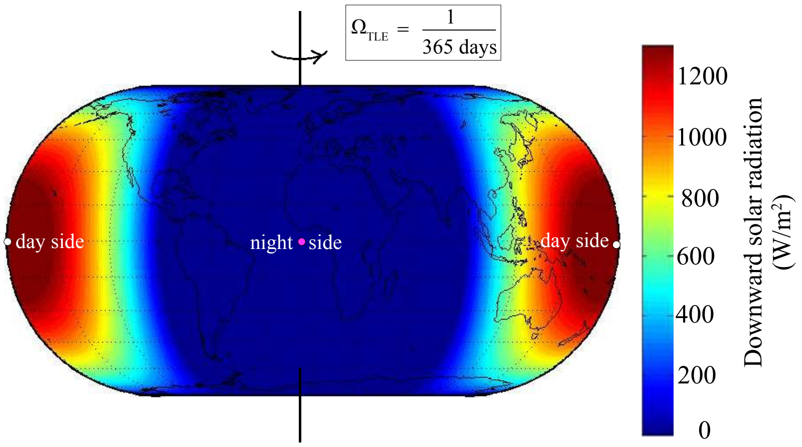

Figure 2 Incident shortwave radiation at the top of the model for both the CTLE and the WTLE Shades of red indicate high incoming solar radiation and define the day side of the planet. Shades of blue indicate low incoming solar radiation. The dark blue visible in the center of the plot indicates a lack of incoming solar radiation and defines the night side of the planet. The subsolar point is indicated with a white point on either side of the figure. It is centred approximately at $(0°, 180°)$ over the Pacific Ocean. The antisolar point is indicated with a magenta point in the center of the figure and is centred approximately at $(0°,0°)$.

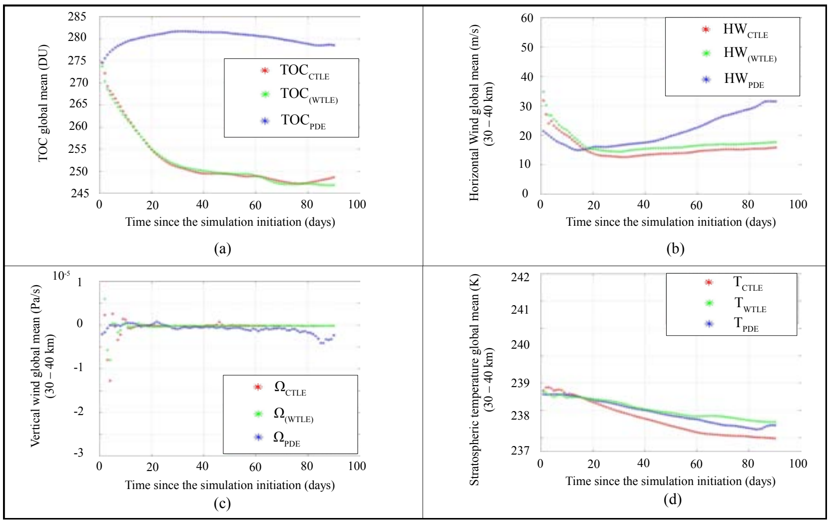

Figure 3 CTLE, WTLE and PDE atmospheric temporal evolution (a) the TOC, (b) the HW, (c) the Ω and (d) the T, respectively. The CTLE and WTLE TOC, HW, and T are exponentially decaying to their steady-state value with an e-folding time of 30, 20 and 40 days, respectively. The CTLE and WTLE vertical winds are exponentially increasing to their steady-state value with an e-folding time of 15 days.

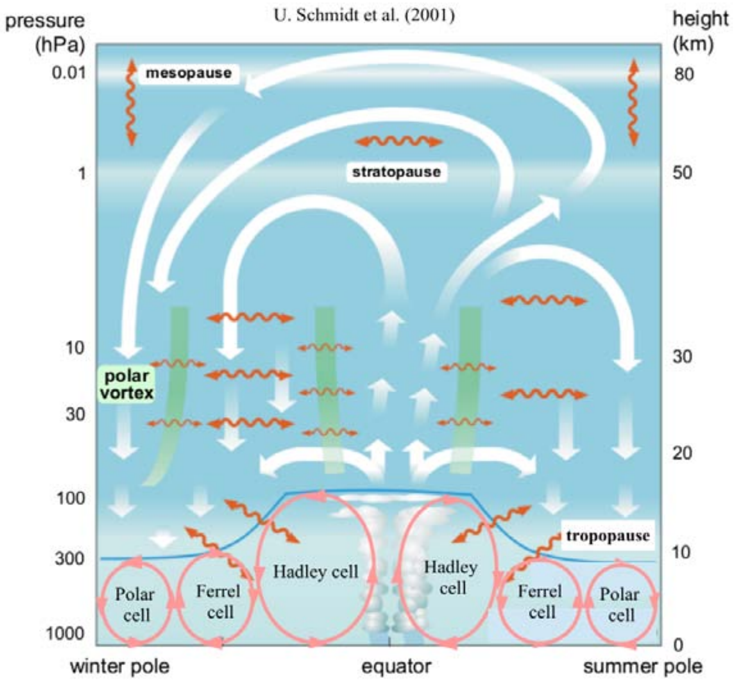

Figure 4 The Brewer Dobson circulation The Brewer-Dobson circulation on Earth. The Hadley, Ferrel and Polar cells are visible in the figure for both hemispheres. The thick white arrows indicate the transformed eulerian mean mass streamfunction. The wavy orange arrows indicate two-way mixing processes. The thick green lines indicate the presence of stratospheric transport and mixing barriers. (Adapted from Bonisch et al. 2011 [Bön11])

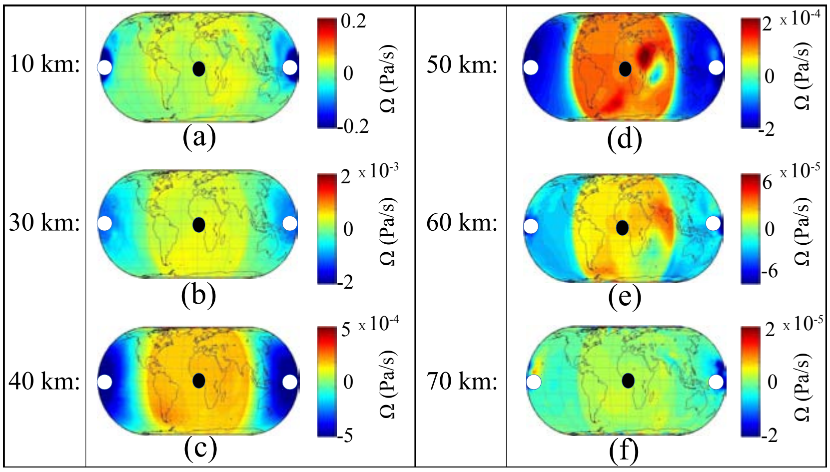

Figure 5 CTLE Longitude-Latitude Vertical wind circulation (a) Vertical wind at 10 km, (b) Vertical wind at 30 km, (c) Vertical wind at 40 km, (d) Vertical wind at 50 km, (e) Vertical wind at 60 km, (f) Vertical wind at 70 km. Warm colours (positive values) indicate a downwelling wind. Cold colours (negative values) indicate an upwelling wind. Each figure is centred on the antisolar point which is indicated with a black dot. The subsolar point is indicated with a white dot on either side of each figure.

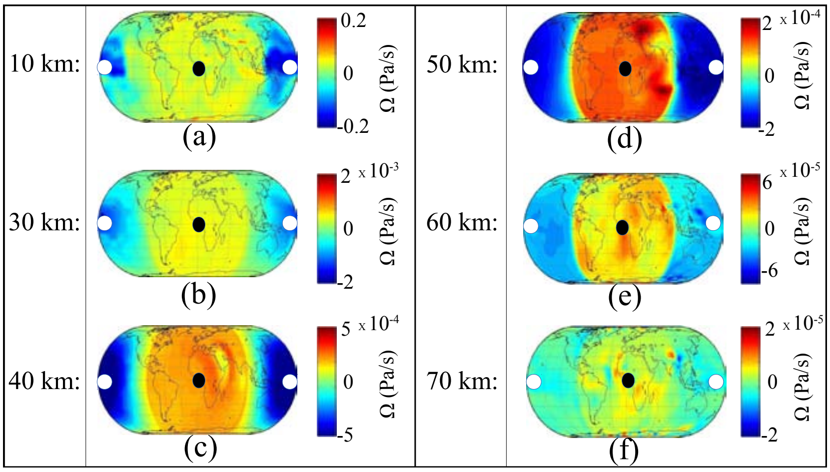

Figure 6 WTLE Longitude-Latitude Vertical wind circulation (a) Vertical wind at 10 km, (b) Vertical wind at 30 km, (c) Vertical wind at 40 km, (d) Vertical wind at 50 km, (e) Vertical wind at 60 km, (f) Vertical wind at 70 km. Warm colours (positive values) indicate a downwelling wind. Cold colours (negative values) indicate an upwelling wind. Each figure is centred on the antisolar point which is indicated with a black dot. The subsolar point is indicated with a white dot on either side of each figure.

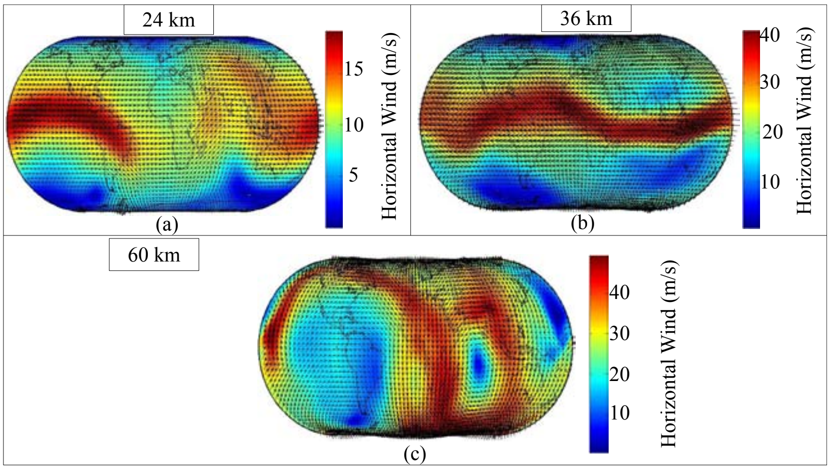

Figure 7 CTLE Horizontal circulation at select altitudes (a) Horizontal wind at 24 km, (b) Horizontal wind at 36 km, (c) Horizontal wind at 60 km. The black arrows indicate the wind vector while the color shading shows the wind speed.

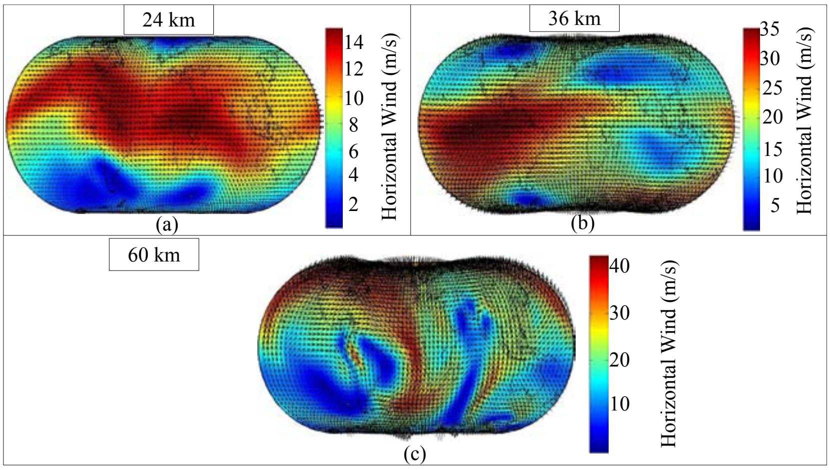

Figure 8 WTLE Horizontal circulation at select altitudes (a) Horizontal wind at 24 km, (b) Horizontal wind at 36 km, (c) Horizontal wind at 60 km. The black arrows indicate the wind vector while the color shading shows the wind speed.

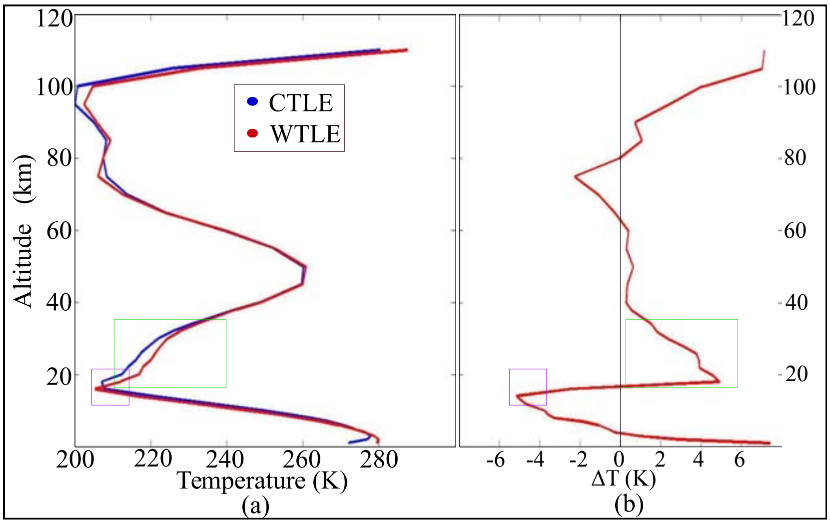

Figure 9 CTLE and WTLE temperature global mean on day 90 The CTLE temperature is depicted using the blue colour line. The WTLE is depicted using the red colour line. The altitude range is 0 - 120 km.

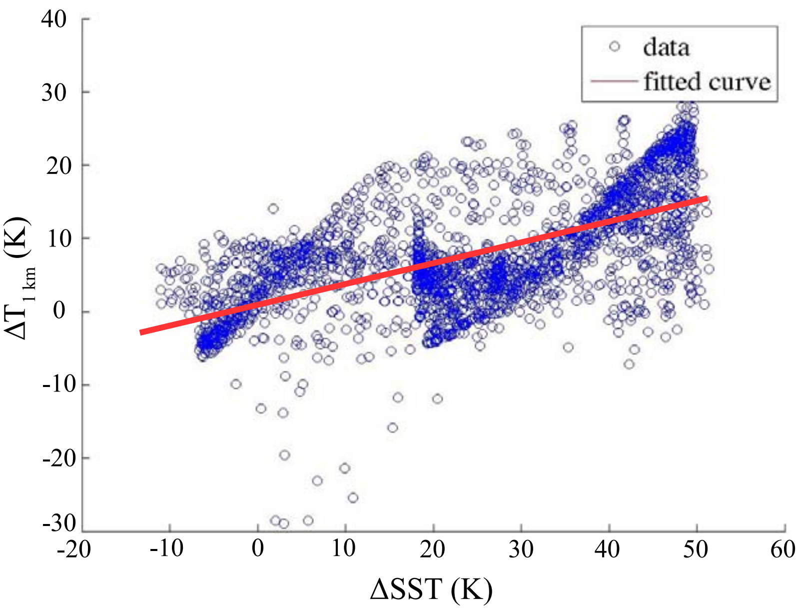

Figure 10 Scatter plot of ΔSST and ΔT_{1km} The plot shows the correlation between the surface ΔSST and the ΔT at 1 km altitude, together with a linear regression to the data.

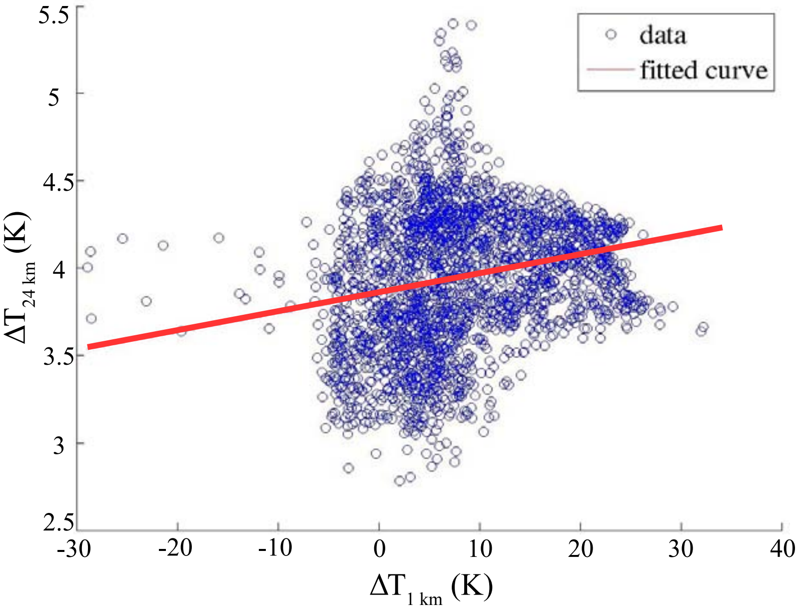

Figure 11 Scatter plot of ΔT_{1km} and ΔT_{24km} The plot shows the correlation between the ΔT at 1 km altitude and the ΔT at 24 km altitude, together with a linear regression to the data.

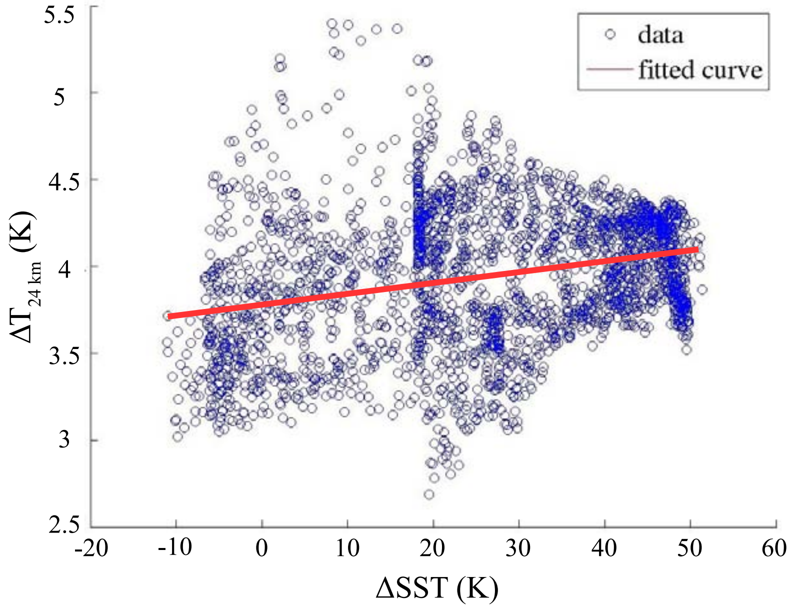

Figure 12 Scatter plot of ΔSST and ΔT_{24km} The plot shows the correlation between the surface ΔSST and the ΔT at 24 km altitude, together with a linear regression to the data.

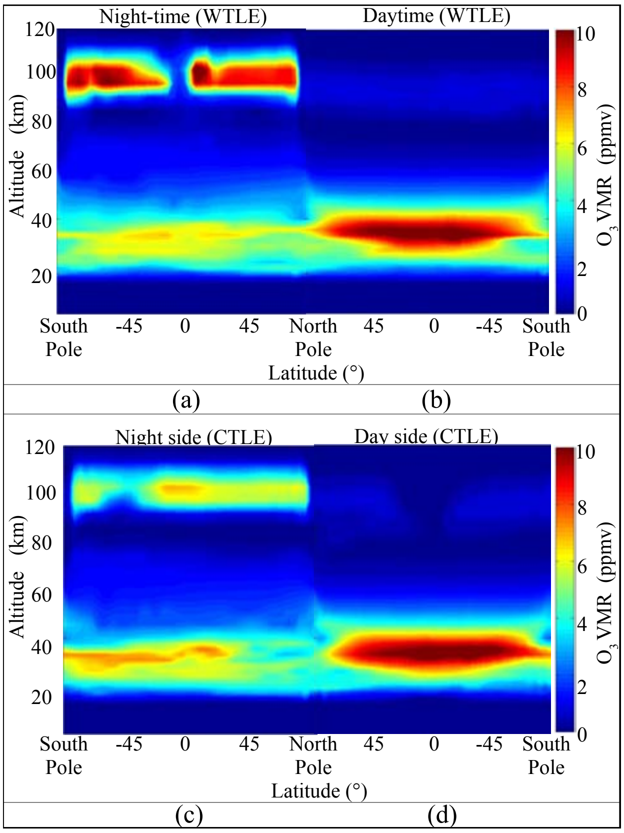

Figure 13 WTLE and CTLE Height-latitude cross section of O_3VMR along the meridian through the subsolar point and the antisolar point (a) Vertical cross section of the WTLE night-time hemisphere. (b) Vertical cross section of the WTLE daytime hemisphere. (c) Vertical cross section of the CTLE night side hemisphere. (d) Vertical cross section of the CTLE day side hemisphere.

Table 1 Comparison of the PDE, CTLE and WTLE TOC and the middle stratospheric HW, Ω and T e-folding times, steady-state mean values and their standard deviations.

	PDE	σ_{PDE}	CTLE	σ_{CTLE}	WTLE	σ_{WTLE}
TOC (DU)	280.1	1.44	248.7	1.00	248.64	1.42
HW (m/s)	21.19	5.21	14.21	1.00	16.10	2.22
Ω (Pa/s)	$-8.6 \cdot 10^{-7}$	$9.6 \cdot 10^{-7}$	$-1.7 \cdot 10^{-7}$	$1.3 \cdot 10^{-7}$	$-2.0 \cdot 10^{-7}$	$-9.7 \cdot 10^{-8}$
$\mathrm{T}_{\mathrm{strat}}$ (K)	239.9	0.85	238.4	0.43	239.6	0.27

Erklärung

gemäss Art. 28 Abs. 2 RSL 05

Name/Vorname:	Proedrou Elisavet
Matrikelnummer:	12-126-553
Studiengang:	Physik Bachelor ☐ Master ☐ Dissertation ☒
Titel der Arbeit:	Titel der Arbeit
Leiter der Arbeit:	PD Dr. Klemens Hocke

Ich erkläre hiermit, dass ich diese Arbeit selbstständig verfasst und keine anderen als die angegebenen Quellen benutzt habe. Alle Stellen, die wörtlich oder sinngemäss aus Quellen entnommen wurden, habe ich als solche gekennzeichnet. Mir ist bekannt, dass andernfalls der Senat gemäss Artikel 36 Absatz 1 Buchstabe o des Gesetzes vom 5. September 1996 über die Universität zum Entzug des auf Grund dieser Arbeit verliehenen Titels berechtigt ist.

Bern, den 22. January 2016

Elisavet Proedrou

Family Name: Proedrou
Given Names: Elisavet

Address: Waldmannstrasse 15, 3027 Bern
Phone: 0 767 104 980
e-mail: bethproedrou@gmail.com

Date of Birth: 01/04/1985
Place of Birth: Kavala, Greece
Nationality: Greek

Swiss residence permit: B

Education

07.2012 - Current **PhD. in Physics**
University of Bern, Switzerland
Expected graduation date : February 2016

01.10.2009 - 31.11.2011 **Master in Physics**
University of Bonn, Germany
Grade: gut (2.2) | Swiss equivalent: 5.0

03.07.2002 - 26.3.2009 **Bachelor in Physics**
University of Thessaloniki, Greece
Grade: 8.14/10 | Swiss equivalent: 5.0

03.07.2002 **Matura**
1st Eniaio Lykeio of Kavala, Greece
Grade: 18/20 | Swiss equivalent: 5.5

Job Experience

7.2012 – Current **Research assistant (Doctoral candidate)**
Institute of Applied Physics, University of Bern

11.2010 – 06.2011 **Teaching assistant for two graduate compulsory courses**
Argenlander Institute, University of Bonn, Germany

11.2004 – 06.2007 **Teaching assistant for two undergraduate courses**
Department of Physics, Aristoteleio University of Thessaloniki, Greece

Language Skills

Greek: Native speaker
English: Full professional proficiency
German: Fluent

Technical skills

Programming: Matlab, Bash, Fortran

Quantitative analysis: Matlab, Origin

Office suites: Microsoft Office:
- Word, Excel, Power Point

OpenOffice/LibreOffice:
- Writer, Calc, Impress

Others: Linux/UNIX systems
Monte Carlo simulations

Publications

- Proedrou and Hocke: A traveling atmospheric disturbance generated by a soil colour change in a high-resolution climate model experiment. *Geoscience Letters* 2014 **1**:13, doi:10.1186/s40562-014-0013-9
- Characterizing the three-dimensional ozone distribution of a tidally locked Earth-like planet. Submitted in Earth, Planets and Space on March 2015
- The middle atmospheric circulation of a tidally locked Earth-like planet and the role of the sea surface temperature. Submitted in Progress in Earth and Planetary Science on June 2015

Interests

Renewable energy sources, infrastructure and distribution networks
Language learning (currently: German, Japanese)

References

References available upon request.